Republic of Iraq
Ministry of Higher Education
and Scientific Research
University of Babylon
College of Education for
Pure Sciences
Department of Physics

Efficiency of CuO Nanoparticle Doped Sb_2O_3/ Etching Si Solar Cell

A Dissertation
Submitted to the Council of the College of Education
for Pure Sciences University of Babylon in Partial Fulfillment of
the Requirement for the Degree Doctorate of Philosophy in
Education/ Physics

By

Ali Abd Aoun Attia Hamad Al-Azawi
B.Sc. in physics
(University of Babylon, 2010)
M.Sc. in physics
(University of Babylon, 2019)

Supervised by

Prof. Dr. Fouad Shaker Hashim **Prof. Dr. Khalid Haneen Abass**

2023 A.D. 1445 A.H.

بِسْمِ اللهِ الرَّحْمٰنِ الرَّحِيمِ

هُوَ ٱلَّذِى
جَعَلَ ٱلشَّمْسَ ضِيَآءً وَٱلْقَمَرَ نُورًا وَقَدَّرَهُۥ
مَنَازِلَ لِتَعْلَمُوا۟ عَدَدَ ٱلسِّنِينَ وَٱلْحِسَابَ ۚ مَا
خَلَقَ ٱللَّهُ ذَٰلِكَ إِلَّا بِٱلْحَقِّ ۚ يُفَصِّلُ ٱلْءَايَٰتِ
لِقَوْمٍ يَعْلَمُونَ

صَدَقَ اللهُ العَظِيم

سورة يونس الاية(5)

Supervisor's certificate

We certify that this thesis entitled " **Efficiency of CuO Nanoparticle Doped Sb_2O_3/Etching Si Solar Cell**" is prepared by the student **(Ali Abd Aoun Attia Hamad Al-Azawi)** under our supervision at the College of Education for Pure Sciences, University of Babylon as partial fulfilment of the requirement for the Degree of Doctorate Philosophe in Physical Sciences.

Signature:	***Signature:***
Name: Dr. Fouad S. Hashim	Name: Dr. Khalid Haneen Abass
Title: Professor	Title: Professor
(Supervisor)	(Supervisor)
Date: / / 2023	Date: / / 2023

Head of the Department Certificate

In view of the available recommendations, I forward this thesis for debate by the examining committee.

***Signature*:**
Name: Dr. Khalid Haneen Abass
Title: Professor
(Head of Physics Department)
Date: / / 2023

Certification of Scientific Expert

I certify that I have read the scientific content of this dissertation **"Efficiency of CuO Nanoparticle Doped Sb_2O_3/Etching Si Solar Cell"** and I have approved this dissertation is qualified for debate.

Signature:

Name: Dr. Mushtaq Talib Jassim

Title: Asst. Prof.

Address: University of Al- Qadisiyah

Date: / / 2023

Certification of Scientific Expert

I certify that I have read the scientific content of this dissertation **"Efficiency of CuO Nanoparticle Doped Sb_2O_3/Etching Si Solar Cell"** and I have approved this dissertation is qualified for debate.

Signature:

Name: Dr. Haider Mohammed Jawad

Title: Prof.

Address: University of Kufa

Date: / / 2023

Certification of linguistic Expert

I certify that I have read this dissertation entitled **" Efficiency of CuO Nanoparticle Doped Sb_2O_3/Etching Si Solar Cell"** and corrected its grammatical mistakes; therefore, it has qualified for debate.

Signature:

Name: Dr. Ahmed Rawdhan Salman

Title: Asst. Prof.

Address: AL- Mustaqbal University

Date: / / 2023

Dedication

To my family

my (father, mother, brothers and sisters, wife and daughters)

Ali✍

Acknowledgments

Praise be to Allah lord of the world, and best prayers and peace be unto his best messenger Mohammed, and his pure descendants.

I want to express my deep gratitude and appreciation to my two supervisors, Prof. Dr. **Fouad S. Hashim** and Prof. Dr. **Khalid Haneen Abass** for their guidance, suggestions, and encouragement throughout the research work. Without them, this thesis work would have been impossible.

I want to thank the staff of Department of Physics in College of Education for Pure Sciences in university of Babylon for their kind attention and encouragement.

Finally, I would like to thank my family for their help and encouragement and every one who helped me during the preparation of this thesis.

Ali✍

Summary

Silicon solar cell technology currently dominates the market and has a high cost. Research into new materials (thin film) for producing cheaper and more efficient solar cells must be intensified to exploit solar energy. In this work, the preparation of pure and CuO-doped Sb_2O_3 nanofilms with various doping ratios (0.02, 0.04, and 0.06) wt.% and different thicknesses (20, 30, and 40) nm deposited on glass (morphology, structural, optical, and electrical properties) and laser-etched p-Si (solar cell efficiency properties) substrates in a vacuum environment (1×10^{-6}) mbar through a thermal evaporation chamber with the rate of deposition 0.3 $nm.s^{-1}$. The prepared films are subjected to heat treatment (annealing) at 473 K for 2 hours.

X-ray diffraction result showed that the pure Sb_2O_3 nanofilms have no distinguishing peaks. In contrast, the phase structure of Sb_2O_3:(0.02, 0.04, and 0.06) wt.%CuO nanofilms at a thickness of 40 nm shows the one small peak existence at 2θ = (31.932°, 31.894°, and 31.945°) respectively, corresponding to the Miller indices (040).

AFM analysis of pure and CuO-doped Sb_2O_3 nanofilms shows a uniform granular surface morphology, homogeneous distribution, and pervasion of CuO particles within Sb_2O_3 matrix. SEM analysis of nanofilms exhibits a smooth surface devoid of islands and voids and consisting of small spherical grain-size nanoparticles (NPs). The particle size of nanofilms increases with increasing thickness and doped ratio.

The optical properties increase (absorbance, absorption coefficient, optical constants) with increasing thickness and ratio doping for nanofilms. These features can be employed for nanofilms in solar cells as the energy gap for direct transition reduces due to the broadening of the sublevels (Urbach energy), which agrees with the value of the average energy gap from the energy of the simple oscillator (Wemple and DiDomenico).

Material composition changes (doping and thickness) lead to surface and volume energy loss functions change. Due to the very low thickness of the nanofilm, it was found that the surface energy is greater than the volume energy. Hall coefficient decreased, and the carrier concentration in the samples increased with thickness and doped ratio for nanofilms.

The solar cell performance and efficiency were evaluated using I-V characteristic curves under dark and illumination for Sb_2O_3/etched p-Si and Sb_2O_3:CuO/etched p-Si. It was observed that the efficiency increased with increasing thicknesses of Sb_2O_3 nanofilms and increased with added CuO to Sb_2O_3. The highest efficiency was 5.965% with (V_{oc} of 11 V, I_{sc} of 3 mA/cm^2, and F.F of 0.180) for pure Sb_2O_3 nanofilms at a thickness of 40 nm. Also, the highest efficiency was 7.625% with (V_{oc} of 12 V, I_{sc} of 3.2 mA/cm^2, and F.F of 0.198) for Sb_2O_3:0.06wt.%CuO at the same thickness. This work's efficiency enhancement can be ascribed to the modified properties of Sb_2O_3 nanofilms due to homogeneity achieved by controlling the deposition process, little thickness, and the high surface area created by the small particle size and laser etching process.

List of Contents

Chapter Three: Experimental Work

Chapter Four: Results and Discussion

List of Symbols and Abbreviations

Symbols	Description
0D	Zero dimensional
1D	One dimensional
2D	Two dimensional
3D	Three dimensional
A	Absorbance
AFM	Atomic force microscope
Ag	Silver
Al	Aluminum
ALE	Atomic layer epitaxy
a-Si	Amorphous silicon
BHJ	Bulk heterojunction
C.B	Conduction band
CdTe	Cadmium telluride
c-Si	Crystalline silicon
Cu_2O	Copper(I) oxide
$CuIn_xGa_{1-x}Se_2$	Copper indium gallium diselenide
CuO	Copper(II) oxide
CVD	Chemical vapour deposition
DC	Direct current
DOS	Density of states
DSSCs	Dye-sensitized solar cells
E_H	Hall electric field
E_U	Urbach energy
FESEM	Field emission scanning electron microscope
FF	Fill Factor
FTIR	Fourier transforms infra-red
FWHM	Full width at the half of the maximum
GaAs	Gallium arsenide
He-Ne	Helium-Neon laser
HJ	Heterojunction
$h\nu$	Photon energy
IR	Infrared

I_{sc}	Short circuit current
ITO	Indium tin oxide
I-V	Current-voltage
M.P	Melting point
MBE	Molecular beam epitaxy
Nd: YAG	Neodymium YAG laser
NIR	Near-infrared
NPs	Nanoparticles
OSCs	Organic solar cells
P_3HT	Poly(3-hexylthiophene)
PCE	Power conversion efficiency
P_{max}	Power maximum
PSCs	Perovskite solar cells
PV	Photovoltaic
PVD	Physical vapour deposition
R_S	Series resistance
R_{SH}	Shunt resistance
RT	Room temperature
SELF	Surface Energy Loss Function
SEM	Scanning electron microscope
T	Transmittance
UV	Ultraviolet
V.B	Valence band
VBO	Valence band offset
V_H	Hall voltage
VELF	Volume Energy Loss Function
Vis	Visible
V_{oc}	Open circuit voltage
WDD	Wemple–DiDomenico
XRD	X-ray diffraction
α-Sb_2O_3	Cubic phase senarmontite
β-Sb_2O_3	Orthorhombic phase valentinite
d_{hkl}	Inter-planar distant (i.e. atoms or ions or molecules).
μ	Mobility

E_g^{opt}	Optical band gap
E_d	Dispersion energy
E_o	Effective single oscillator
k_o	Extinction coefficient
M_{-1}, M_{-3}	Moments of optical spectra
p-Si	p type Silicon
n	Refractive index
P	Positive
R	Reflectance
R_H	Hall coefficient
t	Thickness
$\varepsilon_{(r)}$	Real dielectric constant
$\varepsilon_{(i)}$	Imaginary dielectric constant
η	Conversion efficiency
θ	Theta (Bragg diffraction angle)
λ	Wavelength
ρ	Resistivity
Ω	Ohm
α	Absorption coefficient

List of Figures

List of Tables

Chapter One
Introduction

1.1 Introduction

Energy is essential for human development, and throughout the industrial revolution, people obtained the necessary energy by burning carbon-based fossil fuels like coal, oil, and gas. The widespread use of carbon-based fossil fuels has led to environmental degradation; moreover, the use of fossil fuels is unnecessarily expensive, decreases natural resources that can't be replaced, and contributes to global warming at a time when its effects are becoming more apparent [1]. It is desirable, therefore, to find ways that reduce these negatives. To address this problem, we must rapidly adopt renewable energy sources like hydro, biomass, solar, wind, etc., to meet our future energy needs and mitigate additional environmental damage. To achieve "Energy for All," it is necessary to rapidly adopt renewable energy sources like solar power, which tops the list [2, 3].

Sunlight consists of electromagnetic radiation in ultraviolet (UV), visible light, and infrared (IR) radiation. The solar spectrum reaching the earth’s surface undergoes various absorptions in the air atmosphere, and the average solar energy falling on the earth’s surface is generally known as air-mass 1.5 irradiation, equal to approximately 100 $mWcm^{-2}$. This quantity is equal to ~1.0 kW of power falling on every square meter, which humankind has not yet effectively utilized [4]. Traditionally, there are two ways of capturing solar energy. One method is to absorb mainly the heat energy (or IR radiations), generally known as solar thermal technology. The second method converts UV and visible light (photons) directly into electricity (measured in volts). Since the photons are directly converted into volts, this method is known as ‘photovoltaic conversion’ (PV) [5–7].

1.1.1 Thin film solar cell

Materials science has changed the ability to conceive novel materials with unique chemical, physical, and mechanical properties. Technology increasingly requires thin films for their unique electrical, magnetic, and optical properties, including transmission, reflection, absorption, hardness, abrasion resistance, corrosion, permeation, and electrical behavior [8]. As a result of the unique characteristic features of the film's thickness, structure, and geometry, studies of the thin film have indirectly or directly given rise to several new study disciplines in solid state chemistry and physics [9].

The expression of the thin film is used to describe a film with a thickness between a few nanometers and a few micrometers, which was created ab initio by the random nucleation and growth processes of individually condensing atomic, ionic, and molecular species on a substrate. Many deposition factors and perhaps thickness all have a role in determining how a material behaves: structural, chemical, metallurgical, and physical properties [10].

The adoption of thin film technology and the use of gap semiconductors (which absorb solar radiation with a thickness that is much smaller than the thickness of the silicon wafer) deposited on a cheap and large-area substrate (glass, metal foil or plastic) is one of the most ways to reduce the cost of solar modules and significantly increase their production volume [11, 12].

Thin film solar cells are a viable option compared to crystalline silicon (c-Si) solar cells due to their low cost and ease of manufacturing. The c-Si solar cells are made of highly pure silicon wafers that account for 50% of the total module cost. As thin film solar cells are made of materials having higher optical absorption than c-Si, thickness of the photon-absorbing layer is on the order of a few hundred nanometers. In contrast, the typical thickness of the c-Si layer in a solar cell is a few hundred micrometers [13]. The energy-payback time for a thin film solar cell is almost half compared to a c-Si solar cell. Also, the flexibility of some thin film solar cells makes them attractive for portable purposes such as camping and installation on nonplanar surfaces such as car roofs. Another benefit of thin film solar cells is the control over the composition of a material, i.e., the material's bandgap can be varied by varying the material composition [14].

Manufacturing thin film solar modules based on direct-gap semiconductors does not require costly high purification and crystallinity of the material as it is needed to produce modules based on crystalline, multi-crystalline, or ribbon silicon. Thin film technology has several other significant merits. While Si devices are manufactured from wafers or ribbons and then processed and assembled to form modules, in thin film technology many cells are simultaneously made and formed as a module. The layers of solar cells are deposited sequentially on moving substrates in a continuous highly automated production line (conveyor system) and, importantly, at temperatures not exceeding (200-650) ^{o}C compared with (800-1450) ^{o}C for the main processes of c-Si. This minimises handling and facilitates automation leading to the so-called monolithic integration [11].

Thin film materials have been used in many applications including semiconductor devices, transistors, and solar cells [15, 16]. The wide varieties of thin film materials, their deposition processing and fabrication techniques, spectroscopic characterization, and optical characterization probes are used to produce the devices. Thin film solar cells are fabricated using physical and chemical vapor deposition [17]. The physical deposition processes include vacuum evaporation, laser ablation, molecular beam epitaxy, and sputtering. The chemical deposition processes comprise gas phase deposition methods and solution techniques. The gas phase methods are chemical vapour deposition (CVD) and atomic layer epitaxy (ALE). In contrast, spray pyrolysis, sol-gel, spin, and dip-coating methods employ precursor solutions [18], as shown in Figure (1.1).

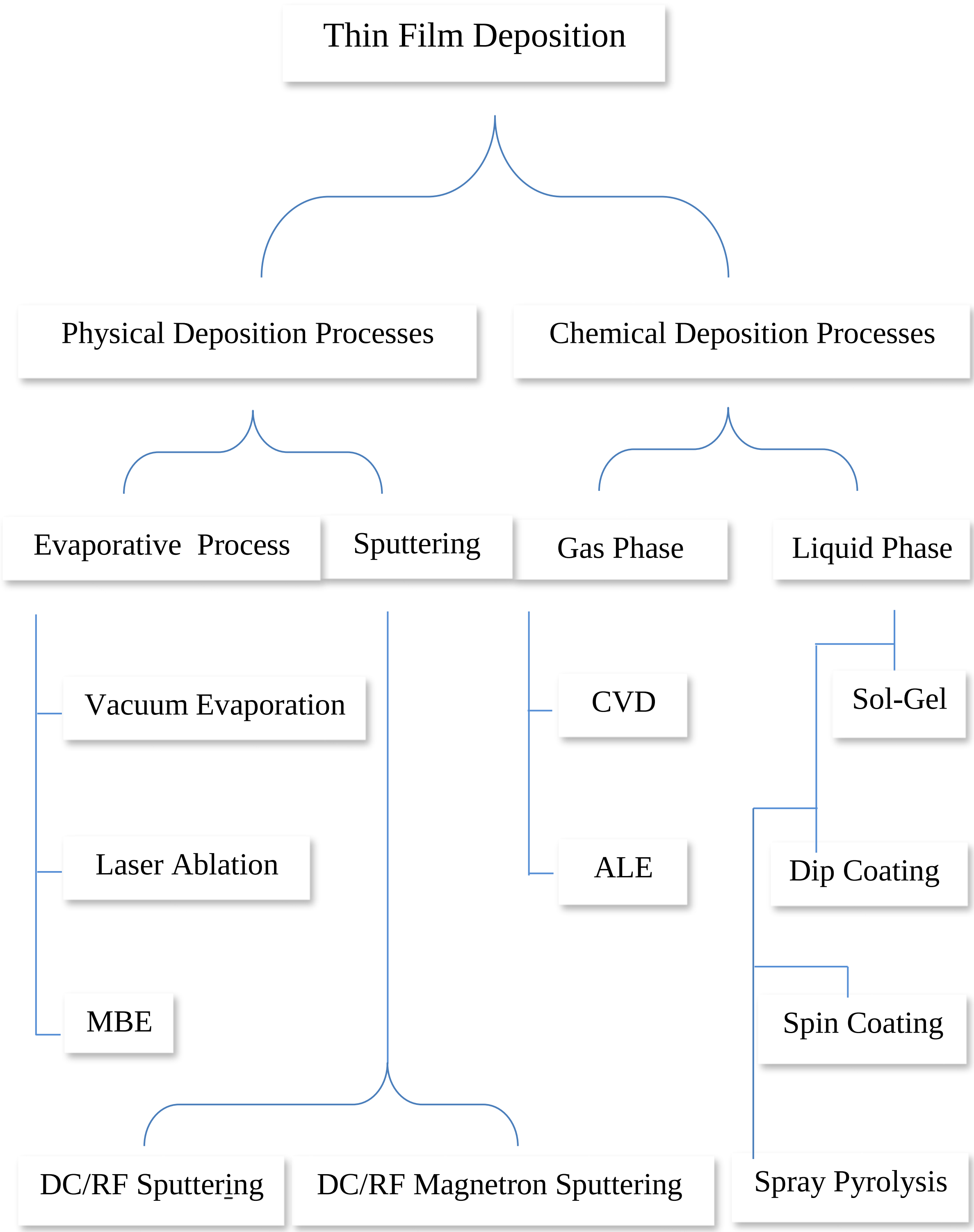

Fig. 1.1: Different physical and chemical thin film deposition processes [18]**.**

1.1.2 Photovoltaic solar cell

Researchers have advanced solar technologies over the past several decades and learned how to use materials to create solar converters rivaling nature's. One renewable energy technology uses solar energy, which can be converted into heat and electricity. Different ways of converting sunlight into electricity have found practical applications [5]. Power plants are widespread in which water is heated by sunlight-concentrating devices, resulting in high temperature steam and the operation of an electric generator. However, solar cells are much more attractive due to the direct conversion of solar radiation into electricity. This is the so-called photovoltaics [15].

The history of the solar cell starts in the late 19th century with the principles of photography. It was discovered that silver chloride (and other silver halides) respond to light. The first photovoltaic cells were measured by Becquerel and others around 1839. Copper Oxide or silver-halide-coated metal electrodes were immersed in an electrolyte solution, creating a “wet photoelectrochemical” effect. Such solar cells were developed in 1954 at Bell Labs by D. M. Chapman and C. S. Fuller using a solid state semiconductor junction. These first silicon solar cells resembled those of today but produced less than a watt of power. Today’s PV solar panels are widely used to power satellites and villages in third world countries to produce power for buildings and utility scale power generation. They are produced in quantities of several hundred megawatts per year [19].

Homojunction solar cells can be fabricated when the junction is constructed from a single semiconductor type, such as a crystalline silicon solar cell. The solar cell may be called a heterojunction cell if two different semiconductors fabricate the solar cell [20, 21].

In general, photovoltaic cells have at least two thin layers (one on top of the other), each having various purposely added impurities called dopants.

One layer is n-type, which contains an addition of (negative) electrons, while the other is p-type and has (positive) holes. These two layer structures, called a p-n junction, result in a (built-in) electric field. The internal electric field causes free holes and electrons near the p-n junction to travel in opposite directions when photons offer them. As a result, the holes go to the p side and the electrons to the n side, resulting in an electromotive force between the two layers p-n, with the positive p-side and negative n-side. Furthermore, a voltage may exist when p and n-type sides have been connected to a load using wires, such as a light bulb, and an electric current flows through the same load [22]. Their actual power output depends on the intensity of sunlight, the operating temperature of the module, and other factors. Additional components, such as electrical switches, diode-protection circuits, inverters, and batteries, connect the PV output with the electrical load. The resulting assembly of components is known as the PV system [23–25], as shown in Figure (1.2).

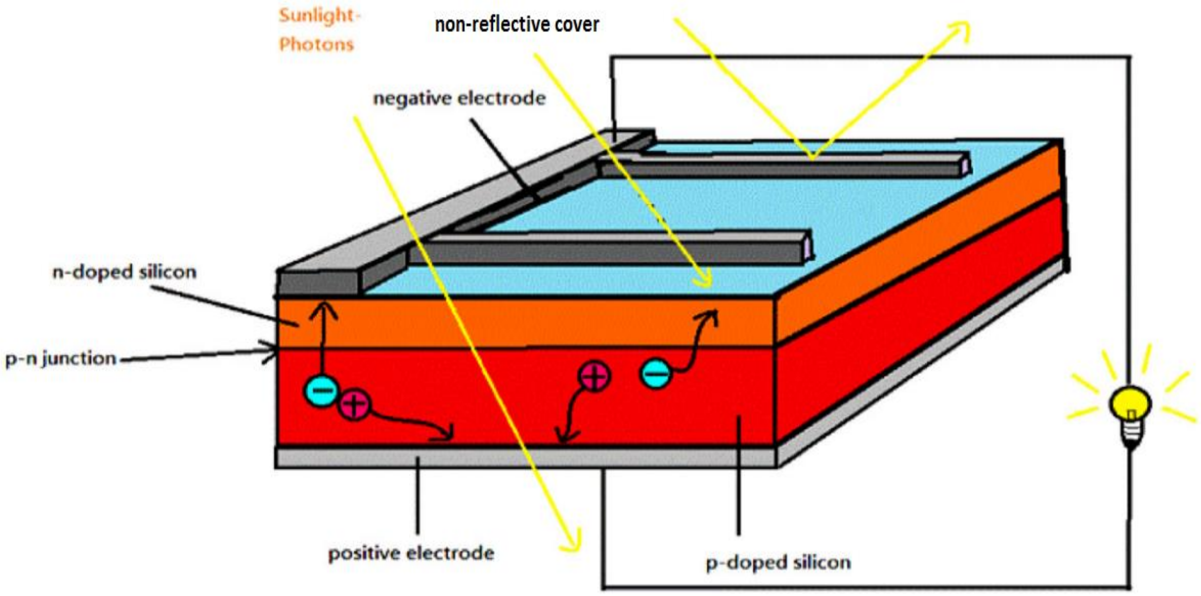

Fig. 1.2: Photovoltaic cell schematic for p-type and n-type layers [25]**.**

Three generations have been involved in the advancement of solar cells. **The first generation** solar cells based on silicon (Si) were highly appreciated owing to their remarkable efficiency (in terms of single-cell devices). Moreover, as one of the most abundant materials with an indirect band gap of 1.12 eV, Si is important for the absorption of photons in the visible region. This generation is well established and commercially mature, covering about 80% of the solar market [26]. First generation solar cells include three types of Si: single crystalline with an efficiency of approximately 28% [27], multi crystalline with a lower efficiency of approximately 21% [28], and amorphous with a substantially lower efficiency of approximately 16% [29]. However, first generation solar cells faced several issues regarding their low efficiency. Furthermore, the limited availability of highly purified Si makes the large-scale production of Si-based solar cells infeasible.

The second generation is based on thin film semiconductors. The major types of thin film technologies exist as amorphous Si [30], copper indium gallium diselenide ($CuInxGa1\text{-}xSe_2$; CIGS) [31], cadmium telluride (CdTe), and Gallium arsenide (GaAs) [32]. Of all types, amorphous Si is the most widely used solar cell material because of its application in manufacturing existing Si solar cell technology [30]. However, amorphous Si-based solar cells are less efficient in light absorption than others and suffer from photodegradation over time. GaAs solar cells have exhibited the highest efficiencies of approximately 27.6% [33], followed by CIGS cells at approximately 17% [34], CdTe cells at approximately 21% [35]. In contrast, amorphous Si cells have an efficiency of 10.2% for single junction and 12.69% for aSi:H/hydrogenated microcrystalline silicon [36]. Thin film solar cells have been established in research communities and industries owing to their affordable production costs and relatively low raw material requirements with new features like flexibility.

The third generation of solar cells is based on the possibility of exploiting novel materials and architectures, aiming at very cheap productions and very high efficiencies. Among them are dye-sensitized solar cells (DSSCs) as well as organic or polymer solar cells, quantum dot sensitized solar cells, and perovskite solar cells (PSCs) [37]. However, organic solar cell (OSC) efficiency is not competitive with other solar cell designs. The highest reported efficiency of this type of solar cell is only 15.2%, although its construction is very cost effective [38]. Although DSSCs involve a reversible and regenerative process, the highest efficiency reported for these cell types is only 11%, owing to their photodegradation over a short period and dye leakage issues [39]. The theoretical maximum efficiency of single-cell solar cells is approximately 31%. Moreover, two-cell and three-cell solar cells exhibit a maximum efficiency of approximately 42.5% and 48.6%, respectively [40, 41]. Figure (1.3) presents schematics of the representative structures of the first, second, and third-generation solar cells [27].

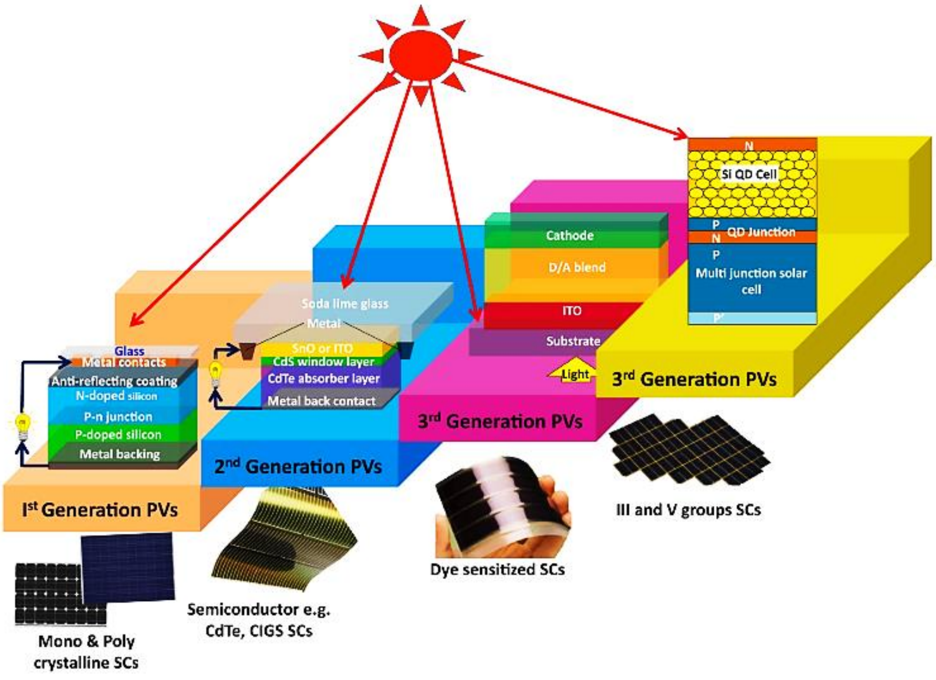

Fig. 1.3: Schematic of representative structures of first, second, and third-generation SCs [27].

1.2 Nanomaterials

Historically, the word nanomaterial has been used to refer to products derived from nanotechnology. The term nanotechnology has been defined since 1974 by Professor Norio Taniguchi as a direct extension of silicon machining down into regions smaller than one μm [42]. In recent years, several definitions of the term nanomaterial have been proposed by various international organizations and committees, all of which have indicated an upper dimension limit of 100 nm [43].

Nanomaterials can exhibit unique physical and chemical properties not seen in their bulk counterparts. An important characteristic that distinguishes nanomaterials from bulk is the reduction of scale, resulting in materials having unique properties arising from their nanoscale dimensions. The most obvious effect associated with scale reduction is the much larger specific surface area or surface area per unit mass [44]. An increase in surface area implies the existence of more surface atoms. As surface atoms have fewer neighbors than atoms in bulk, an increase in surface area will result in more atoms having lower coordination and unsatisfied bonds. Such surface atoms are overall less stable than bulk atoms, which means that the surface of nanomaterials is more reactive than their bulk counterparts [45].

The size reduction thus results in the quantum confinement effect, in which the edges of the nanoparticle confine the excitons in three dimensions. This increases band gap energy as the particle is smaller, causing the previously continuous valence and conduction bands to split into discrete energy levels similar to those in atomic orbitals [46]. The nanomaterials may be assorted as follows: quantum dots (zero-dimensional), quantum wires (one-dimensional), quantum wells (two-dimensional), and bulk materials (three-dimensional) [47], as exposed in Table (1.1).

Table (1.1): Classification of the main types of nanomaterials [47]**.**

Materials	**Criteria**	**Examples**
Quantum dots **(0D)**	All dimensions in the nanoscale.	Nanocrystals, Nanoparticles
Quantum wires **(1D)**	One dimension is outside the nanoscale.	Nanotubes, Nanorods, Nanofibers
Quantum well **(2D)**	Two dimensions are outside the nano scale.	Thin-film, Coatings
Bulk (3D)	All dimensions above 100 nm	Multinanolayers, bundles of nanowires

Nanostructures have completely different densities of electronic states predicted by simple particles in box type models of quantum mechanics. The density of states, which describes the electronic states with energy in the band diagram of the 0D, 1D, 2D, and bulk materials are shown in Figure (1.4) [48].

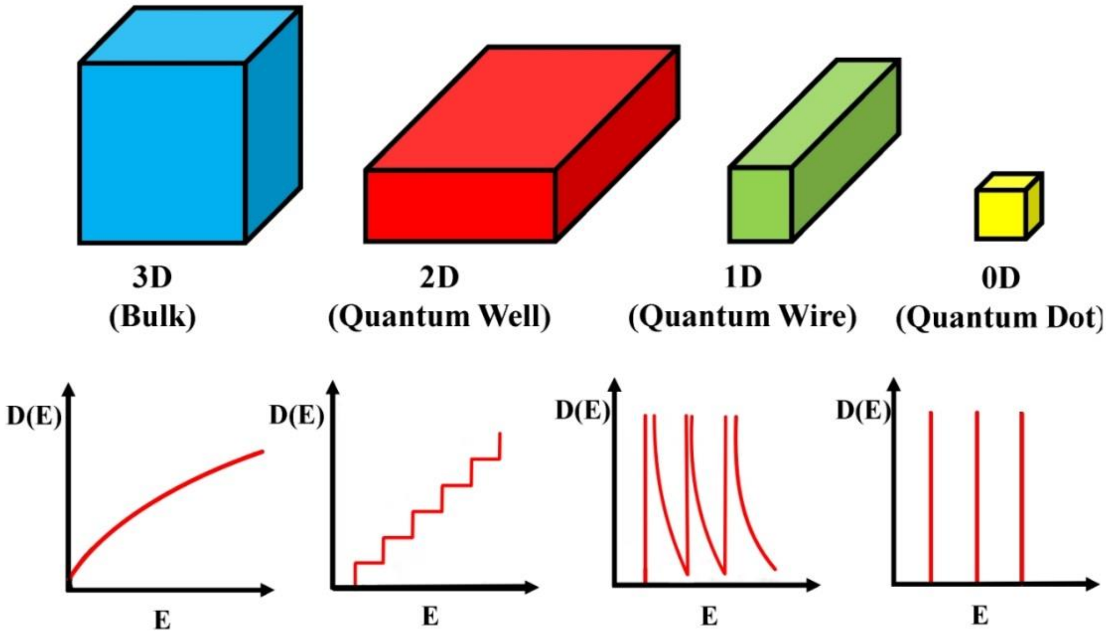

Fig. 1.4: A schematic representation of the DOS in 3D, 2D, 1D, and 0D [48]**.**

A wide variety of methods can synthesize nanomaterials. These methods can be grouped into two general strategies, one in which a **bottom–up** approach is used and the other being a **top–down** approach. A top–down approach involves reducing the size of the bulk material to form nanomaterials, whereas a bottom–up approach generates nanomaterials by assembling atoms or molecules via synthetic chemistry. Top–down approaches involve the attrition (wear) of the source material, whereas bottom–up approaches start with either a solution or a vapor of atoms, molecules, or a precursor that reacts to form the nanomaterial population [49].

Nano-electronics and nanostructure devices based on metal oxides are expected to be similar in shape, perfect in crystalline structure, uniform in size, and free of morphological defects. This is due to their surface and interface area enhancement, increasing surface-to-interface recombination. These properties potentially affect on the photovoltaic properties and have made the metal oxide nanoparticles a promising solar cell material. This emerging technology uses much lower quantities of material to minimize production costs. Nanostructured semiconductor metal oxides such as TiO_2, CuO, Cu_2O, and ZnO have attracted much attention because of their unique, multifunctional properties (especially optical, electrical, and electronic). These properties make them a favorable material for the solar cell fabrication field [50, 51].

1.3 The Used Nanomaterials

1.3.1 Antimony Trioxide (Sb_2O_3)

Oxides of antimony are key members among all the other metal oxides from V to VI groups. There are three phases of well-identified oxides of antimony, which are antimony trioxide (Sb_2O_3), antimony tetroxide (Sb_2O_4), and antimony pentoxide (Sb_2O_5). The change in Gibbs energy is the key parameter that affects the formation of the desired phase. For instance, Sb_2O_5 does not exist above 525 °C, only Sb_2O_3 and Sb_2O_4 are formed [52]. Sb_2O_3 has a high refractive index (2.0–2.5). It possesses three crystalline structures: the cubic senarmontite, which contains the Sb_4O_6 molecule (α-Sb_2O_3); orthorhombic phase valentinite has a polymeric sheet structure built up from eight-member Sb_4O_4 rings (β-Sb_2O_3), and metastable phase (γ-Sb_2O_3) [53].

The cubic form of Sb_2O_3 (structure is shown in Figure 1.5 (a) [54, 55]) is stable at temperatures below 556–665 ^{o}C. Above this temperature range, a phase transformation to the high temperature phase of the orthorhombic (structure is shown in Figure 1.5 (b) [55, 56]) has been observed [54, 56–58]. The melting point of Sb_2O_3 is just above this phase transformation temperature. Below 600 ^{o}C, the valentinite structure is unstable. Recent calculations have shown an indirect band gap of 3.38 eV for the senarmontite Sb_2O_3 and a direct band gap of 2.25 eV for the valentinite Sb_2O_3, and further that their direct optical band gaps are 3.54 and 2.47 eV, respectively [59].

Sb_2O_3 is not acutely poisonous. It is not considered toxic via inhalation, and it is solid and is commercialized as a white, scentless, crystalline powder. According to "handbook data," the melting point is 655 ^{o}C, and the effervescence point is 1550 ˚C, and vapor compression at ambient temperature is deemed to be very small [60].

Due to its large and direct band gap existing in the near ultraviolet region [61–63]. Antimonous oxide is helpful in many applications, such as the effective catalyst [64], solar cells [65], gas sensors and heat mirrors [66–69], and flame-retardant where it promotes the efficiency of flame retardants when used as a component in combination with halogenated flame retardants in plastics, dyeing, rubber, and textile back coatings [70, 71], lithiumion batteries [72–75], and adhesives [76]. The main property for these applications is due to the polymorph nature of the crystalline structure of Sb_2O_3 thin films.

Thin films of Sb_2O_3 may be generated using many different methods: vapor condensation [77], hydrolysis [78], sol-gel method [79], and vacuum thermal evaporation [80]. Comparing vacuum thermal evaporation to alternative physical vapour deposition (PVD) methods like sputtering [81], and chemical vapor deposition (CVD) [82]. The cubic α phase is of particular interest since it is the most thermodynamically stable at standard conditions rings listed in Table (1.2) [83].

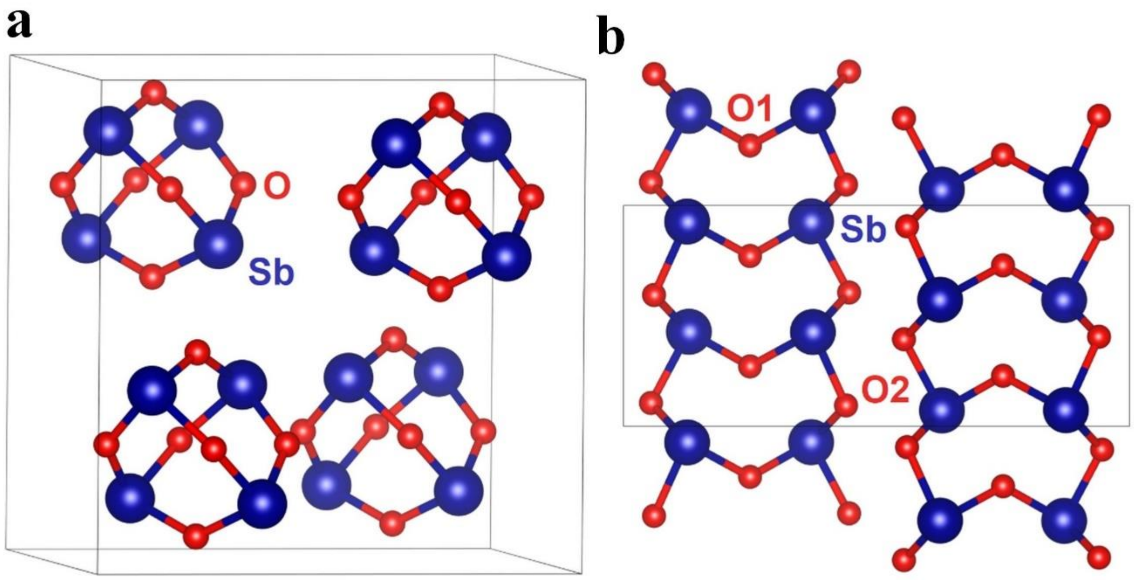

Fig. 1.5: The structures of (a) a- Sb_2O_3**, senarmontite, (b) b-** Sb_2O_3**, valentinite. Darker atoms are antimony** [54, 56]**.**

Table (1.2): Physical properties of antimony trioxide (Sb_2O_3) [83]**.**

Properties	Values
Chemical formula	Sb_2O_3
Structure	Cubic < 570 Orthorhombic > 570
Band gap	3.40−4.00 eV
Refractive index	2.08
Resistivity	$24\,\Omega.\,cm$
Molecular weight	$291.52\ g/mol$
Boiling point	1425 ℃
Melting point	656 ℃
Density	$5.2\ g/cm^3$
Dielectric constant	7.605×10^{-9}
Color	White powder

1.3.2 Copper Oxides (CuO)

Copper(II) oxide (CuO-tenorite) and copper(I) oxide (Cu_2O-cuprite) are the two stable oxide forms of copper. CuO has a monoclinic crystal structure, as shown in Figure (1.6) [84], and a bandgap of (1.2-1.9) eV [85, 86]. This metal oxide has a black color, high absorptivity, and low thermal emittance [87, 88]. The physical properties of CuO are listed in Table (1.3).

On the other hand, Cu_2O with a brownish-red color, has a cubic crystal structure and a bandgap of (1.9-2.3) eV [89, 90]. These oxides are semiconducting and exhibit p-type characteristics due to copper vacancies in the structure [91]. The advantages of copper oxides include their non-toxic nature [92], abundance of their precursor materials [93], cost-effective synthesis routes [94], high chemical and thermal stability [95], and high absorption coefficient in the region of visible light [96]. These advantageous properties have made copper oxide a common material in solar cell fabrication [97], gas sensors [98], secondary batteries [99], photocatalysis [100], superconducting material [101], and field transistors [102].

Table (1.3): Physical Properties of copper oxide (CuO) [88]**.**

Properties	Values
Chemical formula	CuO
Structure	Monoclinic
Band gap	1.2−1.9 eV
Refractive index	2.63
Solubility in water	Insoluble
Molar mass	79.545 g/mol
Boiling point	2000 ℃
Melting point	1326 ℃
Density	6.315 g/cm^3
Color	Black to brown powder

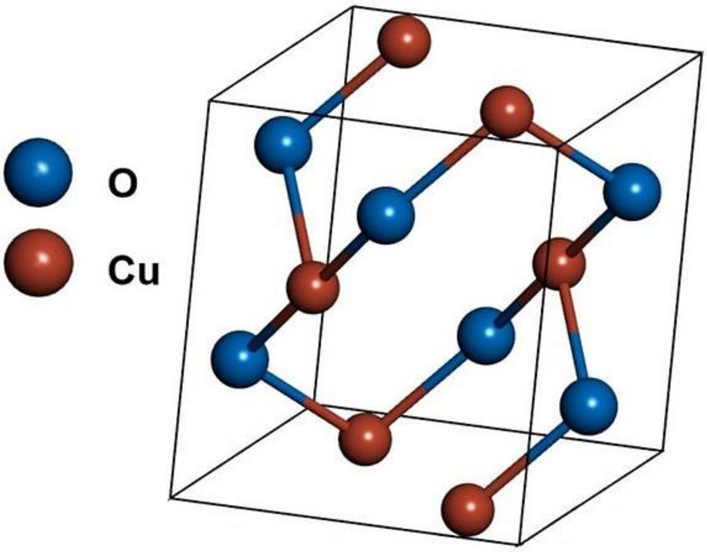

Fig. 1.6: The monoclinic tenorite crystal structure of CuO [84]**.**

1.4 Literature Survey

Due to their remarkable physical, optical, magnetic, exceptional electronic, and optoelectronic properties suitable in optoelectronics, catalysts, transistors, and photocatalytic applications, two-dimensional nanomaterial heterostructure has received a great deal of attention in recent years from the scientific community. An abbreviated rundown of recent developments in the field above is provided below:

Masudy-Panah, *et al.* in (2016) [103] used sol-gel deposition techniques for fabricating a thin cupric oxide film (CuO) straddled with graphene nanoparticles, which is proposed as a promising absorber layer for solar cell applications. Graphene nanoparticles incorporated in CuO (G-CuO) film show a reduction in the optical transmittance and reflectance and an enhancement in its electrical conductivity. Photovoltaic properties, investigated through a p-(G-CuO)/n-Si heterojunction cell, showed open circuit voltage (V_{oc}) =190 mV, short circuit current density (J_{sc}) =0.82 mA/cm^2, Fill Factor (FF) =40, and efficiency (ƞ) 0.062%.

Dolai, *et al.* in (2017) [23] used the direct current (DC) reactive magnetron sputtering technique to synthesize cupric oxide (CuO) thin films. They found ratios of Argon and oxygen gas in the plasma and the substrate temperature during deposition were the critical parameters for forming CuO polycrystalline films. Predominant p-type conductivity in the CuO films was confirmed by Hall measurement. CuO/CdS p-n junction solar cell obtained with non-rationalized layer thicknesses showed an open circuit voltage (V_{oc}) ~421 mV, short circuit current density (J_{sc}) ~3.6 mA/cm^2, Fill Factor (FF) ~0.46, and efficiency (ƞ) ~1.2%.

Iqbal, *et al.* in (2017) [104], Mn-doped CuO nanorods fabricated by the wet chemical method can promote photocatalytic activity. They found that a 2% Mn-doped CuO nanowires photocatalyst is much more highly photoactive than undoped or highly doped CuO nanowires. The solar cell P3HT–CuO–Mn shows excellent diode behavior in the dark; the current density was increased when exposed to light. For 2% doped sample the current density and efficiency of the device they found better than the reference sample (V_{oc} =0.67 mV, J_{sc} = -2.9 mA/cm^2, FF =0.27, and η= 0.55%). Whereas for 6% and 10% doped samples, the current density as well as the efficiency of the device was much lower.

Tigau, *et al.* in (2017) [62] deposited Sb_2O_3 thin films through vacuum thermal evaporation on glass substrates kept at room temperature, and then they were annealed in a vacuum at 250 °C for one hour. The X-ray diffraction analysis showed that both the as-deposited and the annealed Sb_2O_3 thin films are polycrystalline and have a cubic structure. The annealing in a vacuum improved the crystallinity and increased the surface roughness of films and the optical transmittance in the visible and near-infrared regions. It was found that the dispersion of the refractive index obeys the single oscillator model. The optical band gap energy, determined from the variation of the absorption coefficient with wavelength, increases from 3.58 eV for as-deposited films to 3.73 eV for the vacuum-annealed Sb_2O_3 thin films.

Özmenteş, *et al.* in (2018) [89] abricated solar cells of CuO/n-Si heterojunctions using a vacuum coating unit. The band gap energy of the film was determined as 1.74 eV under the indirect band gap assumption. Current-voltage (I-V) measurements of the CuO/n-Si heterojunctions were performed under illumination and in the dark to reveal the photovoltaic and electrical properties of the produced samples. From the I-V measurements, it was revealed that the CuO/n-Si heterojunctions produced by thermal evaporation exhibit excellent rectifying properties in dark and photovoltaic properties under illumination. The best value achieved for conversion efficiency was 1 % with V_{oc} =0.35 V, I_{sc} =0.00986 A/cm^2, and FF =29%.

Iqbal, *et al.* in (2018) [105] used vapor deposition techniques for manufactured solar cell heterojunctions based on inorganic semiconductors at various thermal-annealing temperatures. The active layer consists of a bilayer comprising a hole transporting copper oxide-CuO and an electron transporting zinc oxide-ZnO nanoparticles. It was observed that the power conversion efficiency (PCE) increased from 0.06 to 0.08% with an increase in annealing temperature from 400 to 500 °C, possibly due to increased absorption in the visible region with increasing temperature.

Kadhim, in (2018) [60] fabricated Sb_2O_3 thin films using thermal evaporation in a vacuum with different thicknesses (100, 150, 200, and 250) nm. It was found that transmittance, absorbance, and energy gap depend markedly on the thickness of the films. The absorbance and absorption coefficient for Sb_2O_3 thin films increases with the increase of the film thickness. The transmittance decreases with increasing film thickness. The high transmittance of wavelengths in the (visible and near infrared) regions and the high absorbance in the (ultra-visible) region offered the possibility of using Sb_2O_3 films in various fields, including laser visible diodes and ultraviolet filters, fire-safe plastic casings, switches, resin circuit boards, and microsensors components.

Moumen, *et al.* in (2019) [106] investigated CuO thin films on gas sensors and solar cell applications through CuO thin films deposited using spray pyrolysis. X-ray diffraction showed the appearance of the tenorite phase of cupric oxide CuO. A crystallinity improvement was measured by increasing the temperature from (300 to 375) °C. Low transmittance, high absorbance, and small band gap energy were observed at the highest substrate temperature, these characteristics make CuO an appropriate material to be used as an absorber layer in photovoltaic applications.

Divya, *et al.* in (2019) [107] used the vacuum thermal evaporation technique to synthesize pure and Zn-doped Sb_2O_3 thin films. They studied the effect of zinc doping on the surface modification in Sb_2O_3 thin film, reducing its surface roughness. This reduction in surface roughness increases the NIR reflectance from the film surface because the radiative reflectance of a material is a function of surface roughness and surface contaminants. The transmittance increases for lower Zn concentration and decreases for high Zn concentration. Thus, using Sb_2O_3 in Zn-based thin film solar cells can highly influence solar cell efficiency.

Abass and Obaid in (2019) [108] used a thermal evaporation technique to prepare pure and Sb_2O_3:Ag 0.006wt.% nanofilms with thicknesses of (30, 38, 42, 48, 53, and 60) nm were deposited onto a glass substrate. The surface roughness was affected by low Ag doping examined via AFM. It was found that the transmittance (T), absorbance (A), and optical band gap (E_g^{opt}) depend markedly on the thickness of the film. The transmittance decreased with the increase in film thickness while the absorbance increased. The energy gap value decreased with increasing thickness in the Sb_2O_3:Ag films from 3.6 eV for the film thickness of 60 nm to 3.4 eV for the film thickness of 30 nm. The AFM and optical properties refer that the films are suitable for solar cell fabrication.

Song, *et al.* in (2020) [65] created the dielectric-metal-dielectric multilayer structure with two Sb_2O_3 layers and Ag thin films as the top electrode. The ultrathin Sb_2O_3/Ag/Sb_2O_3 electrode's bottom layer prevented Ag atom diffusion and aggregation, creating homogenous ultra-thin Ag films. Intermediate metal layer thickness affects fill factor, short circuit current density, device resistance, and light reflection. The top Sb_2O_3 layer's thickness caused a dichroic effect by transmitting certain visible light wavelengths and reflecting others. Three colorful active layers and

Sb_2O_3/Ag/Sb_2O_3 electrodes produced OSC_s with vivid colors and PCE of 6.33−7.88% and average visible transmittances of 23−30%.

Yeom, *et al.* in (2020) [109] developed Sb_2O_3-cavity-based Fabry-Perot etalon electrodes for Semitransparent organic solar cells (STOSCs) by thermal evaporation. MDM electrodes have low sheet resistance and high transmittance at tunable wavelengths, resulting in reduced J_{sc} losses and V_{oc} and FF values comparable to reference systems with Ag electrodes. They showed how to increase dichroic OSCs' color saturation and photovoltaic performance by spectrally matching the MDM electrodes' intended transmittance colors to the active layer compositions' inherent light transmittance spectra. This method reduced current losses and increased transmitted light color intensity and saturation. Finally, blue semitransparent electrodes gave PM6:Y6 STOSCs 13.3% efficiency. They believe this is the greatest PCE value for colorful semitransparent organic solar cells.

Divya and Abraham in (2020) [63] fabricated thin films of pure and Ag-doped Sb_2O_3 using vapor deposition techniques. They observed that the properties exhibited by antimony trioxide, which is annealed at variant temperature, varies drastically when their surface is decorated with Ag nanoparticles. Due to the introduction of Ag nanoparticles, the absorption of Sb_2O_3 thin film in the visible region increased. All synthesized films have a roughness coefficient>1 and are hydrophilic. The filling of Ag nanoparticles in the voids between the thorn structures might have prevented the water droplet penetration into these voids. Consequently, partial wetting occurs on the film surface. The high surface-enhanced Raman scattering (SERS) efficiency factor and good Ag/Sb_2O_3/Glass reproducibility make it a good candidate for SERS application.

Shinde, *et al.* in (2020) [110] studied thin films of Sb_2O_3 were prepared by a relatively simple and low-cost chemical spray pyrolysis technique. The XRD analysis shows that films are well indexed with cubic senarmontite phase with an average crystallite size of 58.73 nm. The deposited films have a semiconducting nature, and the measured band gap energy value is around 3.43 eV, which is ideally suitable for the applications of nanostructured Sb_2O_3 in the field of electronics industries. The Raman spectra analysis confirms the homogeneity of the deposited films. The surface resistivity and the activation energy are found to be 26.16×10^2 Ω cm and 0.764 eV respectively.

Patel and Chauhan in (2020) [111] fabricated type-I straddling gap heterojunction solar cells of Ag/CuOx/TiO_2/FTO configuration utilizing an extremely thin p-n junction of 150 nm. They studied four unique devices by varying the oxygen vacancies in CuO_x and its effect on the overall performance of the cells. The solar cell characteristics were recorded for 365nm UV light, which showed a linear increase in open circuit voltage (V_{oc}) from (0.266 to 1.01) V while changing CuOx phases from Cu_2O to CuO. The optimized solar cell with CuO active layer possessed V_{oc} of 1.01 V with 3.48mA/cm^2 current density and fill factor (FF) of 31%, which sums up to an overall efficiency of 16.22% for an input power of 7 mW/cm^2. It was found that CuO/TiO_2 device offered the highest.

Siddiqui, *et al.* in (2020) [112] showed that could be adopted wet chemically synthesized CuO nanoparticles as an active layer in hybrid bulk heterojunction (BHJ) solar cells. The BHJs with CuO-NPs display significantly different physics from customary BHJs, proving a noteworthy performance improvement. They noted that with the addition of CuO-NPs, the morphology of the photoactive layer endures significant changes. Incorporating CuO-NPs is an additional paradigm for BHJs solar cells, which enhances the photocurrent density from 9.43 mA/cm^2 to 11.32 mA/cm^2 and the external quantum efficiency. Also, PCE improved from 2.85% to 3.82% without harming the open circuit voltage and the fill factor.

Tuama, *et al.* in (2021) [113] fabricated solar cells via thermal evaporation technique under a vacuum by depositing pure and Ag-doped thin films of Cu_2O on laser-etched silicon substrates, with minimal ratios of silver doping (0.02, 0.04, and 0.06) wt% and average thickness of 60 nm. The fabricated thin films (pure and Ag-doped) exhibited a direct energy gap (E_g) that decreased from 3.5 to 3 eV as the Ag doping increased. The I-V characteristic results revealed a promising increase in the conversion efficiency of the fabricated solar cell to 6.48% with short circuit current (I_{sc}) of 4.7 mA, open-circuit voltage (V_{oc}) of 3.8 V, and filling factor (F.F) of 0.335 at P = 100 mW/cm^2.

Absike, *et al.* in (2021) [93] proved that CuO thin film prepared through the sol-gel procedure followed by the spin coating technique on a glass sub-strategy. They found from XRD patterns CuO thin layers exhibit a monoclinic structure without any impurities, with a preferential peak relative to the (002) plan. The results showed that the obtained crystals exhibit a uniform and smooth morphology. The Absorption spectra by UV–vis analysis of the obtained thin films reveal high absorbance in the visible range. CuO films showed an optimal gap energy of 1.47 eV and suggested that CuO thin film could be one of the potential solar cell absorbers in PV devices.

Ashika, *et al.* in (2022) [114] pure cubic Sb_2O_3 phase was produced by precipitating $KSbO.C_4H_4O_6$ and KOH in one step. FESEM scans reveal 1.46–1.59 µm octahedron-shaped grains. For the Sb_2O_3 materials produced, the TGA curve indicated a modest total weight loss of ~3.5% and a high exothermic peak at 633 °C in the differential thermal analyses curve. Raman, UV–Vis, and FTIR spectrum characteristics validated the cubic Sb_2O_3 phase's intrinsic optical property. The current study revealed the preliminary innovative single-step synthesis of cubic Sb_2O_3 phase materials with octahedron-shaped grains to 1.46–1.59 µm.

Qassim, *et al*. in (2022) [115] used the thermal evaporation technique to prepare copper oxide (CuO) nanofilms with a thickness of 75 nm. The effect of annealing temperature (200℃ for one and two hours) on the structure was evaluated using a scanning electron microscope (SEM), the particle size ranged from (15.42 to 35.05) nm. The refractive index showed a decline by increasing the annealing temperature, while the same influencer affected the absorbance positively. The annealing for 2 hours decreased the value of the optical bandgap from 3.3 to 3.05 eV. Obviously, the emerging quantization effect was caused by the acquisition of high energy gap values.

Wisz, *et al.* in (2023) [116] investigated thin film solar cells based on copper, zinc, and titanium oxides obtained by DC-reactive magnetron sputtering. They studied the current-voltage (I-V), power–voltage characteristics, and optical properties of TiO_2:ZnO/CuO photocell. The values of the open-circuit voltage (V_{oc}) and short-circuit current density (J_{sc}) of photovoltaic devices reached (11- 15) mV and (6.1 - 6.8) µA, respectively. Furthermore, the P_{max}, FF, RS, and RSH values were calculated and analyzed. The difference in the composition of the upper layer of the structure caused changes in the reflection spectra in the wavelength range of 190–2500 nm and, depending on the wavelength, varies in the range of 0–27%.

1.5 The Aims of the Work

1. Fabricating and optimization of solar cells by nanofilms deposition with varying thicknesses on silicon substrates etched by laser (Sb_2O_3/etched-p-Si and Sb_2O_3:wt.%CuO/etched-p-Si).
2. Studying the effect of thickness and CuO ratios on the prepared films and solar cell efficiency.

Chapter Two

Theoretical Part

2.1 Introduction

This chapter focuses on the theoretical part, which represents thermal evaporation: optimization, advantages, specifications of the system, as well as structural and morphological properties (X-ray diffraction, atomic force microscopy, and scanning electron microscope, optical properties of crystalline semiconductors (absorbance, transmittance, electronic transitions, optical constants, dispersion parameters, and Urbach energy), electrical properties (Hall effect, resistivity, and mobility), and current-voltage (I-V) characteristic.

2.2 Thermal Evaporation

The simplest technique to deposit material onto a substrate under the pressure of 1×10^{-6} mbar is thermal evaporation, illustrated in Figure (2.1). Thermal evaporation methods include the simple emission case at the heated material source, which condenses on the cold substrate. The source can be a refractive wire or an electrically heated boat containing the material to evaporate. The evaporation rate is determined by the vapor pressure of the source material at the evaporation temperature. The Joule heating of a typical tungsten or molybdenum boat allows for reaching 2800 K, which provides appreciable vapor pressures for most metals. A deposition chamber under a high vacuum is necessary to allow the vapor to reach the substrate without reacting or scattering against other gas-phase atoms in the chamber and to reduce the incorporation of impurities from the residual gas in the vacuum chamber [117–120].

The thermal evaporation technique has various benefits compared with solution methods. One of the most important benefits of the thermal evaporation technique is compatibility with industry applications for high-rate fabrication. Another benefit of thermal evaporation is the absence of any solvent. In the case of using solvent method to prepare films, there is a possibility of residing solvent in the final film that can possess a potential effect on application performance in particular with respect to the fabrication of solar cell device’s field. In addition, the evaporated materials in thermal evaporation technique can be uniformly and evenly deposited on substrates, specifically for the thin film layer. The thin film thickness can be managed by monitoring the deposition rates of the required material. Finally, the thermal evaporation is suitable for characterization techniques that only exist under ultra-high vacuum, such as photoemission spectroscopies. This can provide the feasibility of studying the interface's specific properties in a device and understanding the physics of fabricated devices, especially solar cell devices [121–123].

Thermal evaporation is suitable for characterization techniques that only exist under ultra-high vacuum, such as photoemission spectroscopies .This can provide the feasibility of studying the interface's specific properties in a device and understanding the physics of fabricated devices, especially solar cell devices. The thermal evaporation technique has been broadly utilized in the solar cell fabrication field because of the above reasons [80].

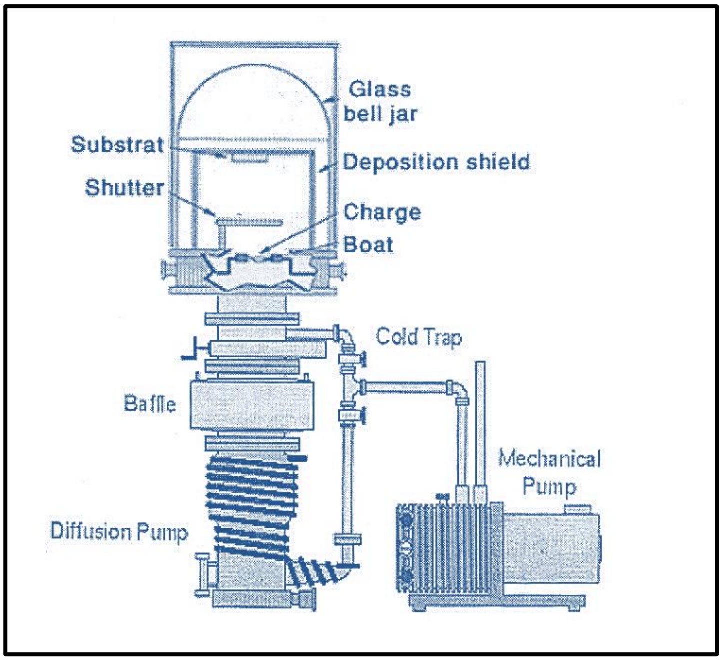

Fig. 2.1: Configuration of a basic coating system [119].

2.3 Structural and Morphological Properties

2.3.1 X-ray diffraction (XRD)

XRD methods are among the most successful methods for determining a material's crystal structure and nanomaterials with crystal structure and micro grain sizes, it can provide analytical data on the crystallite size and the orientation of the prepared films under certain conditions [124]. Chemical compounds can be identified using these methods based on their crystalline structure rather than the composition of their chemical elements. It indicates that similar-composition substances (or phases) can be distinguished [125].

X-rays with energies ranging from about 100 eV to 10 MeV are classified as electromagnetic waves, which only differ from radio waves, light, and gamma rays in wavelength and energy. X-rays show wave nature with wavelength ranging from about (10 to 10^{-3}) nm. According to quantum theory, the electromagnetic wave can be treated as particles called photons or light quanta [126].

The electric field of such waves interacts with the charges of all electrons of an atom, which then emit an almost spherical wave with the same wavelength as the incident radiation. The amplitude of this outgoing wave is proportional to the number of electrons in the atom and, hence, to the atomic number. Light elements with few electrons, e.g., carbon or oxygen, are therefore “poor” scatterers for X-rays, whereas heavy elements such as lead are “good” scatterers. This effect severely influences detection limits. The amplitude of the scattered wave is described by the atom form factor (or atomic scattering factor). Due to interference within individual atoms, especially larger ones, the amplitude of the outgoing wave and hence the atom form factor varies also with the scattering angle 2θ [127, 128].

Constructive in-interference and hence a so called Bragg reflection is obtained when the path of the wavelet scattered of the lower of the two planes is longer by an integer number of wavelengths λ than that of the wavelet scattered off the upper plane, as shown in Figure (2.2). A reflection will thus occur when [129]:

$$2d_{hkl}\sin\theta = n\lambda \tag{2.1}$$

where (n) is integer that shows the order of the reflection, (θ) is Bragg's angle, (λ) is the wavelength of the x-ray beam and (d_{hkl}) is interplanar distant (i.e. atoms or ions or molecules).

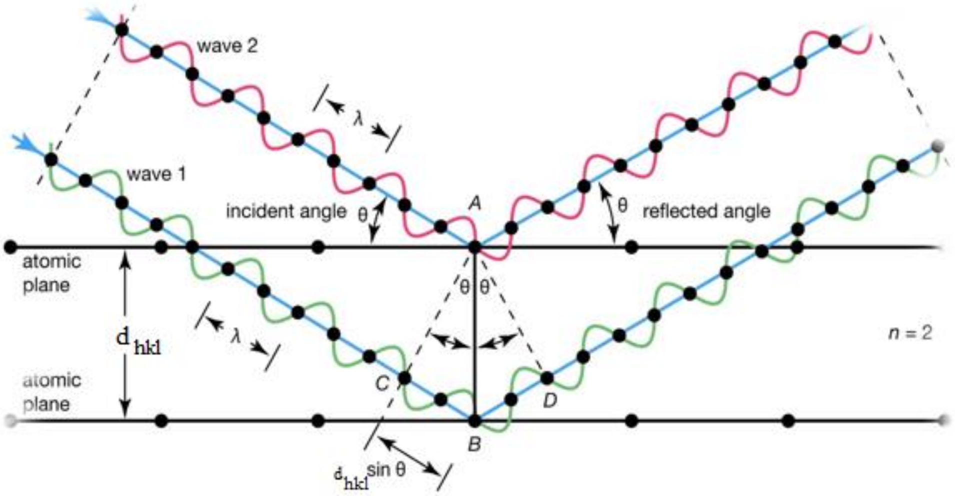

Fig. 2.2: Bragg diffraction [129]**.**

Commonly, XRD is used to calculate different parameters, which could be used to clarify the studies of the deposited films. Full width at half of the maximum intensity (FWHM) of the preferred orientation (peak) could be measured since it is equal to the width of the line profile (in degrees) at half of the maximum intensity [130].

Using Scherer’s formula can be estimated the crystallite size (D) [131]:

$$\mathrm{D} = \frac{k\lambda}{\beta cos\theta} \tag{2.2}$$

where k is a constant of approximately 0.94 (shape factor), λ is the X-ray wavelength (Å), β is the full width at the half of the maximum intensity (FWHM)(radian), θ is Bragg diffraction angle of the XRD peak (degree).

The following equation can be used to determine the lattice constant (a) using Miller indices (hkl) and the d-spacing for the cubic structure [132]:

$$d_{hkl} = \frac{a}{\sqrt{h^2 + k^2 + l^2}} \qquad (2.3)$$

2.3.2 Atomic force microscope (AFM)

The atomic force microscope (AFM) is one of the most successful of these new devices. Binnig got the idea for the atomic force microscope in 1985 [133]. AFM is a newly developed technique for imaging local surface characteristics from submicron to nanometer length scale. It is a powerful, nondestructive analytical technique used in air, liquid, or vacuum [134].

AFM has a great advantage over microscopy techniques with similarly high resolution (mainly electron microscopy) in the flexibility of the imaging environment. For AFM, there is no need to image in a vacuum or to coat the sample to make it conductive. AFM can be carried out at room temperature or elevated or cryogenic temperatures. AFM has become the method to determine the roughness of metals and metal oxides, semiconductors, polymers, composite materials, ceramics, and biological materials [135, 136].

AFM can be used for 3D information on surface defects, scribes, scratches, gouges, corrosion pits, etc [137]. The possibility to carry out imaging at such small scales, its small size, and ease of handling makes AFM one of the few tools capable of characterizing the surface properties around very small features [138].

In AFM scanning, a cantilever with a sharp tip (fabricated from silicon or silicon nitride) is used to scan over the surface of the sample. The cantilever probes the surface by sensing the force between the surface and tip. The atoms respond to the developed Van der Waals force, which can be either short-range repulsive exchange interactions or longer-range attractive, depending on the type of contact. As the tip approaches the surface, the attractive Van der Waals force between the cantilever tip and the sample deflects the cantilever toward the sample surface. When the cantilever tip is brought in contact with the sample surface, the repulsive Van der Waals force develops, which deflects the cantilever in the opposite direction. These deflections, toward or away from the sample surface, are detected by a laser beam. The laser beam strikes the top of the cantilever and reflects back to a position-sensitive four-segment photodetector. The deflection in the cantilever is recorded by the photodetector. The segments of the photodetector are used to track the position of the laser spot on the detector and the angular deflections of the cantilever. While scanning, the AFM tip continuously moves back and forth along the surface features and the resulting deflections are recorded by the detector [139, 140]. Figure (2.3) illustrated the working principle of AFM [141].

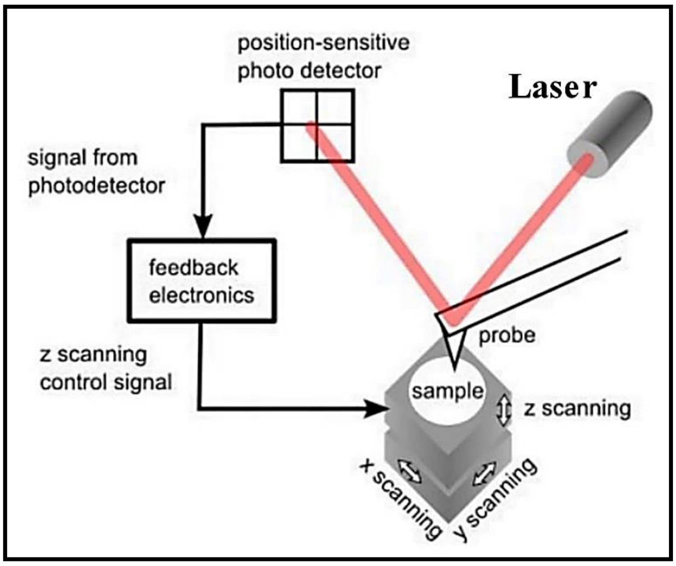

Fig. 2.3: Schematic diagram of the basic working principle of AFM [141]**.**

The most commonly used parameters are the roughness average (S_a) and the root mean squared (RMS) surface roughness (S_q). The average roughness is defined as the mean height of the surface from the centre of the plane in a given area [142]. Root mean square roughness defined as the standard deviation of the surface height profile from the average height, is the most commonly reported measurement of surface roughness [143]. According to the definition, the roughness average (S_a) is given as [137, 144, 145]:

$$S_a = \frac{1}{mn}\sum_{j=1}^{n}\sum_{i=1}^{m}\left|Z_{ij}\right| \tag{2.4}$$

where Zij is the individual pixel height, m and n are the number of pixels in the x and y directions. RMS roughness may be obtained from the scanning data by the following relationship [137]:

$$S_q = \sqrt{\frac{1}{mn}\sum_{j=1}^{n}\sum_{i=1}^{m} Z^2\,(x_i, y_j)} \tag{2.5}$$

2.3.3 Scanning electron microscope (SEM)

A scanning electron microscope (SEM) is a type of electron microscope that produces images of a sample by scanning it with a focused beam of electrons. By using it, we can estimate the diameter, length, thickness, density, shape and orientation of the nanostructures [146].

The SEM consists of two major parts. An electronic console provides switches and knobs for adjusting the intensity of the image on the viewing screen, focusing, and photography. The electron column is the business end of the SEM, where the electron beam is created, focused to a small spot, and scanned across the specimen to generate the signals that control the local intensity of the image on the viewing screen [147].

The electron gun, at the top of the column, provides a source of electrons. Electrons are emitted from either a white-hot tungsten or lanthanum hexaboride or via field emission and accelerated down the evacuated column. Emitted electrons are directed and focused on the sample by using an anode and various electromagnetic lenses between the electron gun and the sample [148].

These projected electrons eject secondary and backscattered electrons after hitting the sample. Secondary electrons are used principally for topographic contrast in the SEM. The topographical image is dependent on how many of the secondary electrons actually reach the detector. A secondary electron signal can resolve surface structures down to the order of 10 nm or better. Although an equivalent number of secondary electrons might be produced as a result of the specimen primary beam interaction, only those that can reach the detector will contribute to the ultimate image (detectors transfer these detected electrons into an electronic signal sent to a computer to display the image). Secondary electrons that are prevented from reaching the detector will generate shadows or be darker in contrast than those regions that have an unobstructed electron path to the detector [149, 150]. The schematic diagram of the SEM apparatus is shown in Figure (2.4).

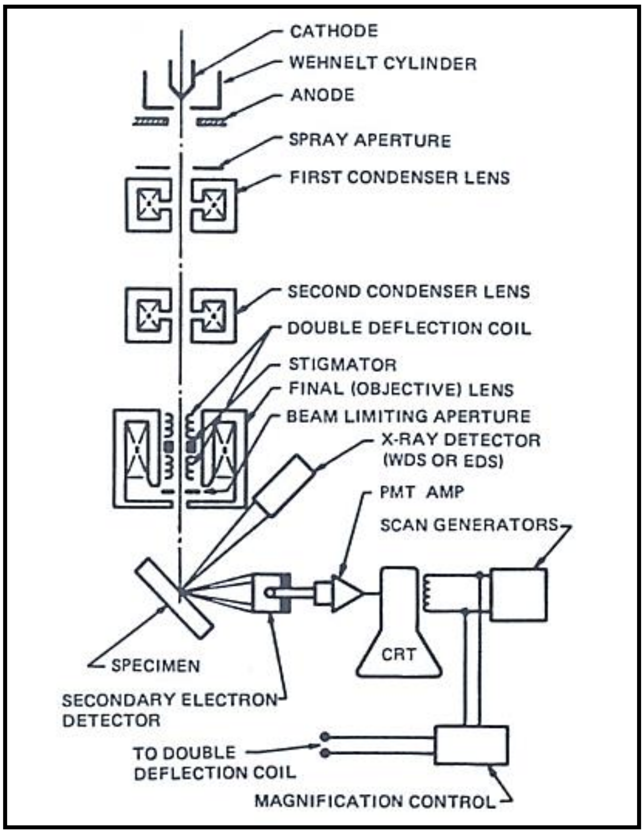

Fig. 2.4: Schematic diagram of the scanning electron microscopy [149].

2.4 Optical properties

When light is incident on a semiconductor, the optical phenomena of absorption, reflection (specular or diffuse) and transmittance are observed. At all instances of light interaction with the materials, the incident light intensity upon the surface is equivalent to the sum of the transmitted, absorbed and reflected intensities as shown in the Figure (2.5). The diffused light is scattered in all directions including some part that is ‘back scattered’ i.e. rays are opposite to the direction of the incident beam of light. Rays that are not reflected, scattered or absorbed are the ones that are transmitted [151].

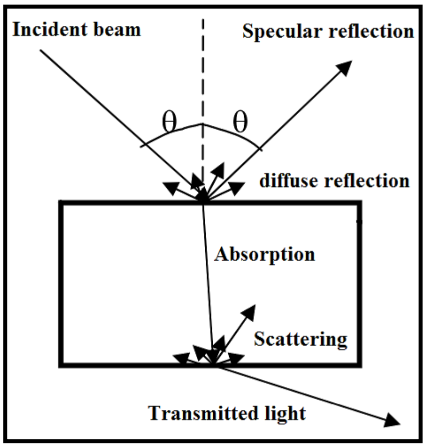

Fig. 2.5: Interaction of light with a transparent material [151]**.**

From the absorbance spectrum as a function of photon energy, a number of processes can be contributed to absorption. At high energies, photons are absorbed by transitions of electrons from filled valence band states to empty conduction band states. For energies just below the lowest forbidden energy gap, radiation is absorbed due to the formation of excitants, and electron transitions between band and impurity states. The transition of free carriers within energy bands produces an absorption continuum which increases with decreasing photon energy. The crystalline lattice itself can absorb radiation, with the energy being given off in optical phonons. Finally, at low energies, or long wavelengths, electronic transitions can be observed between impurities and their associated bands [152].

2.4.1 Absorbance (A)

Absorbance is the ratio between absorbed light intensity (I_A) by the material to the incident light intensity (I_o), ($A = \frac{I_A}{I_o}$). The absorbance happens in semiconductors for an incident light wave when the incident photon has energy greater than or equivalent to E_g ($h\nu \geq E_g$) giving it to an electron via the absorption process. The electron then begins to move from the valence band (V.B) to the conduction band (C.B) is called the essential absorption edge. The fundamental absorption edge is one of the greatest striking features of the absorption spectrum of a semiconductor. It equals the difference between the top V.B and the bottom C.B (energy band gap) [151].

It is also necessary to mention the relationship between the energy gap (E_g) and wavelength (λ) of the light beam is given by [153]:

$$\lambda = \frac{hc}{E_g(eV)} \tag{2.6}$$

where (c) is the light speed in a vacuum and (h) is the Plank constants.

Lambert-Beer-Bouguer's law expresses the intensity beam of photons is incident on the materials (I_o) [154]:

$$I_t = I_o e^{-\alpha t} \tag{2.7}$$

where I_t is the light intensity after travels through the thickness (t) of material, and α is the absorption coefficient given by equation (2.7) [155]:

$$\alpha = 2.303\frac{A}{t} \tag{2.8}$$

This absorption coefficient is defined as the ratio of the decrease in the energy flux of incident radiation relative to the distance unit in the direction of incident wave diffusion.

2.4.2 Transmittance (T)

Transmittance is the ratio between the intensity of the beam passing through the film (I_T) to the intensity of the beam incident on the film (I_o) and is expressed by the equation [155]:

$$T = \frac{I_T}{I_o} \tag{2.9}$$

When light falls on a material, the electrons of atoms on the surface of the material shake for a tiny period of time, after that radiate the energy as a reflected wave. Accordance to the law of conservation of energy, reflectance can be obtained from the absorption and transmission spectrum: [60]:

$$\mathrm{A} + \mathrm{T} + \mathrm{R} = 1 \tag{2.10}$$

2.4.3 Optical band gap ($\mathbf{E_g^{opt}}$)

The energy band gap generally refers to the energy difference between the top of the valence band and the bottom of the conduction band. The energy band gap may either be **direct** or **indirect**.

In semiconductor physics, a **direct band gap** means that the minimum energy of the conduction band lies directly above the maximum energy of the valence band in momentum space. Electrons at the conduction-band minimum can combine directly with holes at the valence band maximum while conserving momentum. The energy of the recombination across the band gap will be emitted in the form of a photon of light. There are two types of direct transitions, they are [155];

Allowed Direct Transition, this transition happens from top points in the V.B and the bottom point in the C.B, as shown in Figure (2.6.a). The empirical relationship for this type of transition is given by the equation [156]:

$$\alpha hv \approx \left[hv - E_g\right]^{\frac{1}{2}} \tag{2.11}$$

Forbidden Direct Transitions, this transition happens from near the top points of V.B and the bottom points of C.B, as shown in Figure (2.6.b). The empirical relationship which corresponds to this transition is given by the equation [156]:

$$\alpha hv \approx \left[hv - E_g\right]^{\frac{3}{2}} \tag{2.12}$$

An indirect bandgap is a bandgap in which the minimum energy in the conduction band is shifted by a k-vector relative to the valence band (k-vector represents difference a difference in momentum). The electron transits from (V.B) are not perpendicularly, where the value of the wave vector of the electron before and after a transition is not equal (Δk≠0). This transition kind occurs with an auxiliary of the other particle known as “Phonons”, for conservation of the energy and momentum law. Therefore, the assistance of a phonon is necessary to conserve momentum :[132]

$$h\nu = E_g \pm E_p \tag{2.13}$$

where E_p is the energy of absorbed or emitted phonon. There are two types of indirect transitions, they are:

Allowed Indirect Transitions, these transitions occurring between the top of V.B and the bottom of C.B which are found in the different regions of (K-space), as shown in Figure (2.6.c). The empirical relationship for this type of transition is given by the equation [156]:

$$\alpha h\nu \approx \left[h\nu - E_g\right]^2 \tag{2.14}$$

Forbidden Indirect Transitions, these transitions occur between near points in the top of V.B and near points in the bottom of C.B, as shown in Figure (2.6.d). The empirical relationship for this type of transition is given by the equation [156]:

$$\alpha h\nu \approx \left[h\nu - E_g\right]^3 \tag{2.15}$$

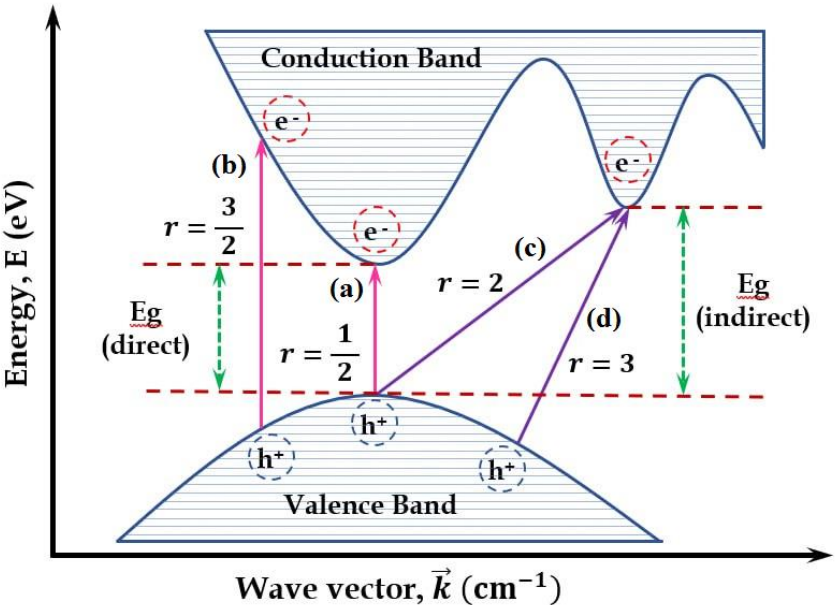

Fig. 2.6: The types of transition (a) allowed direct, (b) forbidden direct, (c) allowed indirect and (d) forbidden indirect [156]**.**

2.4.4 Urbach energy (Absorption band tail)

The optical absorption spectra of semiconducting materials have an important role because it gives the basic information about its composition and its E_g^{opt}. The optical absorption spectra of the semiconductor can be divided into three main regions;

i. Weak absorption region, which arise from defects and impurities.
ii. Absorption edge region, which arise due to perturbation of structural and disorder of the system.
iii. The region of strong absorption that determine the optical energy gap. Along the absorption coefficient curve and near the optical band edge there is an exponential part called Urbach tail.

This exponential tail appears in the low crystalline, poor crystalline, disordered and amorphous materials because these materials have localized states which extended in the band gap [157, 158]. In the low photon energy range, the spectral dependence of the absorption coefficient (α) and photon energy (hν) is known as Urbach empirical rule, which is given by the following equation [159, 160]:

$$\alpha = \alpha_o \exp\left(\frac{h\nu}{E_U}\right) \tag{2.16}$$

where α_o is a constant and E_U denotes the energy of the band tail or sometimes called Urbach energy, which is weakly dependent upon temperature and is often interpreted as the width of the band tail due to localized states in the normally band gap that is associated with the disordered or low crystalline materials [161]. Taking the logarithm of the two sides of the last equation, hence one can get a straight line equation. It is given as follows [162]:

$$\ln\alpha = \ln\alpha_o + \left(\frac{h\nu}{E_U}\right) \tag{2.17}$$

2.5 Optical Constants

The optical constants of the material are essential factors since they interpret the optical behaviour of the materials. One of the fields of widespread interest is optical constants' extraction from various types of optical measurement. Optical constants included extinction coefficient (k_o), refractive index (n), real (ε_r) as well as imaginary (ε_i) parts of the dielectric constant.

2.5.1 Refractive index (*n*)

The refractive index is an important optical constant to know the material's behavior with an electrical field. In an absorbing medium, the refractive index is written using a complex form (n^*) given by equation [163]:

$$n^* = n + ik_\circ \tag{2.18}$$

The real part (n) clarifies as the phase velocity of the electromagnetic wave will be reduce speed when passing in the material owing to the excitement of the charges for each atom inciter by the electric field, that proportional with the electric susceptibility of medium. The similar theory used in the disturbance of the magnetic field. When the electromagnetic fields fluctuate in the wave, the charges in material will also fluctuate in the same frequency of wave. Then the vibrating charges irradiate their electromagnetic wave, which is at the same frequency with the applied field but with a phase delay [164], (thereby the real part represent slowed down applied wave when transmitting in a material).

The imaginary part of refractive index ($k_\circ$) interpretation the decay or damping of the electromagnetic wave after entering the material (thus, it represents the extinction coefficient which shows the amount of absorption and scattering of the applied wave on the material) [106]. The refractive index of the films can be calculated by using the equations (2.18 and 2.19) respectively [106, 165]:

$$n = \frac{R+1}{R-1} + [\frac{4R}{(R-1)^2} - k_o^2]^{1/2} \qquad (2.19)$$

$$k_o = \frac{\alpha\lambda}{4\pi} \qquad (2.20)$$

where (R) Reflectance, (λ) refers to the incident radiation wavelength.

2.5.2 Dielectric constant

The relative permittivity of the materials is considered one of the fundamental electrical properties of semiconductors or dielectrics. The dielectric constant is the proportion of the permittivity of the matter to the permittivity of the vacuum. Also defined it is the quantity of the polarizability in the materials when utilized alternating electric field. The complex permittivity is given by [166]:

$$\varepsilon^* = \varepsilon_r + i\varepsilon_i \tag{2.21}$$

where ε_r, ε_i are represented real and imaginary dielectric constant. The equation (2.17) gives the relation between the refractive index and dielectric function, thus [166]:

$$n^{*2} = \varepsilon^* \Longrightarrow (n - ik_\circ)^2 = (\varepsilon_r + i\varepsilon_i) \tag{2.22}$$

From equation (2.22) we get [167].

$$\varepsilon_r = n^2 - k_\circ^2 \tag{2.23}$$

$$\varepsilon_i = 2nk_\circ \tag{2.24}$$

2.6 Surface and volume energy loss function

Important two parameters that can be used to describe the optical transitions for electrons in this investigated nanofilm were the surface energy loss function (SELF), which describes the electron transition in a thin film, and the second parameter was volume energy loss function (VELF) [168], which describes the electron transitions in the bulk materials. The SELF and VELF are gained from the complex dielectric constants, given by [169]:

$$SELF = \frac{\varepsilon_r}{(\varepsilon_r + 1)^2 + (\varepsilon_i)^2} \tag{2.25}$$

$$VELF = \frac{\varepsilon_i}{(\varepsilon_r)^2 + (\varepsilon_i)^2} \tag{2.26}$$

2.7 Dispersion Energy Parameters

Energy dispersion parameters have an important role in identifying the characteristics of the optical material. As through them one can calculate the necessary factors required to design the optical communication and the spectral dispersion devices [170]. Wemple–DiDomenico (WDD) single effective oscillator model successfully describes the dispersion of the refractive index [171, 172]. This model has an advantage in fitting the experimental data because it provides an intuitive physical interpretation of the measured quantities [173]. The main outputs of this model are the energy of the effective single oscillator (E_o) and the dispersion energy (E_d).

The energy E_o gives quantitative information on the overall band structure of the material. It must be taken into consideration that, the information obtained from E_o is completely different from those obtained from the optical energy gap E_g. Optical energy gap is related to the optical properties near the fundamental absorption edge of the material. In spite of the difference between E_o and E_g, yet there is an approximate empirical equation showing that E_o is often twice E_g i.e. ($E_o \approx 2E_g$) [174].

The dispersion energy (E_d) refers to the component of the total energy of a material that arises from the dispersion forces or van der Waals forces between atoms or molecules. These forces are relatively weak compared to other types of chemical bonding, such as covalent or ionic bonds. Dispersion forces are a result of temporary fluctuations in electron distribution within atoms or molecules. These fluctuations give rise to temporary dipoles, which can induce dipoles in neighbouring atoms or molecules. As a result, attractive forces occur between the induced dipoles, leading to the dispersion energy.

On the other hand, E_d which represents oscillator strength, measures the average energy of interband optical transitions and is associated with adjustment in the structural order of the sample i.e., it is related to the ionicity, anion valency and coordination number of the material. It is worth to mention here that, E_d is very nearly independent on E_o. This is because E_d is proportional to the dielectric loss, while E_o does not rely on the dielectric loss, either close or from afar. According to (WDD) model, the relationship between (E_o, E_d) and the incident photon energy (hv) is given as follows [171]:

$$(n^2 - 1) = \frac{E_d E_o}{E_o^2 - (hv)^2} \qquad (2.25)$$

The moments of optical spectra (M_{-1} and M_{-3}) can be calculate from the next relations [175]:

$$E_o^2 = \frac{M_{-1}}{M_{-3}} \tag{2.26}$$

$$E_d^2 = \frac{M_{-1}^2}{M_{-3}} \tag{2.27}$$

2.8 Electrical Properties

The study of electrical properties of semiconductor consists of:

2.8.1 Hall effect

Hall effect is one of the most important effects in the determination of the parameters that characterize from the electrical point of view the semiconductor materials. Hall effect was used in common practice to measure certain properties of semiconductors: namely, the carrier concentration, the mobility, and the type (n or p). It is an important analytical tool since a simple conductance measurement can only give the product of concentration and mobility.

Hall device in the form of a rectangular plate. Modern Hall plates are usually of microscopic dimensions. For example, the thickness might be t = 10 mm. The length *l* = 200 mm and the width w = 100 mm. A bias voltage V is applied to the plate via the two current contacts (C1) and (C2). The bias voltage creates an electric field (E_e) and forces a current I. If the plate is exposed to a perpendicular magnetic induction (B), the Hall electric field (E_H) occurs in the plate. The Hall electric field gives rise to the appearance of Hall voltage (V_H) between the two sense contacts (S1) and (S2) [176, 177], as shown in Figure (2.7).

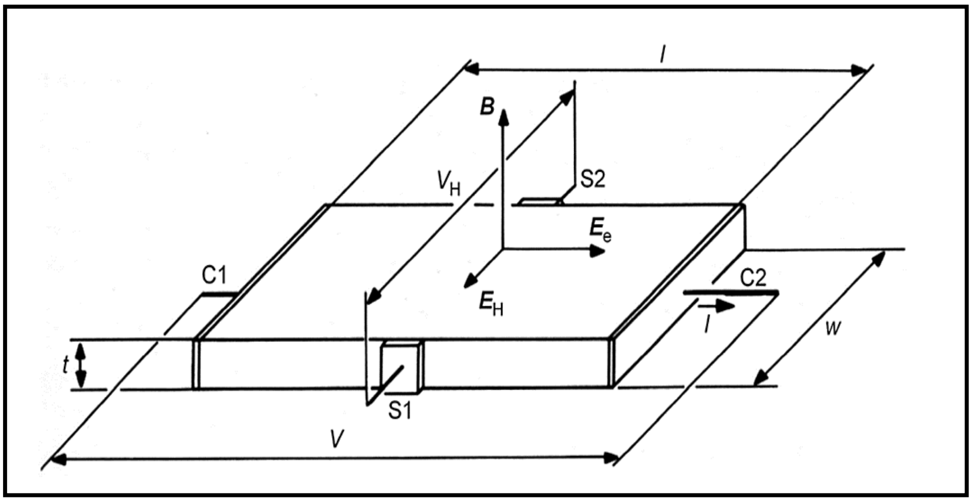

Fig. 2.7: Hall effect measurement circuit [176]**.**

The electric field is directly proportional to the product of the current density (J) and the magnetic induction as [178]:

$$E_H = R_H\, J\, B \tag{2.28}$$

where (R_H) is Hall coefficient and ($J = I/A'$), where (Á) is the cross section area. The generated electric field (E_H) is called Hall field which is related to Hall voltage (V_H) by the relation [179]:

$$V_H = E_H W \tag{2.29}$$

where (W) is the distance between the two electrode**s**. By scheming Hall voltage as a function of current, Hall coefficient can be determined by the relation [176]:

$$R_H = \frac{V_H}{I} . \frac{t}{B} \tag{2.30}$$

Carrier's concentration (n) can be determined by using the relation [180]:

$$n = \frac{-1}{q\, R_H} \qquad \text{for electrons} \tag{2.31}$$

or

$$n = \frac{+1}{q\, R_H} \qquad \text{for holes} \tag{2.32}$$

where (q) is the charge of electron. From Hall measurements, Hall mobility can be obtained according to the relation [176]:

$$\mu_H = R_H \, \sigma_{R.T} \qquad (2.33)$$

where ($\sigma_{R.T}$) is the conductivity at room temperature.

2.8.1.1 Resistivity (ρ)

The conductivity of semiconducting material, in addition to being dependent on electron and/or hole concentration, is also a function of the charge carriers mobilities. The resistivity of the films related to the electric field and the current passing through the film is [176]:

$$\rho = \frac{E}{J} \qquad (2.34)$$

where (E) is the electric field equals to (V/d). It depends on the resistivity (or conductivity), that is on the carrier concentration (electrons or holes). It is affected by so many parameters or conditions mainly the doping, temperature and deposition technique.

2.8.1.2 Mobility (μ)

Mobility is an important parameter for carrier transport because it refers to how strongly the motion of a drift velosity electron is influenced by an applied electric field and given by [180]:

$$\nu_n = \mu_n \, E \qquad (2.35)$$

where (ν_n) is the electron drift velocity. Analogous expressions can be written for electrons in the conduction band and holes in the valence band respectively [176]:

$$\nu_p = \mu_p \, E \qquad (2.36)$$

where (μ_n) and (μ_p) are the electrons and holes mobility respectively and (ν_p) is the hole drift speed. The negative sign is removed in eq. (2.36) because the holes drift in the same direction as the electric field.

2.8.2 Current-voltage characteristic (I-V)

The electrical characteristics of a solar cell can be investigated by considering it as a diode. An ideal solar cell may be modelled as a current source in parallel with a diode [181]. Since the diode cannot be ideal, shunt resistance and series resistance are added. This is represented by an equivalent circuit as shown in Figure (2.8).

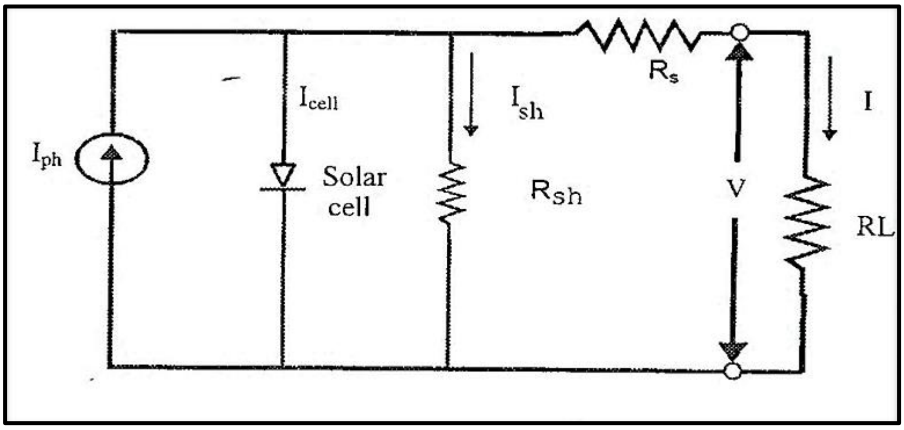

Fig. 2.8: Equivalent circuit of solar cell with load [181]**.**

The main parameters that are used to characterize the performance of solar cells are the peak power (P_{max}), the short-circuit current density (J_{sc}), the open-circuit voltage (V_{oc}), and the fill factor (F.F). These parameters are determined from the illuminated J-V characteristic as illustrated in Figure (2.9). The conversion efficiency (η) is selected from these parameters [182].

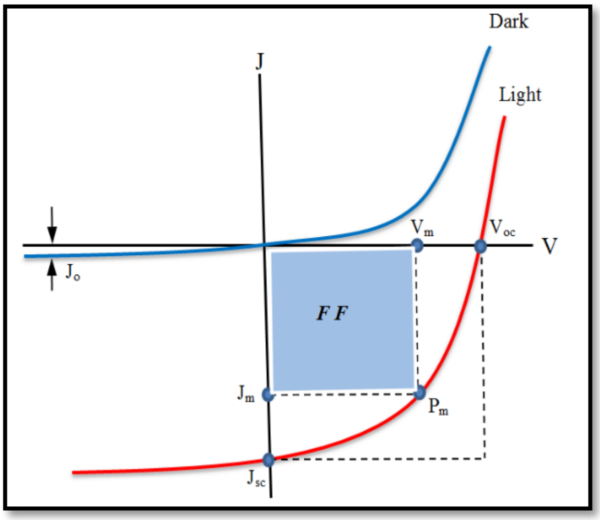

Fig. 2.9: The I-V characteristic curve for the ideal solar cell with respect to the dark and illuminated condition [182].

The basic concepts required to understand and characterize the performance of solar cells are:

2.8.2.1 Short circuit current (I_{sc})

It is the maximum current that flows in the device at zero voltage (i.e. the current generated in the cell when the load resistance is zero) is given by the equation [181]:

$$I_{sc} = I_S \left[\exp\left(\frac{qV_{oc}}{K_B T}\right) - 1\right] + \frac{V_{oc}}{R_{sh}} \qquad (2.37)$$

where (I_s) is the saturation current, (q) is the electron's charge, (K_B) is Boltzmann constant and $k_B T/q = 0.0259$ eV at ($T = 27$ °C), (V_{oc}) open circuit voltage, R_{sh} is the shunt resistant.

2.8.2.2 Open Circuit Voltage (V_{oc})

Open circuit voltage (V_{oc}) is the maximum voltage that the cell can deliver at zero current (i.e. the voltage produced when the load resistance is infinite), given by the relation [183]:

$$V_{oc} = \frac{k_B T}{q} \ln\left(\frac{I_{sc}}{I_s} + 1\right) \qquad (2.38)$$

2.8.2.3 Fill Factor (FF)

The fill factor (FF) is a measure of the quality of the solar cell. It is calculated by comparing the maximum power to the theoretical power (PT) that would be output at both the open circuit voltage and short circuit current together. FF can also be interpreted graphically as the ratio of the rectangular areas (Figure 3.8). This relation is given by [51]:

$$\mathrm{FF} = \frac{\mathrm{I_m V_m}}{\mathrm{I_{sc} V_{oc}}} \qquad (2.39)$$

where V_m and I_m are the voltage and current density corresponding to the power (P_m).

2.8.2.4. The conversion efficiency (η)

The photovoltaic conversion efficiency is an important parameter in solar cells, and it is a measure of the amount of light energy that is converted into electrical energy and is given by [89]:

$$\eta = \frac{\mathrm{P_m}}{\mathrm{P_{in}}} \times 100\% \qquad (2.40)$$

where ($P_m = P_{out}$) is the power generated by the cell, and (P_{in}) is power of the incident light.

Chapter Three

Experimental Work

3.1 Introduction

The purpose of this chapter is to provide an overview of the experimental procedures, the characterization techniques, as the materials used in this work to prepare pure and CuO-doped Sb_2O_3 films and assess the performance of the Sb_2O_3:CuO/etched-Si solar cells.

The research methodology and materials used to achieve the objectives stated in **section (1.5)** are illustrated in the flowchart (see Figure 3.1). The experimental work started with the preparation of Sb_2O_3 nanofilms (weighing 0.01 g) via the thermal evaporation vacuum method and doping Sb_2O_3 with very small ratios (0.02, 0.04, and 0.06) wt.% of CuO NPs (total material prepared for thermal evaporation is 0.01 g) to form pure and CuO-doped Sb_2O_3 nanofilms on glass substrates and laser etched silicon wafer with different thicknesses. The prepared films are subjected to heat treatment (annealing) at 473 K for 2 hours.

Moreover, the thermal evaporation technique was also used in fabricating the solar cells by depositing the front and back contacts on the front and back of the prepared nanofilms using two types of masks (aluminum foils) that have two specific shapes, one for measurements of the solar cell efficiency, and another one for Hall effect measurements.

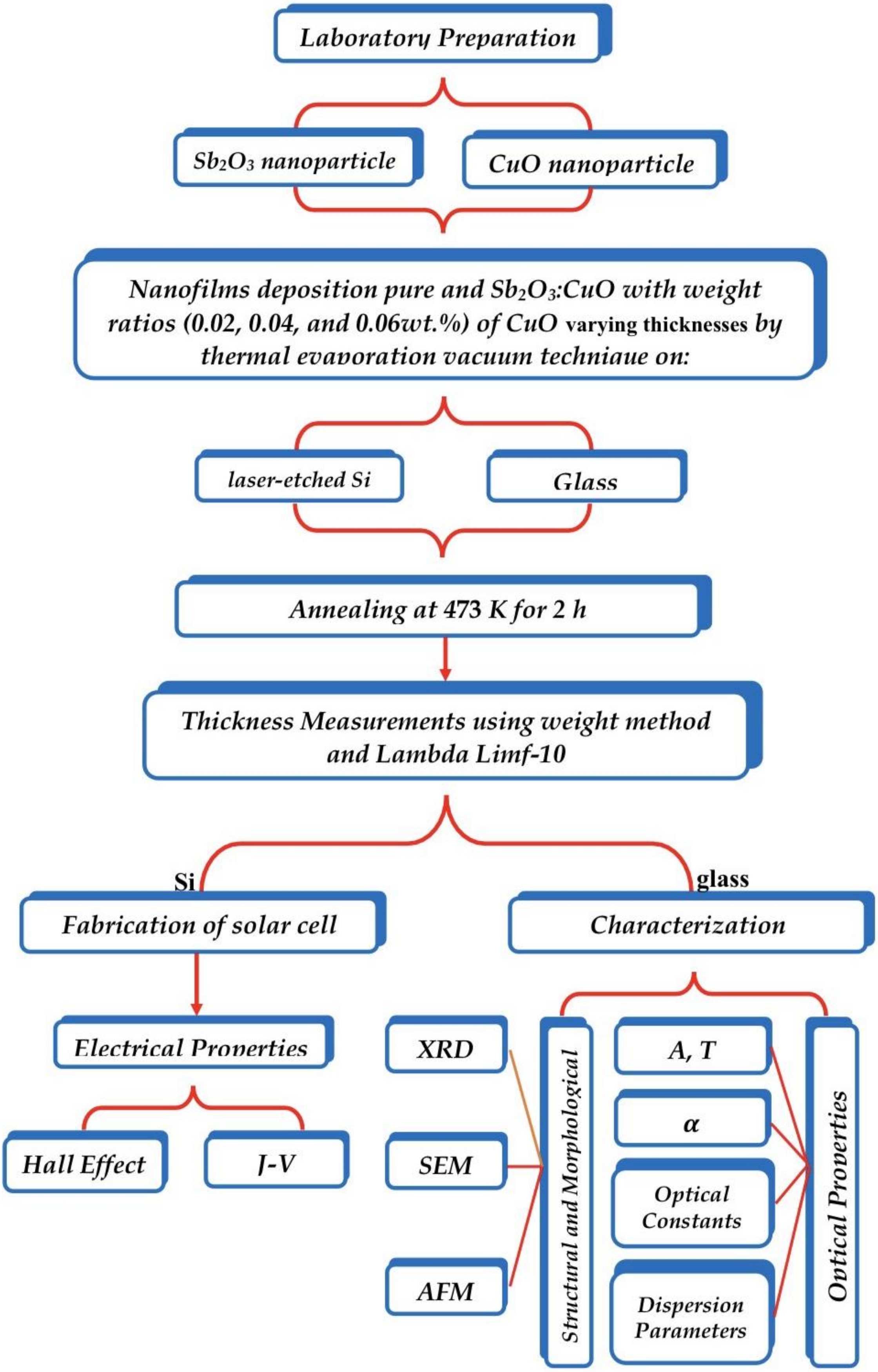

Fig. 3.1: Schematic diagram of experimental work.

3.2 Nanomaterial Used

The raw materials used in preparing Sb_2O_3:CuO nanofilms and Sb_2O_3:CuO/etched-p-Si solar cells are pure antimony trioxide (Sb_2O_3), observed as superfine nanopowder from (Zhengzhou dongyao nano materials Co. LTD) china company) company, with nano grain size (20-30) nm, color white, and high purity (99.5%). The doping material is the copper oxide nanopowder (CuO) observed as a black powder, and high purity (99%) with a size of 40 nm obtained from (SkySpring Nanomaterials, lnc). They are shown in Figure (3.2).

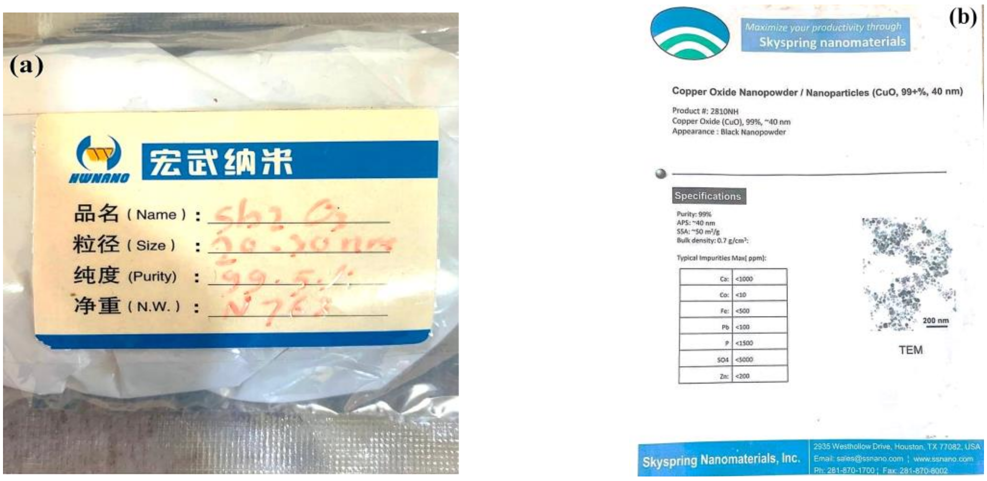

品名 (Name) : Sb2 O3
粒径 (Size) : 20-30 nm
纯度 (Purity) : 99.5%
净重 (N.W.) : N 7[illegible]

Copper Oxide Nanopowder / Nanoparticles (CuO, 99+%, 40 nm)

Product #: 2810NH
Copper Oxide (CuO), 99%, ~40 nm
Appearance : Black Nanopowder

Specifications

Purity: 99%
APS: ~40 nm
SSA: ~50 m²/g
Bulk density: 0.7 g/cm³:

Typical Impurities Max(ppm):

Ca:	<1000
Co:	<10
Fe:	<500
Pb	<100
P	<1500
SO4	<5000
Zn:	<200

Skyspring Nanomaterials, Inc.
2935 Westhollow Drive, Houston, TX 77082, USA
Email: sales@ssnano.com ¦ www.ssnano.com
Ph: 281-870-1700 ¦ Fax: 281-870-8002

Fig. 3.2: Nanomaterial used (a) antimony trioxide and (b) copper oxide.

3.3 Substrate Preparation

Two types of substrates were used for depositing thin films by thermal evaporation, these are glass substrate and silicon wafer.

3.3.1 Glass substrate

The glass substrate is used as a microscope glass for medical labs and other lab applications, each area of $(2.54 \times 7.62)\ \mathrm{cm}^2$ with thickness $(0.10 - 0.12)$ cm. These glass slides were subjected to the following steps:

1- The substrates were cleaned with alcohol.

2- The substrates were immersed in a clean beaker containing distilled water and then washed ultrasonically for 10 min.

3- Lastly, the glass substrates were dried by an blower and were rubbed with soft paper.

Using a glass substrate is to measure the optical properties concerning the prepared films caused by the glass's transparency. It is easy to monitor the color changing of the prepared films using glass substrates.

3.3.2 Silicon wafer

The silicon wafer used for Sb_2O_3:CuO/etched-p-Si heterojunction is the commercially obtainable monocrystalline p-type silicon wafer with orientation (100) and resistivity $(1 - 10\ )\ \Omega.\mathrm{cm}$. Before the film deposition, the wafer silicon was cut into small pieces with suitable size of about $(0.75 \times 0.75\ )\ \mathrm{cm}^2$ and cleaned, which is summarized as follows;

1. Si wafers were cleaned with alcohol.
2. These specimens were rinsed with distilled water several times and dried using soft paper.

3.4 Laser Etching of Silicon Substrates

The experimental setup used for the laser etching process consisted of a Q-switched Nd: YAG laser (Model HF -301, Huafei Technology, China), a beam delivery system, and a focusing lens as portrayed in Figure (3.3), where the distance of about 90 cm between the laser source and the substrate. The laser energy (E) employed for the etching process was 250 (mJ/pulse), the frequency = 3 Hz, and the wavelength = 1064 nm. The laser beam focused on the substrate's surfaces utilising a 120 mm focal length lens. The sample position is perpendicular and faces the laser beam direction, where the entire surface area of the $0.75 \times 0.75\ \mathrm{cm}^2$ samples was exposed to laser beam.

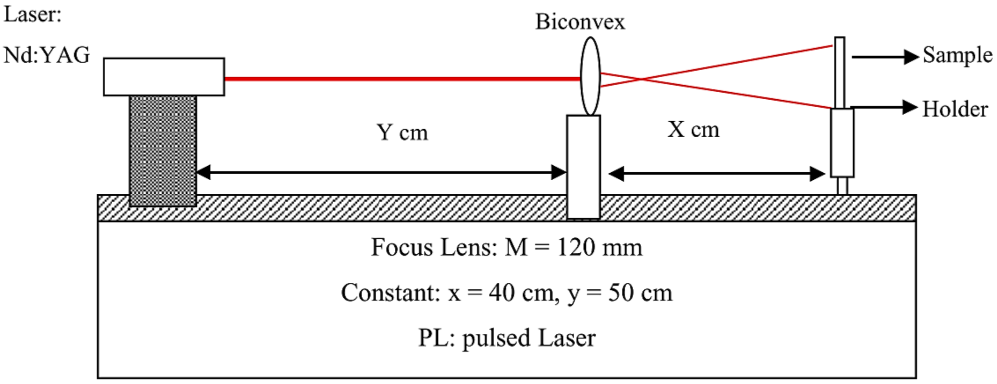

Fig. 3.3: Sketch diagram of the laser-etching process.

3.5 Masking Techniques

The primary aim of employing masks is the electrical measurements (solar cell and Hall effect). Usually, these masks take a form according to the characterization mechanism and characterization instrument, the mask is generally formed by a metal (Al foil). These masks are positioned closest to the substrate where the film is deposited. Masks of different shapes are portrayed in Figure (3.4).

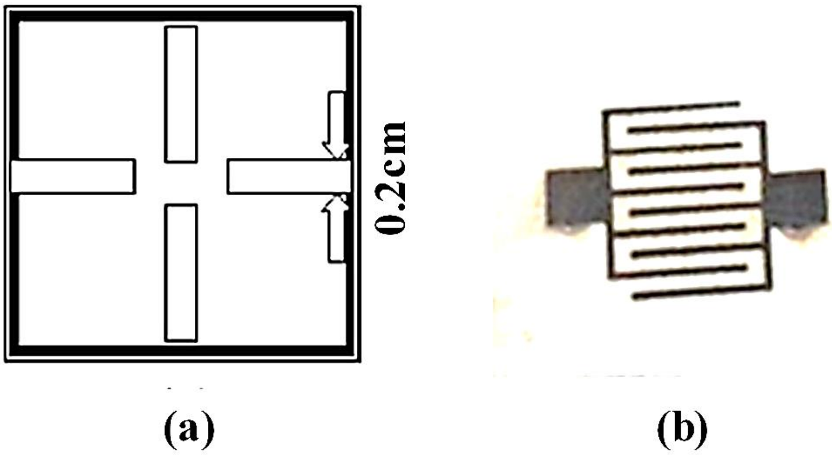

Fig. 3.4: The masks used for (a) Hall effect and (b) I-V characteristic.

3.6 Evaporation Boat

The most commonly used materials for evaporation boats are metals with a high melting point, for instance, tungsten (W) (M.P = 3370 °C) and molybdenum (Mo) (M.P = 2622 °C). In this work, two types of boats were used for the evaporation; a spiral boat of tungsten material used for the (Al) evaporation and a molybdenum boat utilised for the deposition of Sb_2O_3:CuO thin films, as portrayed in Figure (3.5).

Fig. 3.5: Evaporation Boat (a) Tungsten spiral (b) Molybdenum boat.

3.7 The Coating Unit

The vacuum unit system characteristics are listed as follows. The vacuum device, called Edwards Auto 306, was upgraded to perform the deposition processes at low pressure (1×10^{-6}) mbar. The deposition process is carried out using two main types of filaments. Tungsten and Molybdenum filaments are used in the vacuum unit to heat and evaporate the materials to be evaporated or deposited. The typical filament currents are between 100-200 A. The substrates inside the vacuum unit are usually subjected to visible or IR radiation. The maximum deposition thickness that can be achieved using this type of coating is about 1.5 µm. The main construction of the typical vacuum coating unit is portrayed in Figure (3.6).

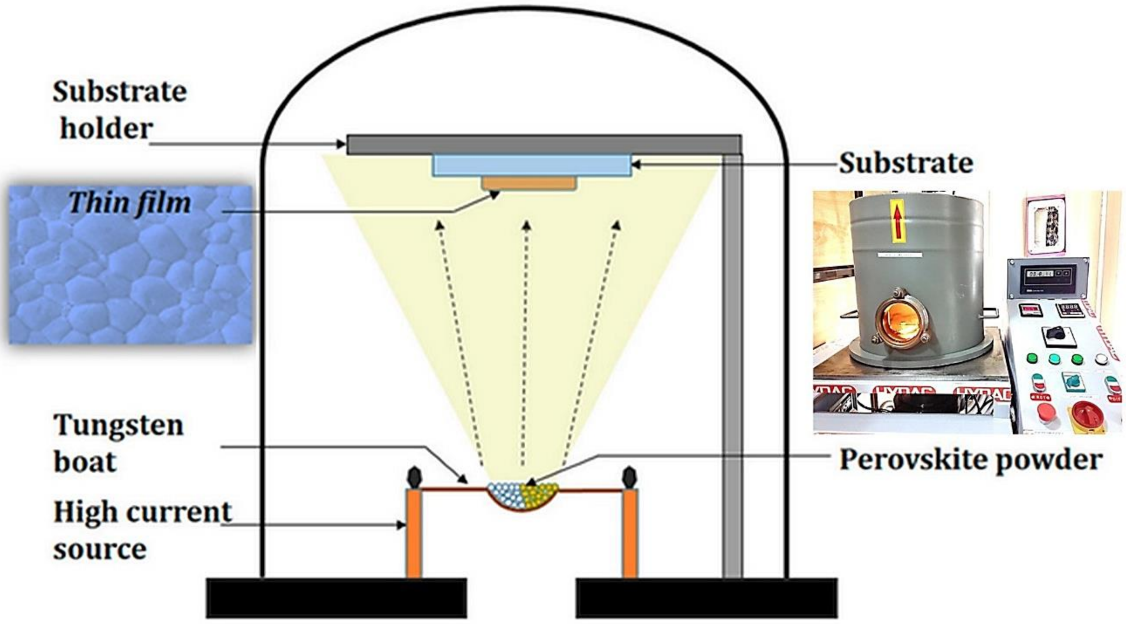

Fig. 3.6: Thermal evaporation (vacuum unit) system.

3.8 Growth of Thin Film

In the present work, thin films of Sb_2O_3:CuO have been obtained by the Sb_2O_3 powder (purity 99.5%) and CuO nanoparticle (purity 99%) according to Table (3.1). The deposition of thin films has been performed by an electrical resistance heated thermal evaporation process. In this process, the electrical power is passed through the boat to create a vapor that travels in straight line paths to the substrate. Generally, there are three steps in any vacuum deposition process: creating an evaporate from the source material, transporting the evaporator from the source to the substrate, and condensing the evaporator onto the substrate to form the thin film deposited as in Figure (3.7). In this work, the evaporation processes have been performed at room temperature (RT). The pressure during the evaporation was approximated to 10^{-6} mbar with a deposition rate 0.3 nm.s^{-1}. The distance between the source and substrate was kept at 15 cm.

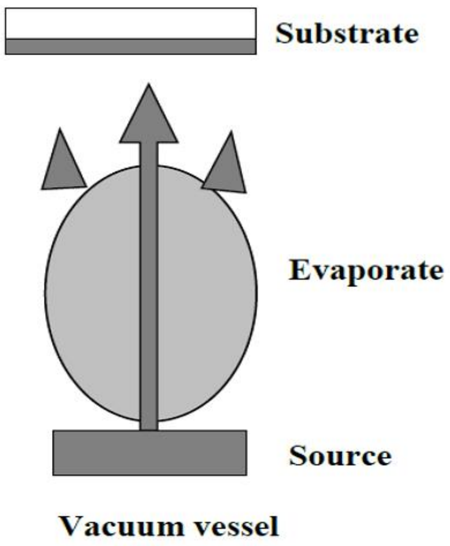

Fig. 3.7: Basic steps deposition processes.

Table (3.1): Weight percentage for (Sb_2O_3:CuO) nanoparticles.

Sb_2O_3 (g)	CuO (g)
0.01	0.0000
0.0098	0.0002
0.0096	0.0004
0.0094	0.0006

3.9 Solar Cell Preparation and Ohmic Contact

Sb_2O_3:CuO nanofilms were provided employing a thermal evaporation vacuum technique on the laser etched silicon wafer substrates at room temperature. The formation of p-n junction solar cells and Ohmic contacts for the prepared films is achieved by evaporating Aluminum, a high purity material, to deposit the solar cell electrodes, as portrayed in Figure (3.8). The electrode deposition process is accomplished by placing the masks on the prepared films' front and back to get the solar cell's desired shape.

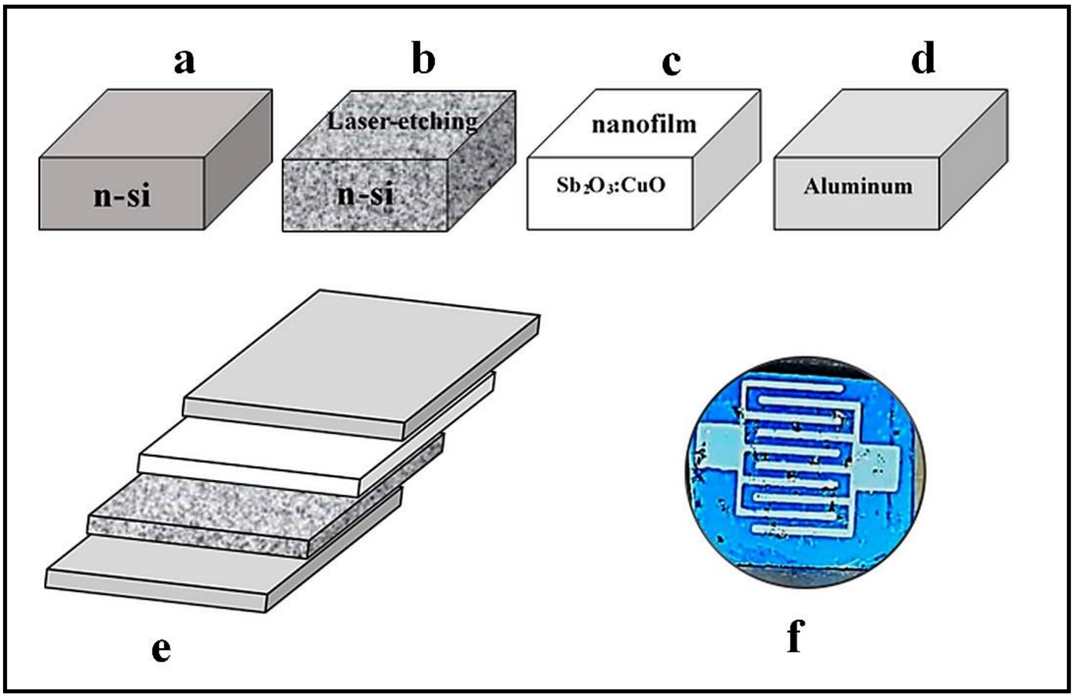

Fig. 3.8: Schematic of solar cell fabrication process (Sb_2O_3:CuO): (a) silicon substrates, (b) silicon substrates have laser-etched, (c) deposited of (Sb_2O_3:CuO) nanofilm by thermal evaporation, (d) the contact layer is deposited from Al (front and back) on the p-Si layer, (e) solar cell structure, and (f) fabrication solar cell.

3.10 Films Thickness Measurement

Via an optical thin film measurement instrument (Lambda Limf-10), the thickness was estimated by the difference in optical path lengths of the two reflections employing a He-Ne laser (632 nm). The nanofilms' thicknesses (t) were (20, 30, and 40) nm, which is comparable with the weight method calculated by the equation [184, 185]:

$$t = \frac{m}{2\pi\rho r^2} \tag{3.1}$$

where t is the thickness of the thin films (nm), m mass of the materials in (g), ρ is the density of materials (g/cm^3), and r is the distance between the substrate and the boat (cm). This method gives an approximate thickness because not all the material is deposited on the substrate, but some is lost or fleeing on the sides of the heater.

3.11 Structural and Morphological Measurements

3.11.1 X-ray diffraction (XRD)

The main purpose of these measurements is to investigate the type of the structure of the prepared thin films. This experimental technique has long been used to determine the overall structure of bulk solids, including lattice constants, identification of unknown materials, orientation of single crystals, orientation of polycrystals, defects, stresses, etc. X-ray diffraction using SHIMADZU X-ray diffraction meter system (XRD-6000) records the intensity as a function of Bragg's angle, as shown in Figure (3.9). Samples were tested in Iran/Tehran. The conditions of the system were:

Source CuKα with radiation of wavelength $\lambda = 1.5406$ Ǻ.
Target: Cu
Current = 30 mA.
Voltage = 40 kV.
Scanning speed = 0.25 deg/min

X-ray scans are performed between 2θ values of 10^{o} and 80^{o}.

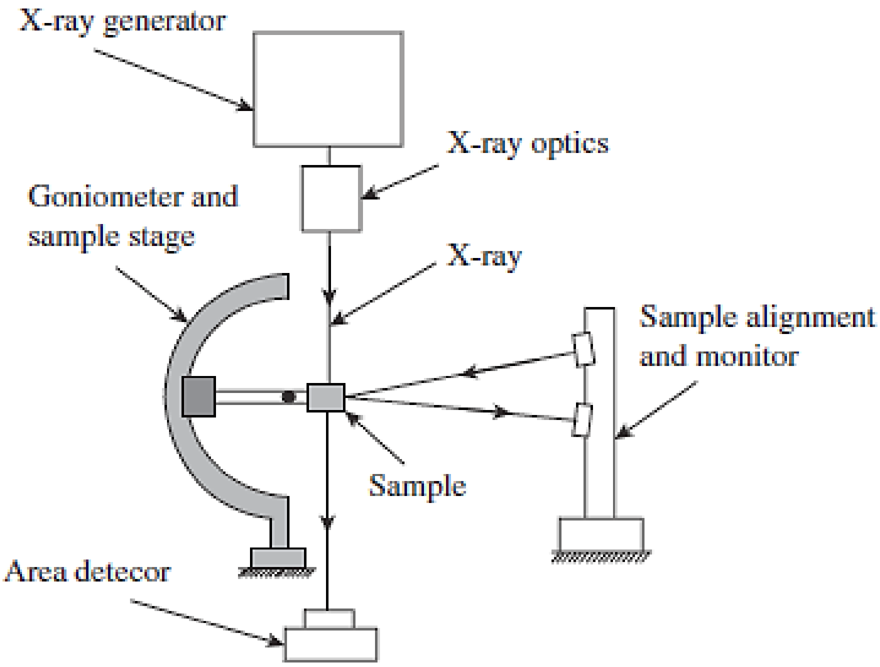

Fig. 3.9: The system of XRD.

3.11.2 Atomic Force Microscope (AFM)

This instrument is used to take a look at surfaces on a molecular level. It observes the surface roughness and topography of deposited thin films. This device determines the size and other characteristics of the synthesized nanoparticles, an atomic force microscope (AFM) is used, as shown in Figure (3.10). The most important part of an atomic force microscope is the tip with its nanoscale radius of curvature. The tip is attached to a micron scale cantilever which reacts to the Van der Waals interaction and other forces between the tip and sample. The surface topography of the samples was examined at 473 K with a scan size of (5×5) µm and a high resolution of (256×256) pixels. The root mean square, surface skewness, mean particle height, distribution, and particle diameter were all calculated from the picture data using nanoscope software. Samples were tested in University of Babylon/College of Education for Pure Sciences/Department of Physics.

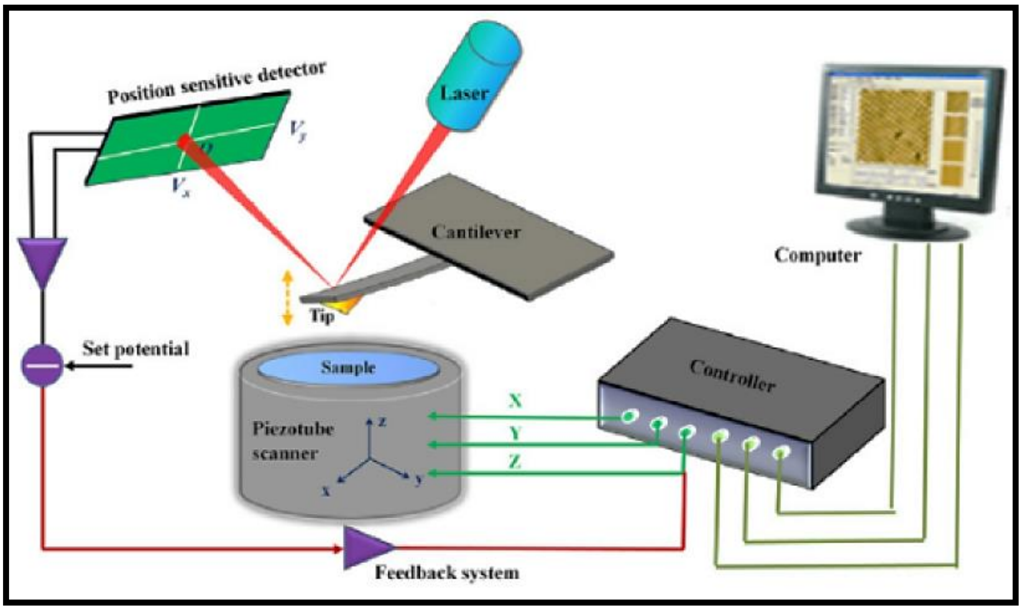

Fig. 3.10: Schematic diagram of the basic working principle of AFM.

3.11.3 Scanning electron microscope (SEM)

A scanning electron microscope (SEM) is an electron microscope that images the surface of a sample by scanning it with a high-energy beam of electrons in a point scanning pattern. SEM test samples must be electrically conductive, at least on the surface, and electrically grounded to prevent the buildup of electrostatic charges on the surface. A small fraction (2×2) cm of the sample was examined by SEM. This work used a low vacuum SEM, as shown in Figure (3.11). The surface morphology of the (Sb_2O_3:CuO) thin films was observed using (Bruker Nano GmbH, company, German original, type vertex 5600 LV SEM) Iran/Tehran.

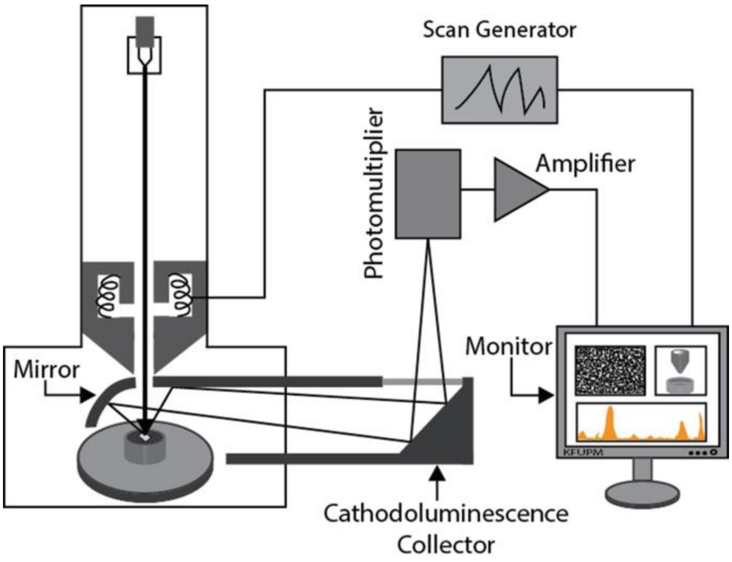

Fig. 3.11: Diagram for system of SEM device.

3.12 Optical Properties Measurements

UV-Vis spectroscopy was used to measure the amount of absorbed UV and visible radiation in this study. The absorption properties of produced thin films are investigated using a UV-Vis spectrophotometer (Shimadzu, UV-1800 A0, Japan). The optical properties with respect to the thin films were measured employing an empty glass as a reference with wavelength (λ) ranging from (200-1100) nm.

The UV spectrometer light source includes two different lamps: a tungsten lamp for visible wavelengths and a UV deuterium lamp. The monochromatic is constructed of numerous slits and gratings or prisms that permit only a short wavelength range of radiation to pass through. The monochromatic is adjustable so that the entire UV-Vis spectrum can be recorded. The monochromatic radiation passes through the sample and reference, after which its intensity is measured using a detector, as shown in Figure (3.12). Samples were tested in University of Babylon/College of Education for Pure Sciences/Department of Physics.

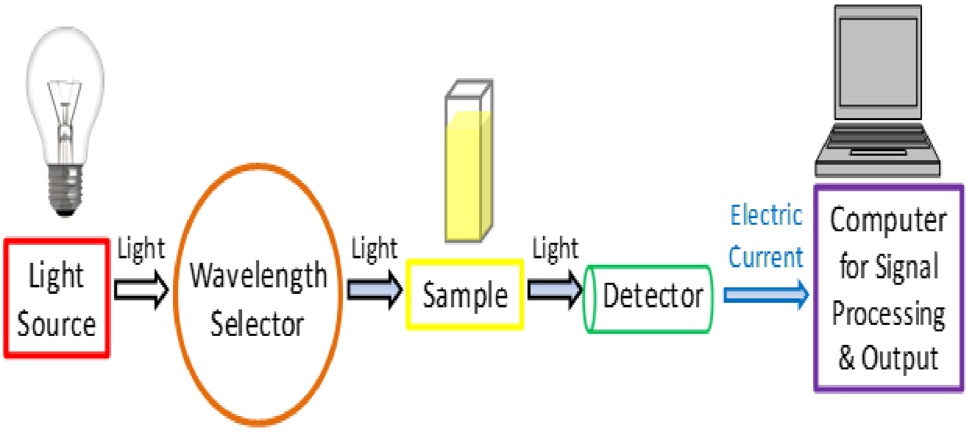

Fig. 3.12: UV photographic of spectrophotometer.

3.13 Electrical Properties Measurements

The electrical measurements are achieved on prepared thin films including, Hall effect and I-V characteristics.

3.13.1 Hall effect measurements

When a magnetic field is applied on a current-carrying semiconductor, the charge carriers experience a force perpendicular to the magnetic field and the current. This is called the Hall Effect. By measuring the strength of this effect, the type of electron/hole transport materials (p- or n-type) and the carrier type and concentration can be determined. Samples were tested in Al-Nahrain University/thin films examination centre.

3.13.2 Current-Voltage measurements for the heterojunction under illumination

The electrical properties and photovoltaic study of Sb_2O_3:CuO/etched-p-Si solar cells have been done by using an electrical circuit, as in Figure (3.13), which consists of the following equipment:

i. D.C. power is supplied of type (6291A), and the voltage range is from (0-30) volt.
ii. A digital voltmeter (siemens digital multimeter B1031) for measuring voltages, and this device has a range between $(200 \times 10^{-3} - 2000)$ volts.
iii. A digital electrometer (Keithely 616 digital electrometer) to measure the current in the cell. This device has a current range between $(4 \times 10^{-16} - 200 \times 10^{-3})$ amperes.
iv. Halogen light with power (120 W) gives radiation density from shunt voltage since power density is given by each volt measured using a power meter.
v. A device for measuring the intensity of light (Solar meter dp Mod. 776).

These parameters (V_{oc}, I_{sc}, FF, and η) were measured under normal conditions of cell temperature of 25 °C, and incident solar radiation of 100 mW/cm^2. Samples were tested in Al-Nahrain University/thin films examination centre.

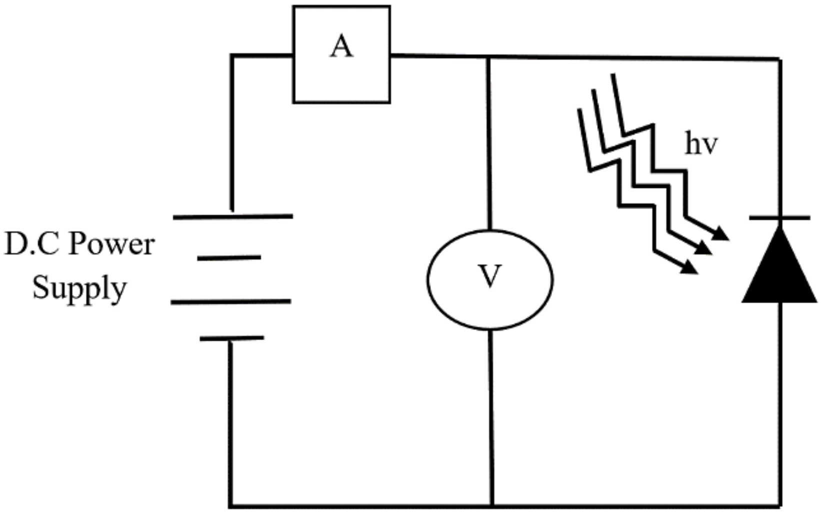

Fig. 3.13: The circuit diagram with respect to I-V measurement of the heterojunction under the dark and illuminated condition.

Chapter Four

Results and Discussions

4.1 Introduction

This chapter presents the results and discussion of the structural, morphological, and optical (the dispersion parameters were also investigated using Wemple-Didominco model) and electrical properties of pure Sb_2O_3 and CuO-doped Sb_2O_3 with different CuO ratios. In addition, the effect of thickness on the prepared films and the effect of CuO-doped on the efficiency of Sb_2O_3:CuO/etched-p-Si solar cell.

4.2 Structural and Morphological Properties

4.2.1 X-ray diffraction of Sb_2O_3 and Sb_2O_3:CuO nano films

At the beginning of this work, the X-ray diffraction (XRD) diagnostic was shown for antimony trioxide powder in Figure (4.1). In general, after matching the diffraction peaks that appeared in the X-ray diffraction data with the diffraction peaks of the Joint Committee of Powder Diffraction Standard (JCPDS), card file data (96-900-7610, a=1.11520 nm) show the crystalline system for antimony trioxide powder of the cubic type (senarmontite), the space group, Fd -3 m (227). The parameters of Sb_2O_3 powder are listed in Table (4.1).

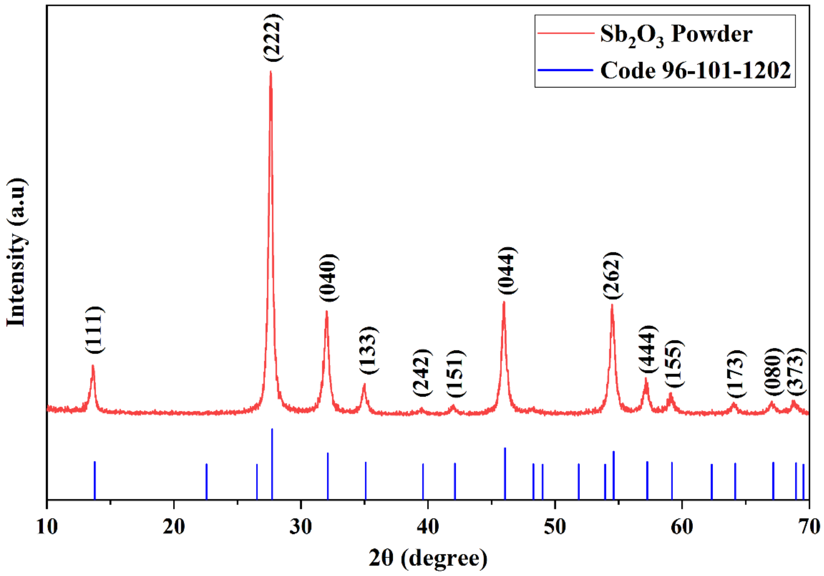

Fig. 4.1: XRD patterns of Sb_2O_3 powder.

These sharp peak reflections indicate the highly crystalline nature of the obtained cubic Sb_2O_3 phase, similar to the previous reports [114].

Table (4-1): The obtained result of the XRD of Sb_2O_3 powder.

2θ degree	hkl	$FWHM$ degree	d_{hkl}	Average crystallite size (nm)	$Structure$
13.742	(111)	0.2755	6.483	25.062	Cubic (Senarmontite)
27.578	(222)	0.096	3.231	29.448	
32.036	(040)	0.2755	2.793	28.681	
34.967	(133)	0.1968	2.566	8.571	
39.464	(242)	0.6297	2.283	8.370	
41.947	(151)	0.3936	2.153	11.075	
45.991	(044)	0.2755	1.973	16.162	
54.452	(262)	0.2361	1.685	17.537	
57.110	(444)	0.3148	1.612	25.326	
59.125	(155)	0.3148	1.562	7.350	
64.098	(173)	0.3148	1.452	21.249	
67.048	(080)	0.3148	1.395	13.489	
68.765	(373)	0.2755	1.365	29.657	

X-ray diffraction spectra of pure Sb_2O_3 and CuO-doped Sb_2O_3 nanofilms with (0.02, 0.04, and 0.06) $wt.$% doping of CuO, prepared by thermal evaporation technique at room temperature (RT) under pressure up to 10^{-6} mbar, rate of deposition 0.3 nm.s^{-1}, which annealed at temperature 473 K for 2 hours and thicknesses of (20, 30 and 40) nm. Peaks of XRD were recorded between $(10^{\circ} - 80^{\circ})$.

Figures (4.2 - 4.5) display the XRD patterns for Sb_2O_3 and Sb_2O_3:CuO nanofilms with varying thicknesses (20, 30, and 40) nm. The XRD data indicate that the pure Sb_2O_3 nanofilms at (20, 30, and 40) nm have no distinguishing peaks, referring to the films as amorphous.

Only one small peak was determined for Sb_2O_3:(0.02, 0.04, and 0.06) wt.%CuO nanofilms at a thickness of 40 nm at $2\theta = 31.932^o$, 31.894^o and 31.945^o respectively, corresponding to the Miller indices (040), these results are in good agreement with research [63]. The Sb_2O_3 nanofilm diffraction peak is readily indexed to cubic Sb_2O_3 (JCPDS 96-101-1202). From the peak position (2θ) and full width at half maximum (FWHM), the crystallite size (D) was calculated using Scherer's Formula (2.2). The values are tabulated in Table (4.2).

The width given in such figures refers to the broadening of the diffraction peak for the following reasons: X-ray diffractometers have a limited resolution, meaning they cannot distinguish between very similar crystal planes. If the crystal size is polycrystalline or consists of small crystallites (compatible with the analyses SEM), it can lead to a broadened peak due to the presence of different orientations and varying lattice spacings within the crystal. Crystal defects, such as vacancies, dislocations, or impurities, can cause lattice distortions and lead to peak broadening in the X-ray pattern [186]. Similarly, the presence of disorder in the arrangement of atoms within the crystal can also contribute to a wider peak [187]. One of the appears peaks refers to no disorder in the arrangement of atoms or crystal defects. These results are in good agreement with research [113, 188].

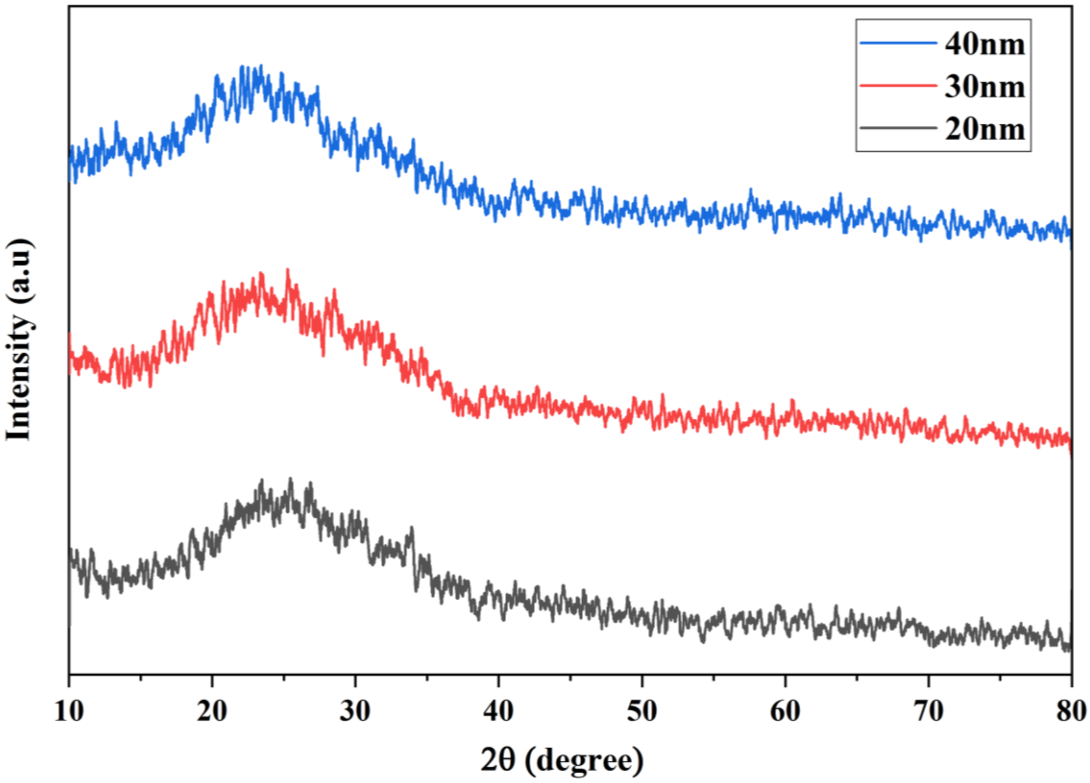

Fig. 4.2: XRD patterns of pure Sb_2O_3 nanofilms.

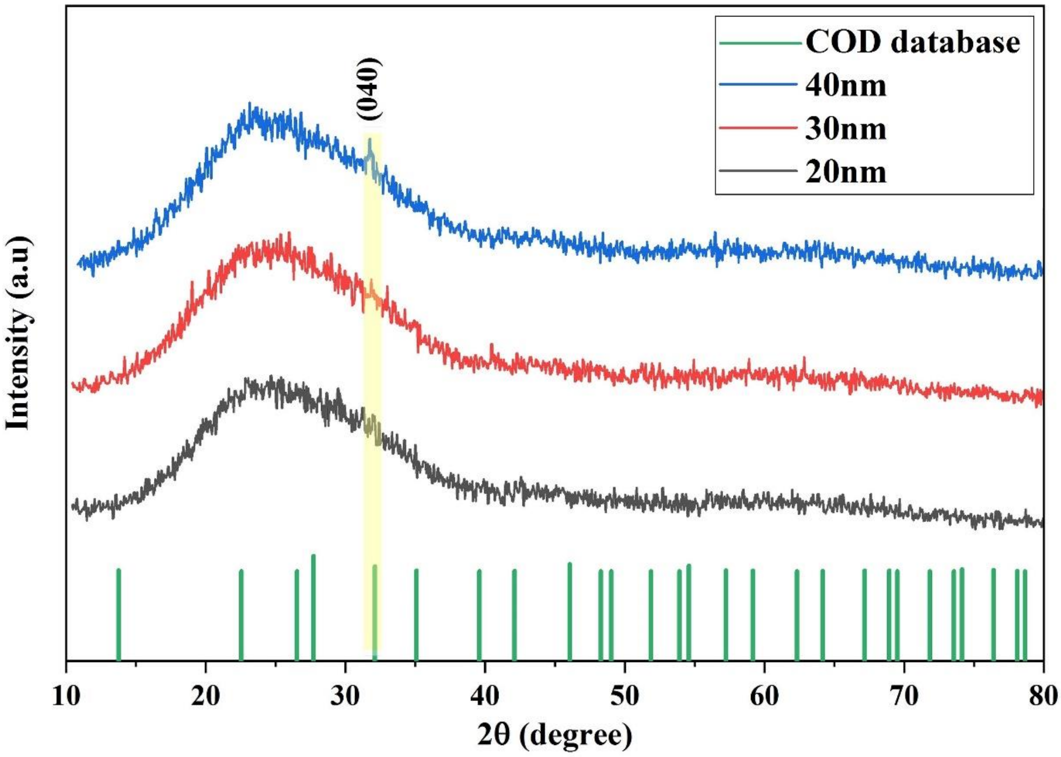

Fig. 4.3: XRD patterns of Sb_2O_3: 0.02wt% CuO nanofilms.

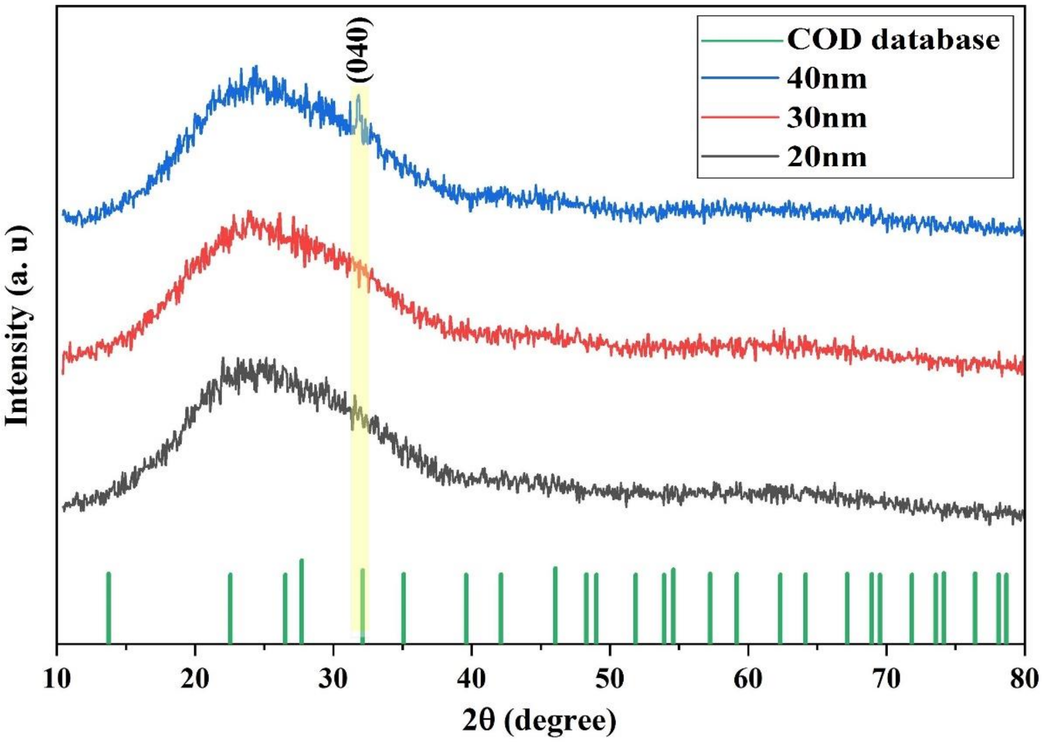

Fig. 4.4: XRD patterns of Sb_2O_3: 0.04wt% CuO nanofilms.

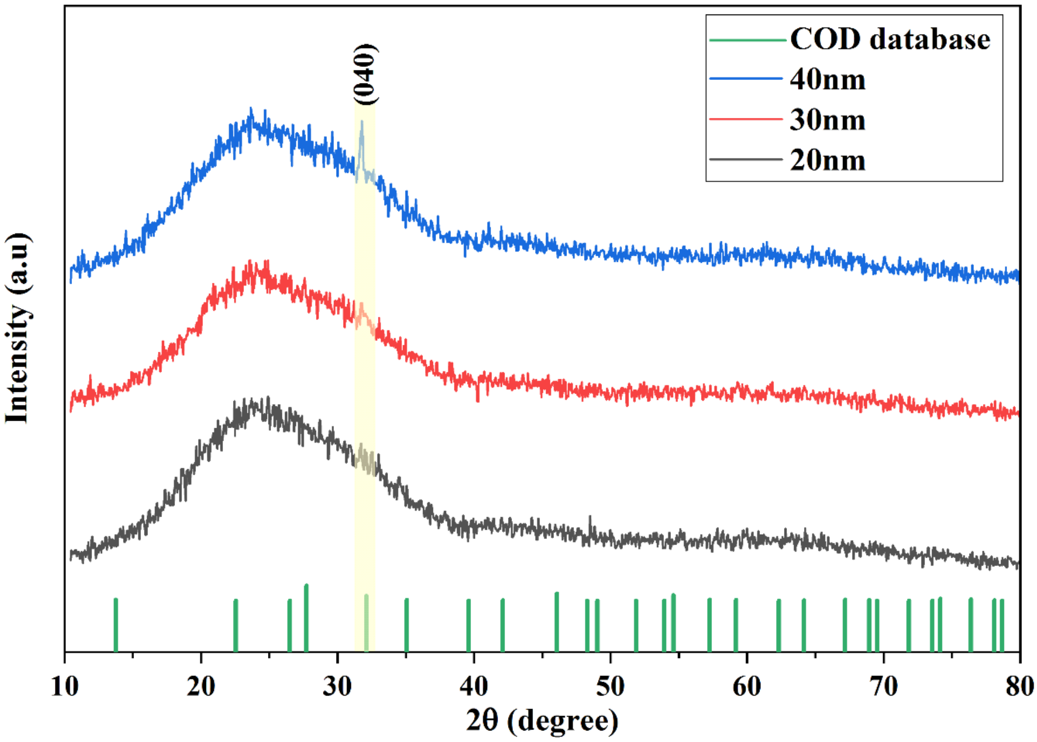

Fig. 4.5: XRD patterns of Sb_2O_3: 0.06wt% CuO nanofilms.

Table (4-2): The obtained result of the XRD of Sb_2O_3:CuO nanofilms.

CuO-doped Sb_2O_3 (wt.%)	Thickness (nm)	2θ (degree)	hkl	FWHM degree	d_{hkl}	Crystallite size (nm)	Structur
0.02	**40**	31.932	(040)	0.704	2.824	11.395	**Cubic**
0.04	**40**	31.894	(040)	0.643	2.823	12.537	
0.06	**40**	31.945	(040)	0.697	2.819	11.490	

4.2.2 Atomic force microscopy (AFM)

Figures (4.6 - 4.9) show that the pure Sb_2O_3 and CuO-doped Sb_2O_3 nanofilms at a thickness (20, 30, and 40) nm. The AFM images of pure and CuO-doped Sb_2O_3 nanofilms show uniform granular surface morphology, homogeneous distribution, and dispersion of CuO particles within the Sb_2O_3 matrix. Moreover, the AFM scanning images revealed an obvious smooth surface morphology composed of small grains of the prepared films. Surface roughness decreased for pure Sb_2O_3 nanofilms from 0.544 nm to 0.236 nm at a thickness of 40 nm, as shown in Figure (4.6). The surface roughness increased with increased CuO NP content in Sb_2O_3 nanofilms and decreased with the increased thickness of nanofilms. The observed increase in roughness is attributed to the concentration of CuO nanoparticles in the Sb_2O_3 nanofilms, which is consistent with the research results [113, 189].

When the thickness of a nanofilm increases, the surface homogeneity improves, leading to a reduction in surface roughness. This can be attributed to the well-distributed Sb_2O_3 particles at the films' surface and the high interaction between the Sb_2O_3 and the minimal content of CuO particles. In other words, increasing nucleation sites after every deposition and doping process could increase the surface area of the fabricated films. It is well-known that the absorption of a large number of photons can be related to the higher surface area, yielding an enhancement in photocurrent for photovoltaic applications, which are suitable and compatible with the research [108].

As seen in Table (4.3), AFM images exhibit grain heights of a few tens of nanometers. The ten-point height increases with increasing doped ratio and decreased with increasing thickness of nanofilms. This result could probably be the evaporated particles' movement that possesses the energy to reach the surface. The arrived particles with energy remain unstable in a specific place but look for holes and low places to settle in until all holes are closed, and the surface becomes smooth according to the Stranski-Krastanov model [190].

The average grain diameter decreased with the increasing thickness of nanofilms. The high values of the average grain diameter refer to the agglomeration of many fine particles with small sizes, where the tip of the AFM device detects them as one particle. In contrast, the values of the ten point height refer to the homogeneity of the fabricated films, as shown by the convergence of roughness average and root mean square values. The results are in accordance with the findings of the research [108]. Table (4.3) has a list of the results.

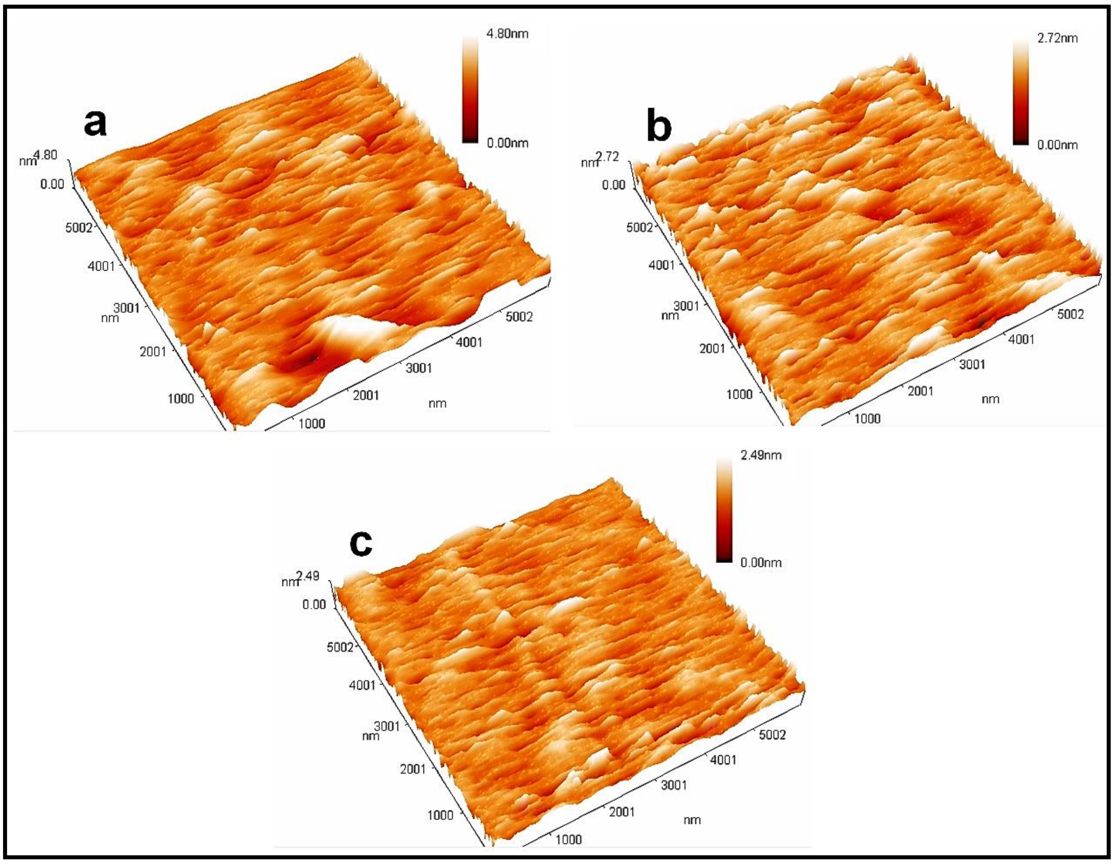

Fig. 4.6: AFM images of Sb_2O_3 nanofilms at a thickness of (a) 20nm, (b) 30nm, and (c) 40nm.

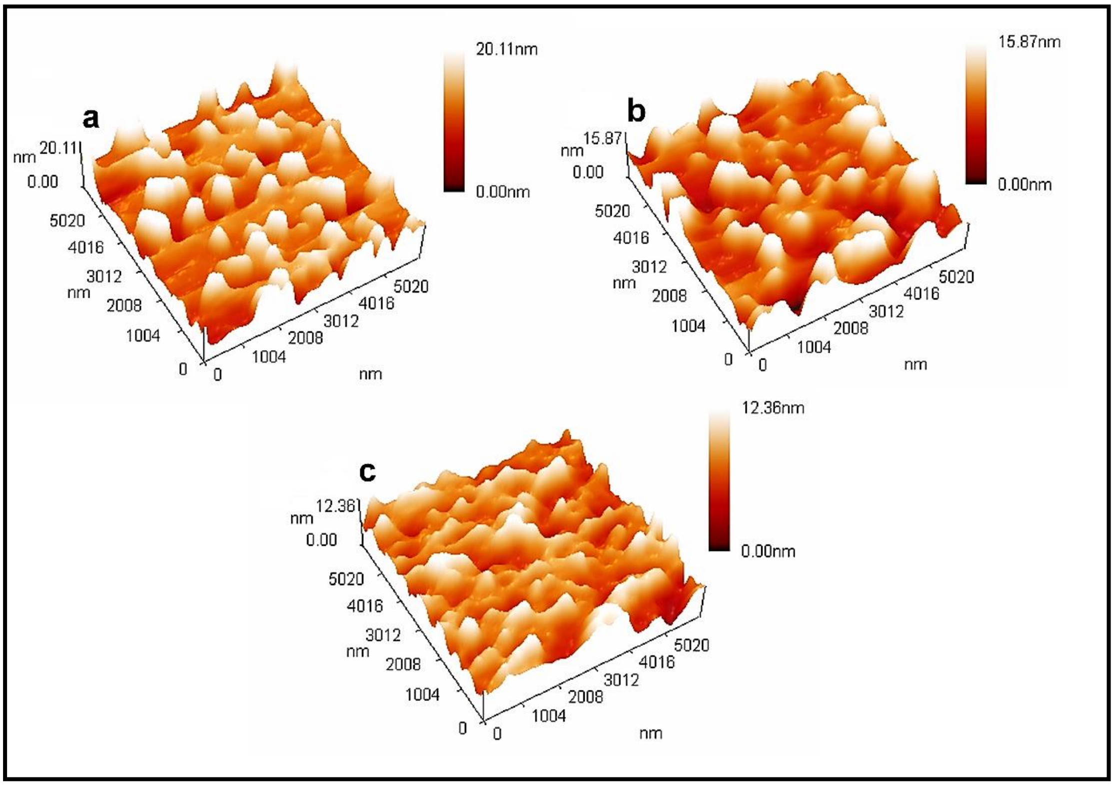

Fig. 4.7: AFM images of Sb_2O_3: 0.02wt% CuO nanofilms at a thickness of (a) 20nm, (b) 30nm, and (c) 40nm.

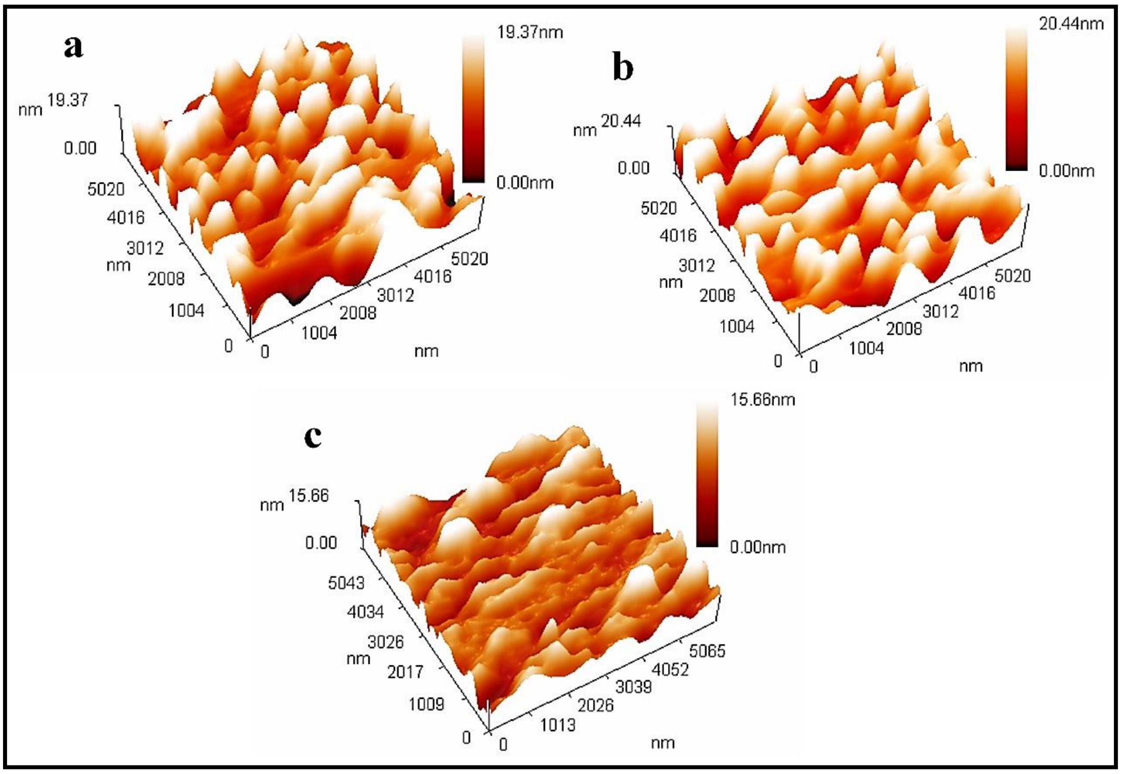

Fig. 4.8: AFM images of Sb_2O_3: 0.04wt% CuO nanofilms at a thickness of (a) 20nm, (b) 30nm, and (c) 40nm.

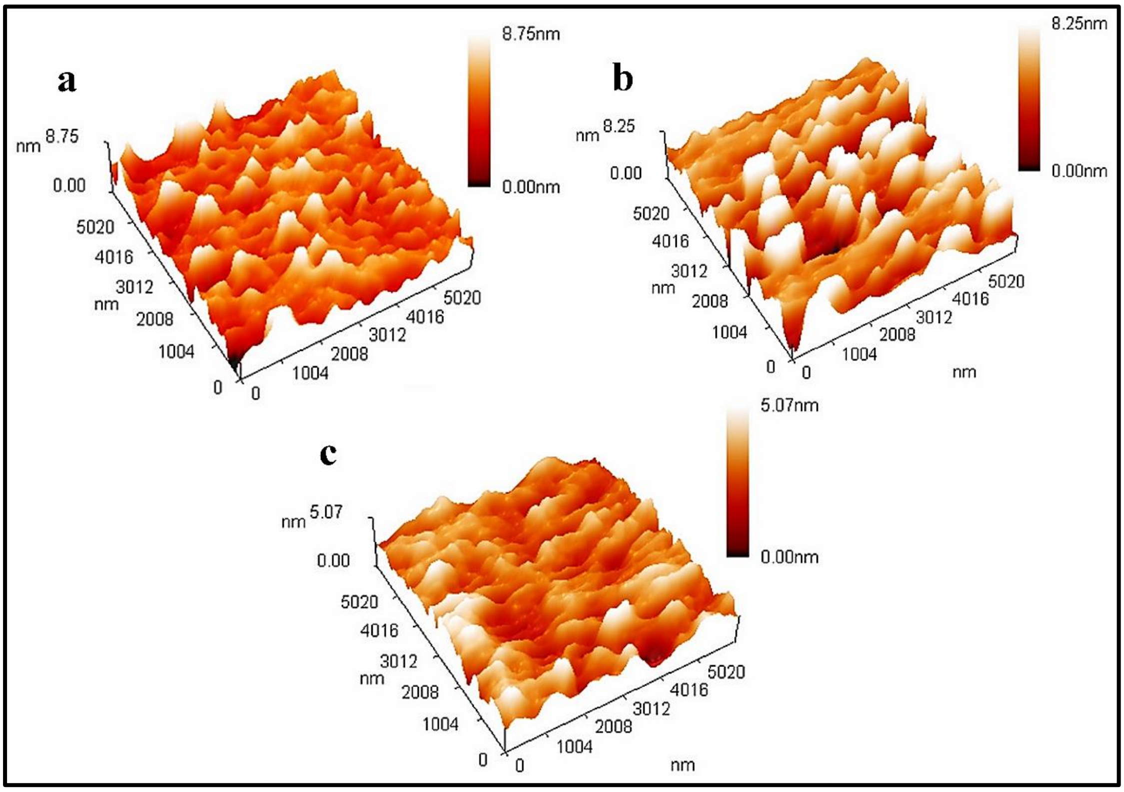

Fig. 4.9: AFM images of Sb_2O_3: 0.06wt% CuO nanofilms at a thickness of (a) 20nm, (b) 30nm, and (c) 40nm.

Table 4.3: Morphological characteristics of pure and Sb_2O_3: CuO nanofilms at different thicknesses and annealing temperature at 473 K

CuO-doped Sb_2O_3 (wt.%)	Thickness (nm)	Roughness average Sa (nm)	Root mean square Sq (nm)	Ten point height Sz (nm)	Average diameter (nm)
0.00	**20**	0.393	0.544	3.45	230.2
	30	0.252	0.341	2.38	201.2
	40	0.172	0.236	1.99	172.6
0.02	**20**	4.45	5.11	14.8	753
	30	3.71	4.53	6.22	611
	40	1.54	1.94	2.27	523.8
0.04	**20**	4.23	5.05	12.1	640.6
	30	3.96	4.77	5.79	631.7
	40	2.06	2.66	6.79	498.6
0.06	**20**	1.49	1.97	7.91	499.8
	30	1	1.36	3.77	429.3
	40	0.591	0.753	3.68	420.5

4.2.3 Scanning electron microscopy (SEM)

SEM images of pure and CuO-doped Sb_2O_3 with different doping of CuO (0.02, 0.04, and 0.06) wt.% nanofilms have been prepared by thermal evaporation technique under the pressure of 1×10^{-6} mbar with the rate of deposition 0.3 nm.s^{-1}, which are annealed at a temperature of 473 K for 2 hours and thicknesses of (20, 30, and 40) nm.

The size and shape of the nanoparticles present in the fabricated nanofilms were analyzed using SEM [191]. Figures (4.10 - 4.21) show that the pure and CuO-doped Sb_2O_3 nanofilms at a thickness of (20, 30, and 40)

nm respectively and varius content of CuO doping, at the same magnification (135KX), which exhibit a smooth surface devoid of islands and voids and consisting of small spherical grain size nanoparticles (NPs). The surface morphology of the pure and CuO-doped Sb_2O_3 nanofilms appears to be influenced by their thickness and CuO-doping, as shown by these micrographs. The SEM micrographs of pure and CuO-doped Sb_2O_3 nanofilms clearly show the improvement in the crystallite size with increased thickness. Observe that adding CuO nanoparticles increases the particulate size and homogenization of the morphology. So, it can be observed there is a considerable effect in developing some grains, which grow in uniform directions and a homogenous distribution. With CuO doping increases, the new structures grow especially with increasing thickness. These structures seem to contain CuO and Sb_2O_3 because of the bright and dark places in the same new particle.

Analysis of SEM images revealed the presence of some larger spherical and near-spherical objects, likely due to the regular arrangement of particles without holes or defects in certain regions on the glass substrate. It is clear from the indicated particle sizes in SEM images and the distribution function that there is an increase in the size of the granules with the increase in thickness and ratio doped, which is in accordance with the findings of the researcher [52].

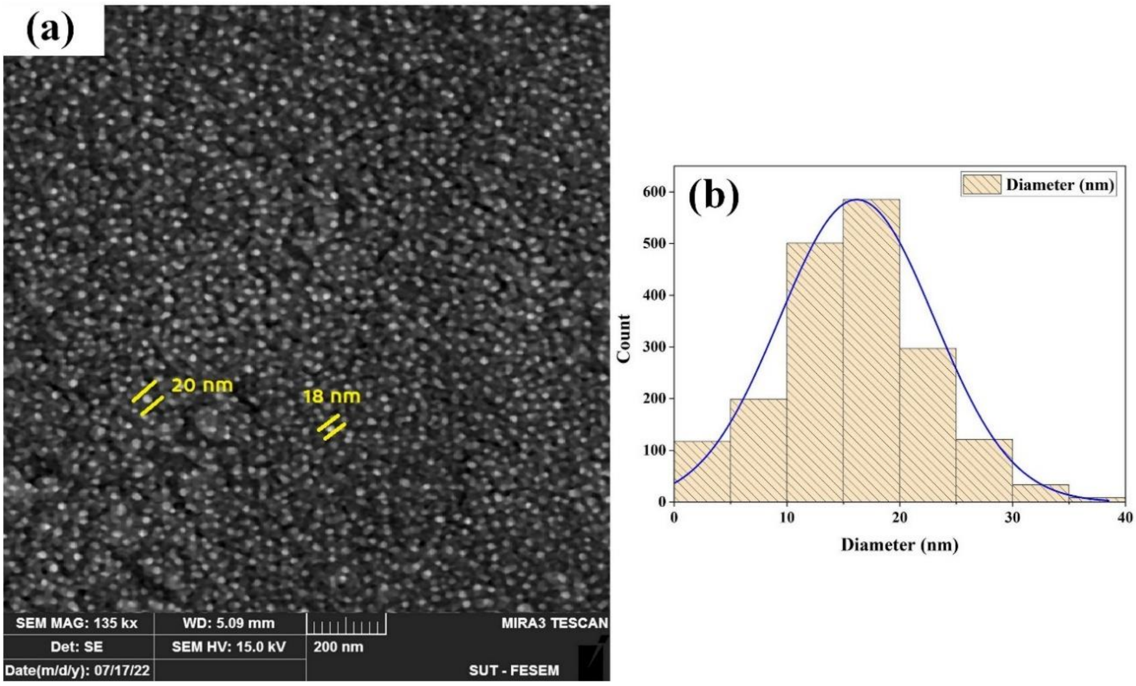

Fig. 4.10: (a) SEM images of Sb_2O_3 nanofilms at a thickness of 20nm (b) histograms of diameters with Gaussian distribution.

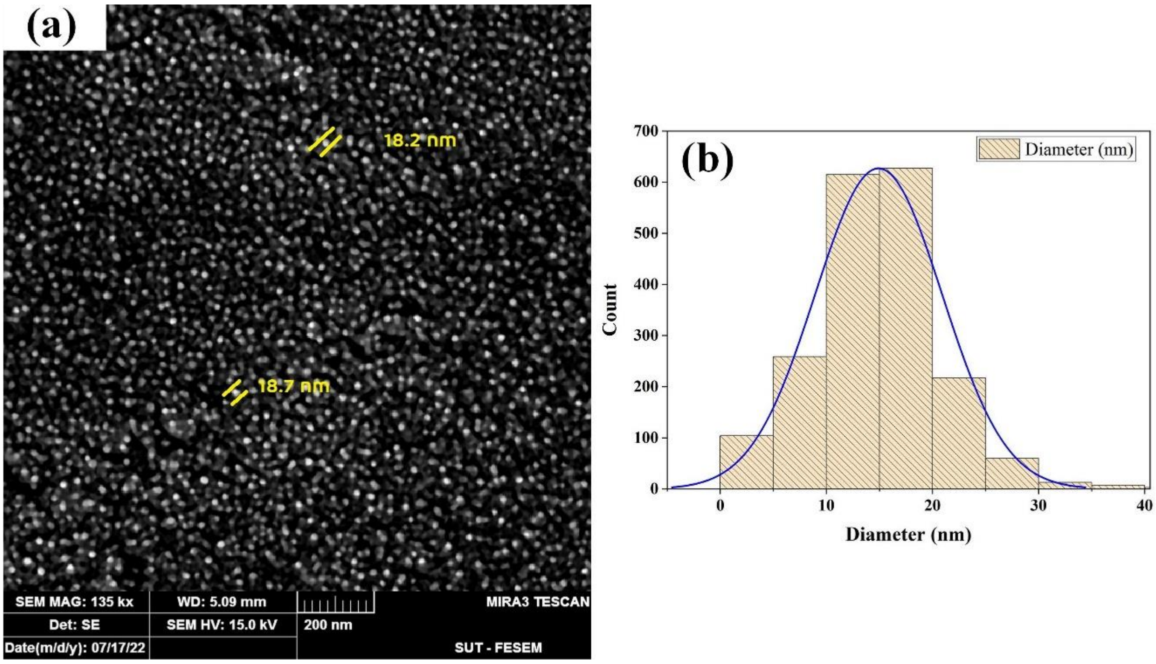

Fig. 4.11: (a) SEM images of Sb_2O_3 nanofilms at a thickness of 30nm (b) histograms of diameters with Gaussian distribution.

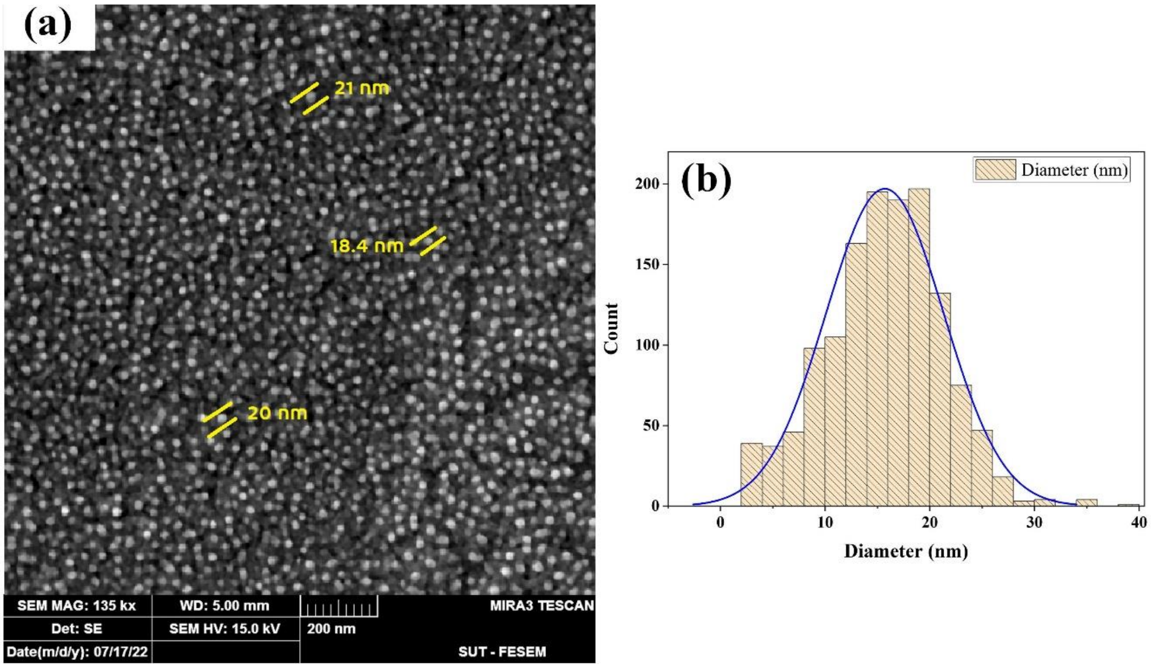

Fig. 4.12: (a) SEM images of Sb_2O_3 nanofilms at a thickness of 40nm (b) histograms of diameters with Gaussian distribution.

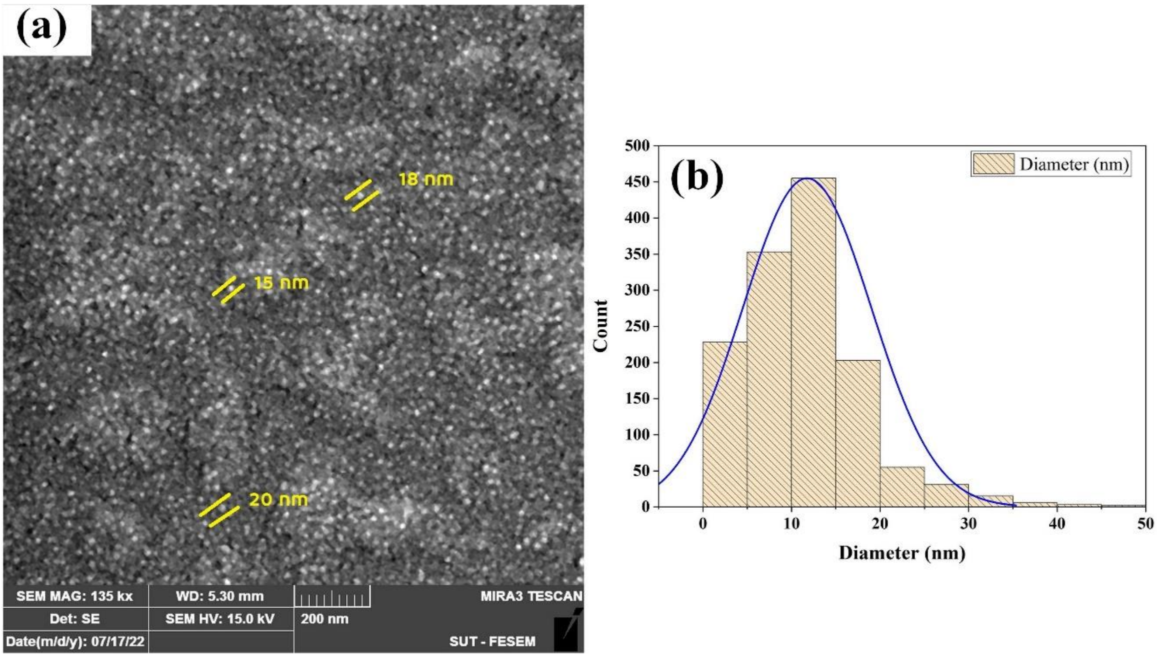

Fig. 4.13: (a) SEM images of Sb_2O_3: 0.02wt% CuO nanofilms at a thickness of 20nm (b) histograms of diameters with Gaussian distribution.

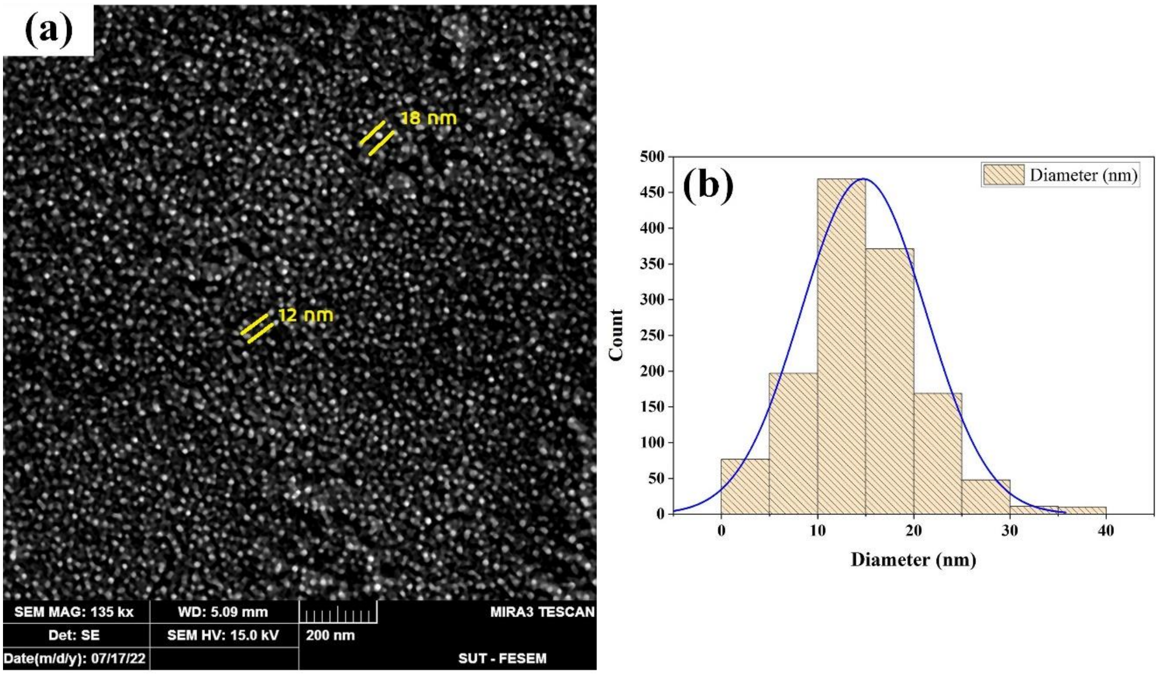

Fig. 4.14: (a) SEM images of Sb_2O_3: 0.02wt% CuO nanofilms at a thickness of 30nm (b) histograms of diameters with Gaussian distribution.

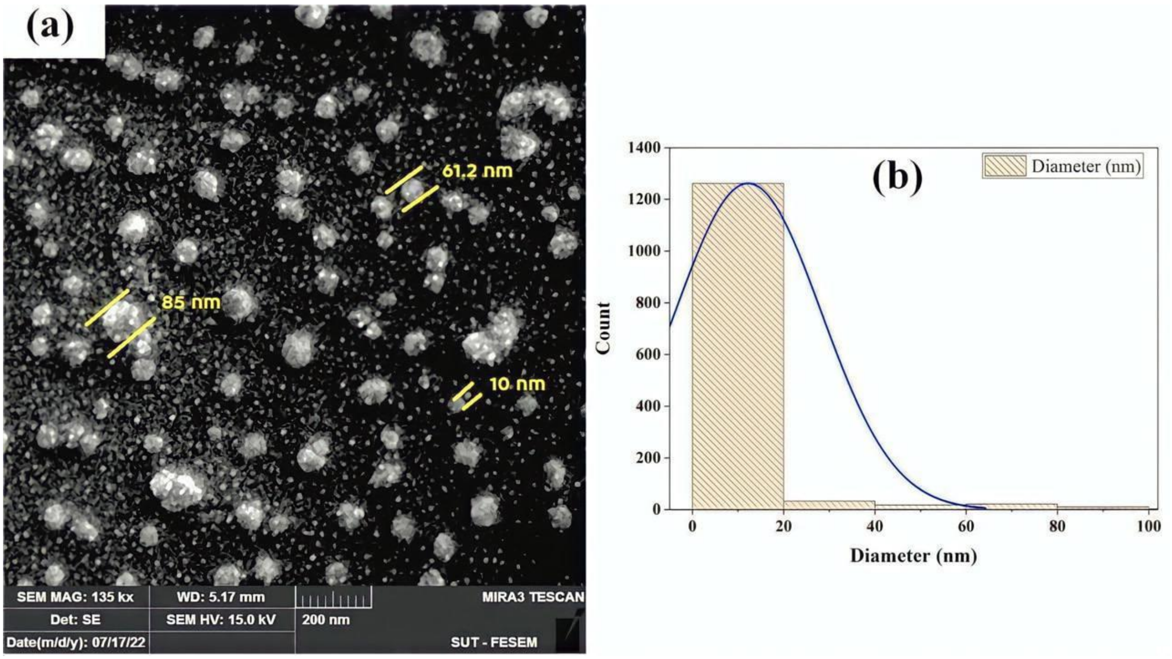

Fig. 4.15: (a) SEM images of Sb_2O_3: 0.02wt% CuO nanofilms at a thickness of 40nm (b) histograms of diameters with Gaussian distribution.

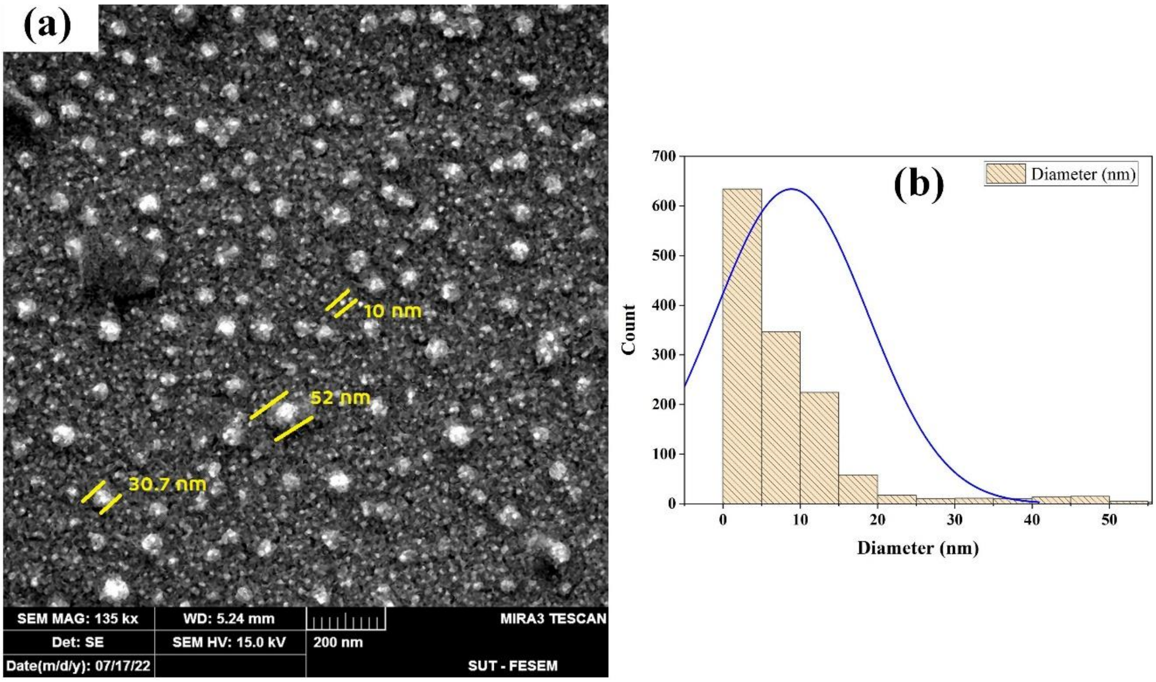

Fig. 4.16: (a) SEM images of Sb_2O_3: 0.04wt% CuO nanofilms at a thickness of 20nm (b) histograms of diameters with Gaussian distribution.

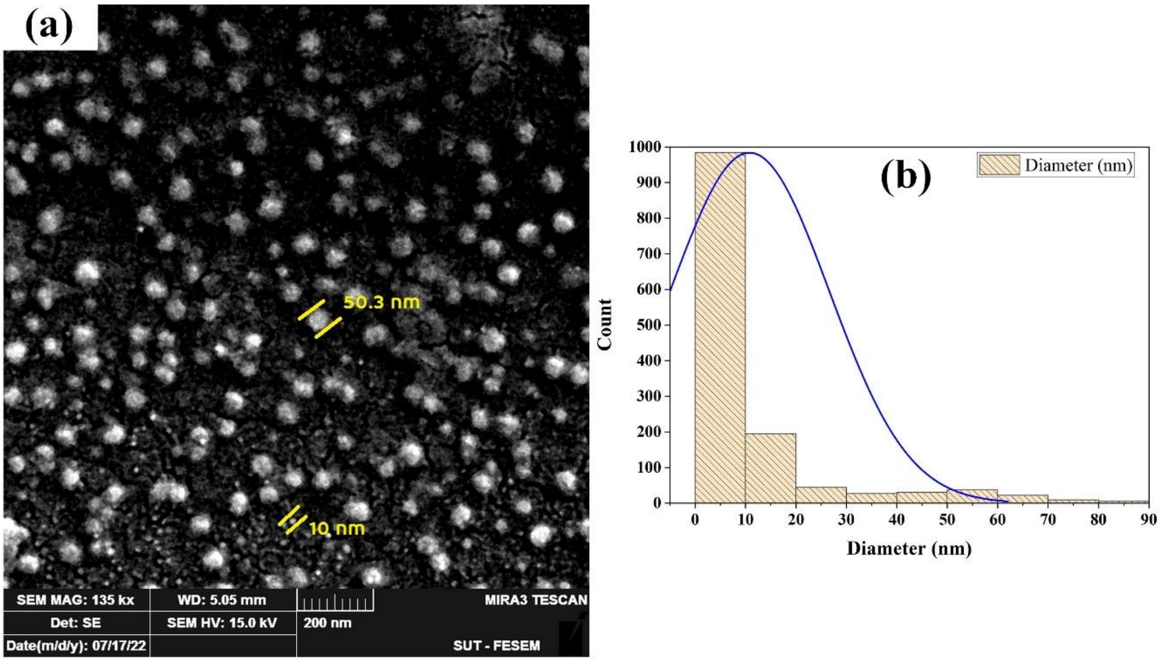

Fig. 4.17: (a) SEM images of Sb_2O_3: 0.04wt% CuO nanofilms at a thickness of 30nm (b) histograms of diameters with Gaussian distribution.

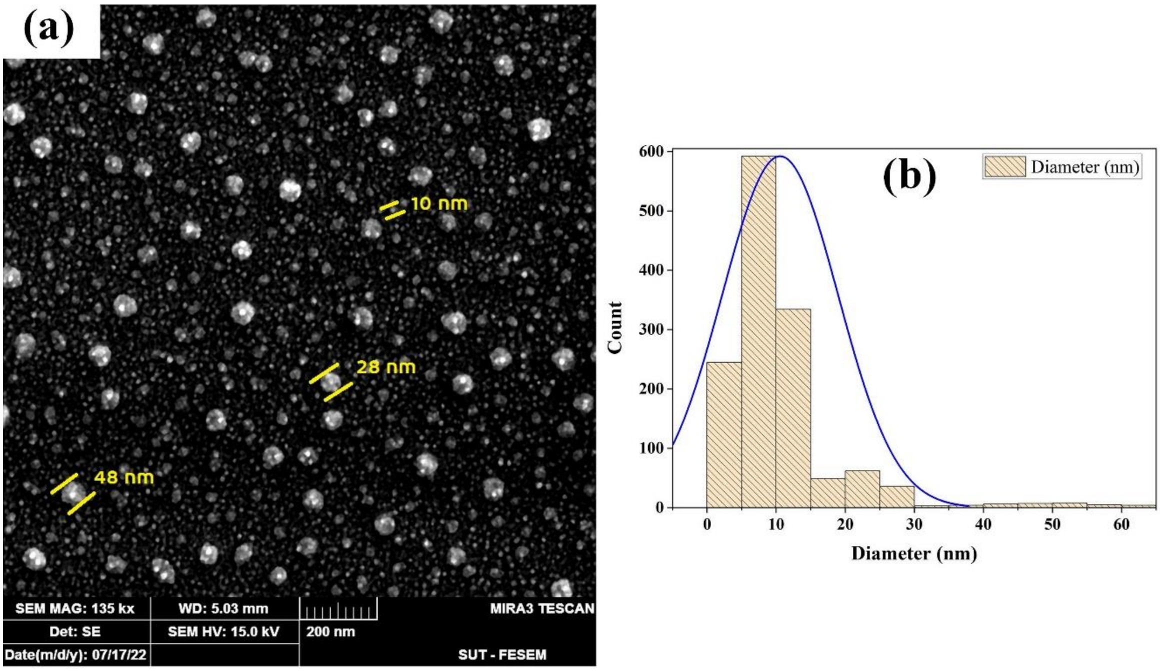

Fig. 4.18: (a) SEM images of Sb_2O_3: 0.04wt% CuO nanofilms at a thickness of 40nm (b) histograms of diameters with Gaussian distribution.

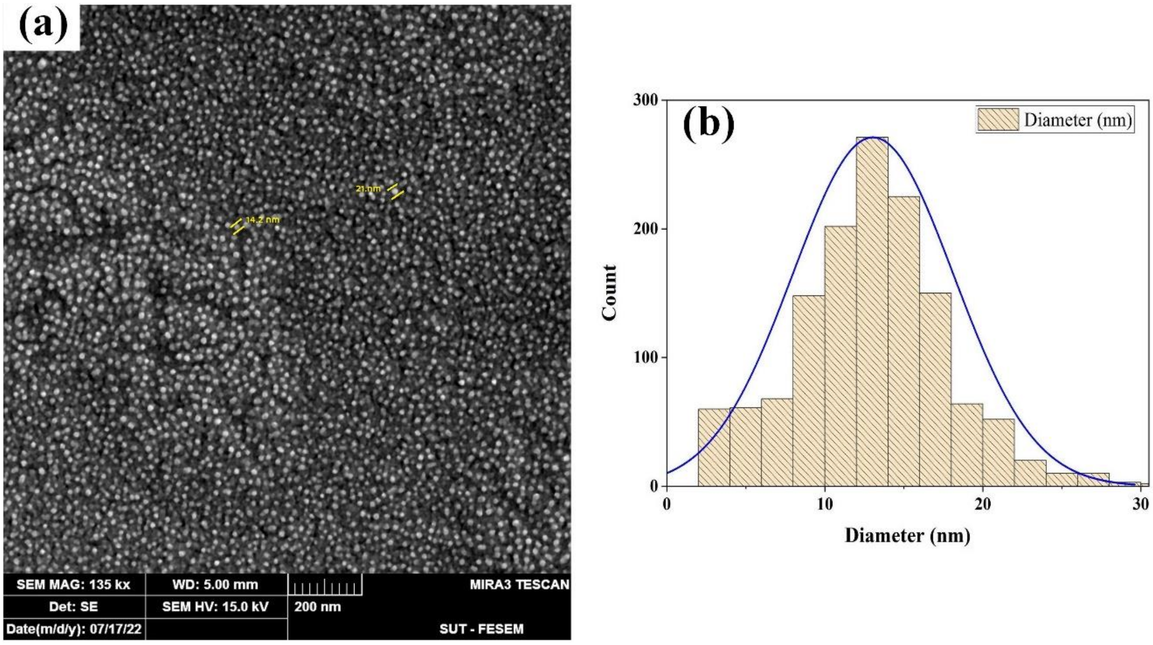

Fig. 4.19: (a) SEM images of Sb_2O_3: 0.06wt% CuO nanofilms at a thickness of 20nm (b) histograms of diameters with Gaussian distribution.

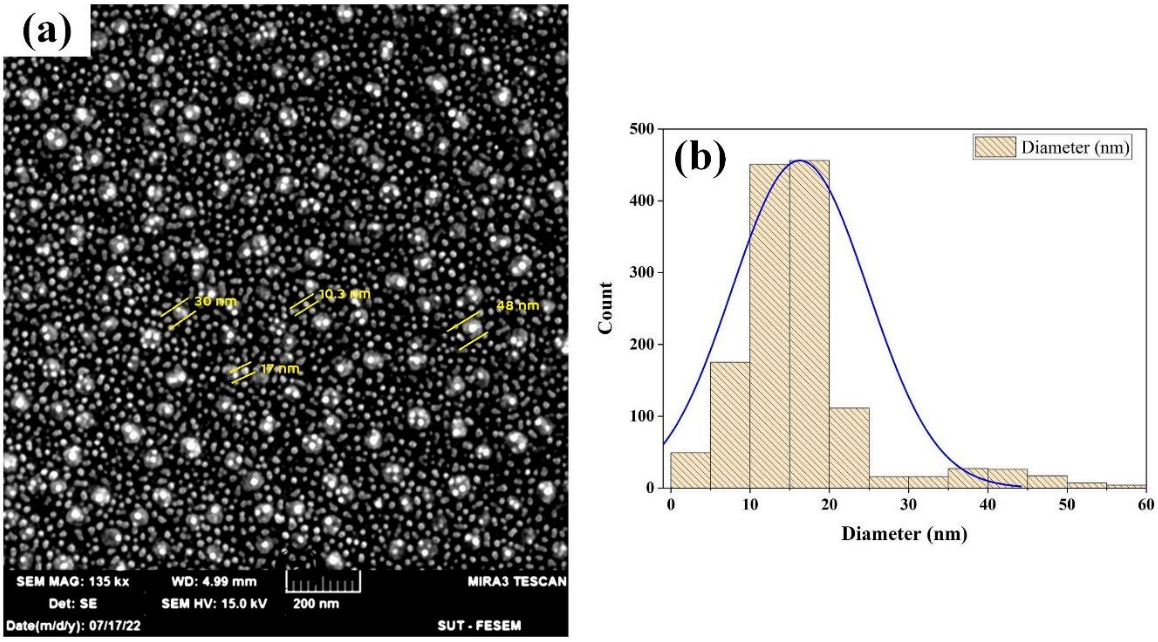

Fig. 4.20: (a) SEM images of Sb_2O_3: 0.06wt% CuO nanofilms at a thickness of 30nm (b) histograms of diameters with Gaussian distribution.

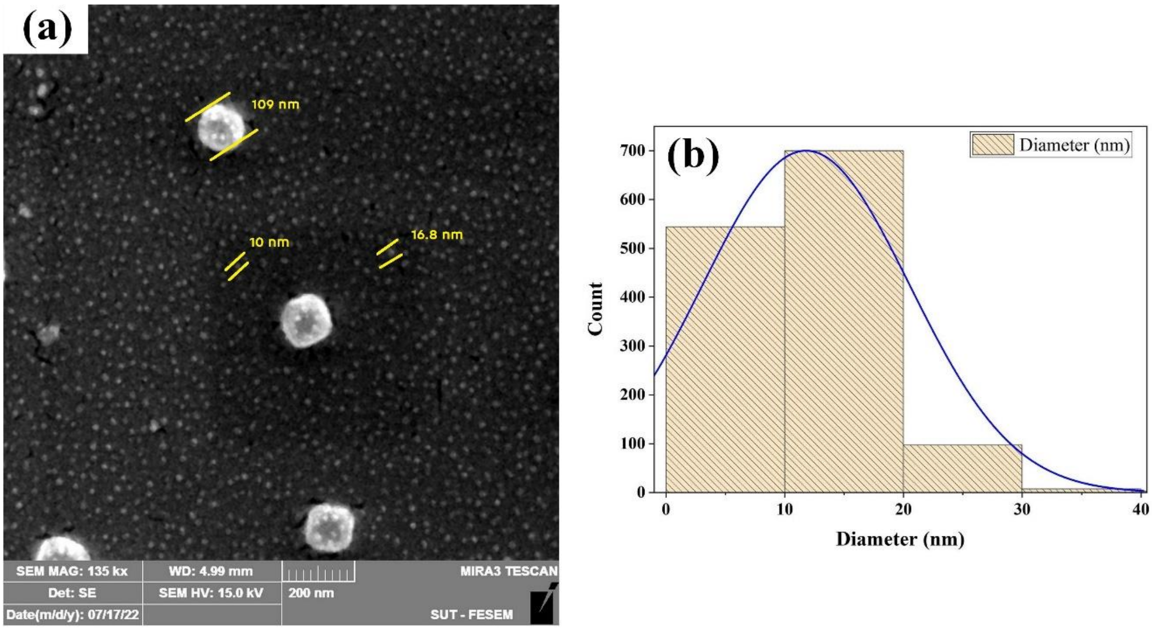

Fig. 4.21: (a) SEM images of Sb_2O_3: 0.06wt% CuO nanofilms at a thickness of 40nm (b) histograms of diameters with Gaussian distribution.

4.3 Optical Properties

The optical properties of the Sb_2O_3 and CuO-doped Sb_2O_3 with different doping of CuO (0.02, 0.04, and 0.06) wt.% nanofilms are prepared by thermal evaporation technique under pressure of (1×10^{-6}) mbar with rate of deposition 0.3 nm. s^{-1}, which is annealed at a temperature of 473 K for 2 hours and different thicknesses (20, 30, and 40) nm, are investigated using a UV-Vis spectrophotometer in the wavelength range (200-1100) nm. It is possible to determine optical properties, such as absorbance, transmittance, absorption coefficient (α), optical energy gap (E_g^{opt}), refractive index (n), extinction coefficient (k_o), real and imaginary dielectric constants (ε_r, ε_i), surface and volume energy loss functions, dispersion parameters, and Urbach energy by analyzing absorbance spectrum.

4.3.1 Absorbance (A)

The absorbance spectra of Sb_2O_3 and CuO-doped Sb_2O_3 versus wavelength with different thicknesses (20, 30, and 40) nm as shown in Figures (4.22 - 4.26). It can be observed that the absorbance spectra of Sb_2O_3 and Sb_2O_3:CuO nanofilms have two peaks appear in an absorption spectrum due to the presence of multiple energy levels or sublevels within a specific electronic transition (orbitals split). When neighbouring atoms or groups interact with the electronic system, the energy levels associated with the electronic transition can split into two or more distinct levels. These split levels correspond to different energy states that the electrons can occupy. As a result, when the molecule is exposed to electromagnetic radiation, such as visible or ultraviolet light, it can absorb photons with energies corresponding to these split energy levels. This leads to two or more distinct absorption peaks in the spectrum, indicating light absorption at different wavelengths [192].

It can be observed that the absorbance spectra of Sb_2O_3 nanofilms increased with the increasing thickness of the films, as shown in Figure (4.22). This behavior can be attributed to the increase in the number of particles in the film, which is in accordance with the findings of researchers [108].

Figures (4.23 - 4.25) show that the absorbance increases with the increase of CuO-doped for the prepared films due to secondary levels formed within the energy gap. From the figures, all samples show absorption in the UV regions of the electromagnetic spectrum. The high absorption in the UV regions is due to the energy of the incoming photons matching the energy difference between the occupied electron orbitals (e.g., valence electrons) and the vacant ones (e.g., higher energy orbitals, such as the antibonding orbitals). UV absorption is often associated with transitions involving molecules' π (pi) electrons, which are responsible for the absorption of UV [193]. Figure (4.26) represents the amount of variation of absorption between the undoped and the highest doping ratio.

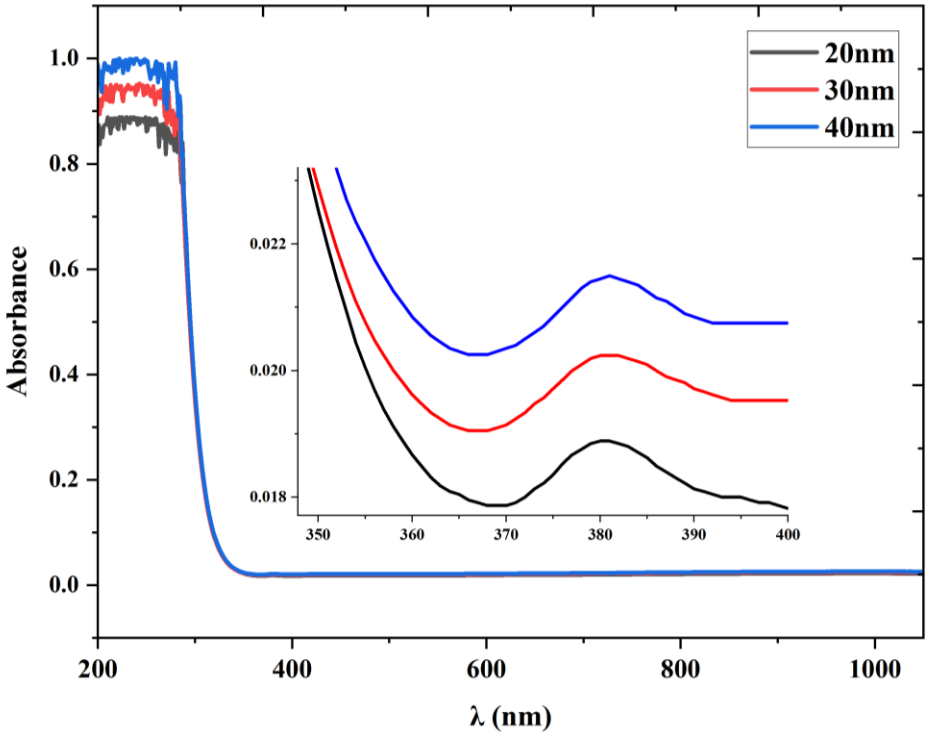

Fig. 4.22: Absorbance spectra for Sb_2O_3 nanofilms of varying thicknesses.

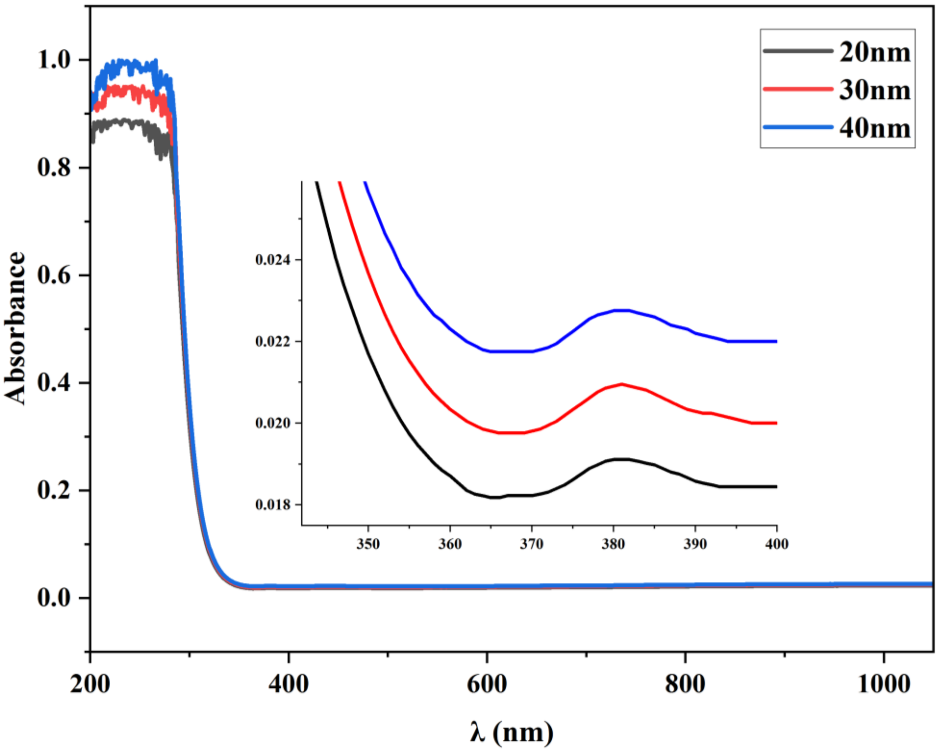

Fig. 4.23: Absorbance spectra for Sb_2O_3: 0.02wt.% CuO nanofilms of varying thicknesses.

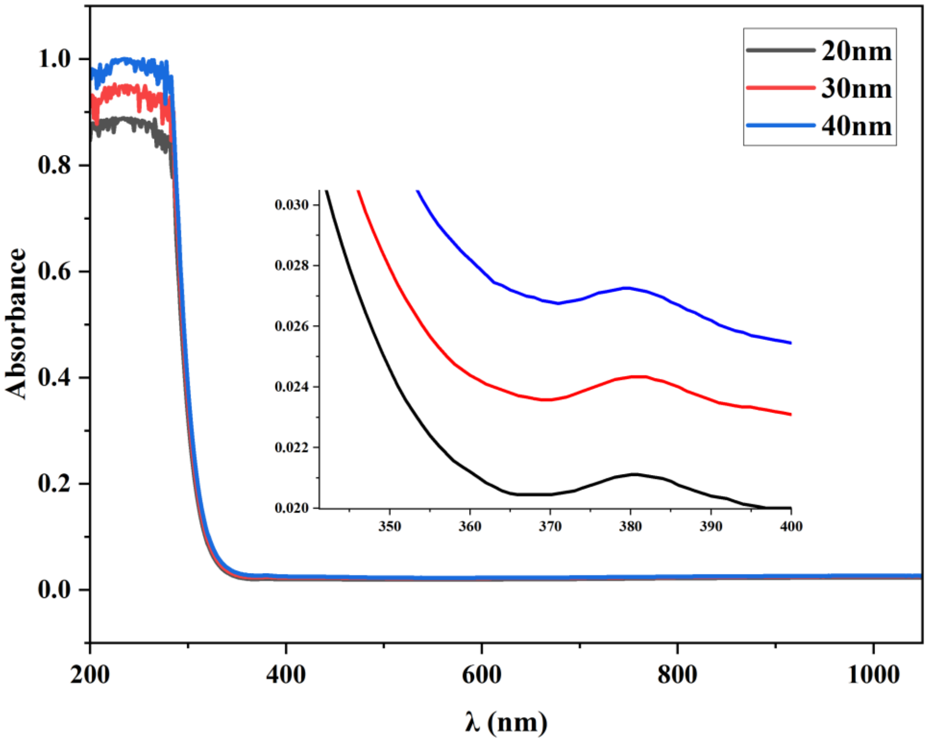

Fig. 4.24: Absorbance spectra for Sb_2O_3: 0.04wt.% CuO nanofilms of varying thicknesses.

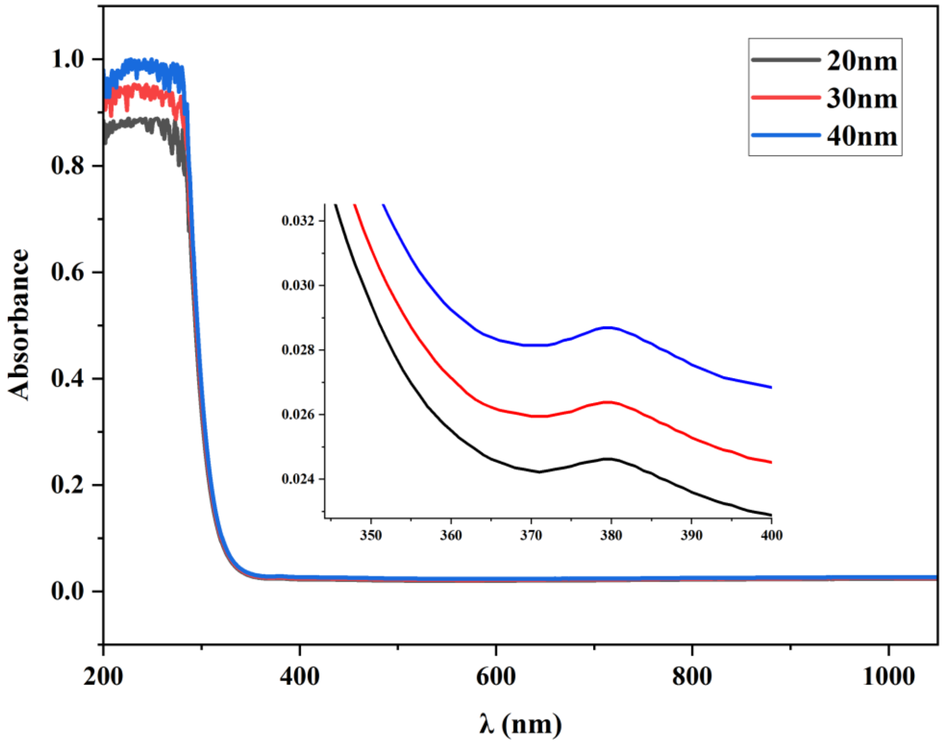

Fig. 4.25: Absorbance spectra for Sb2O3: 0.06wt.% CuO nanofilms of varying thicknesses.

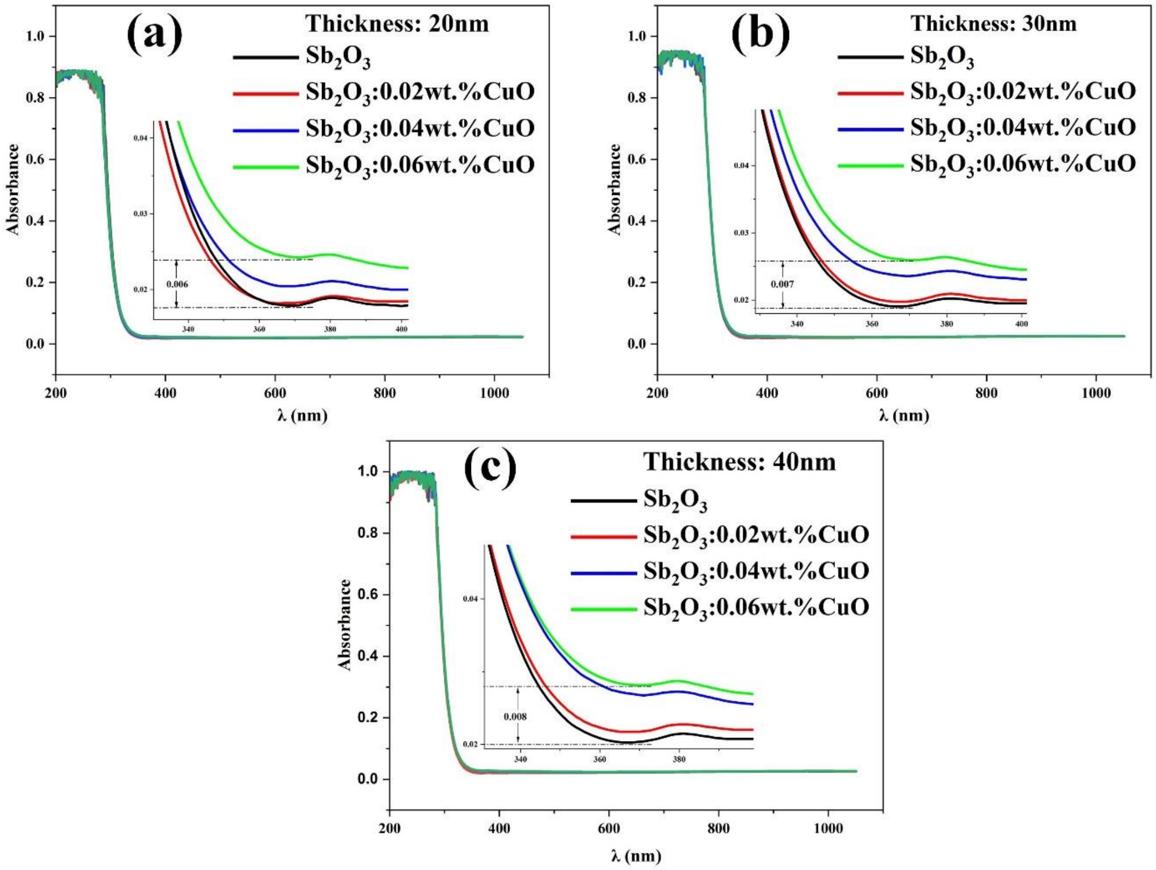

Fig. 4.26: Absorbance spectra for pure and Sb2O3: wt.% CuO nanofilms of varying thicknesses: (a) 20nm, (b) 30nm, and (c) 40nm.

4.3.2 Transmittance (T)

In general, the transmittance of pure and Sb_2O_3:CuO nanofilms decreases with increasing thickness due to the increase in the absorbance of these nanofilms. Figure (4.27) shows the transmittance spectra of Sb_2O_3 nanofilms due to an increase in the number of atoms, which increases the number of incident photons colliding with atoms. Also, due to the development of the absorption edge for nanofilm became less sharp, which is attributable to the fact that larger crystallite volumes are deposited because since more atoms are found in the material, more states would be required for photons to be absorbed, which is in accordance with the findings of researchers [194].

Figures (4.28 - 4.30) show the transmittance spectra slightly decreasing with increasing thickness and ratios doped for CuO-doped Sb_2O_3 nanofilms. This could be attributed to a rise in film homogeneity and surface roughness, which encourages light surface scattering. These results are compatible with the AFM results in **section 4.2.2.** The decline in transmittance behaviour might also be attributed to a rise in doped atoms, increasing collisions between the atoms, and incident photons [108]. Figure (4.31) represents the amount of variation of transmittance between the undoped and the highest doping ratio.

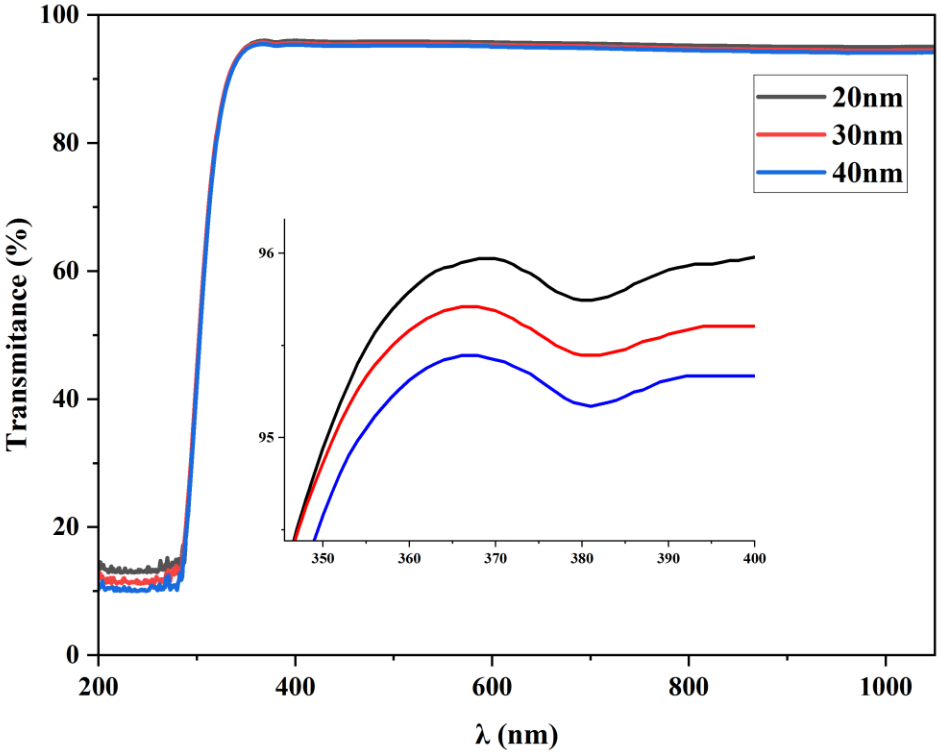

Fig. 4.27: Transmittance spectra for Sb_2O_3 nanofilms of varying thicknesses.

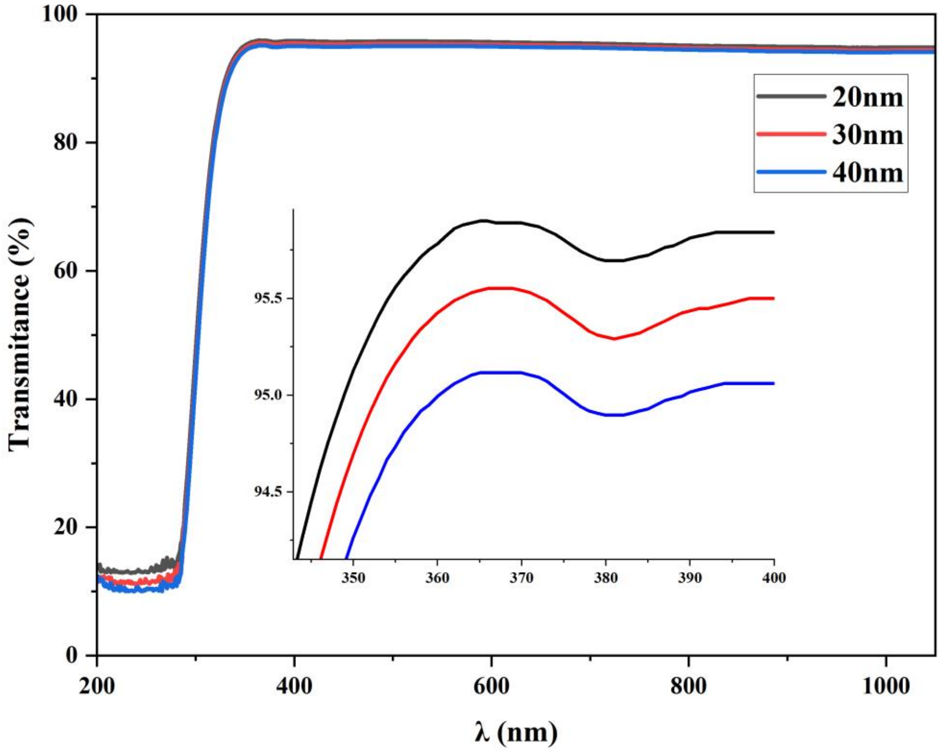

Fig. 4.28: Transmittance spectra for Sb_2O_3: 0.02wt.% CuO nanofilms of varying thicknesses.

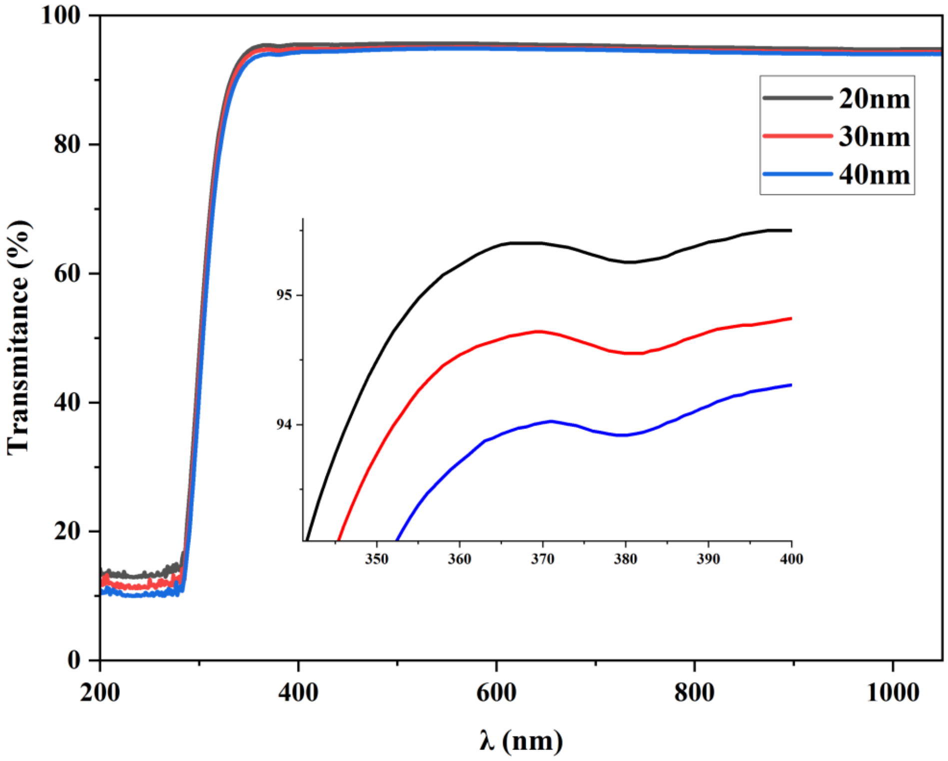

Fig. 4.29: Transmittance spectra for Sb_2O_3: 0.04wt.% CuO nanofilms of varying thicknesses.

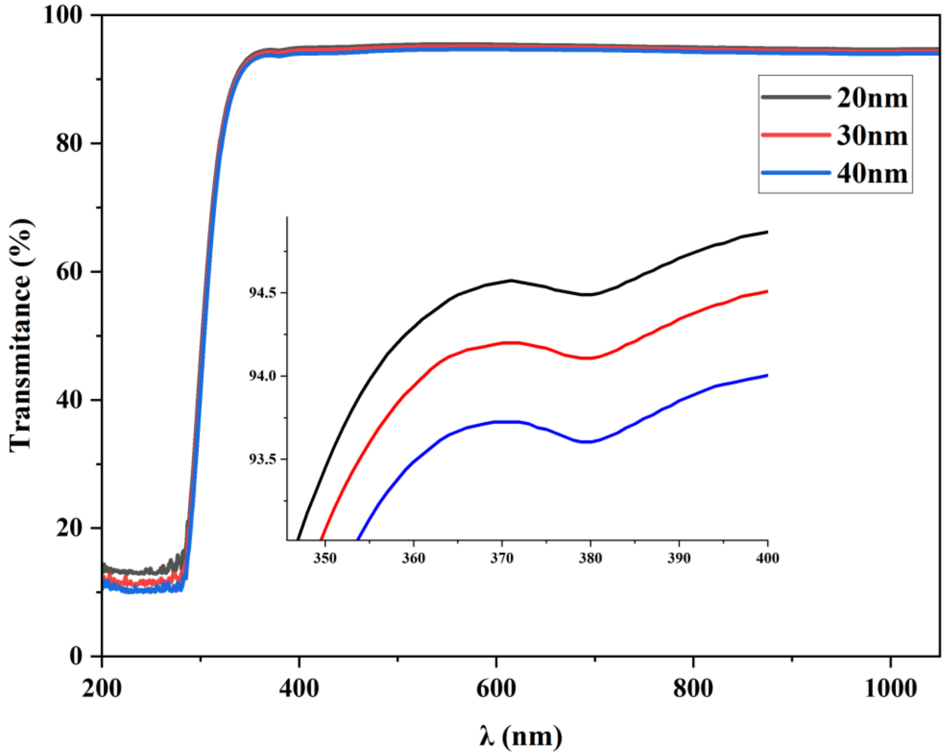

Fig. 4.30: Transmittance spectra for Sb_2O_3: 0.06wt.% CuO nanofilms of varying thicknesses.

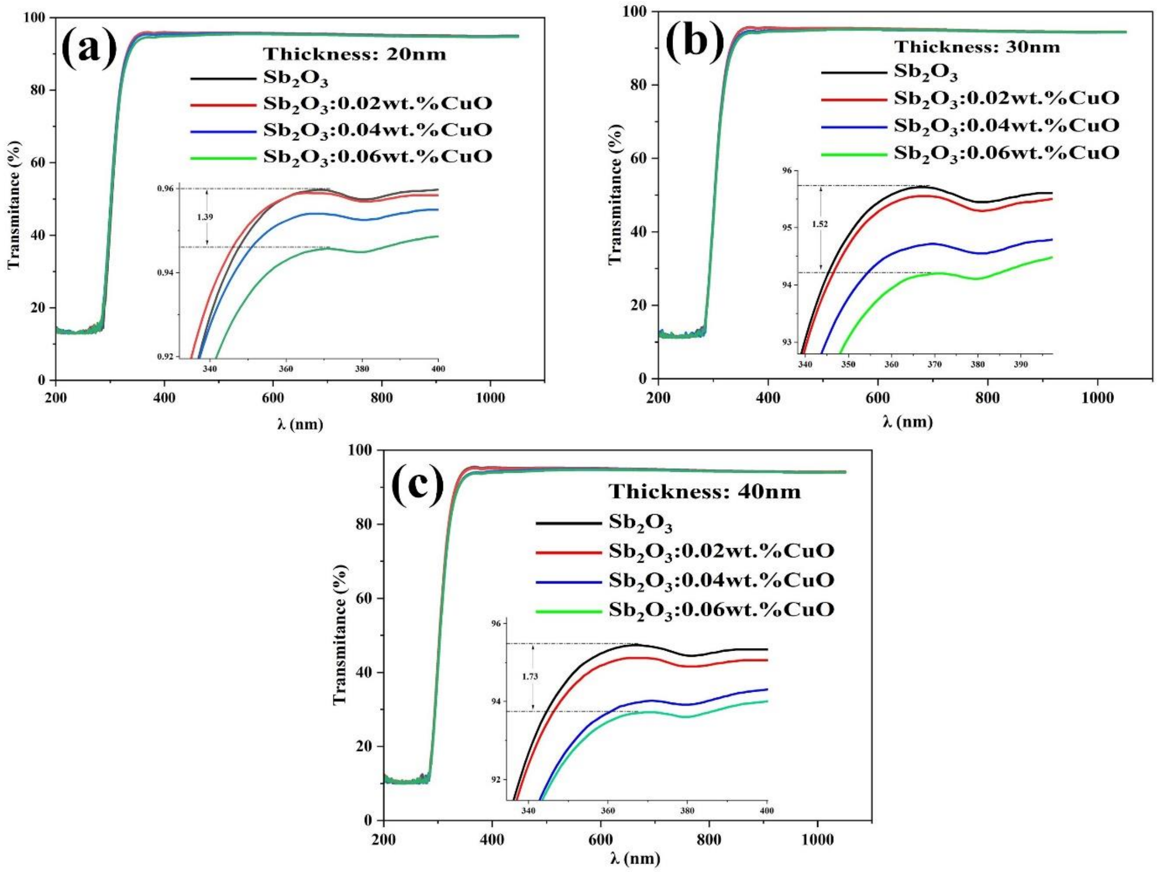

Fig. 4.31: Transmittance spectra for pure and Sb_2O_3: wt.% CuO nanofilms of varying thicknesses: (a) 20nm, (b) 30nm, and (c) 40nm.

4.3.3 The absorption coefficient (α)

The absorption coefficient (α) of Sb_2O_3 and Sb_2O_3:CuO nanofilms are calculated using equation (2.8). The absorption coefficient is determined from the region of high absorption at the fundamental absorption edge of the film. The variation of the absorption coefficient versus wavelength for pure Sb_2O_3 and CuO-doped Sb_2O_3 with different ratios of CuO (0.02, 0.04, and 0.06) wt.% with annealing temperature 473 K at 2 hours, and different thicknesses (20, 30, and 40) nm are presented in Figures (4.32 - 4.35).

The figures show that the absorption coefficient is increased with increasing thicknesses and ratios of CuO doping due to the absorption coefficient being directly proportional to the absorbance according to the relationship (2.8). Its value is larger than (10^4 cm^{-1}), which indicates an increase in the probability of the occurrence of direct transitions. This can be linked with the increase in grain size and it may be attributed to the light scattering effect of its high surface roughness, which agrees with the findings of researchers [60, 195].

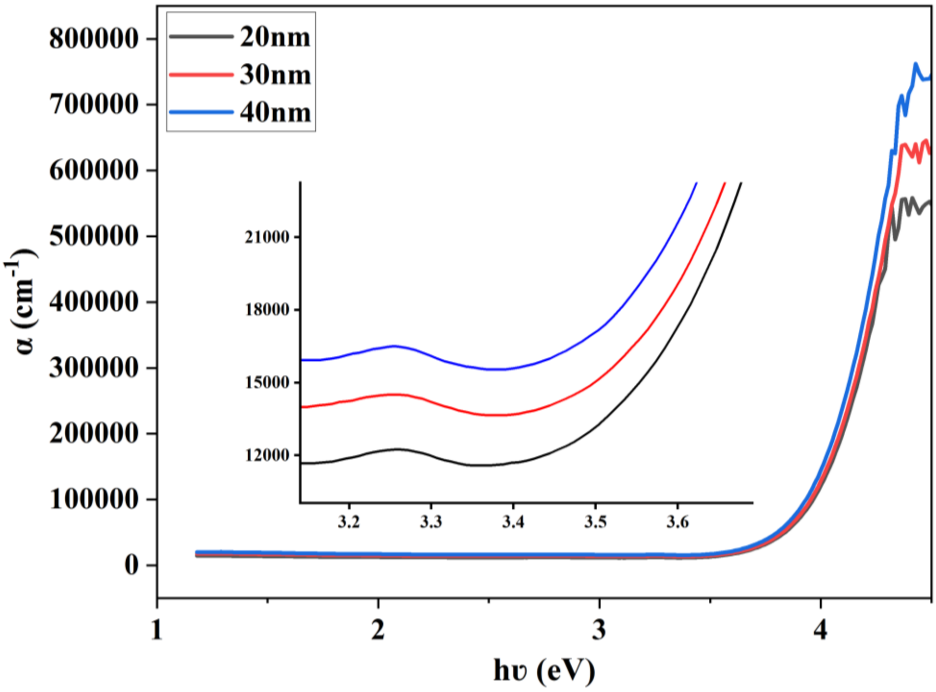

Fig. 4.32: The absorption coefficient spectra as a function of wavelength of Sb_2O_3 nanofilms at different thickness.

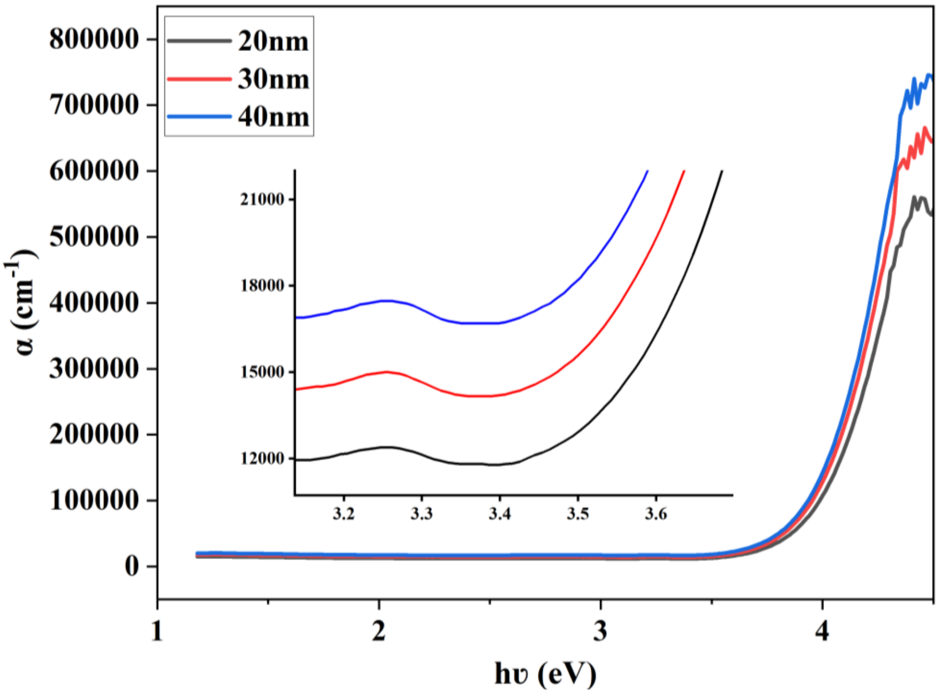

Fig. 4.33: The absorption coefficient spectra as a function of wavelength of Sb_2O_3:0.02wt.% CuO nanofilms at different thickness.

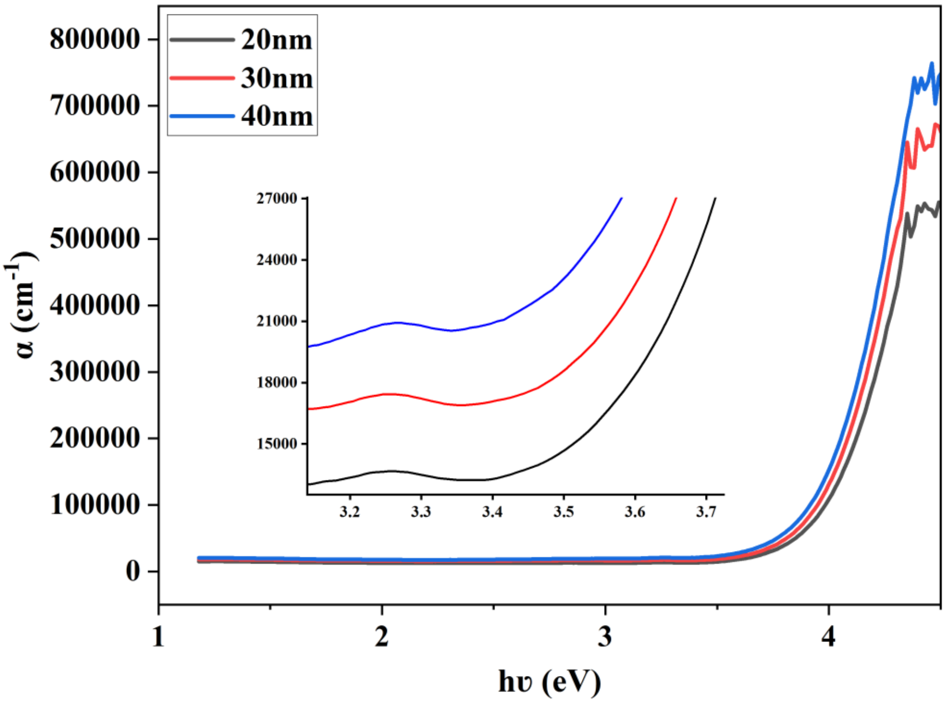

Fig. 4.34: The absorption coefficient spectra as a function of wavelength of Sb_2O_3:0.04wt.% CuO nanofilms at different thickness.

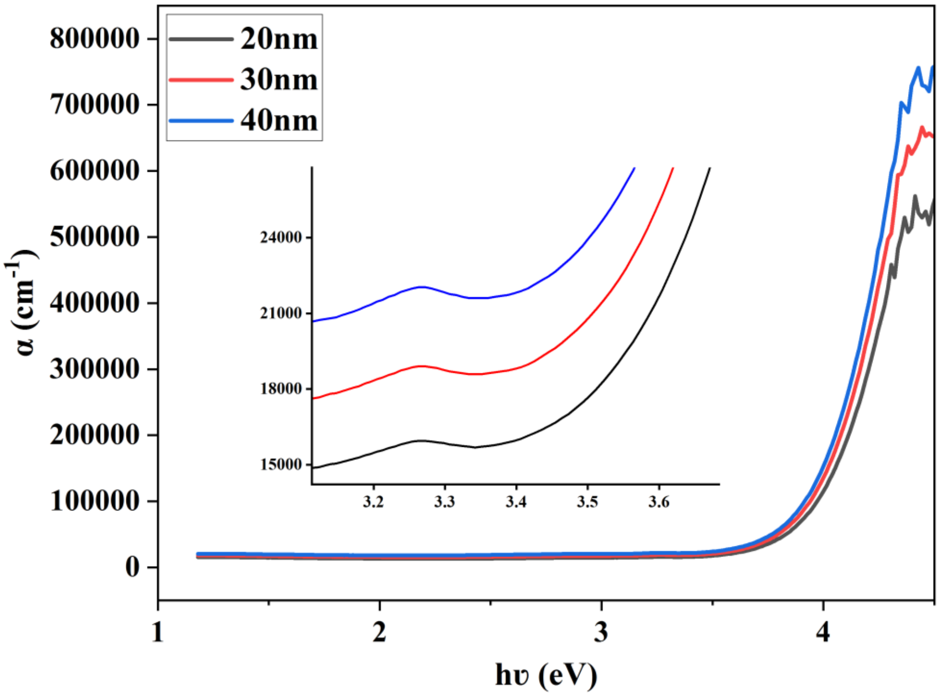

Fig. 4.35: The absorption coefficient spectra as a function of wavelength of Sb_2O_3:0.06wt.% CuO nanofilms at different thickness.

4.3.4 Optical energy gap (E_g^{opt})

The optical energy gap of Sb_2O_3 and Sb_2O_3:CuO nanofilms is calculated using equation (2.11). The plot of $(\alpha h\nu)^2$ with energy $(h\nu)$ indicates that nanofilms are direct transition. The material's band gap is determined by extrapolating the linear region of the graph to the hν axis. The curve can be fitted with a straight line very well for a higher energy range.

As clearly in the figures, these nanofilms have a double band gap near UV and visible, which agrees with the researchers' findings [196]. Figure (4.36) shows that the direct energy gap of Sb_2O_3 films decreased from (E_{g1}=2.77, E_{g2}=3.22) eV to (E_{g1}=2.59, E_{g2}=3.10) eV as the thickness increased. This is due to the increased localized density of states near the band edges, decreasing the value of E_g^{opt}. Also, the decrease in the direct band gap can be attributed to an increase in particle size. These results are in good agreement with the findings of the researchers [108, 197].

Figures (4.37 - 4.39) show the energy gap of CuO-doped Sb_2O_3 with different ratios (0.02, 0.04, and 0.06) wt.% with thicknesses (20, 30, and 40) nm. An obvious decrease is observed in the energy gap values with the increased CuO ratio. This decrease in the energy gap can be due to the prohibited impurities that led to the formation of donor levels within the energy gap near the conduction band. Thus, it will absorb photons of low energy. These results show a good agreement with the researchers' findings [108].

The value of the optical energy gap at annealing is decreased because the annealing has led to a decrease in the value of the optical energy gap, and the explanation for this decrease is that the heat has resulted in additional energy levels within the prohibited gap and near the conduction band to reduce the energy required for direct electronic transitions, which makes the transition of electrons from the valence to the conduction band. These results show a good agreement with the findings of researchers [63, 198]. The values of E_g^{opt} are listed in Table (4.4).

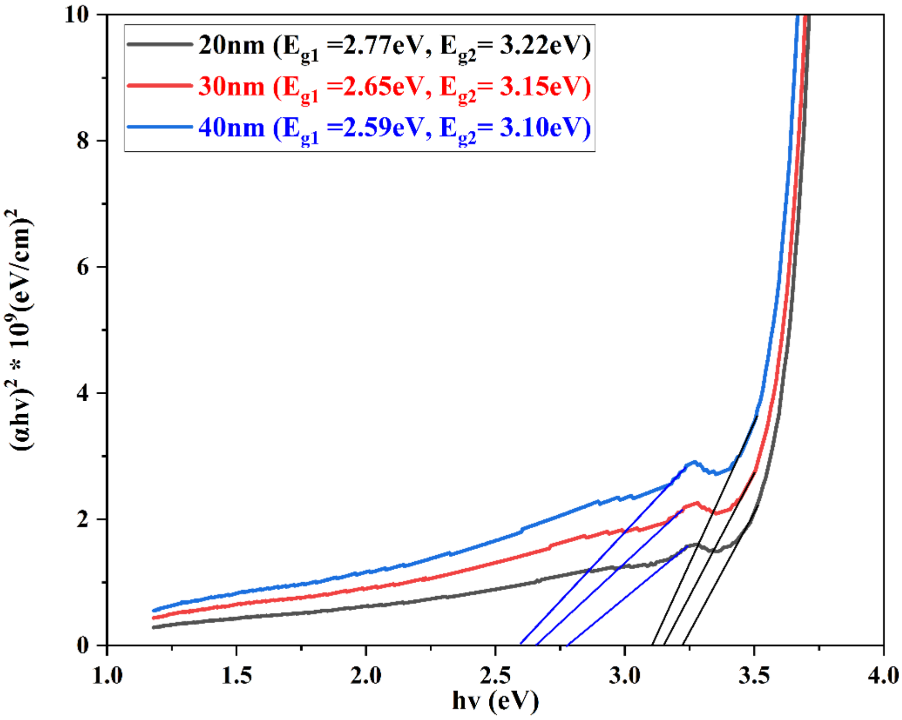

Fig. 4.36: A plots of $(\alpha h\nu)^2$ verses photon energy ($h\nu$) of Sb_2O_3 nanofilms at different thickness.

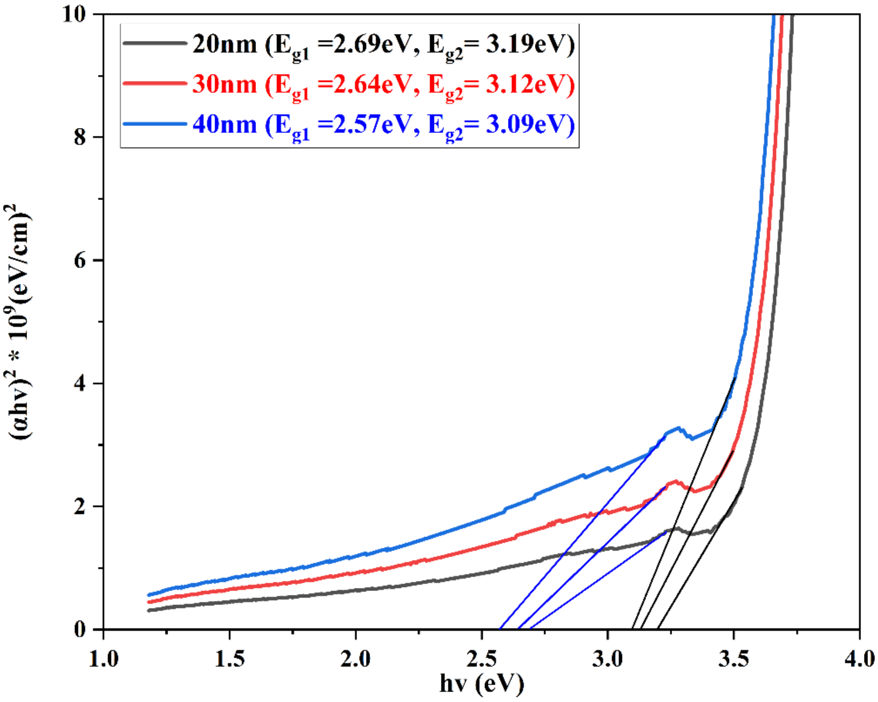

Fig. 4.37: A plots of $(\alpha h\nu)^2$ verses photon energy (hν) of Sb_2O_3:0.02wt.% CuO nanofilms at different thickness.

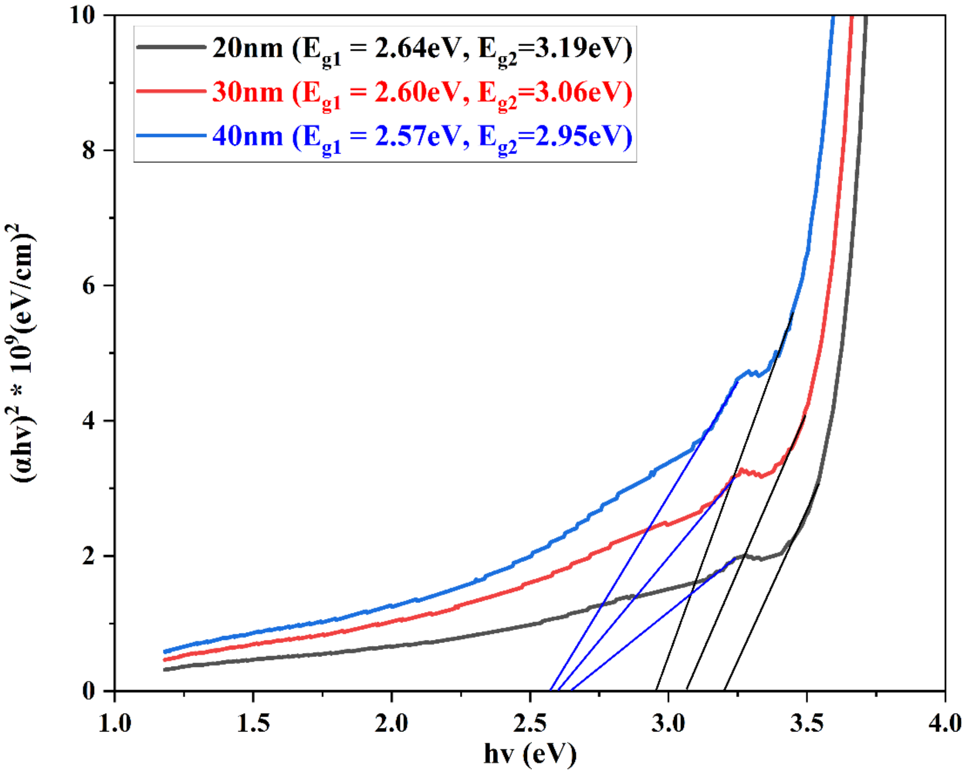

Fig. 4.38: A plots of $(\alpha h\nu)^2$ verses photon energy ($h\nu$) of Sb_2O_3:0.04wt.% CuO nanofilms at different thickness.

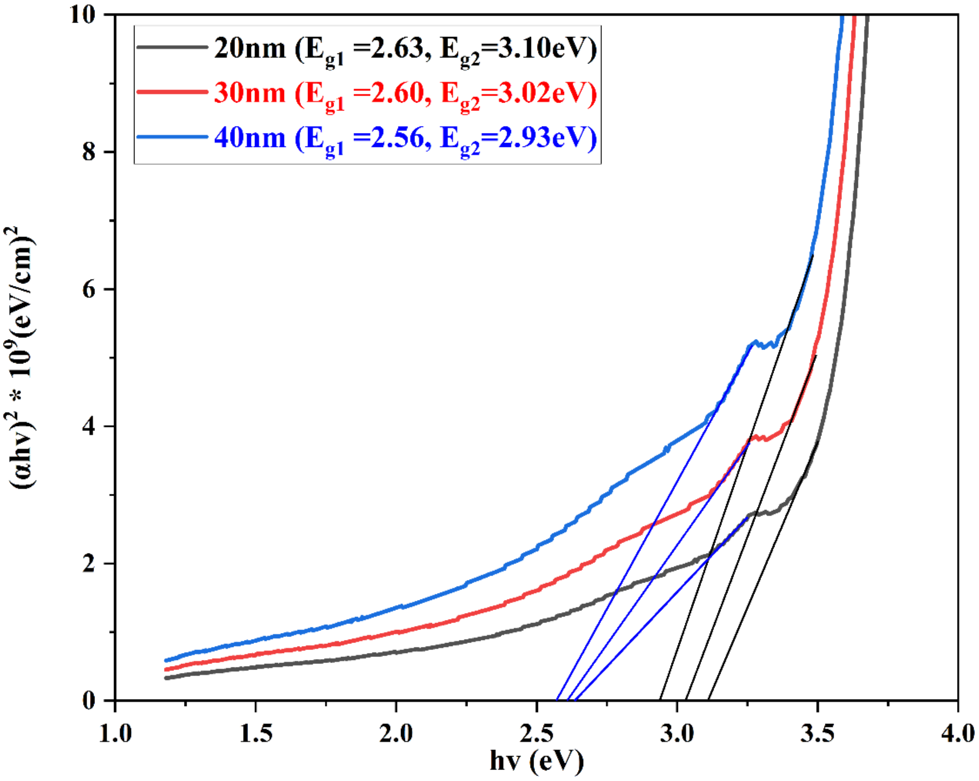

Fig. 4.39: A plots of $(\alpha h\nu)^2$ verses photon energy ($h\nu$) of Sb_2O_3:0.06wt.% CuO nanofilms at different thickness.

Table 4.4: Results of E_g^{opt} of Sb_2O_3 and Sb_2O_3: CuO at various thicknesses.

		CuO-doped Sb_2O_3 (wt.%)			
	Thickness (nm)	0.00	0.02	0.04	0.06
E_{g1}^{opt}(eV)	20	2.77	2.68	2.64	2.63
	30	2.65	2.64	2.60	2.60
	40	2.59	2.57	2.57	2.56
E_{g2}^{opt}(eV)	20	3.22	3.19	3.19	3.10
	30	3.15	3.12	3.06	3.02
	40	3.10	3.09	2.95	2.93

4.3.5 Refractive index (*n*)

The refractive index (*n*) for Sb_2O_3 and Sb_2O_3:CuO nanofilms is determined using equation (2.19). The variation of the refractive index versus wavelength for pure and CuO-doped Sb_2O_3 nanofilms with different doping ratio of CuO prepared at RT and different thicknesses (20, 30, and 40) nm have been investigated and analysed, as shown in Figures (4.40 - 4.43).

The figures show that the refractive index of pure and CuO-doping Sb_2O_3 nanofilms increases with increasing thickness and doping of CuO. The behavior explanation is the increase of the absorbance or the absorption coefficient. An increase in doping increases the refractive index. In other words, when the incident light interacts with a material with a high amount of particles, then the refractivity of the films increases. This agrees with the researchers' findings [60, 108].

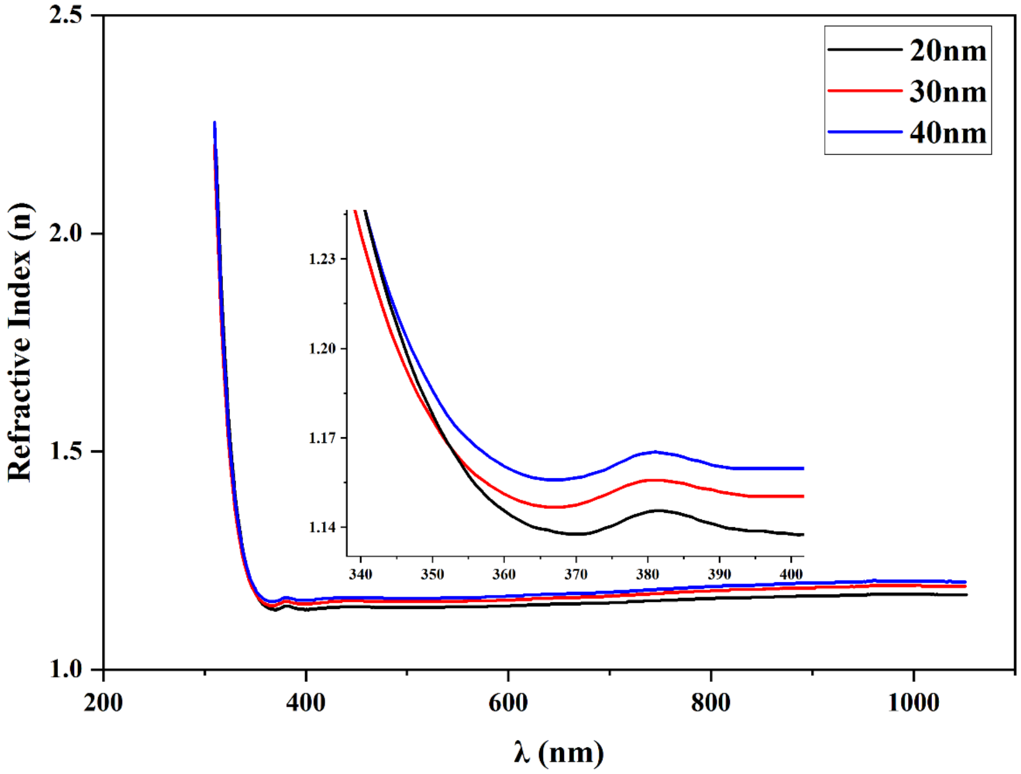

Fig. 4.40: Variation of refractive index with wavelength of Sb_2O_3 nanofilms at different thicknesses.

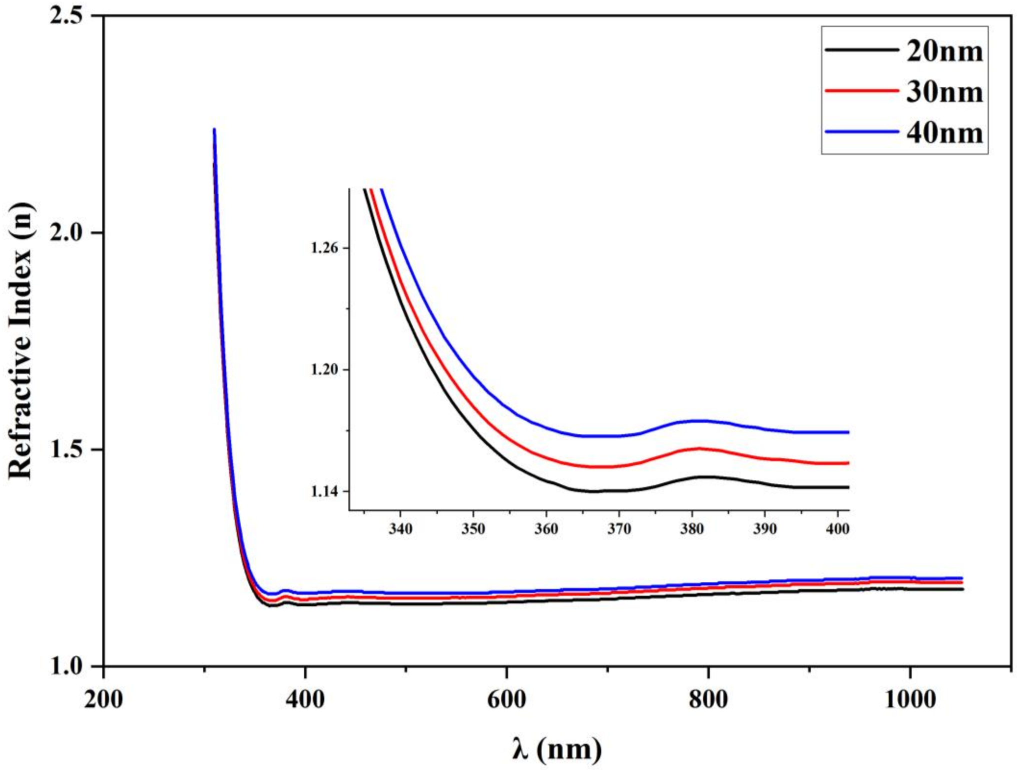

Fig. 4.41: Variation of refractive index with wavelength of Sb_2O_3:0.02wt.% CuO nanofilms at different thicknesses.

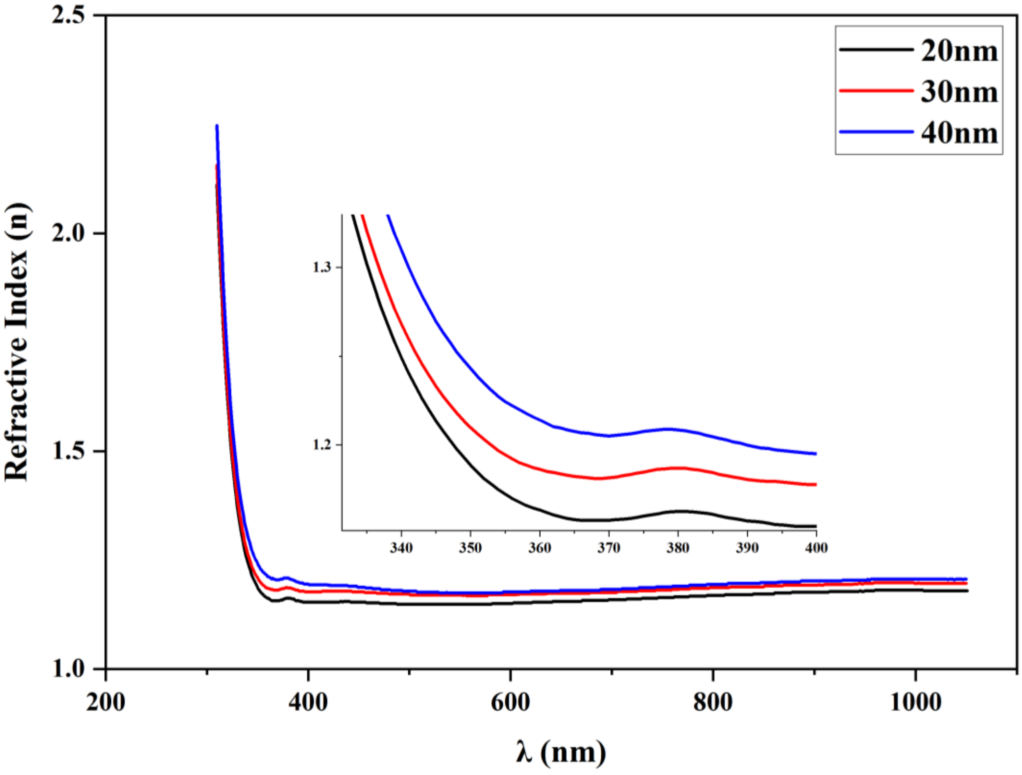

Fig. 4.42: Variation of refractive index with wavelength of Sb_2O_3:0.04wt.% CuO nanofilms at different thicknesses.

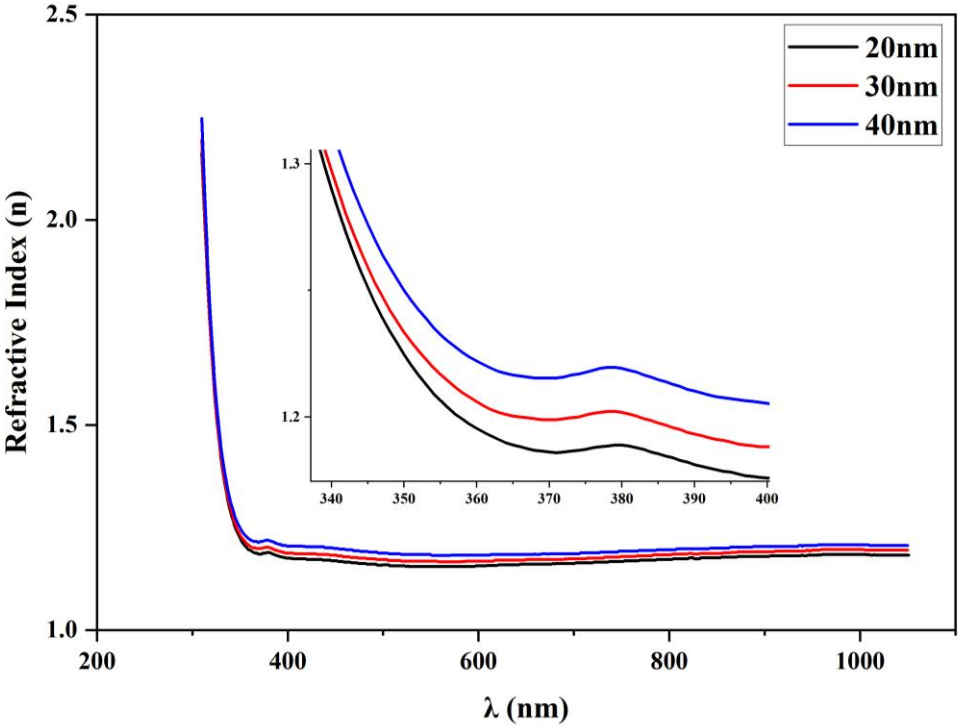

Fig. 4.43: Variation of refractive index with wavelength of Sb_2O_3:0.06wt.% CuO nanofilms at different thicknesses.

4.3.6 Extinction coefficient (k_o)

The extinction coefficient (k_o) of pure and CuO-doped Sb_2O_3 nanofilms is determined using equation (2.20). The variation of the extinction coefficient versus the wavelength for pure and Sb_2O_3:CuO with different doping ratio of CuO (0.02, 0.04, and 0.06) wt.% with annealing temperature 473 K for 2 hours and different thickness (20, 30, and 40) nm are presented in Figures (4.44 - 4.47).

The figures show that the extinction coefficient increases with the increase of thickness and the increase of CuO doping for all prepared nanofilms. The behaviour can be ascribed to the increase in the absorption coefficient, leading to a rise in the k_o value caused by the direct relationship between α value and k_o value. Increasing k_o values can also be ascribed to the increase in concentration of CuO nanoparticles, which leads to eliminating the density of localized states by adding CuO content, which is in accordance with the researchers [60, 108, 199].

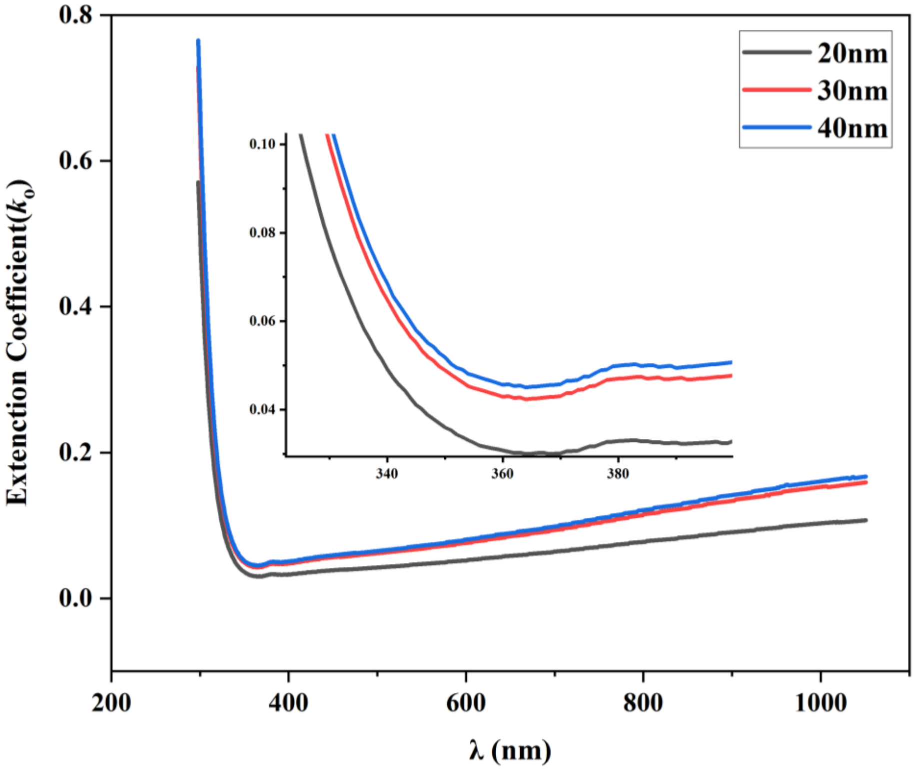

Fig. 4.44: Variation of extinction coefficient with wavelength of Sb_2O_3 nanofilms at different thicknesses.

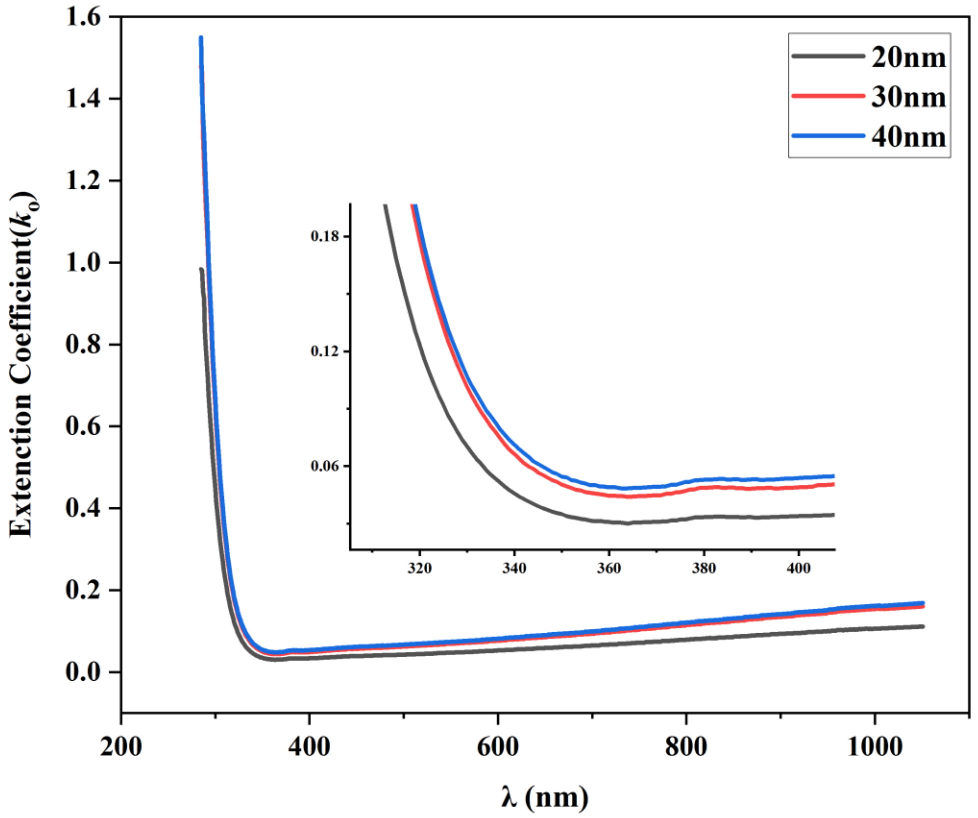

Fig. 4.45: Variation of extinction coefficient with wavelength of Sb_2O_3:0.02wt.% CuO nanofilms at different thicknesses.

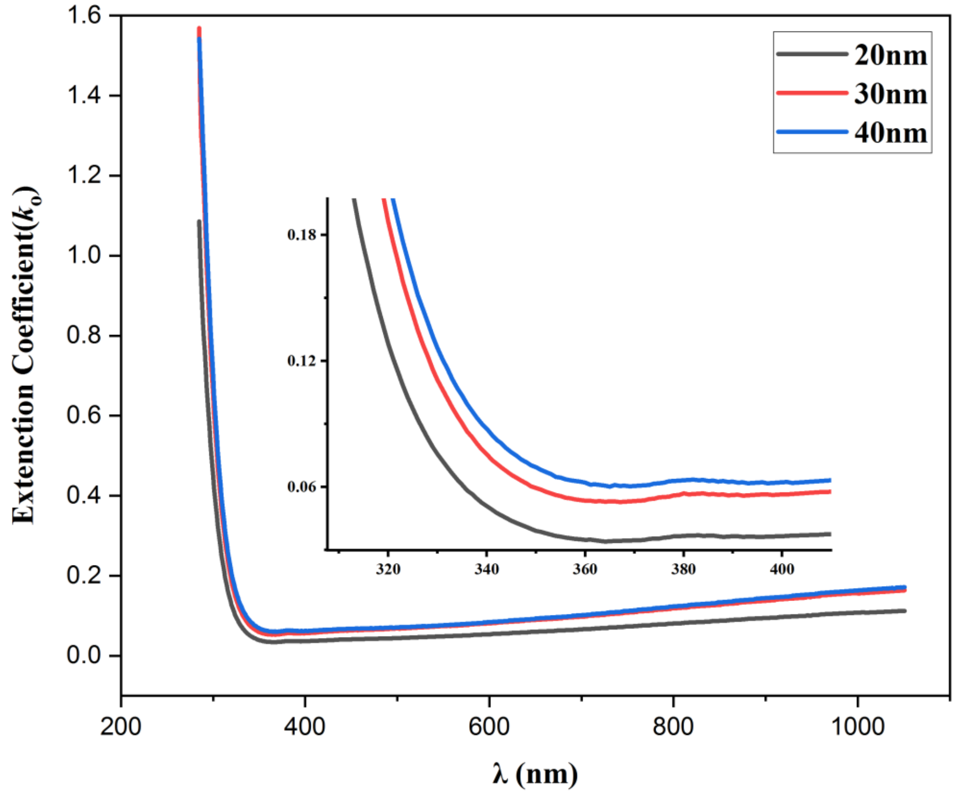

Fig. 4.46: Variation of extinction coefficient with wavelength of Sb_2O_3:0.04wt.% CuO nanofilms at different thicknesses.

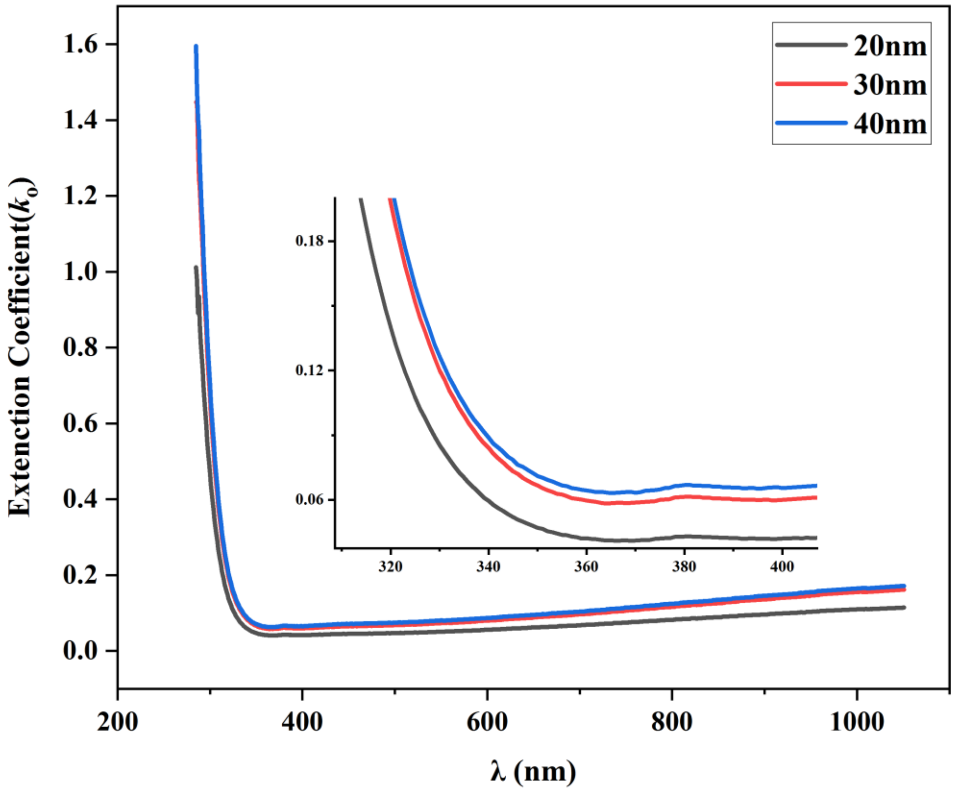

Fig. 4.47: Variation of extinction coefficient with wavelength of Sb_2O_3:0.06wt.% CuO nanofilms at different thicknesses.

4.3.7 The dielectric constants (ε_r, ε_i)

The dielectric constants give information about the materials' electronic band structure. The real part of the dielectric constant (ε_r) determines the refractive index of a material, which governs the behavior of light as it passes through the material. The imaginary part (ε_i) is associated with the absorption and scattering of light by the material. Equations (2.23) and (2.24) were used to calculate (ε_r) and (ε_i) parts of the dielectric constant.

Figures (4.48-4.55) demonstrate how the dielectric constant's (real and imaginary parts) changes as a wavelength function for the pure and Sb_2O_3:CuO nanofilms.

The real and imaginary parts of the dielectric constant increase with the increasing doped ratio and thickness of nanofilms. A higher value of ε_r

indicates a higher ability to store electric charge and redistribute electrical energy in response to an electric field, while a higher value of ε_i indicates a higher energy loss.

Furthermore, the real part of dielectric constant values is greater than the imaginary part. This behavior is in agreement with the researchers [108].

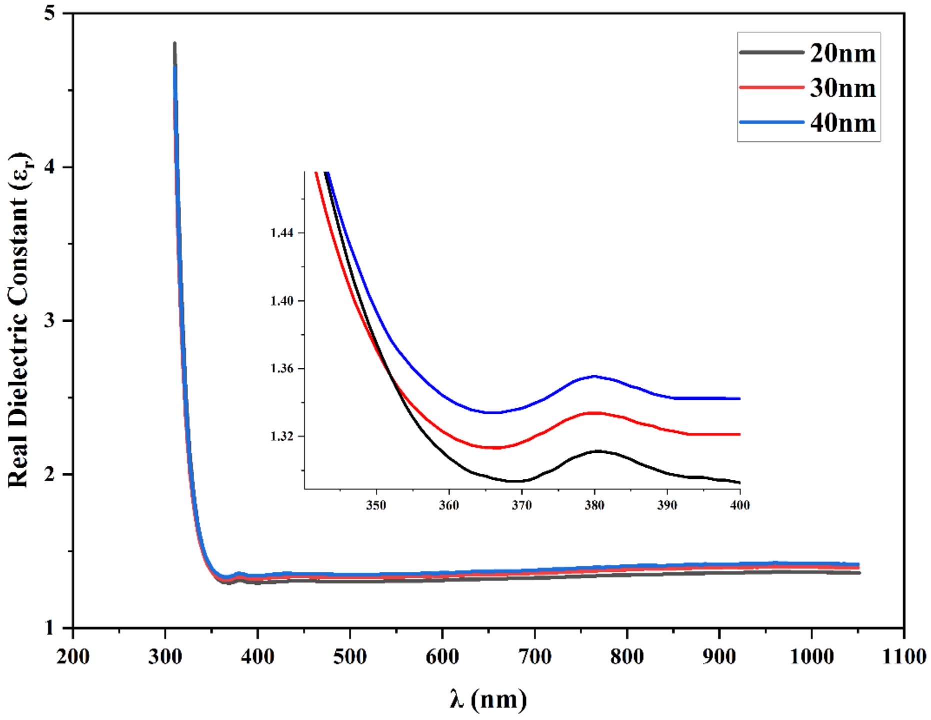

Fig. 4.48: Variation of $\mathcal{E}_r$ with wavelength of Sb_2O_3 nanofilms at different thicknesses.

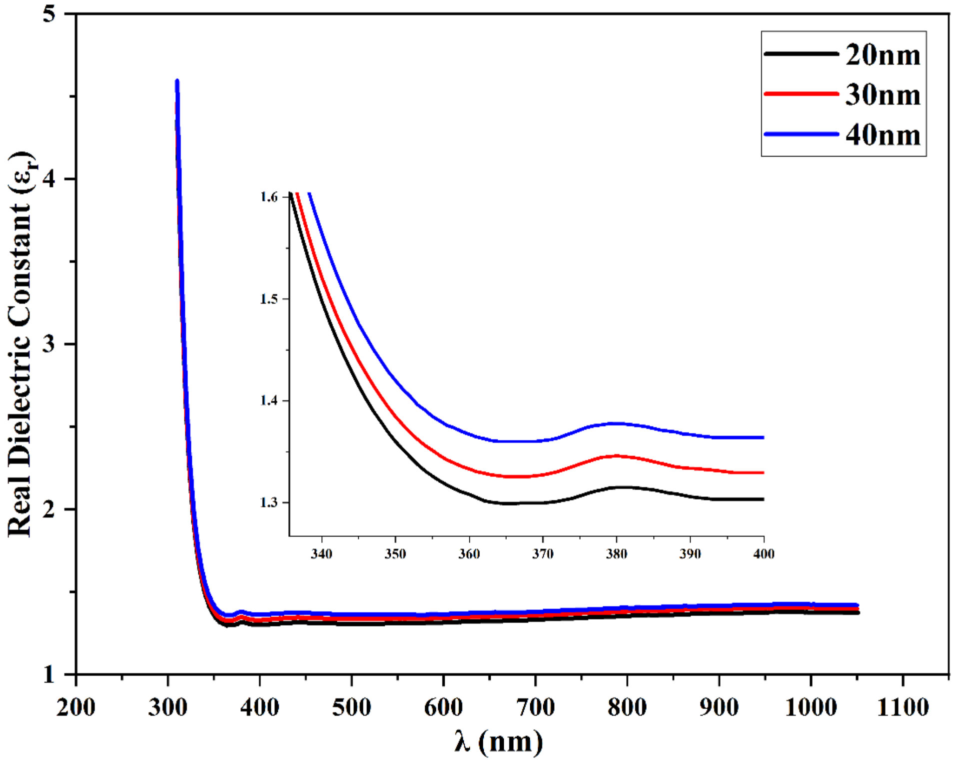

Fig. 4.49: Variation of ε_r with wavelength of Sb_2O_3:0.02wt.% CuO nanofilms at different thicknesses.

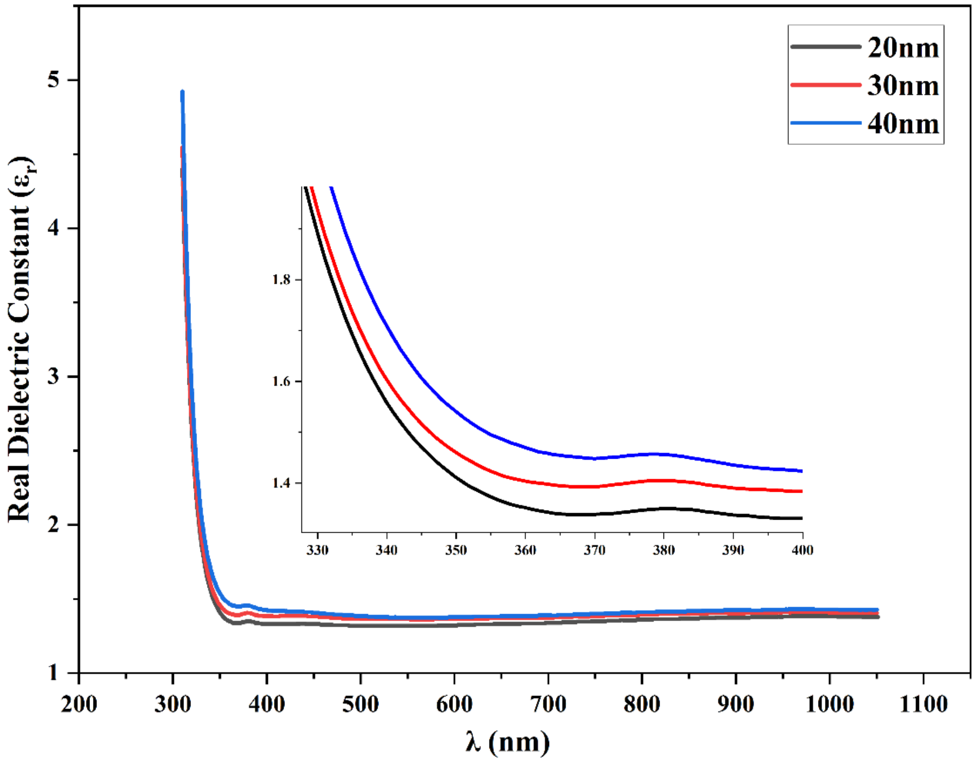

Fig. 4.50: Variation of ε_r with wavelength of Sb_2O_3:0.04wt.% CuO nanofilms at different thicknesses.

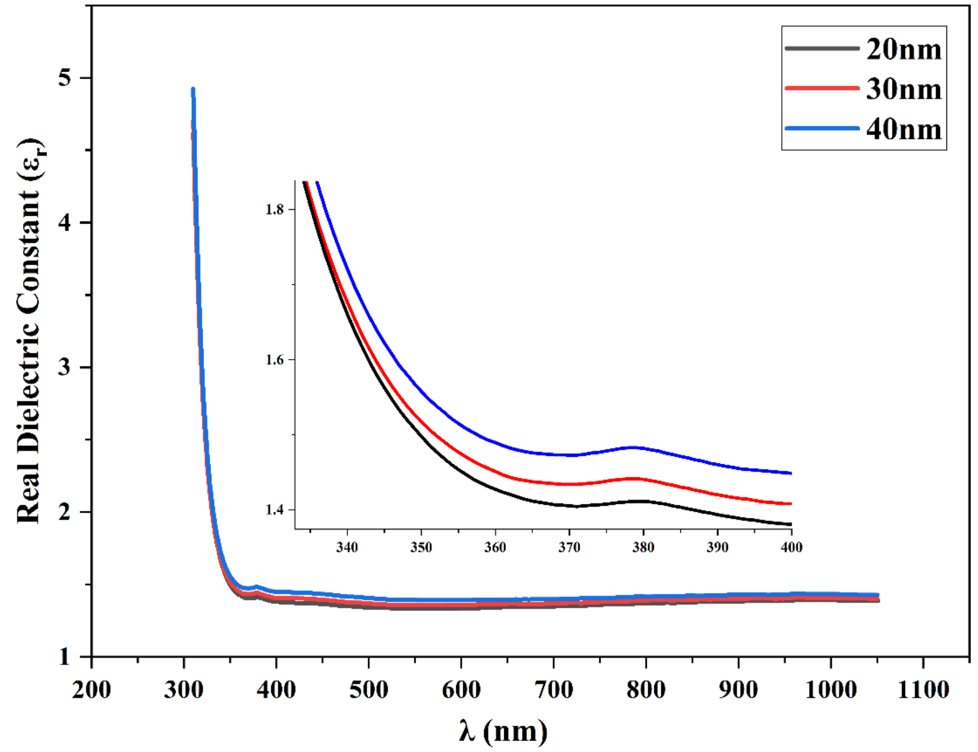

Fig. 4.51: Variation of Ɛr with wavelength of Sb_2O_3:0.06wt.% CuO nanofilms at different thicknesses.

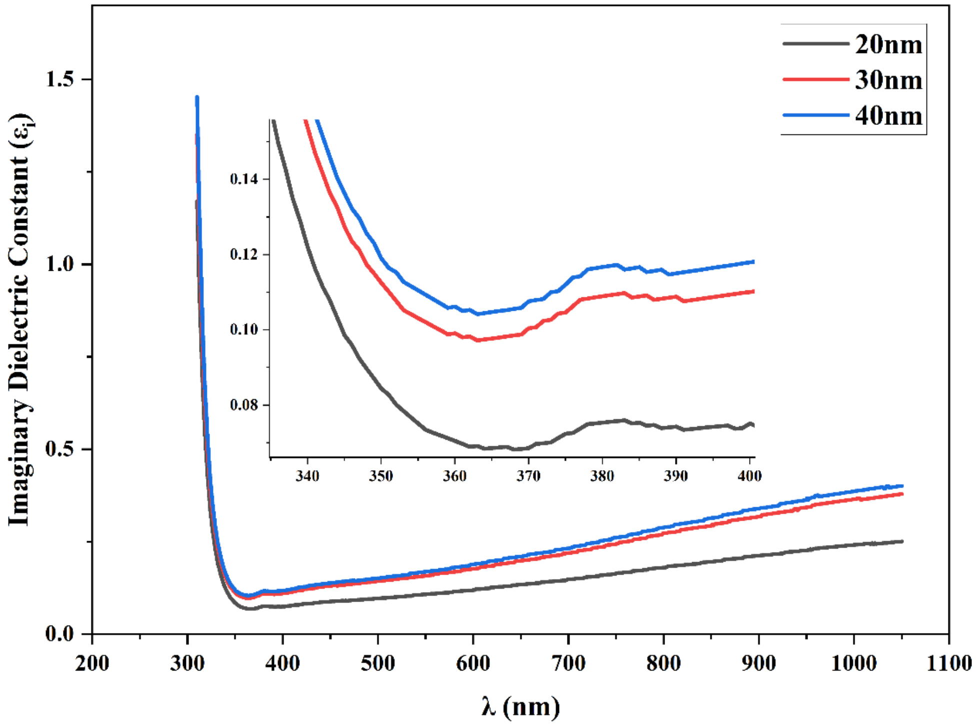

Fig. 4.52: Variation of Ɛi with wavelength of Sb_2O_3 nanofilms at different thicknesses.

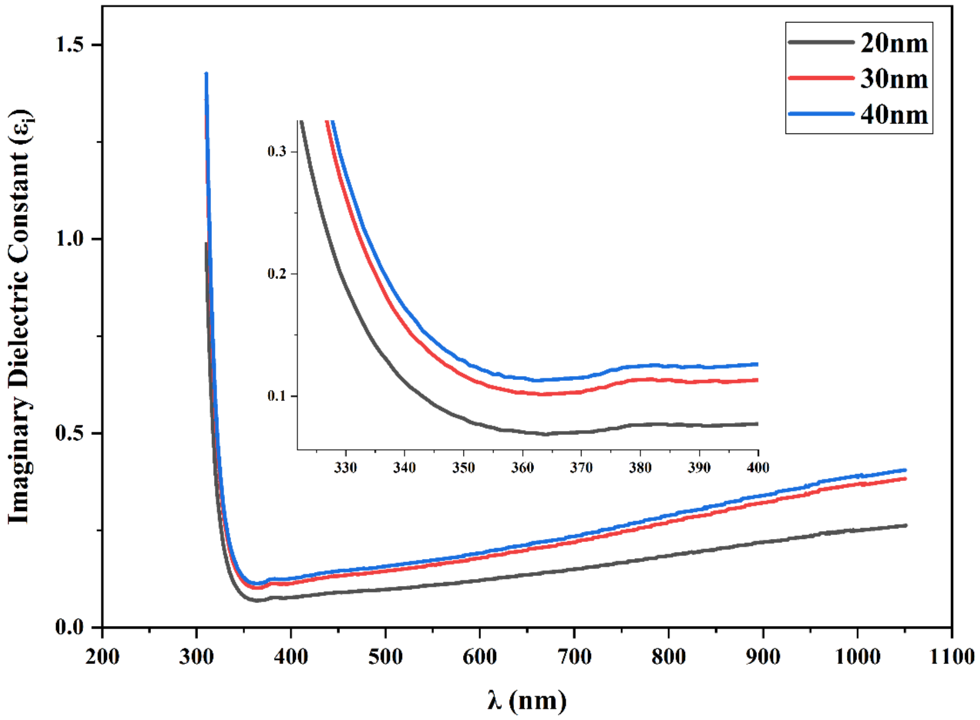

Fig. 4.53: Variation of Ɛi with wavelength of Sb_2O_3:0.02wt.% CuO nanofilms at different thicknesses.

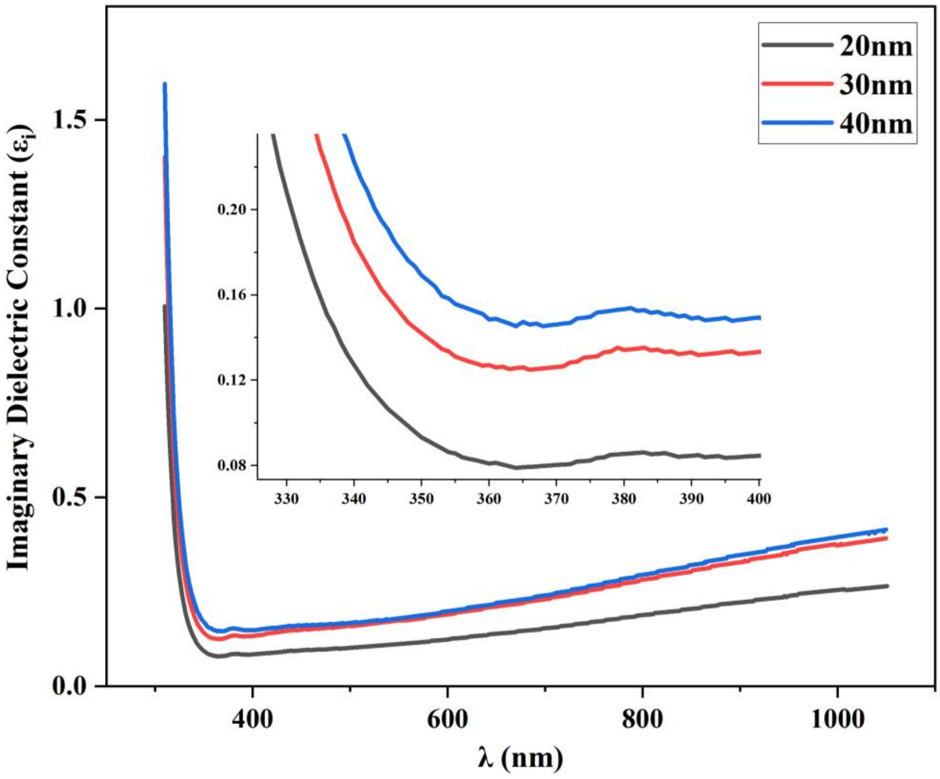

Fig. 4.54: Variation of Ɛi with wavelength of Sb_2O_3:0.04wt.% CuO nanofilms at different thicknesses.

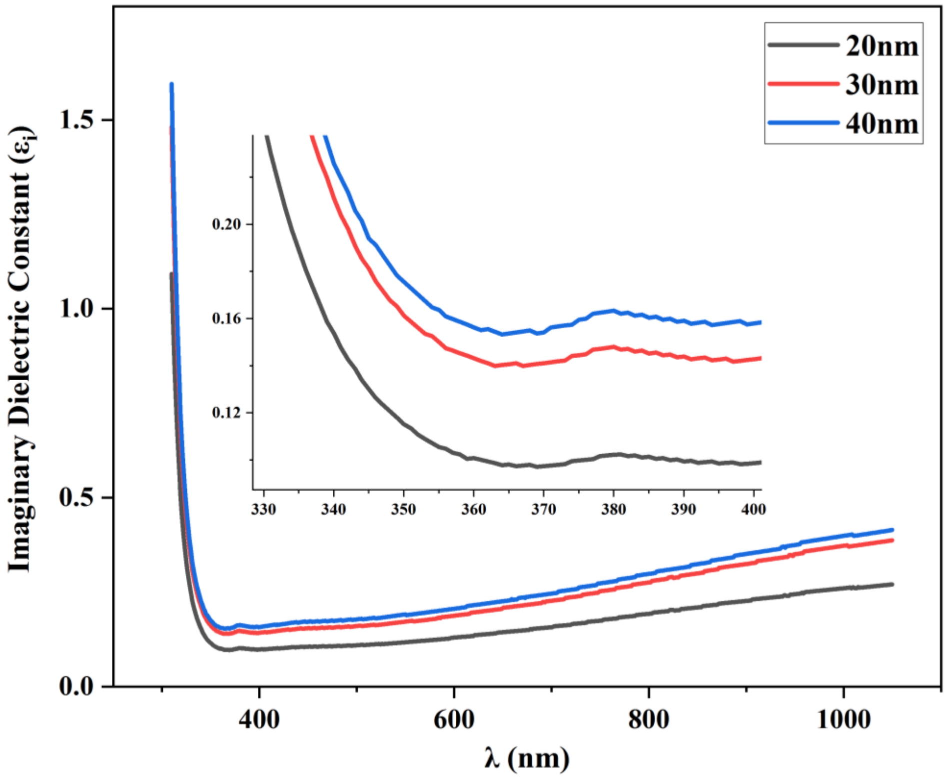

Fig. 4.55: Variation of ε_i with wavelength of Sb_2O_3:0.06wt.% CuO nanofilms at different thicknesses.

4.4 Surface and Volume Energy Loss Function

The surface energy loss function (SELF) and volume energy loss function (VELF) were calculated from the relations (2.25) and (2.26), respectively. Figures (4.56 - 4.63) demonstrate the fluctuation of SELF and VELF values as a wavelength function concerning pure and CuO-doped Sb_2O_3 nanofilms with different thicknesses. VELF and SELF rise with increased thicknesses and CuO doping, regardless of the modest doping ratios, as seen from the results. The surface and volume energy loss functions change as the material composition changes due to doping and thickness, resulting in a change in electron transition energy [200].

Due to the lattice mismatch of films with substrates exactly, the total energy includes both surface and elastic energy. Therefore, the film's overall growth mechanisms depend on the competition and balance of these two energy terms (Stranski–Krastanov model) [201].

For surface energy, it assumes the film will thoroughly wet the surface as it does in the Frank– Van der Merwe model, so the surface energy is proportional to the film's surface area. However, the elastic energy accumulates as each layer grows, so it is proportional to the total volume [202].

Therefore, at the initial stage, the film is very thin; the surface energy is the dominant factor, while the elastic energy is almost negligible. At this time, the films will follow layer-by-layer continuous growth, just as in the Frank–Van der Merwe model. However, as the film thickness increases, the elastic strain energy due to lattice mismatch increases and grows gradually (volume energy) [203].

Figure (4.64) shows the surface energy is greater than the volume energy due to the very little thickness of the nanofilm. It can be noted that the prepared thicknesses are less than the critical thickness, making the films with the best performance and properties. These results are in the findings in the AFM and SEM results.

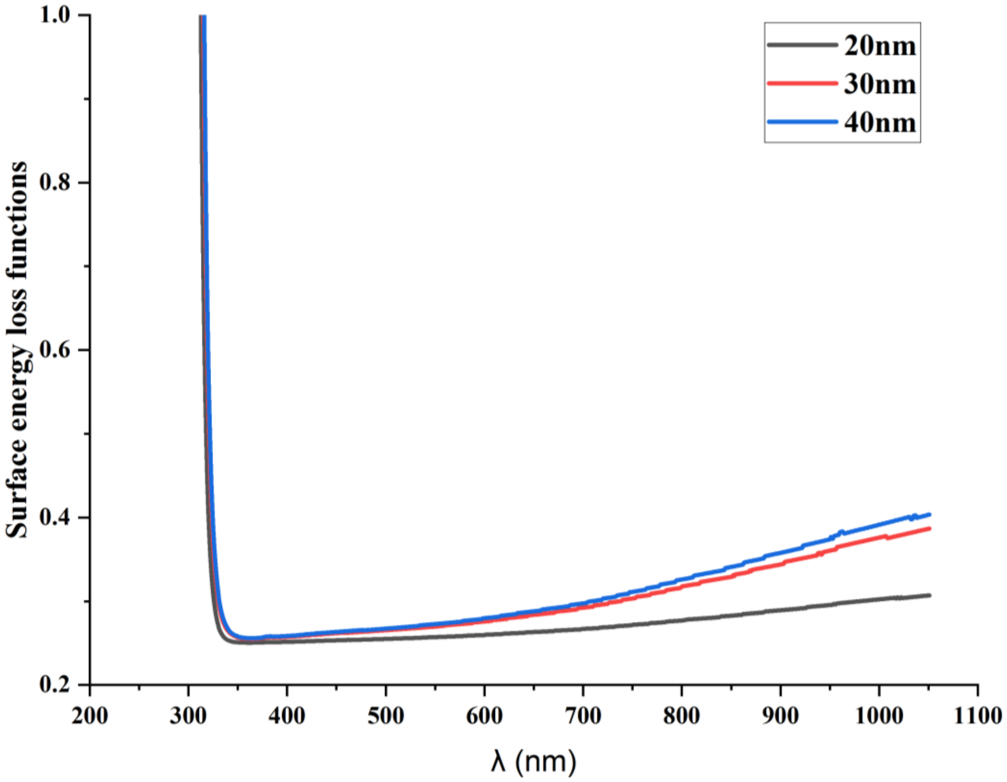

Fig. 4.56: Surface energy loss functions as a function of wavelength for pure Sb_2O_3 nanofilms.

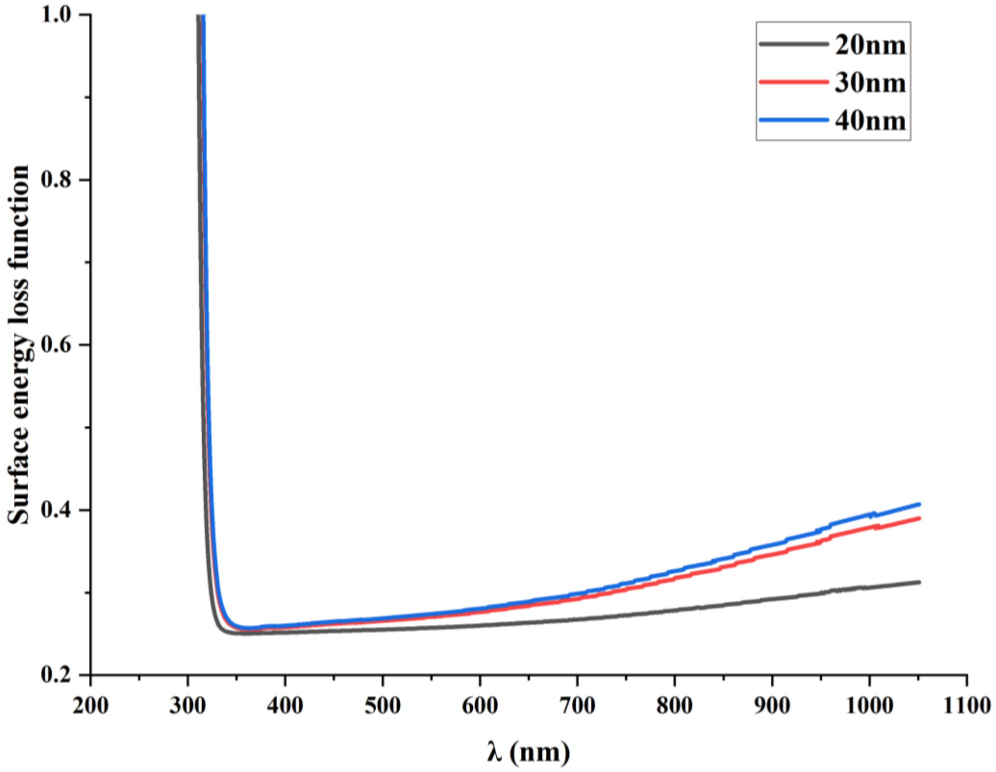

Fig. 4.57: Surface energy loss functions as a function of wavelength for Sb_2O_3:0.02wt.%CuO nanofilms.

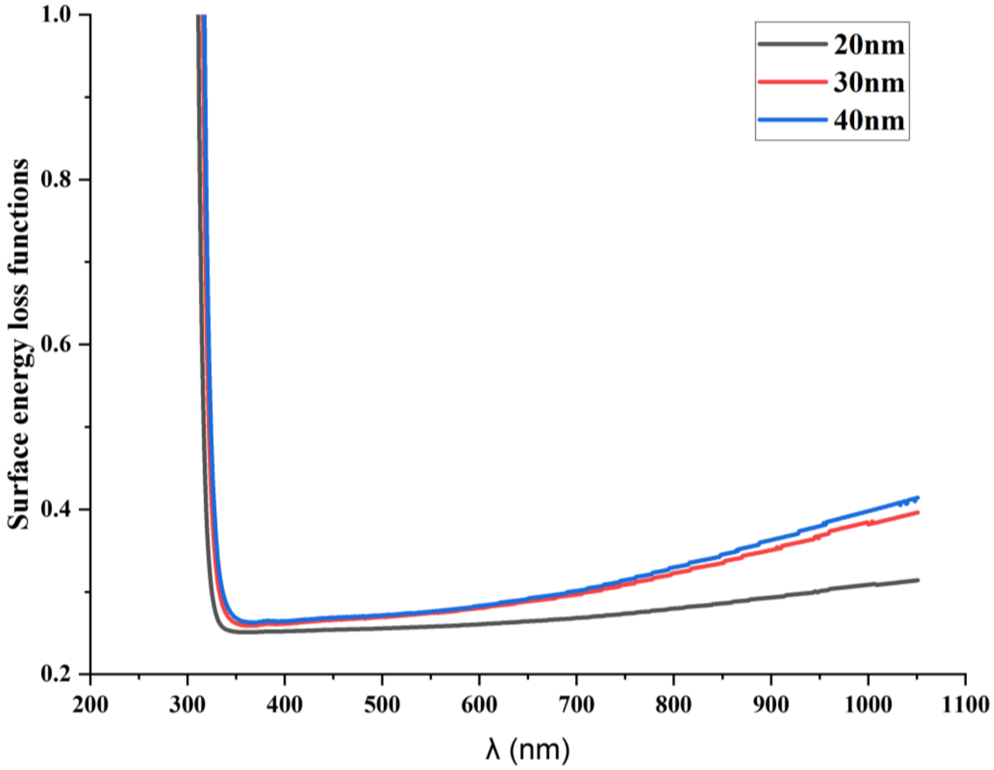

Fig. 4.58: Surface energy loss functions as a function of wavelength for Sb_2O_3:0.04wt.%CuO nanofilms.

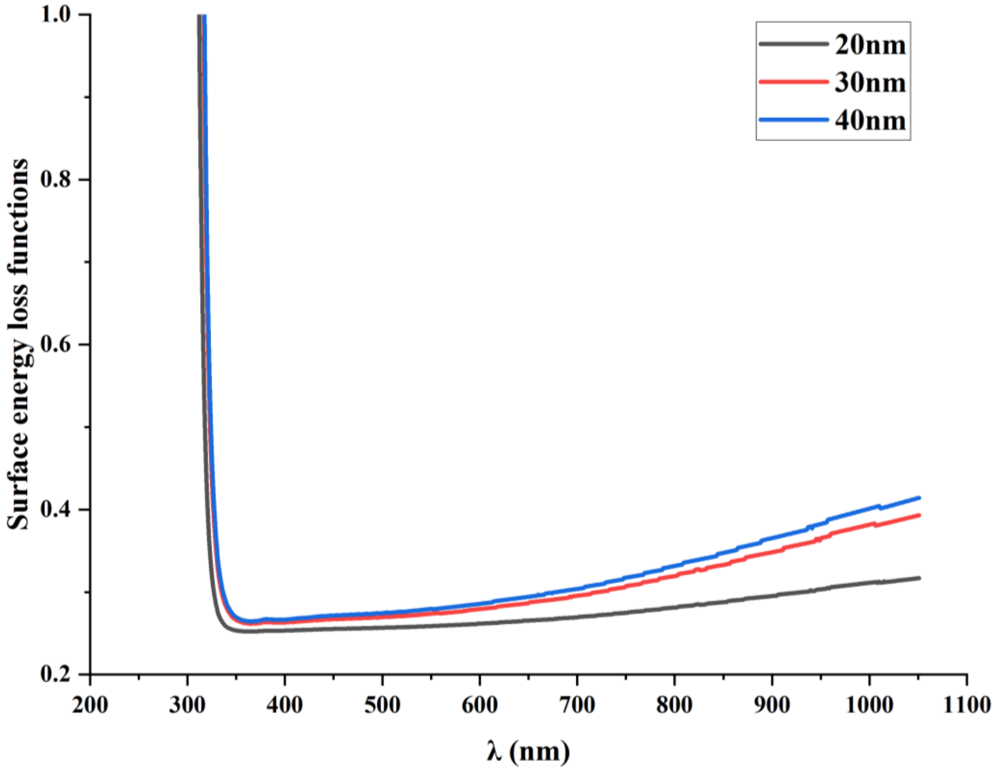

Fig. 4.59: Surface energy loss functions as a function of wavelength for Sb_2O_3:0.06wt.%CuO nanofilms.

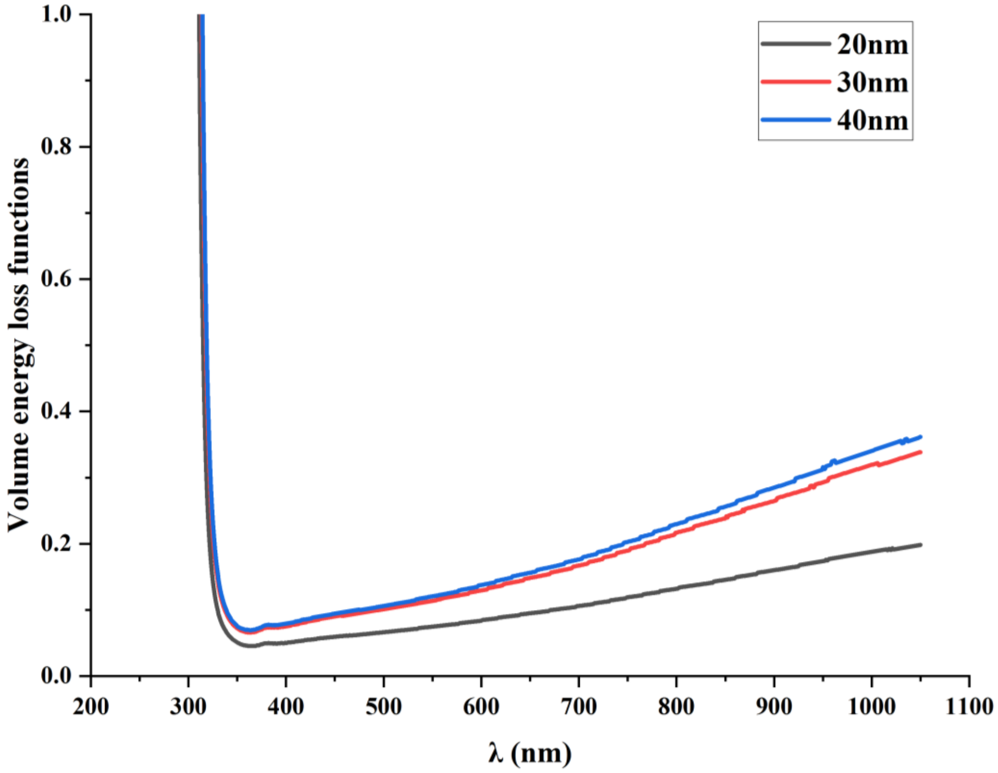

Fig. 4.60: Volume energy loss functions as a function of wavelength for pure Sb_2O_3 nanofilms.

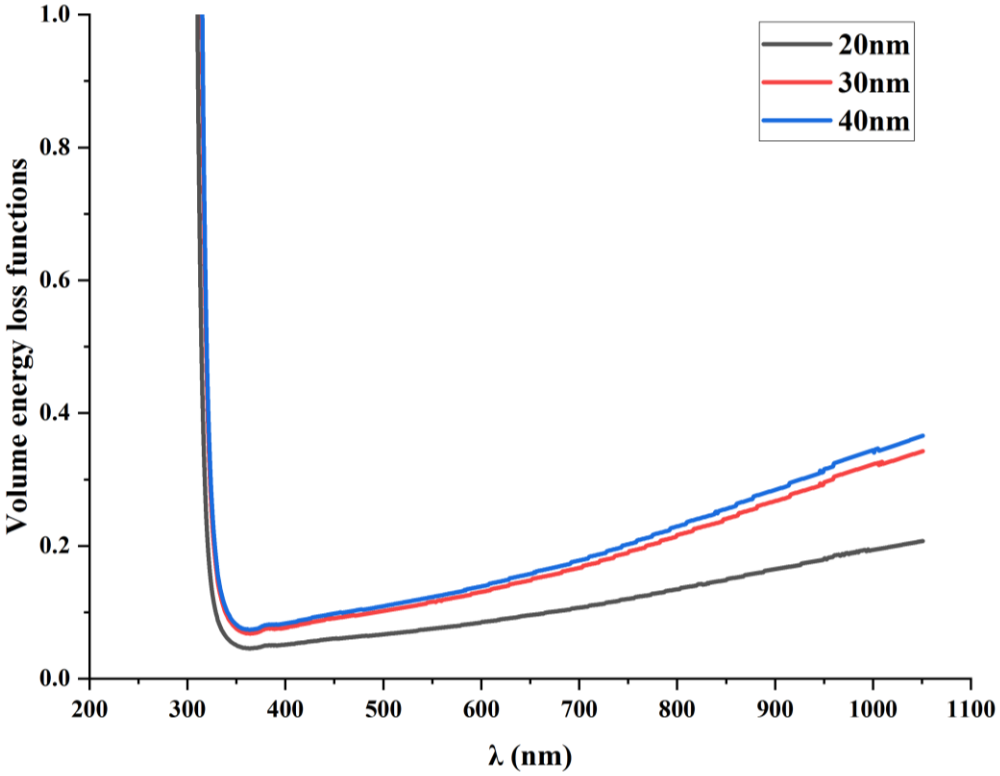

Fig. 4.61: Volume energy loss functions as a function of wavelength for Sb_2O_3:0.02wt.%CuO nanofilms.

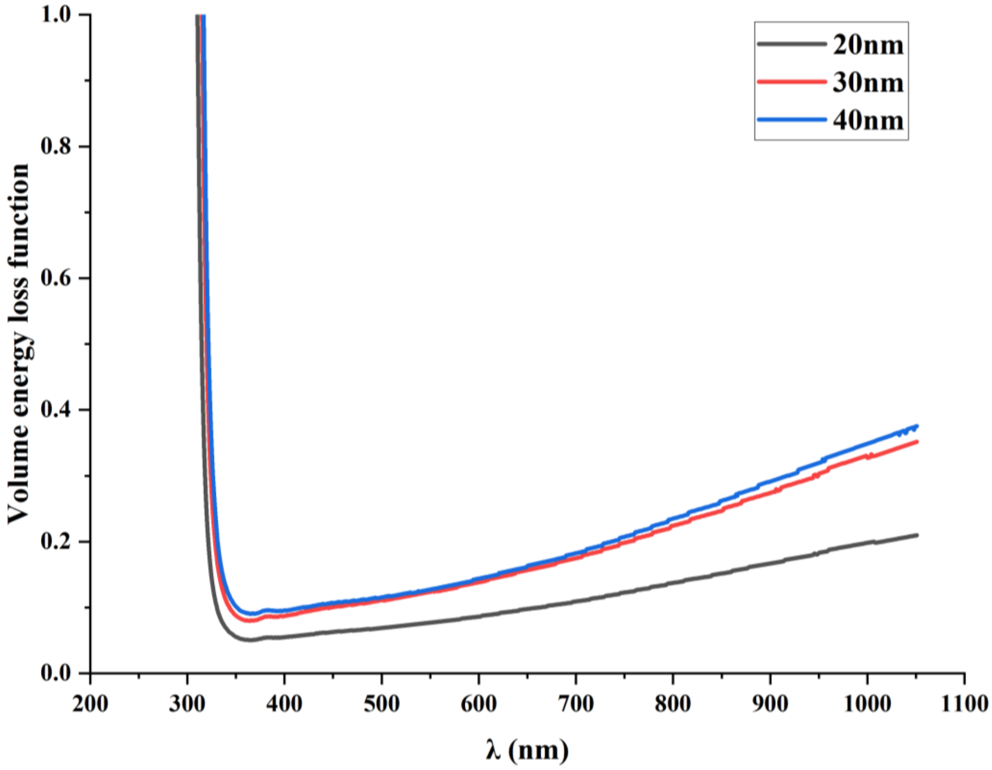

Fig. 4.62: Volume energy loss functions as a function of wavelength for Sb_2O_3:0.04wt.%CuO nanofilms.

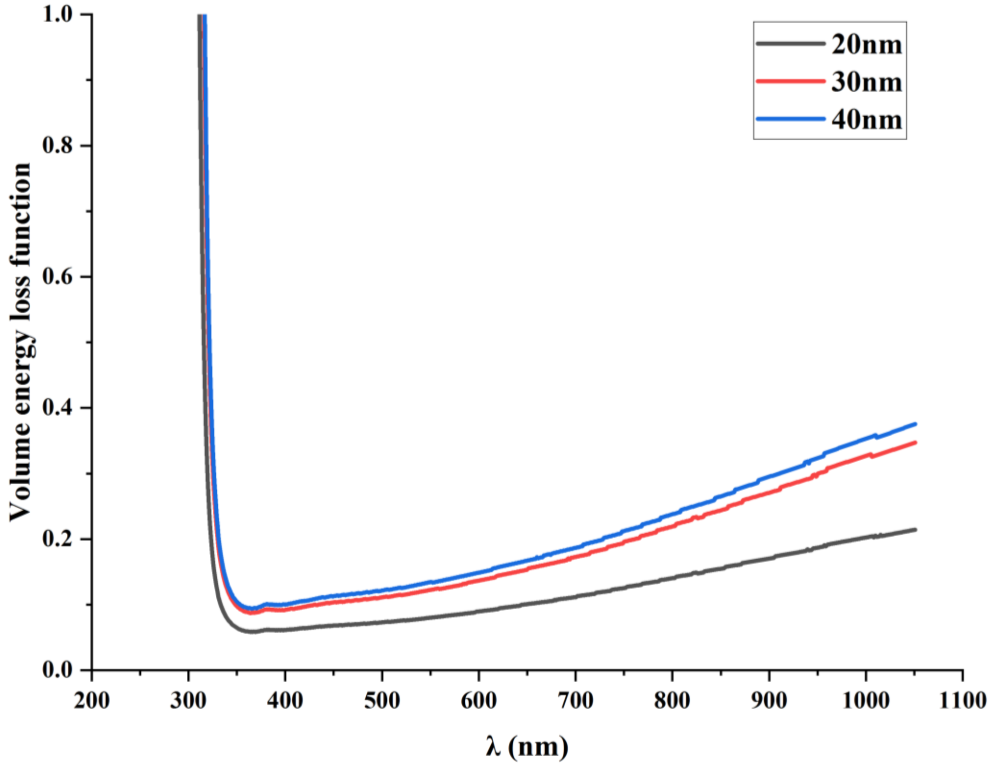

Fig. 4.63: Volume energy loss functions as a function of wavelength for Sb_2O_3:0.06wt.%CuO nanofilms.

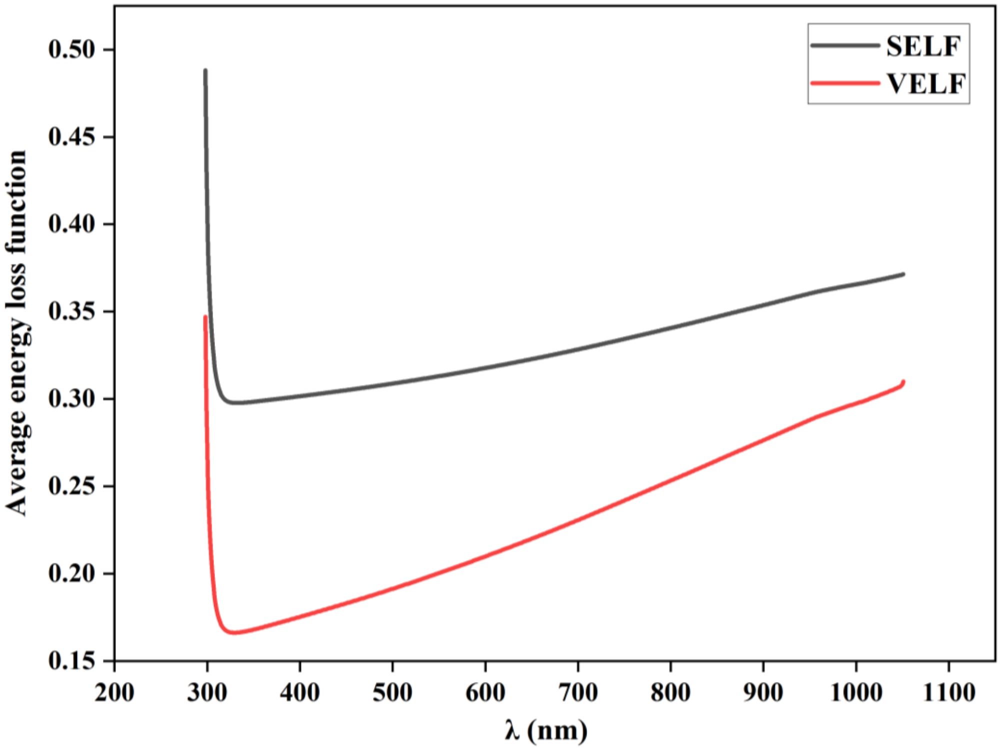

Fig. 4.64: Average energy loss functions as a function of wavelength for nanofilms.

4.5 Dispersion Parameters

The construction of optical systems and many other uses, such as optical transmission and the design of optical devices, depend heavily on dispersion factors [170, 204]. The refractive index dispersion data in semiconductors has been analyzed using the concept of the single–oscillator. Within this concept, the energy parameters E_d and E_o are introduced, and the refractive index at a photon energy hυ can be expressed by Wemple and DiDomenico model [175].

The physical meaning of E_o is that it simulates all the electronic excitation involved and, E_d is the dispersion energy related to the average strength of the optical transitions [205]. In practice, the dispersion parameters E_d and E_o can be obtained according to equation (2.25) by a simple plot of $(n^2\text{-}1)^{-1}$ versus $(h\nu)^2$ as shown in Figures (4.65 - 4.68). The values of E_d and

E_o can be directly determined from the slope and the intercept on the vertical axis. The variation of E_o and E_d with increased thicknesses for Sb_2O_3 and CuO-doped Sb_2O_3 nanofilms, as shown in the figures.

The oscillator energy E_o decreases slightly with increasing thicknesses of nanofilms and increase with doping ratios. This can be attributed to the shift of the optical transmission spectra towards the longer wavelength, which corresponds to the shift of the absorption edge towards shorter energy. This can be described as a decrease in the optical energy gap due to increasing thicknesses of nanofilms and doping ratios [170, 173]. Using the equation ($E_o \approx 2E_g$), we can determine the value of the energy gap from the energy of the simple oscillator, which agrees with the value of the optical energy gap derived from the Tauc relation. The optical spectra's M_{-1} and M_{-3} moments can be determined by the equations (2.26) and (2.27). Table (4.5) displays the computed values.

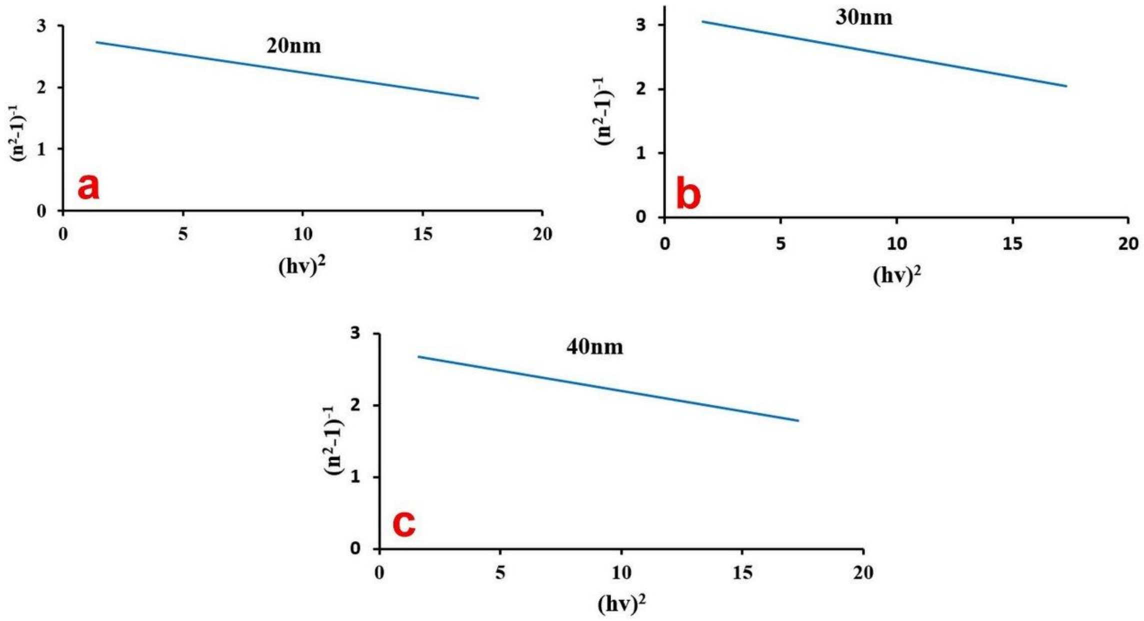

Fig. 4.65: (n^2 - 1)$^{-1}$ versus (hν)^2 of Sb_2O_3 nanofilms at different thickness: (a) 20nm, (b) 30nm, and (c) 40nm.

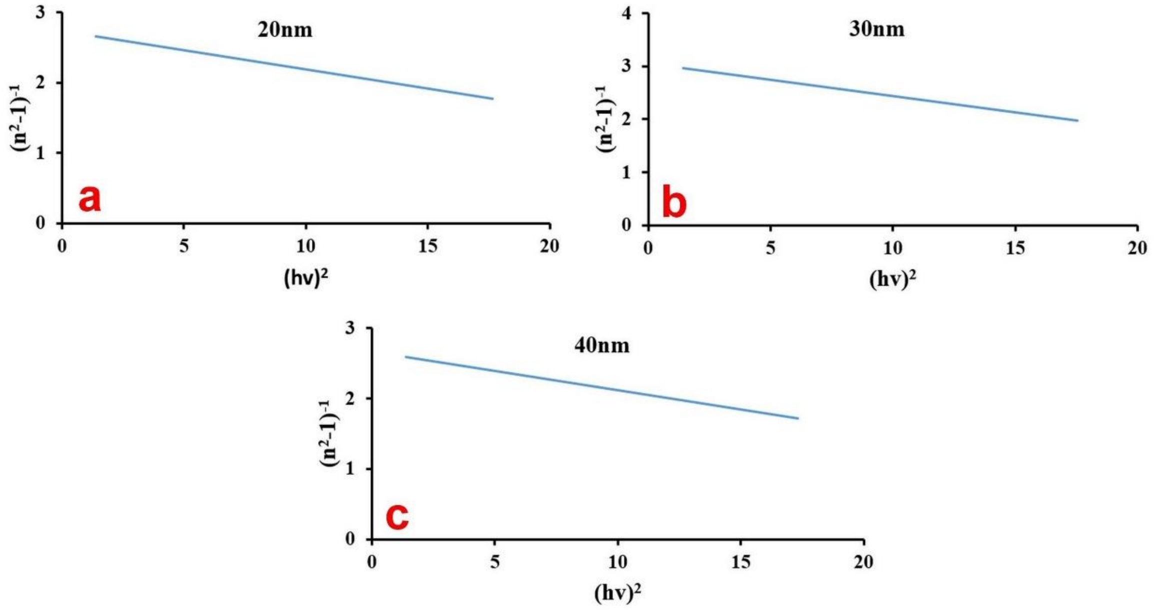

Fig. 4.66: (n^2 - 1)$^{-1}$ versus (hv)^2 of Sb_2O_3:0.02wt.%CuO nanofilms at different thickness: (a) 20nm, (b) 30nm, and (c) 40nm.

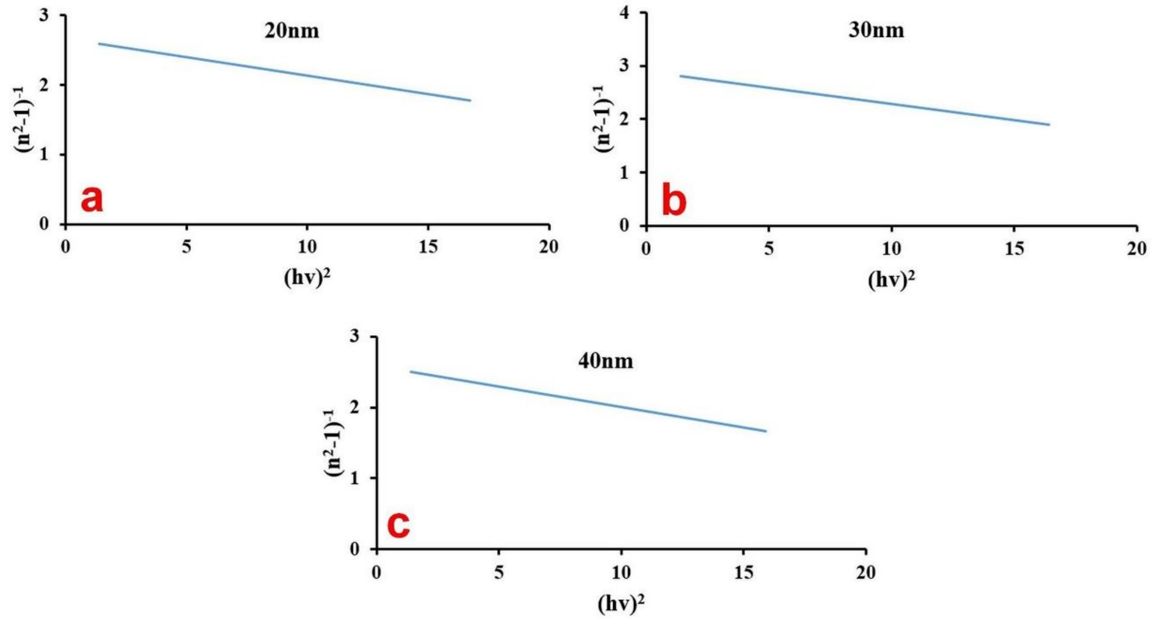

Fig. 4.67: (n^2 - 1)$^{-1}$ versus (hv)^2 of Sb_2O_3:0.04wt.%CuO nanofilms at different thickness: (a) 20nm, (b) 30nm, and (c) 40nm.

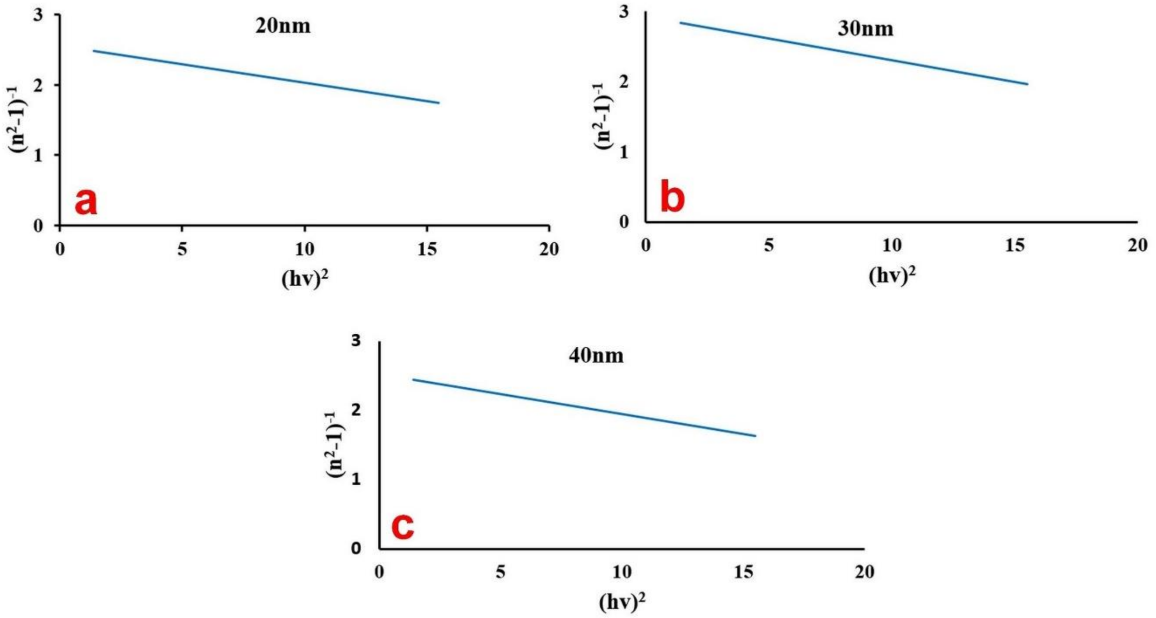

Fig. 4.68: $(n^2 - 1)^{-1}$ versus $(h\nu)^2$ of Sb_2O_3:0.06wt.%CuO nanofilms at different thickness: (a) 20nm, (b) 30nm, and (c) 40nm.

Urbach tail is regarded as the width of the localized state that exists in the optical band gap and is linked to the exponential tails of the density of states via the equation (2.17), which characterizes the optical transition occurring between the filled states in the valence band tail and the unfilled states of the conduction band edge. Figures (4.69 - 4.72) show Urbach's nanofilms plots. The inverse of the slope of $\ln\alpha$ versus hυ was used to calculate the value of U_E, which is given in Table (4.5). Urbach energy increased for the Sb_2O_3 and Sb_2O_3:CuO with increased thicknesses of nanofilms and doped ratio. This behavior is attributed to the broadening of the sublevels in the structure of Sb_2O_3:CuO nanofilms (atomic structural disorder). This behavior is in agreement with the researchers [206].

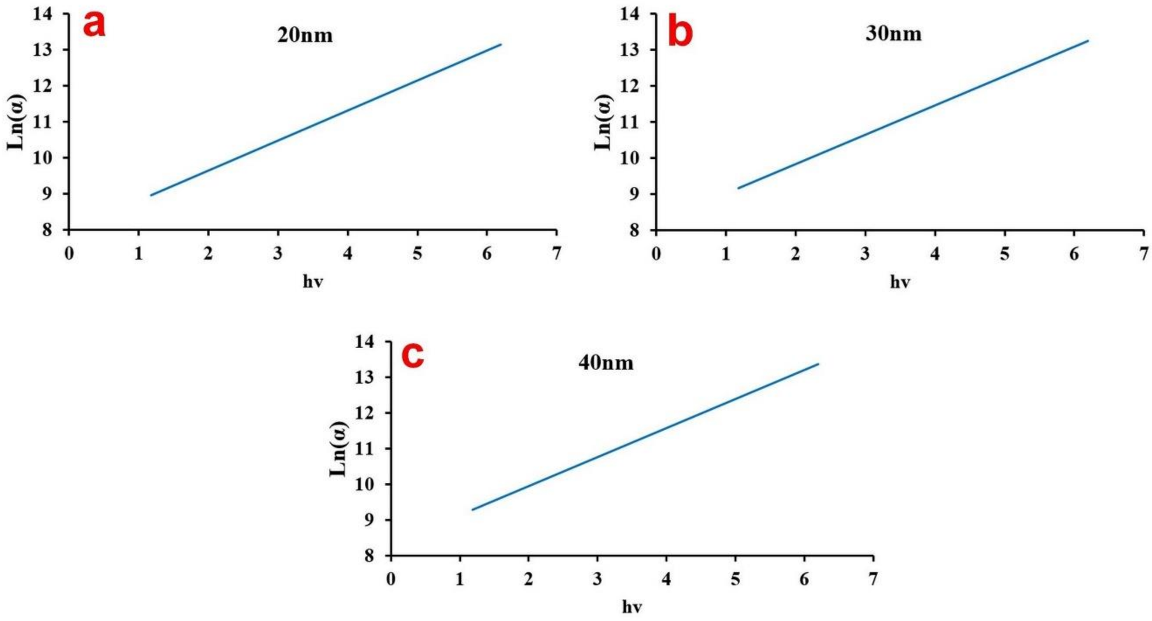

Fig. 4.69: Ln(α) versus (hν) of Sb_2O_3 nanofilms at different thickness: (a) 20 nm, (b) 30 nm, and (c) 40 nm.

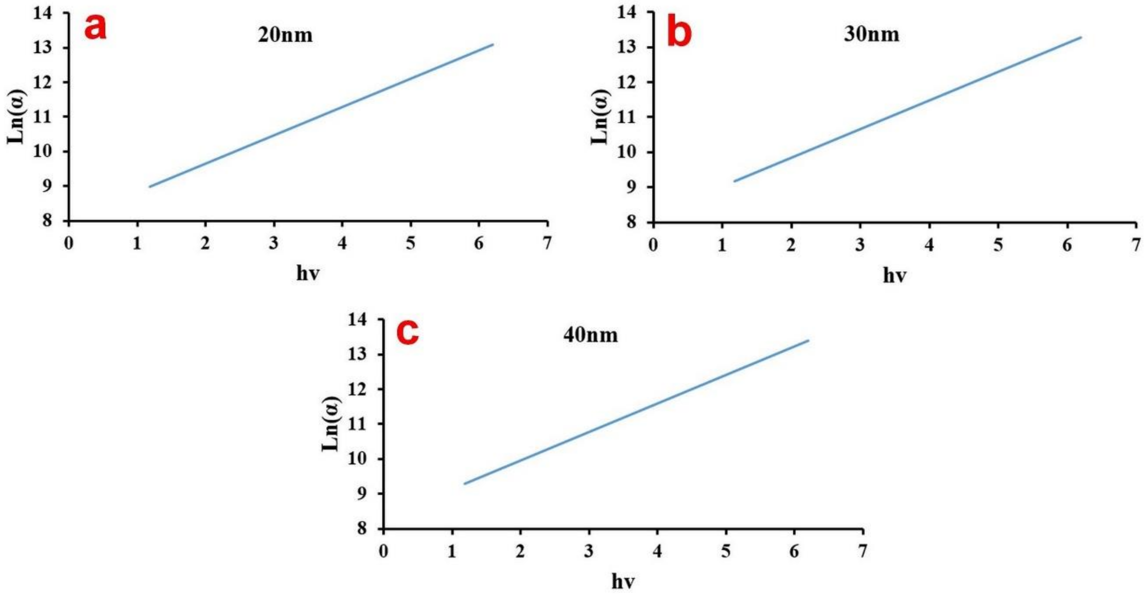

Fig. 4.70: Ln(α) versus (hν) of Sb_2O_3:0.02wt.%CuO nanofilms at different thickness: (a) 20 nm, (b) 30 nm, and (c) 40 nm.

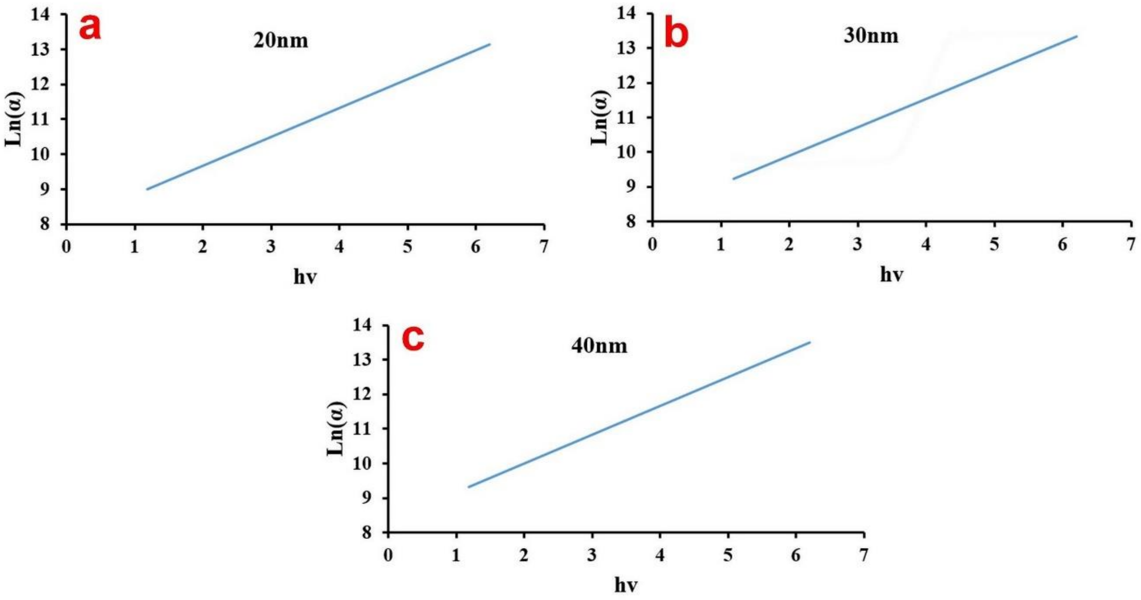

Fig. 4.71: Ln(α) versus (hv) of Sb_2O_3:0.04wt.%CuO nanofilms at different thickness: (a) 20 nm, (b) 30 nm, and (c) 40 nm.

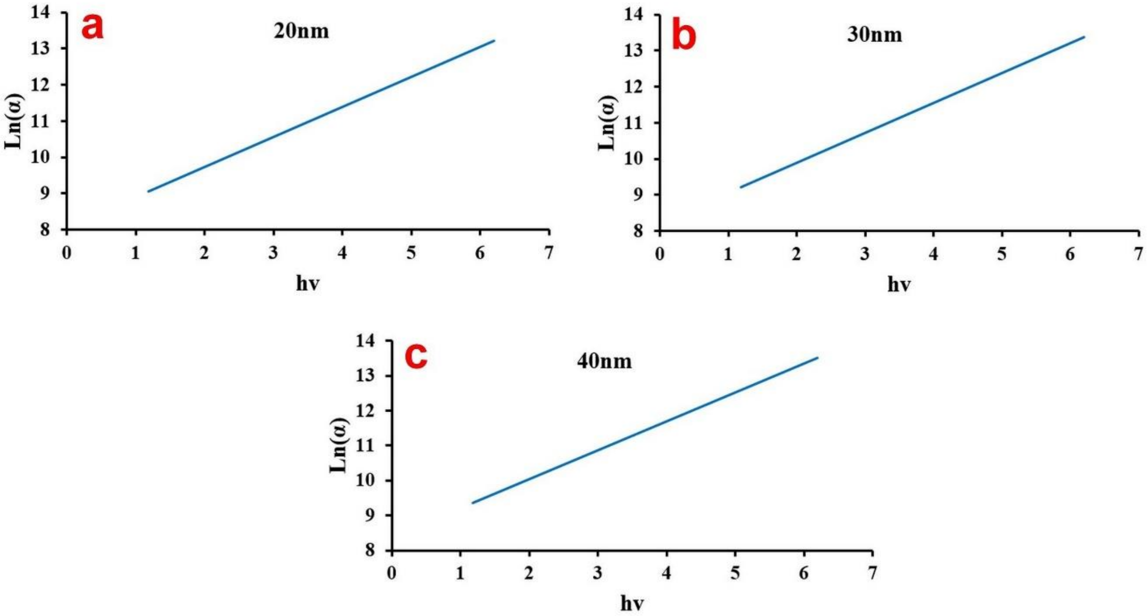

Fig. 4.72: Ln(α) versus (hv) of Sb_2O_3:0.06wt.%CuO nanofilms at different thickness: (a) 20 nm, (b) 30 nm, and (c) 40 nm.

Table 4.5: Dispersion parameters and Urbach energy of Sb_2O_3 and CuO-doped Sb_2O_3 nanofilms.

CuO-doped Sb_2O_3 (wt.%)	**thickness**	$E_\circ$**(eV)**	E_d**(eV)**	E_g**(eV)**	M_{-1}	M_{-3}**(eV)**$^{-2}$	U_E**(eV)**
0.00	**20nm**	7.02	2.51	3.51	0.357	0.007	1.1994
	30nm	7.01	2.22	3.50	0.317	0.006	1.2282
	40nm	6.98	2.52	3.49	0.361	0.007	1.2276
0.02	**20nm**	7.07	2.58	3.53	0.365	0.007	1.2222
	30nm	7.05	2.31	3.52	0.327	0.006	1.2271
	40nm	6.98	2.62	3.49	0.375	0.007	1.2276
0.04	**20nm**	7.11	2.67	3.55	0.375	0.007	1.2291
	30nm	6.88	2.37	3.44	0.344	0.007	1.2294
	40nm	6.68	2.58	3.34	0.387	0.008	1.2303
0.06	**20nm**	6.98	2.72	3.49	0.390	0.008	1.2316
	30nm	6.86	2.35	3.43	0.342	0.007	1.2338
	40nm	6.63	2.63	3.31	0.396	0.009	1.2361

4.6 Electrical Properties

4.6.1 Hall Effect

Hall voltage parameters were made of pure and CuO-doped Sb_2O_3 films prepared by thermal evaporation using (Van-der Pau) method at different thicknesses (20, 30, and 40) nm. The Hall parameters, such as Hall coefficient (R_H), carrier concentrations (n), electrical conductivity (σ), and Hall mobility (μ_H), have been determined by using (Van-der Pau) system tabulated in Table (4.6).

Hall coefficient decreased with increased thickness of the pure and CuO-doped Sb_2O_3 nanofilms. However, at a thickness of 40 nm, the carrier concentration in the samples increased for pure and CuO-doped Sb_2O_3, as shown in Figures (4.73 - 4.76). Moreover, R_H of the samples is negative, which indicates that the Sb_2O_3:CuO nanofilms are n-type conduction. The electrical conductivity of nanofilms decreased with the increasing thickness and increased with the increasing doped ratio (higher resistance due to continuous collisions). This was explained by the fact that the ionised impurity scattering increased carrier concentration, reducing carrier mobility, these results are in good agreement with research [207].

Table (4.6): The results of Hall measurement for CuO-doping Sb_2O_3 at different thicknesses.

CuO-doped Sb_2O_3 (wt.%).	Thickness (nm)	R_H (cm^3/C)	Carrier type	n (cm^{-3})	σ (1/Ω.cm)	μ_H(cm^2/V.s)
0.00	**40nm**	-2.2727	n	2.75×10^{18}	0.87719298	16.3
	30nm	-5.2083	n	1.2×10^{18}	3.44827586	12.7
	20nm	-2.5720	n	2.43×10^{18}	13.5135135	33.12
0.02	**40nm**	-1.5625	n	4.0×10^{18}	0.98039216	17.5
	30nm	-2.3148	n	2.7×10^{18}	5	14.9
	20nm	-1.9531	n	3.2×10^{18}	19.6078431	42.15
0. 04	**40nm**	-1.6891	n	3.7×10^{18}	0.91743119	17.0
	30nm	-2.5	n	2.5×10^{18}	4.16666667	15.5
	20nm	-2.0833	n	3.0×10^{18}	18.1818182	40.11
0. 06	**40nm**	-2.0161	n	3.1×10^{18}	0.82644628	16.8
	30nm	-3.125	n	2.0×10^{18}	4.76190476	14.0
	20nm	-2.3320	n	2.68×10^{18}	16.3934426	37.16

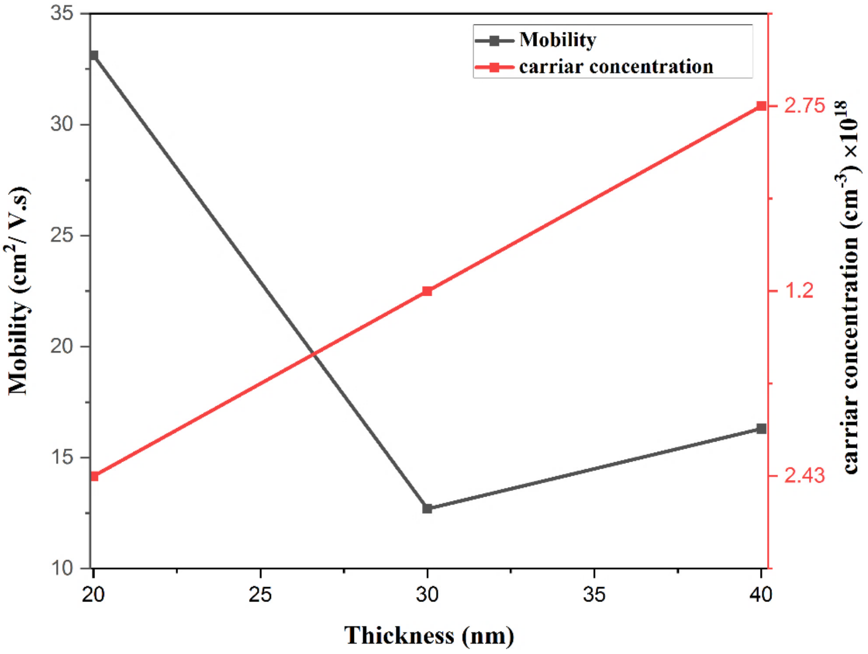

Fig. 4.73: Mobility and carrier concentration of Sb_2O_3 nanofilms of different thicknesses (20, 30, and 40) nm.

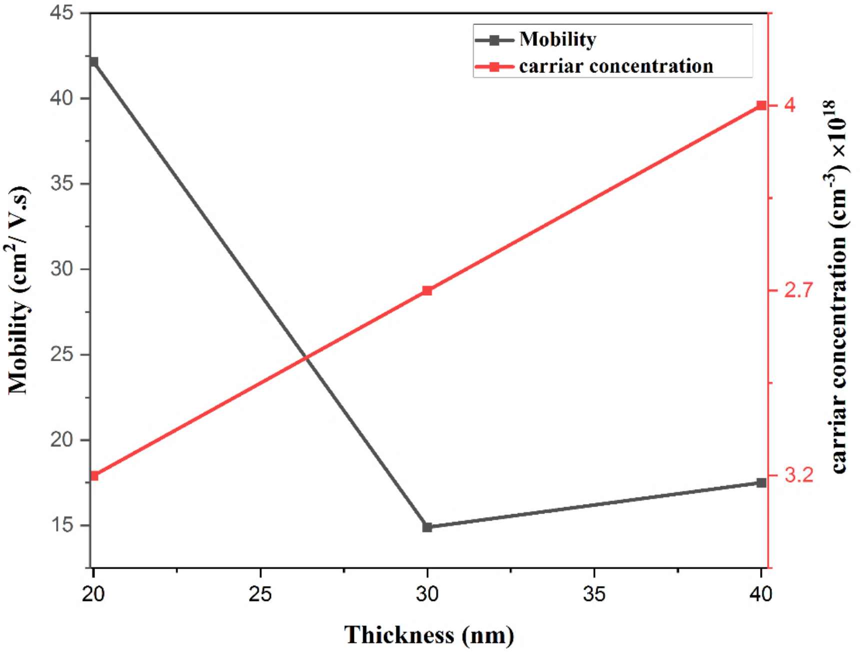

Fig. 4.74: Mobility and carrier concentration of Sb_2O_3:0.02% CuO nanofilms of different thicknesses (20, 30, and 40) nm.

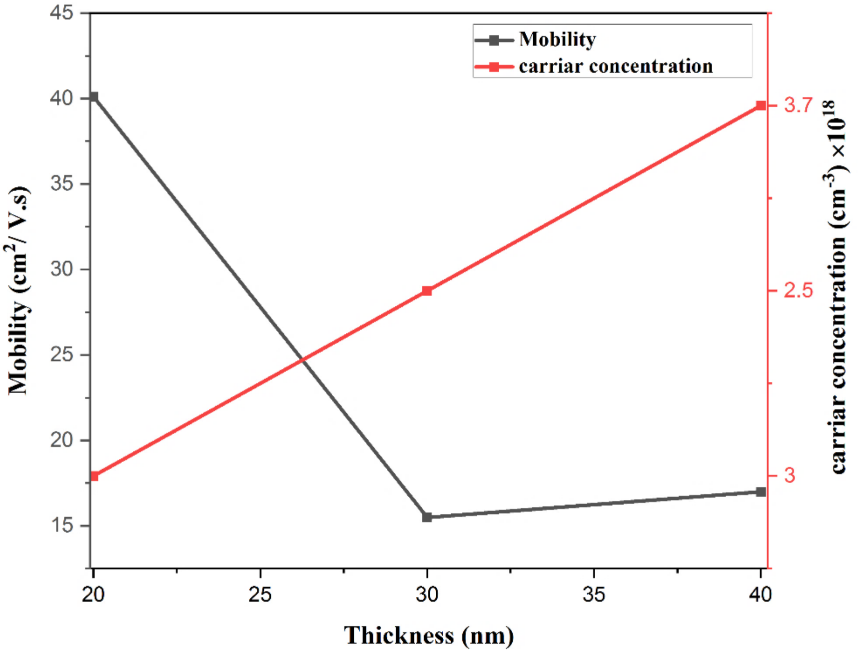

Fig. 4.75: Mobility and carrier concentration of Sb_2O_3:0.04% CuO nanofilms of different thicknesses (20, 30, and 40) nm.

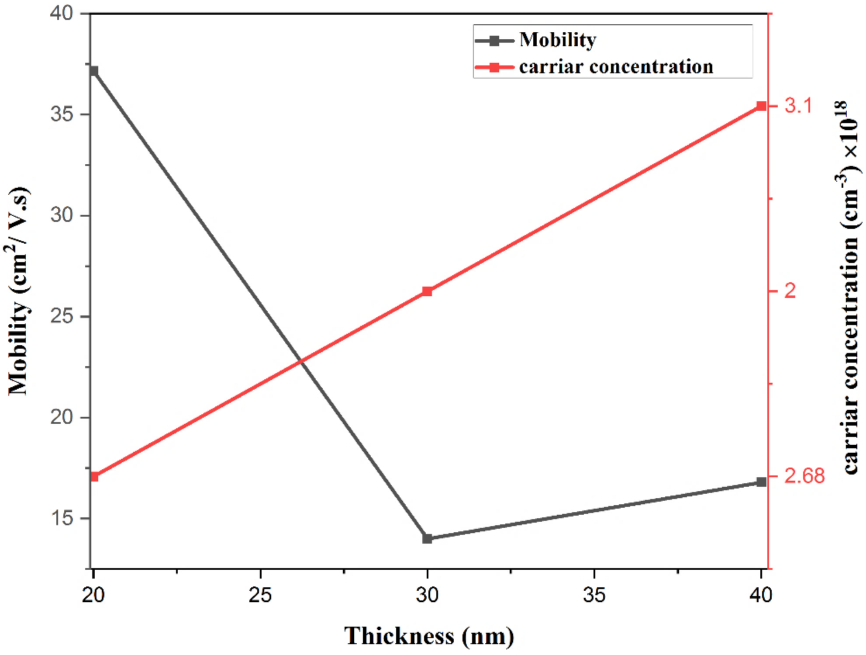

Fig. 4.76: Mobility and carrier concentration of Sb_2O_3:0.06% CuO nanofilms of different thicknesses (20, 30, and 40) nm.

4.6.2 I-V characteristic of Sb_2O_3:CuO/p-Si heterojunction

Fabrication of the junction of Sb_2O_3:CuO/etched-p-Si solar cell is by thermal evaporation technique. The fabricated solar cell of an area of 0.75 cm^2 gave the following I-V curves, which exhibited different behaviors depending on the environment in which the junction was prepared. Sb_2O_3:CuO/etched-p-Si will obtain anisotype p-n heterojunction (HJ) for (0.02, 0.04, and 0.06) wt.% with various thicknesses for nanofilms because Sb_2O_3:CuO are p-type according to the measurements of the Hall and Si is n-type.

Short circuit current and open circuit voltage values were achieved from the I-V characteristic. When current is not flowing through the cell, open circuit voltage (V_{oc}) is obtained, V (at I = 0) = V_{oc}. When the resistance is low, the short circuit current (I_{sc}) corresponds to the short circuit state and is attained when the voltage is zero. I (at V = 0) = I_{sc}. In the power quadrant, the maximum current is achieved, known as I_{sc}, which occurs at the starting point of the forward-bias sweep.

The I-V curves of Sb_2O_3:CuO/etched-p-Si heterojunction are explained in Figures (4.77 - 4.88) for dark and illuminated conditions. Under dark state, the current-voltage (I-V) characteristics are essential to identify the various components' importance under reverse and forward bias.

The I-V characteristic for Sb_2O_3:CuO/etched-p-Si HJ at forward bias voltage for different CuO doping and thicknesses within the range (-6 to 6 Volt). These curves exhibit the behavior of the current with the forward and reverse bias voltage. The current-voltage characteristic under illumination is one of the optoelectronics typical for HJ. The measurements are passed out under incident power densities equal to (100 mW/cm^2)

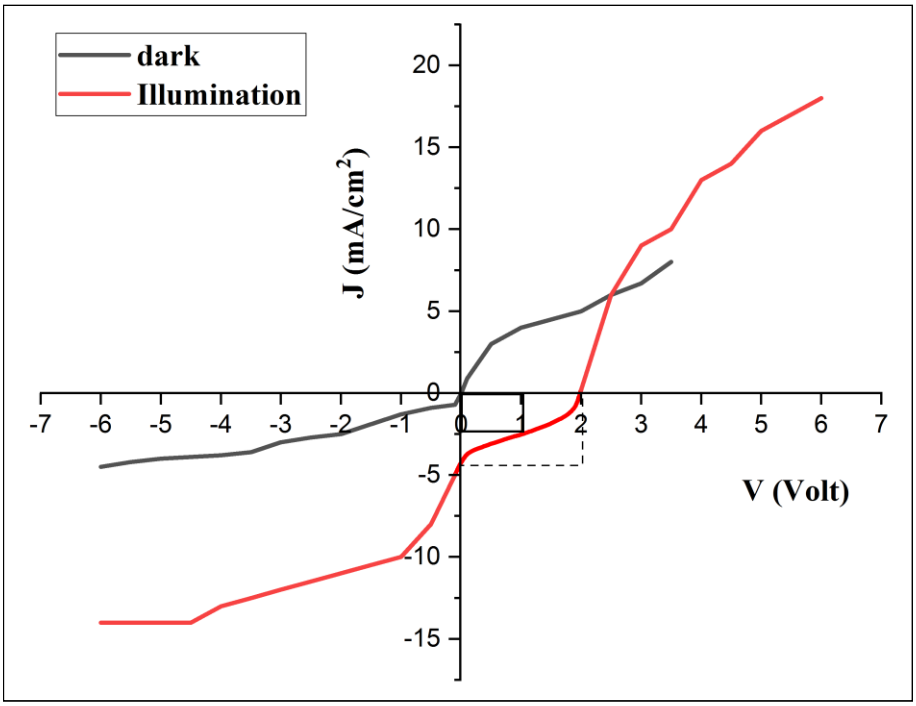

Fig. 4.77: I-V characteristic of Sb_2O_3 nanofilms under dark and illumination in a solar cell with thickness of 20 nm.

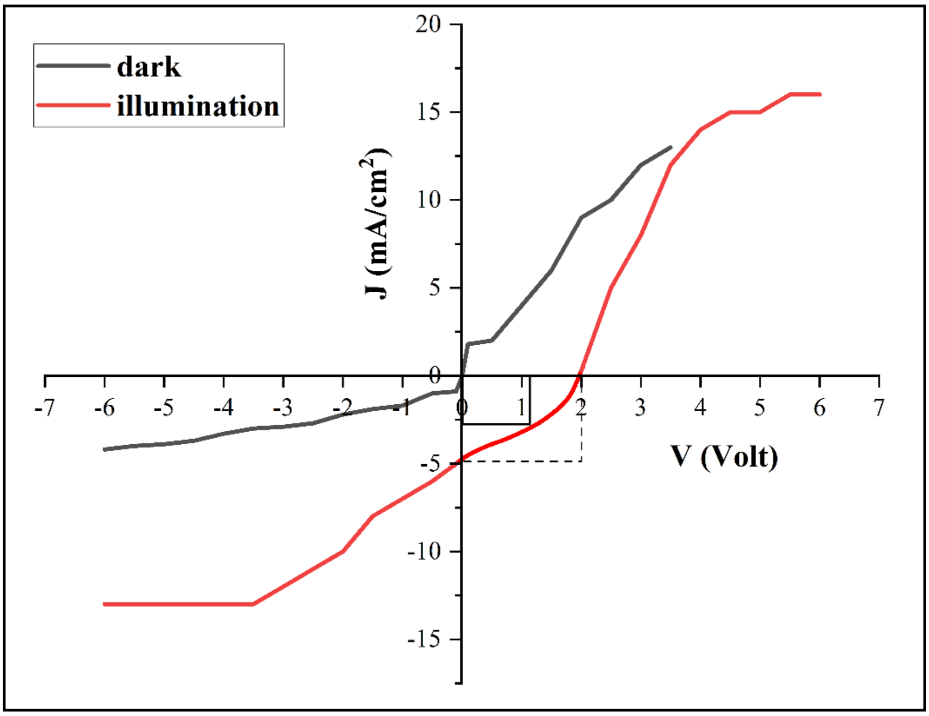

Fig. 4.78: I-V characteristic of Sb_2O_3 nanofilms under dark and illumination in a solar cell with thickness 30 nm.

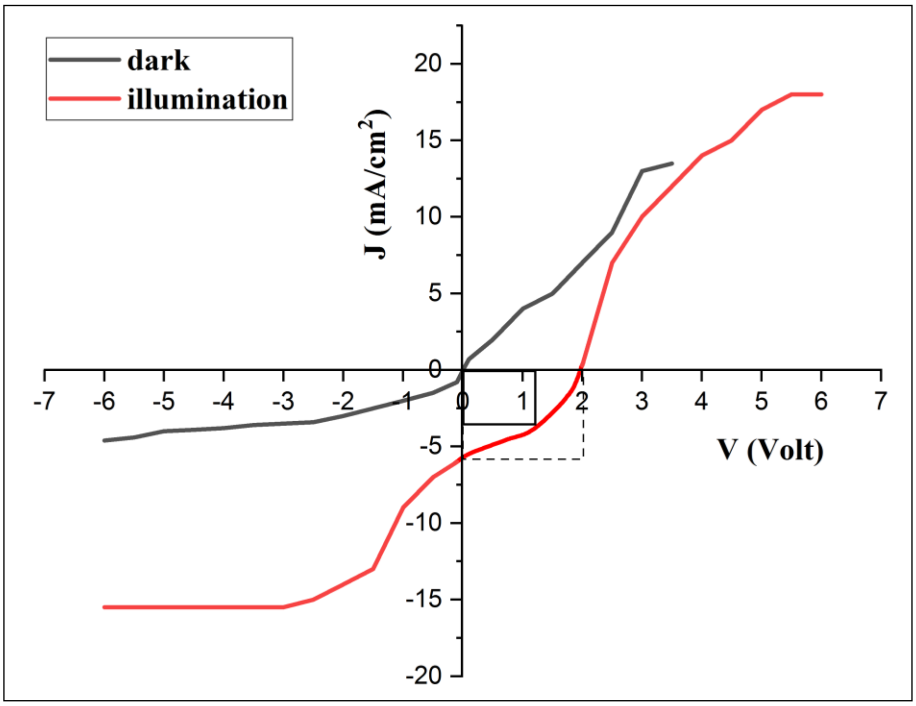

Fig. 4.79: I-V characteristic of Sb_2O_3 nanofilms under dark and illumination in a solar cell with thickness 40 nm.

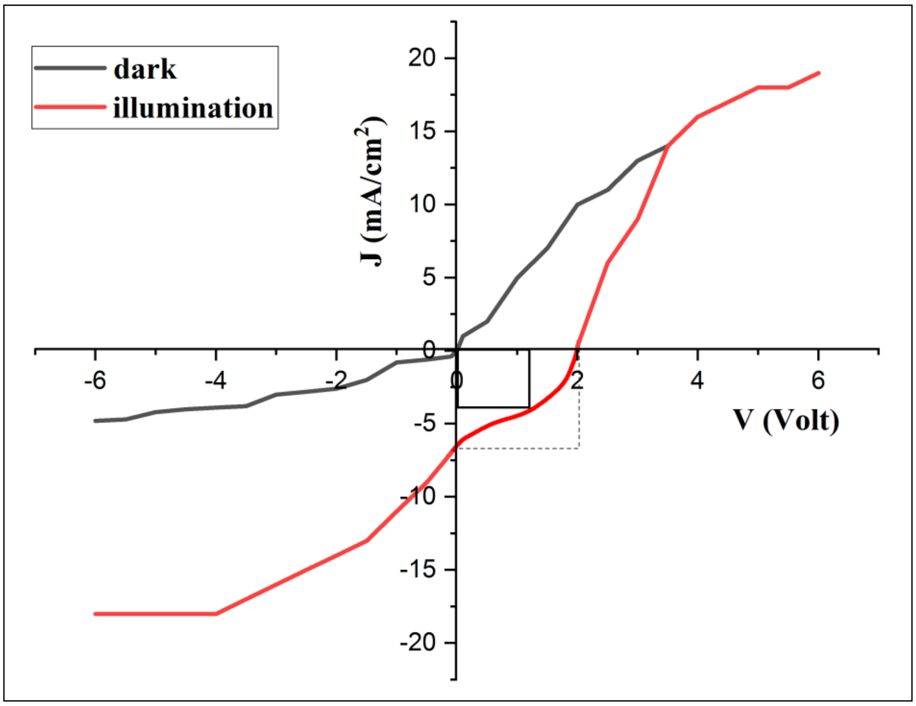

Fig. 4.80: I-V characteristic of Sb_2O_3: 0.02wt.% CuO nanofilms under dark and illumination in a solar cell with thickness 20 nm.

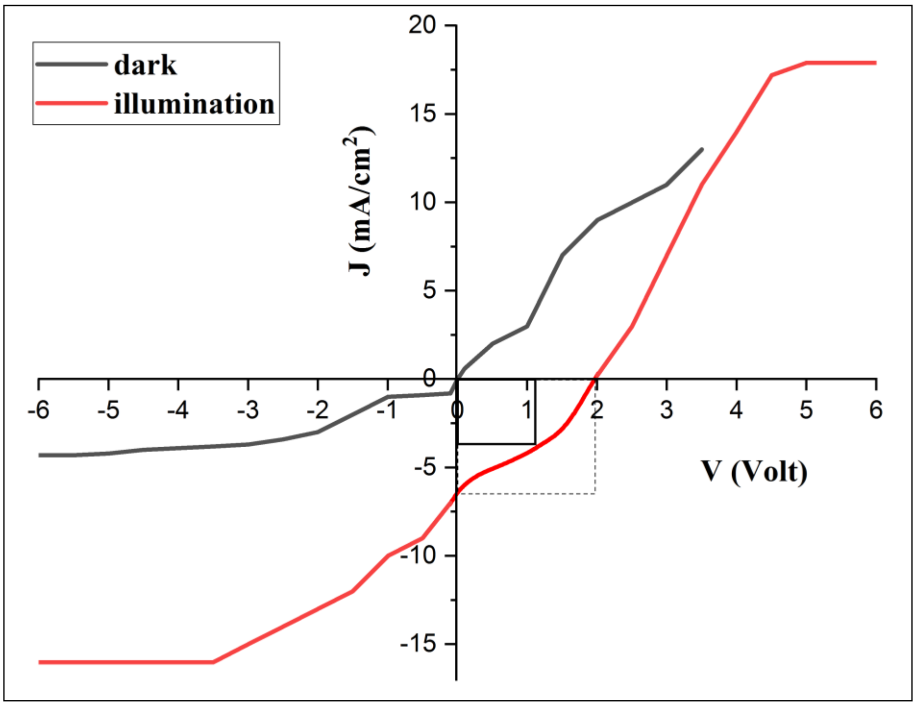

Fig. 4.81: I-V characteristic of Sb_2O_3: 0.02wt.% CuO nanofilms under dark and illumination in a solar cell with thickness 30 nm.

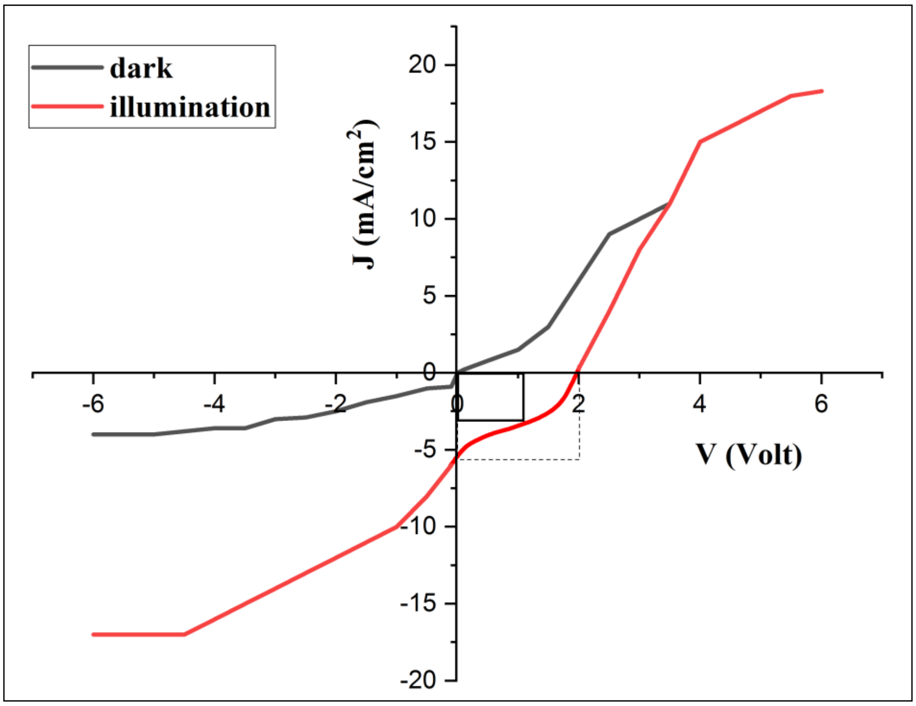

Fig. 4.82: I-V characteristic of Sb_2O_3: 0.02wt.% CuO nanofilms under dark and illumination in a solar cell with thickness 40 nm.

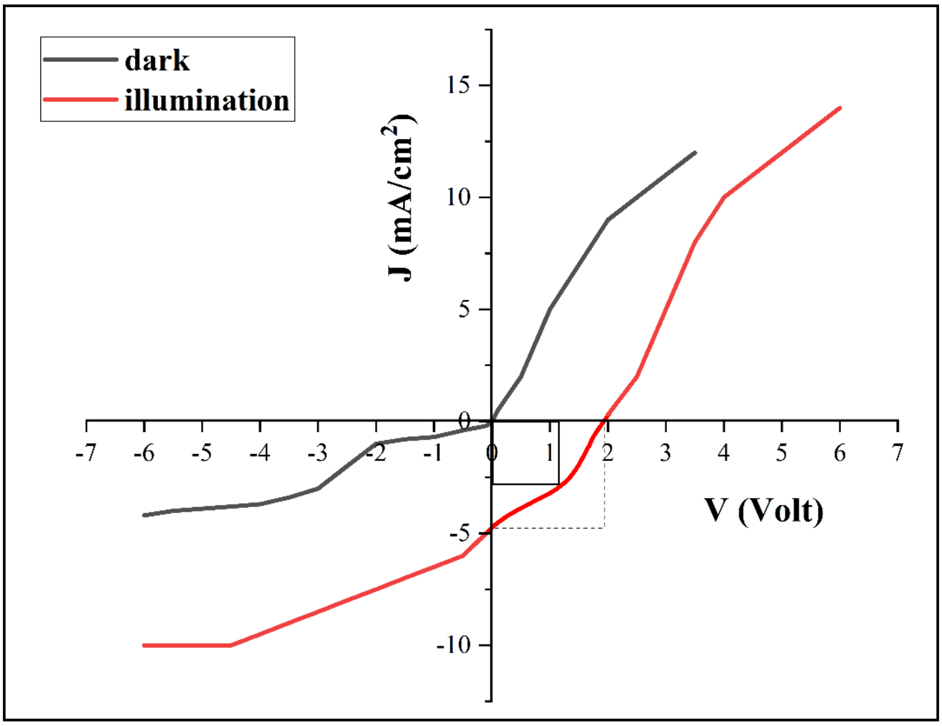

Fig. 4.83: I-V characteristic of Sb_2O_3: 0.04wt.% CuO nanofilms under dark and illumination in a solar cell with thickness 20 nm.

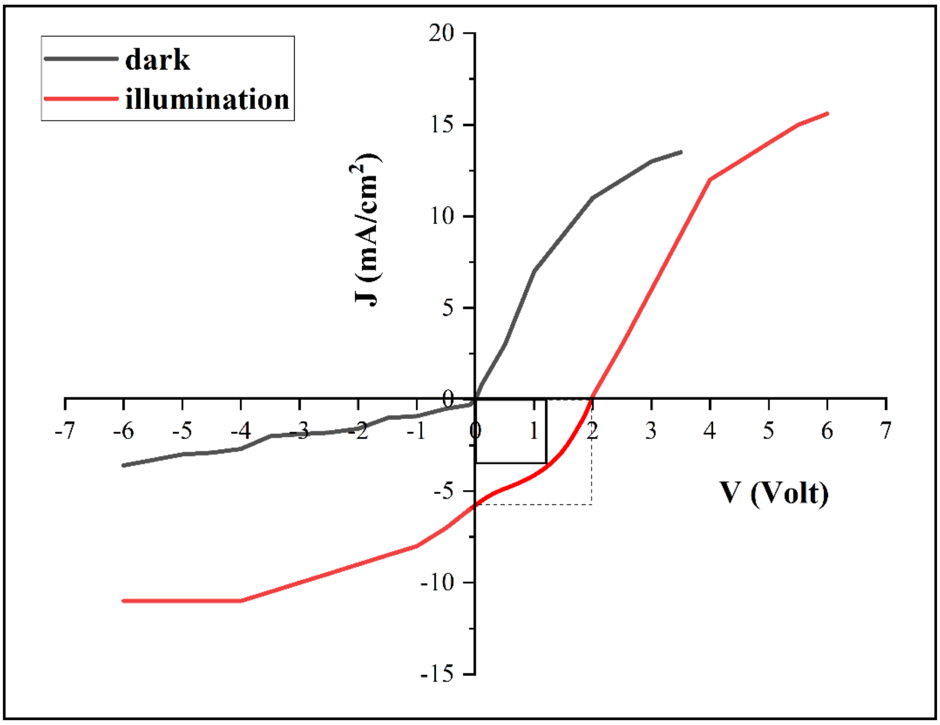

Fig. 4.84: I-V characteristic of Sb_2O_3: 0.04wt.% CuO nanofilms under dark and illumination in a solar cell with thickness 30 nm.

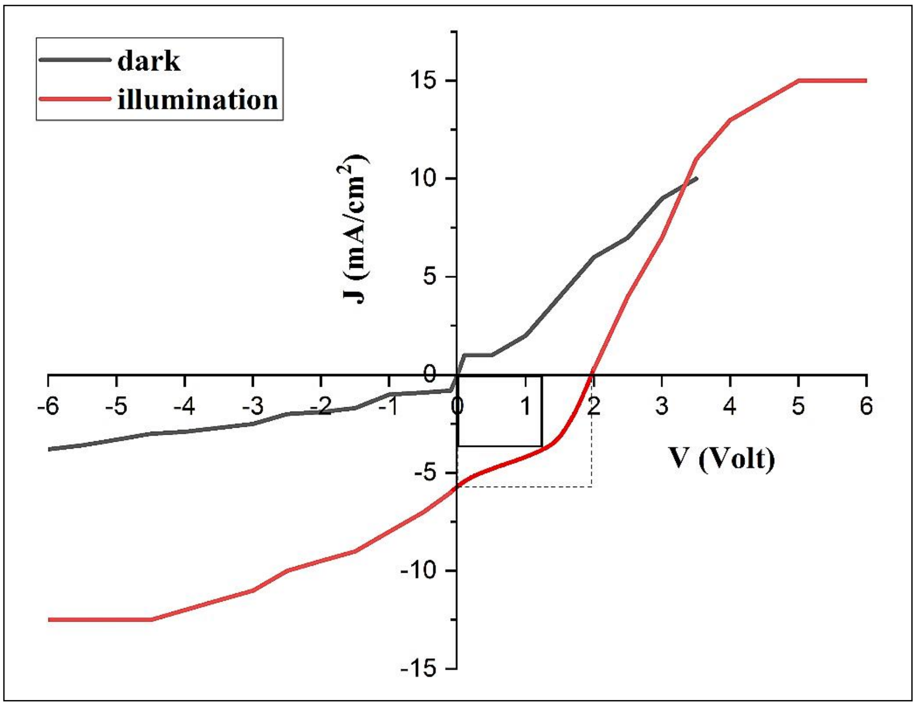

Fig. 4.85: I-V characteristic of Sb_2O_3: 0.04wt.% CuO nanofilms under dark and illumination in a solar cell with thickness 40 nm.

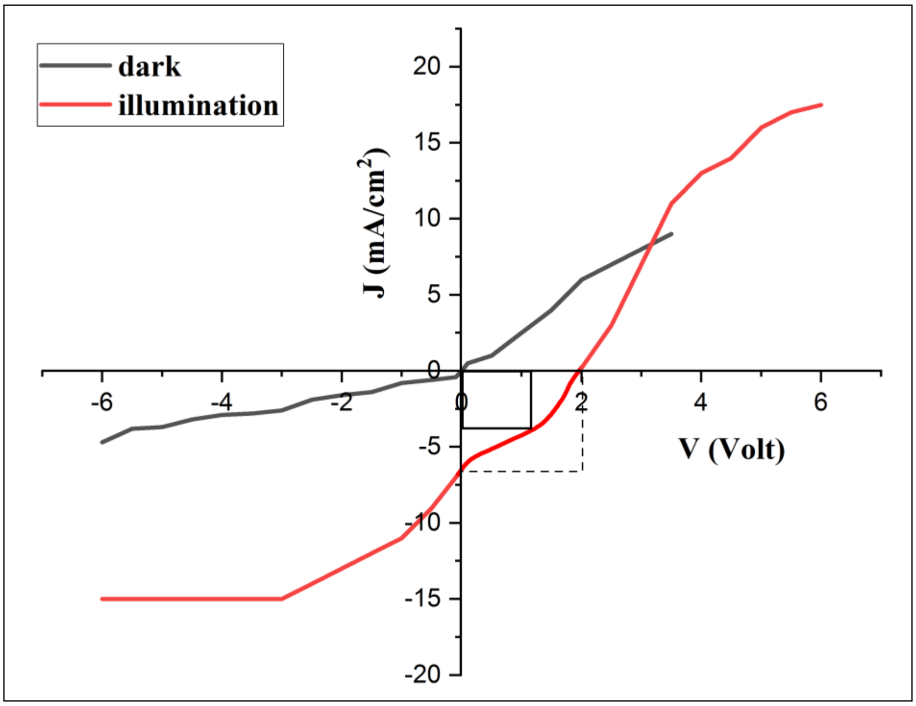

Fig. 4.86: I-V characteristic of Sb_2O_3: 0.06wt.% CuO nanofilms under dark and illumination in a solar cell with thickness 20 nm.

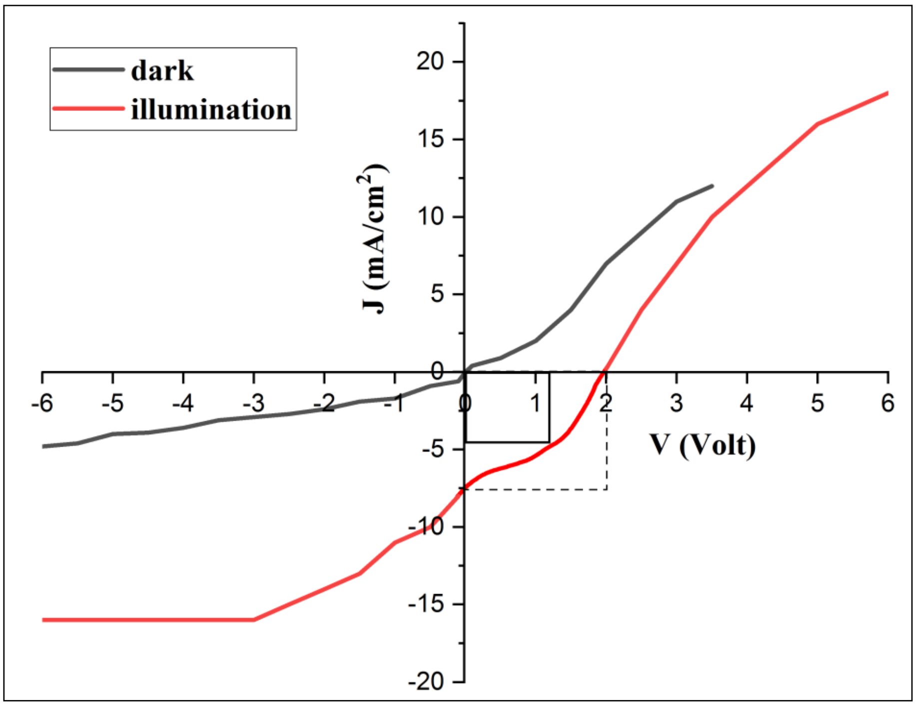

Fig. 4.87: I-V characteristic of Sb_2O_3: 0.06wt.% CuO nanofilms under dark and illumination in a solar cell with thickness 30 nm.

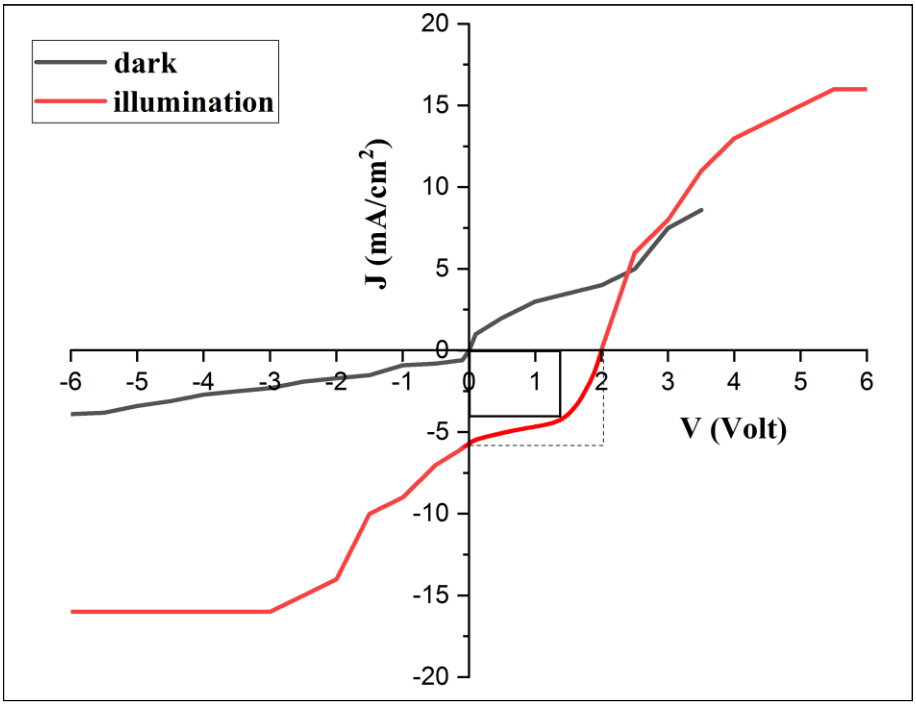

Fig. 4.88: I-V characteristic of Sb_2O_3: 0.06wt.% CuO nanofilms under dark and illumination in a solar cell with thickness 40 nm.

Figures show that the photocurrent increases when the bias voltage is increased. The photocurrent in the reverse bias is also bigger than in the forward bias. This is because the width of the depletion region widens when the reverse bias voltage is increased, causing the electron-hole pairs to separate. Therefore, the photocurrent is a function of the generation and diffusion of the carriers.

Furthermore, with the rise of CuO-doping, the value of the current rises, which can be attributed to emerging flaws and dislocations that affect the charge carriers' mobility. Energy levels can be within the energy gap because of defect evolutions. These flaws are found in the depletion zone and operate as active recombination centers, enhancing the current flow through the junction. Increased current can also be rationalized since increased doping rearranges the interface atoms and lowers the dangling bond, resulting in improved junction properties.

By measuring the short circuit current (I_{sc}) and open circuit voltage (V_{oc}) of the samples, fill factor (FF) and conversion efficiency (ɳ) were calculated using relationships shown in equation (2.39) and equation (2.40), respectively.

The efficiency increased with increasing thicknesses of Sb_2O_3 nanofilms and increased with added CuO to Sb_2O_3. The highest efficiency was 5.965% with V_{oc} of 11 V, I_{sc} of 3 mA/cm^2, and F.F of 0.180 for Sb_2O_3 nanofilms at a thickness of 40 nm (Figure 4.79). Also, the highest efficiency was 7.625% with V_{oc} of 12 V, I_{sc} of 3.2 mA/cm^2, and F.F of 0.198 for Sb_2O_3:0.06wt.%CuO at a thickness of 40 nm (Figure 4.88), as given in Table (4.7).

The conversion efficiency enhancement can be attributed to the change of materials, such as silicon substrates' laser etching, the prepared films' low thickness, and the low CuO doping ratios. The use of etching may provide two purposes in terms of its application to solar cells: an improved contact between the layers of the solar cell and a decrease in optical reflection caused by the high refractive index of crystalline silicon. Furthermore, the addition of CuO-doping works to retarding electron-hole recombination, this agreement with the findings of the researchers [113, 185]. The contribution of the scattering from CuO NPs to the elevated efficiency observed in this study is noteworthy. The increased dispersion caused by nanoparticles may increase the length of the optical path of light entering the cell, which may cause a higher release of charge carriers.

This study observed a solar cell efficiency increase of 0.825% from the values obtained on other Antimony trioxide based solar cells. Noor and Khalid (2019) fabricated a Sb_2O_3:Ag/p-Si solar cell and reported the following cell parameters: short circuit photocurrent density of 5.5 mA/cm^2, open circuit voltage of 1.25 V, a fill factor of 0.57 and conversion efficiency of 6.8% [208].

Table 4.7: Results of I-V of pure and CuO-doped Sb_2O_3/etched p-Si solar cells with various doping ratios and various thicknesses at 473 K.

CuO-doped $Sb_2O_3 (wt.\%)$	Thickness nm	J_{sc} mA/cm^2	V_{oc} (v)	J_{max} mA/cm^2	V_{max} (v)	$F.F$	η (%)
0.00	**20**	2.4	10	3.21	1.05	0.141	3.393
	30	3.4	11	3.79	1.16	0.117	4.409
	40	3	11	4.83	1.23	0.180	5.965
0.02	**20**	3.4	10	4.24	1.10	0.138	4.705
	30	2.8	9	5.00	1.13	0.224	5.669
	40	2.6	4	3.80	1.67	0.612	6.373
0.04	**20**	2.9	12	4.71	1.22	0.166	5.782
	30	3.2	10	4.95	1.25	0.194	6.230
	40	3	12	5.28	1.22	0.179	6.540
0.06	**20**	1.9	13	5.17	1.12	0.235	5.807
	30	2.6	9	6.16	1.21	0.319	7.466
	40	3.2	12	5.47	1.39	0.198	7.625

4.7 Conclusions

Using pure and CuO-doped Sb_2O_3 nanofilms with various doping ratios (0.02, 0.04, and 0.06) wt.% with varying thicknesses (20, 30, and 40) nm deposited on glass (optical properties) and laser-etched p-Si (solar cell) substrates in a vacuum environment (1×10^{-6}) mbar through a thermal evaporation chamber. **From the obtained results and discussions, the following conclusions were noticed:**

1. The X-ray analysis of Sb_2O_3 nanofilms indicates that the concluded films are amorphous (or crystal-poor). While at a thickness of 40 nm, exhibited (040) orientation for Sb_2O_3:(0.02, 0.04, and 0.06)wt%CuO.
2. Surface morphology (AFM) of pure and Sb_2O_3:CuO nanofilms show a uniform granular and homogeneous distribution, while appearing SEM analysis of nanofilms exhibits a smooth surface devoid of islands and voids and consisting of small spherical grain size nanoparticles (NPs). The particle size of nanofilms increases with thickness and doped ratio.
3. The optical properties increase with increasing thickness and ratio doped for nanofilms. The energy gap for direct transition reduces due to the broadening of the sublevels (Urbach energy), which agrees with the value of the average energy gap from the energy of the simple oscillator (Wemple and DiDomenico).
4. Material composition changes (doping and thickness) lead to surface and volume energy loss functions change. Due to the low thickness of the nanofilm, it was found that the surface energy is greater than the volume energy.
5. Hall coefficient decreased, and the carrier concentration in the samples increased with thickness and doped ratio for nanofilms.

6. The efficiency increased with increasing thicknesses of Sb_2O_3 nanofilms and added wt.%CuO to Sb_2O_3. The highest efficiency was 5.965% for Sb_2O_3 nanofilms at a thickness of 40 nm, and the highest efficiency was 7.625% for Sb_2O_3:0.06wt.%CuO at the same thickness.

4.8 Suggestions For Future Work

1. Preparation and characterization of Sb_2O_3 solar cells by chemical spray pyrolysis method.
2. Fabrication and characterization of n-Sb_2O_3:CaF_2/p-Si Solar cell by thermal evaporation technique.
3. Laser etching on silicon to prepare solar cells from metal oxide.

References

[1] Park, H.J.: Inorganic Nanocrystal Solar Cells. Energies. **15**, 1–2 (2022). https://doi.org/10.3390/en15155450

[2] Leitão, D., Torres, J.P.N., Fernandes, J.F.P.: Spectral irradiance influence on solar cells efficiency. Energies. **13**, 2-18 (2020). https://doi.org/10.3390/en13195017

[3] Torres, J.P.N., Nashih, S.K., Fernandes, C.A.F., Leite, J.C.: The effect of shading on photovoltaic solar panels. Energy Syst. **9**, 195–208 (2018). https://doi.org/10.1007/s12667-016-0225-5

[4] Dharmadasa, I.M.: Advances in Thin-Film Solar Cells. Pan Stanford Publishing Pte. Ltd.1-224 (2012).

[5] Campos, C.S., Torres, J.P.N., Fernandes, J.F.P.: Effects of the heat transfer fluid selection on the efficiency of a hybrid concentrated photovoltaic and thermal collector. Energies. **12**, 1–12 (2019). https://doi.org/10.3390/en12091814

[6] Marques, L., Torres, J.P.N., Branco, P.J.C.: Triangular shape geometry in a Solarus AB concentrating photovoltaic-thermal collector. Int. J. Interact. Des. Manuf. **12**, 1455–1468 (2018). https://doi.org/10.1007/s12008-018-0489-1

[7] Hamammu, I.M., Khalaf Jehad, A.: Calculating the Efficiency of Solar Cells. 243-247 (2018). https://www.researchgate.net/publication/329191790

[8] Frey, H., Khan, H.R.: Handbook of Thin-Film Technology. Springer-Verlag Berlin Heidelberg. 379 (2015). https://doi 10.1007/978-3-642-05430-3

[9] Adeyeye, A.O., Shimon, G.: Growth and Characterization of Magnetic Thin Film and Nanostructures. Elsevier. **5**, 1-41 (2015).

http://dx.doi.org/10.1016/B978-0-444-62634-9.00001-1

[10] Grätzel, M.: Nanocrystalline Injection Solar Cells. John Wiley & Sons Ltd. 363-385 (2006).

[11] Kosyachenko, L.A.: Solar Cells – Thin-Film Technologies. Tech Janeza Trdine. **9**, 468 (2011).

[12] Mylvaganam, K., Chen, Y., Liu, W., Liu, M., Zhang, L.: Hard thin films: Applications and challenges. Anti-Abrasive Nanocoatings Curr. Futur. Appl. 544–567 (2014). https://doi.org/10.1016/B978-0-85709-211-3.00021-2

[13] Green, M.A.: Thin-film solar cells: Review of materials, technologies and commercial status. J. Mater. Sci. Mater. Electron. **18**, 15–19 (2007). https://doi.org/10.1007/s10854-007-9177-9

[14] Celik, I., Philips, A.B., Song, Z., Yan, Y., Ellingson, R.J., Heben, M.J., Apul, D.: Energy payback time (EPBT) and energy return on energy invested (EROI) of perovskite tandem photovoltaic solar cells. IEEE J. Photovoltaics. **8**, 305–309 (2018). https://doi.org/10.1109/JPHOTOV.2017.2768961

[15] Petti, C.J., Hilali, M.M., Prabhu, G.: Thin Films in Photovoltaics. Elsevier Inc. 313–359 (2012). http://dx.doi.org/10.1016/B978-1-4377-7873-1.00010-3

[16] Aberle, A.G.: Thin-film solar cells. Thin Solid Films. **517**, 4706–4710 (2009). https://doi.org/10.1016/j.tsf.2009.03.056

[17] Chopra, K.L., Paulson, P.D., Dutta, V.: Thin-Film Solar Cells: An overview. Prog. Photovoltaics Res. Appl. **12**, 69–92 (2004). https://doi.org/10.1002/pip.541

[18] Cernea, M.: Methods For Preparation of $BaTiO_3$ Thin Films. J. Optoelectron. Adv. Mater. **6**, 1349–1356 (2004)

[19] Grattan, K.T..: Optoelectronics of solar cells. Optics & Laser Technology. **36**, 1-113 (2004).

[20] Sengupta, S., Aggarwal, R., Raula, M.: A review on chemical bath deposition of metal chalcogenide thin films for heterojunction solar cells. J. Mater. Res. **38**, 142–153 (2023).

[21] Ali, N., Ahmed, R., Luo, J.T., Wang, M., Kalam, A., Al-Sehemi, A.G., Fu, Y.Q.: Advances in nanostructured homojunction solar cells and photovoltaic materials. Mater. Sci. Semicond. Process. **107**, 104810 (2020). https://doi.org/10.1016/j.mssp.2019.104810

[22] Nicholson, R.: Understanding the context. Springer Optim. Its Appl. **102**, 37–56 (2015). https://doi.org/10.1007/978-3-319-15030-7_3

[23] Dolai, S., Dey, R., Das, S., Hussain, S., Bhar, R., Pal, A.K.: Cupric oxide (CuO) thin films prepared by reactive d.c. magnetron sputtering technique for photovoltaic application. J. Alloys Compd. **724**, 456–464 (2017). https://doi.org/10.1016/j.jallcom.2017.07.061

[24] Soonmin, H., Hardani, Nandi, P., Mwankemwa, B.S., Malevu, T.D., Malik, M.I.: Overview on Different Types of Solar Cells: An Update. Appl. Sci. **13**, 1-39 (2023). https://doi.org/10.3390/app13042051

[25] Kant, N., Singh, P.: Review of next generation photovoltaic solar cell technology and comparative materialistic development. Mater. Today Proc. **56**, 3460–3470 (2022). https://doi.org/10.1016/j.matpr.2021.11.116

[26] Righini, G.C., Enrichi, F.: Solar cells’ evolution and perspectives: A short review. Solar Cells and Light Management. 1-32 (2019).

https://doi.org/10.1016/B978-0-08-102762-2.00001-X

[27] Deshmukh, M.A., Park, S.J., Hedau, B.S., Ha, T.J.: Recent progress in solar cells based on carbon nanomaterials. Sol. Energy. **220**, 953–990 (2021). https://doi.org/10.1016/j.solener.2021.04.001

[28] Deng, W., Ye, F., Xiong, Z., Chen, D., Guo, W., Chen, Y., Yang, Y., Altermatt, P.P., Feng, Z., Verlinden, P.J.: Development of High-efficiency Industrial p-type Multi-crystalline PERC Solar Cells with Efficiency Greater Than 21%. In: Energy Procedia. **92**. 721–729 (2016)

[29] Garud, S., Trinh, C.T., Abou-ras, D., Stannowski, B., Schlatmann, R., Rech, B., Amkreutz, D.: Toward High Solar Cell Efficiency with Low Material Usage : 15 % Efficiency with 14 μ m Polycrystalline Silicon on Glass. Solar RRL, **258**, 1–8 (2020). https://doi.org/10.1002/solr.202000058

[30] Cao, S., Cao, S., Yu, D., Yu, D., Lin, Y., Zhang, C., Zhang, C., Lu, L., Yin, M., Zhu, X., Chen, X., Chen, X., Li, D., Li, D., Lu, L.: Light Propagation in Flexible Thin-Film Amorphous Silicon Solar Cells with Nanotextured Metal Back Reflectors. ACS Appl. Mater. Interfaces. **12**, 26184–26192 (2020). https://doi.org/10.1021/acsami.0c05330

[31] Colombara, D., Werner, F., Schwarz, T., Cañero Infante, I., Fleming, Y., Valle, N., Spindler, C., Vacchieri, E., Rey, G., Guennou, M., Bouttemy, M., Manjón, A.G., Peral Alonso, I., Melchiorre, M., El Adib, B., Gault, B., Raabe, D., Dale, P.J., Siebentritt, S.: Sodium enhances indium-gallium interdiffusion in copper indium gallium diselenide photovoltaic absorbers. Nat. Commun. **9**, 1–12 (2018). https://doi.org/10.1038/s41467-018-03115-0

[32] Khatibi, A., Razi Astaraei, F., Ahmadi, M.H.: Generation and combination of the solar cells: A current model review. Energy Sci.

Eng. **7**, 305–322 (2019). https://doi.org/10.1002/ese3.292

[33] Kayes, B.M., Nie, H., Twist, R., Spruytte, S.G., Reinhardt, F., Kizilyalli, I.C., Higashi, G.S.: 27.6% Conversion efficiency, a new record for single-junction solar cells under 1 sun illumination. In: Conference Record of the IEEE Photovoltaic Specialists Conference. 4–8 (2011).

[34] Nakamura, M., Yamaguchi, K., Kimoto, Y., Yasaki, Y., Kato, T., Sugimoto, H.: Cd-Free $Cu(In,Ga)(Se,S)_2$ thin-film solar cell with record efficiency of 23.35%. IEEE J. Photovoltaics. **9**, 1863–1867 (2019). https://doi.org/10.1109/JPHOTOV.2019.2937218

[35] Green, M.A., Dunlop, E.D., Siefer, G., Yoshita, M., Kopidakis, N., Bothe, K., Hao, X.: Solar cell efficiency tables (Version 61). Prog. Photovoltaics Res. Appl. **31**, 3–16 (2023). https://doi.org/10.1002/pip.3646

[36] Matsui, T., Bidiville, A., Maejima, K., Sai, H., Koida, T., Suezaki, T., Matsumoto, M., Saito, K., Yoshida, I., Kondo, M.: High-efficiency amorphous silicon solar cells: Impact of deposition rate on metastability. Appl. Phys. Lett. **106**, 1-5 (2015). https://doi.org/10.1063/1.4907001

[37] Mirabi, E., Akrami Abarghuie, F., Arazi, R.: Erratum: Integration of buildings with third-generation photovoltaic solar cells: A review. Clean Energy. **5**, 741 (2021). https://doi.org/10.1093/ce/zkab051

[38] Würfel, U., Herterich, J., List, M., Faisst, J., Bhuyian, M.F.M., Schleiermacher, H.F., Knupfer, K.T., Zimmermann, B.: A 1 cm^2 Organic Solar Cell with 15.2% Certified Efficiency: Detailed Characterization and Identification of Optimization Potential. Sol. RRL. **5**, 1–7 (2021). https://doi.org/10.1002/solr.202000802

[39] Song, J., Wang, P., Chan, L., Chen, C.-M., Ho, W., Chen, S.: Efficiency Enhancement of Dye-Sensitized Solar Cells Using Ti–Nb Alloy Photoanodes with Mesoporous Oxide Surface. J. Electrochem. Soc. **167**, 046501 (2020). https://doi.org/10.1149/1945-7111/ab6fef

[40] Geisz, J.F., France, R.M., Schulte, K.L., Steiner, M.A., Norman, A.G., Guthrey, H.L., Young, M.R., Song, T., Moriarty, T.: Six-junction III–V solar cells with 47.1% conversion efficiency under 143 Suns concentration. Nat. Energy. **5**, 326–335 (2020). https://doi.org/10.1038/s41560-020-0598-5

[41] Futscher, M.H., Ehrler, B.: Efficiency Limit of Perovskite/Si Tandem Solar Cells. ACS Energy Lett. **1**, 863–868 (2016). https://doi.org/10.1021/acsenergylett.6b00405

[42] Nimesh, S., Chandra, R.: Theory, techniques and applications of nanotechnology in gene silencing. River Publishers. **2**, 1-218 (2011). https://doi.org/10.1201/9781003357193

[43] Tantra, R.: Nanomaterial characterization: An introduction. John Wiley & Sons. 1-317 (2016).

[44] Ju-Nam, Y., Lead, J.R.: Manufactured nanoparticles: An overview of their chemistry, interactions and potential environmental implications. Sci. Total Environ. **400**, 396–414 (2008). https://doi.org/10.1016/j.scitotenv.2008.06.042

[45] Li, Y., Somorjai, G.A.: Nanoscale advances in catalysis and energy applications. Nano Lett. **10**, 2289–2295 (2010). https://doi.org/10.1021/nl101807g

[46] Chuang, C.H.M., Brown, P.R., Bulović, V., Bawendi, M.G.: Improved performance and stability in quantum dot solar cells through band

alignment engineering. Nat. Mater. **13**, 796–801 (2014). https://doi.org/10.1038/nmat3984

[47] Rizwan, M., Shoukat, A., Ayub, A., Razzaq, B., Tahir, M.B.: Types and classification of nanomaterials. Nanomater. Synth. Charact. Hazards Saf. 31–54 (2021). https://doi.org/10.1016/b978-0-12-823823-3.00001-x

[48] Kailasa, S.K., Cheng, K.H., Wu, H.F.: Semiconductor nanomaterials-based fluorescence spectroscopic and matrix-assisted laser desorption/ionization (MALDI) mass spectrometric approaches to proteome analysis. Materials (Basel). **6**, 5763–5795 (2013). https://doi.org/10.3390/ma6125763

[49] Arole, V.M., Munde, S. V: Fabrication of Nanomaterials By Top-Down and Bottom-Up Approaches-an Overview. JAASTMaterial Sci. **1**, 2–89 (2014).

[50] Akin, S., Sonmezoglu, S.: Metal oxide nanoparticles as electron transport layer for highly efficient dye-sensitized solar cells. Elsevier Inc. 39-79 (2018). https://doi.org/10.1016/B978-0-12-813794-9.00002-8

[51] Omayio, E.O., Karimi, P.M., Njoroge, W.K., Mugwanga, F.K.: Current-voltage characteristics of p-CuO/n-ZnO:Sn Solar cell. NSP Nat. Sci. Publ. Cor. Int. J. Thin Film. Sci. Technol. **2**, 25 (2013).

[52] Chin, H.S., Cheong, K.Y., Razak, K.A.: Review on Oxides of antimony nanoparticlaes: Synthesis, properties, and applications. Materials Science. **45**, 5993-6008 (2010). https://doi.org/10.1007/s10853-010-4849-x

[53] Opitz-Coutureau, J., Fielicke, A., Kaiser, B., Rademann, K.: Antimony and bismuth oxide cluster ions. Phys. Chem. **3**, 3034–3041 (2001).

https://doi.org/10.1039/b103009b

[54] Cooper, M.A., Hawthorne, F.C.: Refinement of the crystal structure of schneiderhöhnite. Can. Mineral. **54**, 707–713 (2016). https://doi.org/10.3749/canmin.1500102

[55] Moseley, D.H., Bridges, C.A., Daemen, L.L., Zhang, Q., Mcguire, M.A., Cakmak, E., Hermann, R.P.: Structure and Anharmonicity of α - and β -Sb_2O_3 at Low Temperature. Crystals.1–11 (2023). https://doi.org/10.3390/ cryst13050752

[56] Hamilton, W.C.: The crystal structure of orthorhombic acetamide. Acta Crystallogr. **18**, 866–870 (1965). https://doi.org/10.1107/s0365110x65002128

[57] Yasir, M., Kuzmin, M., Punkkinen, M.P.J., Mäkelä, J., Tuominen, M., Dahl, J., Laukkanen, P., Kokko, K.: Synthesis and properties of crystalline thin film of antimony trioxide on the Si (1 0 0) substrate. Appl. Surf. Sci. **349**, 259–263 (2015). https://doi.org/10.1016/j.apsusc.2015.05.021

[58] Cebriano, T., Méndez, B., Piqueras, J.: Study of luminescence and optical resonances in Sb_2O_3 micro- and nanotriangles. J. Nanoparticle Res. **14**, (2012). https://doi.org/10.1007/s11051-012-1215-8

[59] Allen, J.P., Carey, J.J., Walsh, A., Scanlon, D.O., Watson, G.W.: Electronic structures of antimony oxides. J. Phys. Chem. C. **117**, 14759–14769 (2013). https://doi.org/10.1021/jp4026249

[60] Kadhim, W.K.: Preparation and Studying the Optical Properties of (Sb_2O_3) Thin Films. J. Univ. BABYLON Pure Appl. Sci. **26**, 249–256 (2018). https://doi.org/10.29196/jubpas.v26i10.1881

[61] Tigau, N., Ciupina, V., Prodan, G.: Structural, optical and electrical

properties of Sb_2O_3 thin films with different thickness. J. Optoelectron. Adv. Mater. **8**, 37–42 (2006).

[62] Tigau, N., Condurache-Bota, S., Drasovean, R., Cringanu, J., Gavrila, R.: Vacuum annealing effect on the structural and optical properties of antimony trioxide thin films. Rom. J. Phys. **62**, (2017).

[63] Divya, K. V, Abraham, K.E.: Ag nanoparticle decorated Sb_2O_3 thin film: synthesis, characterizations and application. Nano Express. **1**, (2020). https://doi.org/10.1088/2632-959X/aba103

[64] Akinay, Y., Kazici, H.C., Akkuş, I.N., Salman, F.: Synthesis of 3D Sn doped Sb_2O_3 catalysts with different morphologies and their effects on the electrocatalytic hydrogen evolution reaction in acidic medium. Ceram. Int. **47**, 29515–29524 (2021). https://doi.org/10.1016/j.ceramint.2021.07.278

[65] Song, S., Cho, H.W., Jeong, J., Yoon, Y.J., Park, S.Y., Song, S., Woo, B.H., Jun, Y.C., Walker, B., Kim, J.Y.: Dichroic Sb_2O_3/Ag/ Sb_2O_3 Electrodes for Colorful Semitransparent Organic Solar Cells. Sol. RRL. **4**, (2020). https://doi.org/10.1002/solr.202000201

[66] Nemade, K.R., Waghuley, S.A.: Role of defects concentration on optical and carbon dioxide gas sensing properties of Sb_2O_3/graphene composites. Opt. Mater. (Amst). **36**, 712–716 (2014). https://doi.org/10.1016/j.optmat.2013.11.024

[67] Tudorache, F., Tigau, N., Condurache-Bota, S.: Humidity sensing characteristics of Sb_2O_3 thin films with transitional electrical behavior. Sensors Actuators, A Phys. **285**, 134–141 (2019). https://doi.org/10.1016/j.sna.2018.11.002

[68] Bai, H., Guo, H., Wang, J., Dong, Y., Liu, B., Guo, F., Chen, D.,

Zhang, R., Zheng, Y.: Hydrogen gas sensor based on SnO_2 nanospheres modified with Sb_2O_3 prepared by one-step solvothermal route. Sensors Actuators, B Chem. **331**, 129441 (2021). https://doi.org/10.1016/j.snb.2021.129441

[69] Jamal, A., Rahman, M.M., Khan, S.B., Faisal, M., Akhtar, K., Rub, M.A., Asiri, A.M., Al-Youbi, A.O.: Cobalt doped antimony oxide nano-particles based chemical sensor and photo-catalyst for environmental pollutants. Appl. Surf. Sci. **261**, 52–58 (2012). https://doi.org/10.1016/j.apsusc.2012.07.066

[70] Li, Y., Lv, L., Wang, W., Zhang, J., Lin, J., Zhou, J., Dong, M., Gan, Y., Seok, I., Guo, Z.: Effects of chlorinated polyethylene and antimony trioxide on recycled polyvinyl chloride/acryl-butadiene-styrene blends: Flame retardancy and mechanical properties. Polymer (Guildf). **190**, 122198 (2020). https://doi.org/10.1016/j.polymer.2020.122198

[71] Niu, L., Xu, J., Yang, W., Zhao, J., Su, J., Guo, Y., Liu, X.: Research on nano- Sb_2O_3 flame retardant in char formation of PBT. Ferroelectrics. **523**, 14–21 (2018). https://doi.org/10.1080/00150193.2018.1391532

[72] Deng, M., Li, S., Hong, W., Jiang, Y., Xu, W., Shuai, H., Zou, G., Hu, Y., Hou, H., Wang, W., Ji, X.: Octahedral Sb_2O_3 as high-performance anode for lithium and sodium storage. Mater. Chem. Phys. **223**, 46–52 (2019). https://doi.org/10.1016/j.matchemphys.2018.10.043

[73] Liu, Y., Wang, H., Yang, K., Yang, Y., Ma, J., Pan, K., Wang, G., Ren, F., Pang, H.: Enhanced electrochemical performance of Sb_2O_3 as an anode for lithium-ion batteries by a stable cross-linked binder. Appl. Sci. **9**, 1–12 (2019). https://doi.org/10.3390/app9132677

[74] Du, Y., Zhang, Y., Li, L., Wang, N., Chai, Y.: Nano SnO_2 and Sb_2O_3

combined with CNTs as a high-capacity lithium storage material. Appl. Surf. Sci. **543**, 148870 (2021). https://doi.org/10.1016/j.apsusc.2020.148870

[75] Wang, Z., Zeng, F., Zhang, D., Wang, X., Yang, W., Cheng, Y., Li, C., Wang, L.: Equably-dispersed Sb/ Sb_2O_3 nanoparticles in ionic liquid-derived nitrogen-enriched carbon for highly reversible lithium/sodium storage. Electrochim. Acta. **395**, 139210 (2021). https://doi.org/10.1016/j.electacta.2021.139210

[76] Xavier, J.R.: Enhanced Adhesion and Corrosion Protection Properties of Surface Modified Sb_2O_3–Epoxy Nanocomposite Coatings on Mild Steel. J. Fail. Anal. Prev. **20**, 523–531 (2020). https://doi.org/10.1007/s11668-020-00847-4

[77] Zeng, D.W., Xie, C.S., Zhu, B.L., Song, W.L.: Characteristics of Sb_2O_3 nanoparticles synthesized from antimony by vapor condensation method. Mater. Lett. **58**, 312–315 (2004). https://doi.org/10.1016/S0167-577X(03)00476-2

[78] Hu, Y., Zhang, H., Yang, H.: Direct synthesis of Sb_2O_3 nanoparticles via hydrolysis-precipitation method. J. Alloys Compd. **428**, 327–331 (2007). https://doi.org/10.1016/j.jallcom.2006.03.057

[79] Yadav, N., Nagar, M., Bohra, R.: New sol-gel precursors for binary oxides of antimony, Sb_2O_3 (senarmonite) and α-Sb_2O_4: Synthesis and characterization of some ketoximate modified antimony(III) alkoxides. J. Sol-Gel Sci. Technol. **54**, 119–128 (2010). https://doi.org/10.1007/s10971-010-2166-0

[80] Kim, H.W., Kim, H.S., Na, H.G., Yang, J.C., Kebede, M.A., Lee, C.: Growth of Sb_2O_3 submicron rods by the thermal evaporation of a mixture of Zn and Sb powders. Ceram. Int. **37**, 593–598 (2011).

https://doi.org/10.1016/j.ceramint.2010.09.050

[81] Lin, S.S., Peng, C.K., Li, C.W.: Wettability and optical properties of SnO–SnO_2– Sb_2O_3 thin films deposited by simultaneous RF and DC magnetron sputtering. J. Alloys Compd. **770**, 433–440 (2019). https://doi.org/10.1016/j.jallcom.2018.08.110

[82] Ye, K., Liu, L., Huang, J., Nie, A., Zhai, K., Wang, B., Wen, F., Mu, C., Zhao, Z., Gong, Y., Xiang, J., Tian, Y., Liu, Z.: High-Performance Broadband Photodetectors of Heterogeneous 2D Inorganic Molecular Sb_2O_3/Monolayer MoS_2 Crystals Grown via Chemical Vapor Deposition. Adv. Opt. Mater. **8**, 1–9 (2020). https://doi.org/10.1002/adom.202000168

[83] Biver, M., Shotyk, W.: Stibiconite (Sb_3O_6OH), senarmontite (Sb_2O_3) and valentinite (Sb_2O_3): Dissolution rates at pH 2-11 and isoelectric points. Geochim. Cosmochim. Acta. **109**, 268–279 (2013). https://doi.org/10.1016/j.gca.2013.01.033

[84] Ungeheuer, K., Marszalek, K.W., Mitura-Nowak, M., Perzanowski, M., Jelen, P., Marszalek, M., Sitarz, M.: Influence of Cr Ion Implantation on Physical Properties of CuO Thin Films. Int. J. Mol. Sci. **23**, 1-14 (2022). https://doi.org/10.3390/ijms23094541

[85] Shabu, R., Moses Ezhil Raj, A., Sanjeeviraja, C., Ravidhas, C.: Assessment of CuO thin films for its suitablity as window absorbing layer in solar cell fabrications. Mater. Res. Bull. **68**, 1–8 (2015). https://doi.org/10.1016/j.materresbull.2015.03.016

[86] Welegergs, G.G., Gebretinsae, H.G., Tsegay, M.G., Mtshali, C., Mongwaketsia, N., Cloete, K., Nuru, Z.Y., Dube, S., Maaza, M.: Single-Layered Biosynthesized Copper Oxide (CuO) Nanocoatings as Solar-Selective Absorber. Appl. Sci. **13**, 1–15 (2023).

https://doi.org/10.3390/app13031867

[87] Qamar-Kane, H., Fall, A., Diop, L.: New MX_2 oxalato polynuclear adducts (M = Cd, Hg, Zn; X = Cl, Br): Synthesis and infrared study. Sci. Study Res. Chem. Eng. Biotechnol. Food Ind. **12**, 357–362 (2011).

[88] Akgul, F.A., Akgul, G., Yildirim, N., Unalan, H.E., Turan, R.: Influence of thermal annealing on microstructural, morphological, optical properties and surface electronic structure of copper oxide thin films. Mater. Chem. Phys. **147**, 987–995 (2014). https://doi.org/10.1016/j.matchemphys.2014.06.047

[89] Özmenteş, R., Temirci, C., Özkartal, A., Ejderha, K., Yildirim, N.: Characterization of CuO/n-Si heterojunction solar cells produced by thermal evaporation. Mater. Sci. Pol. **36**, 668–674 (2018). https://doi.org/10.2478/msp-2018-0092

[90] Abdelfatah, M., El Sayed, A.M., Ismail, W., Ulrich, S., Sittinger, V., El-Shaer, A.: SCAPS simulation of novel inorganic ZrS_2/CuO heterojunction solar cells. Sci. Rep. **13**, 4553 (2023). https://doi.org/10.1038/s41598-023-31553-4

[91] Johan, M.R., Suan, M.S.M., Hawari, N.L., Ching, H.A.: Annealing effects on the properties of copper oxide thin films prepared by chemical deposition. Int. J. Electrochem. Sci. **6**, 6094–6104 (2011). https://doi.org/10.1016/s1452-3981(23)19665-9

[92] Candan, I., Gezgin, S.Y., Baturay, S., Kilic, H.S.: Structural, Morphological, Optical Properties and Modelling of Ag Doped CuO/ZnO/AZO Solar Cell. J. Coat. Sci. Technol. **9**, 26–37 (2022). https://doi.org/10.6000/2369-3355.2022.09.04

[93] Absike, H., Essalhi, Z., Labrim, H., Hartiti, B., Baaalla, N., Tahiri, M.,

Jaber, B., Ez-zahraouy, H.: Synthesis of CuO thin films based on Taguchi design for solar absorber. Opt. Mater. (Amst). **118**, 111224 (2021). https://doi.org/10.1016/j.optmat.2021.111224

[94] Candan, I.: The Photovoltaic Performance of the Modelled CdS / CuO Solar Cell 1st International Conference on Scientific and Academic The Photovoltaic Performance of the Modelled CdS / CuO Solar Cell. ICSAR. 1-80 (2023). https://www.researchgate.net/publication/369649741

[95] Atri, A., Echabaane, M., Bouzidi, A., Harabi, I., Soucase, B.M., Ben Chaâbane, R.: Green synthesis of copper oxide nanoparticles using Ephedra Alata plant extract and a study of their antifungal, antibacterial activity and photocatalytic performance under sunlight. Heliyon. **9**, 1–16 (2023). https://doi.org/10.1016/j.heliyon.2023.e13484

[96] Abdelfatah, M., Salah, H., Bakry, M., Ismail, W., El-Shaer, A., Abdelgawad, S.: Influence of band gap and carrier concentration on ZnO/CuO solar cells performance. Egypt. J. Solids. **43**, 158–173 (2021). https://doi.org/10.21608/ejs.2021.92116.1018

[97] Ali M. B., Rajpar A.H., Salih E. Y., Ahmed E. M.: Preparation and Photovoltaic Evaluation of CuO@Zn(Al)O- Mixed Metal Oxides for Dye Sensitized Solar Cell. Nanomaterials. **13**, 1–11 (2023). https://doi.org/10.3390/nano13050802

[98] Steinhauer, S., Brunet, E., Maier, T., Mutinati, G.C., Köck, A., Freudenberg, O., Gspan, C., Grogger, W., Neuhold, A., Resel, R.: Gas sensing properties of novel CuO nanowire devices. Sensors Actuators, B Chem. **187**, 50–57 (2013). https://doi.org/10.1016/j.snb.2012.09.034

[99] Feng, J.K., Xia, H., Lai, M.O., Lu, L.: Electrochemical performance of CuO nanocrystal film fabricated by room temperature sputtering. Mater.

Res. Bull. **46**, 424–427 (2011). https://doi.org/10.1016/j.materresbull.2010.12.006

[100] Khiavi, N.D., Katal, R., Eshkalak, S.K., Masudy-Panah, S., Ramakrishna, S., Jiangyong, H.: Visible light driven heterojunction photocatalyst of CuO-Cu2O thin films for photocatalytic degradation of organic pollutants. Nanomaterials. **9**, 1-12 (2019). https://doi.org/10.3390/nano9071011

[101] Hajilou, R., Sedghi Gamchi, H.: Irreversibility Line and Enhancement of Magnetic Flux Pinning in Sm-Doped Y_{123} Superconductor with CuO Nanoparticles. J. Low Temp. Phys. **198**, 70–89 (2020). https://doi.org/10.1007/s10909-019-02244-0

[102] Yousefizad, M., Zarasvand, M.M., Baqeritabar, M., Ghezelayagh, M.M., Farahi, A., Ghafouri, T., Raissi, F., Zeidabadi, M.A., Manavizadeh, N.: Performance investigation of low-power flexible n-ZnO/p-CuO/n-ZnO heterojunction bipolar transistor: Simulation study. Micro and Nanostructures. 207594 (2023). https://doi.org/10.1016/j.micrna.2023.207594

[103] Masudy-Panah, S., Kakran, M., Lim, Y.F., Chua, C.S., Tan, H.R., Dalapati, G.K.: Graphene nanoparticle incorporated CuO thin film for solar cell application. J. Renew. Sustain. Energy. **8**, 1-8 (2016). https://doi.org/10.1063/1.4961590

[104] Iqbal, M., Thebo, A.A., Shah, A.H., Iqbal, A., Thebo, K.H., Phulpoto, S., Mohsin, M.A.: Influence of Mn-doping on the photocatalytic and solar cell efficiency of CuO nanowires. Inorg. Chem. Commun. **76**, 71–76 (2017). https://doi.org/10.1016/j.inoche.2016.11.023

[105] Iqbal, K., Ikram, M., Afzal, M., Ali, S.: Efficient, low-dimensional nanocomposite bilayer CuO/ZnO solar cell at various annealing

temperatures. Mater. Renew. Sustain. Energy. **7**, 1–7 (2018). https://doi.org/10.1007/s40243-018-0111-2

[106] Moumen, A., Hartiti, B., Comini, E., El khalidi, Z., Arachchige, H.M.M.M., Fadili, S., Thevenin, P.: Preparation and characterization of nanostructured CuO thin films using spray pyrolysis technique. Superlattices Microstruct. **127**, 2–10 (2019). https://doi.org/10.1016/j.spmi.2018.06.061

[107] Divya, K. V., Kurien, N.A., John, N.R., Abraham, K.E.: The effect of zinc doping on the surface roughness, near IR transmitting and reflecting properties of antimony trioxide thin film. AIP Conf. Proc. **2162**, 1–5 (2019). https://doi.org/10.1063/1.5130341

[108] Abass, K. H., Obaid N. H.: 0.006wt.%Ag-Doped Sb_2O_3 Nanofilms with Various Thickness: Morphological and optical properties. J. Phys. Conf. Ser. **1294**, 1–10 (2019). https://doi.org/10.1088/1742-6596/1294/2/022005

[109] Yeom, H.R., Song, S., Park, S.Y., Ryu, H.S., Kim, J.W., Heo, J., Cho, H.W., Walker, B., Ko, S.J., Woo, H.Y., Kim, J.Y.: Aesthetic and colorful: Dichroic polymer solar cells using high-performance Fabry-Pérot etalon electrodes with a unique Sb_2O_3 cavity. Nano Energy. **77**, 1-9 (2020). https://doi.org/10.1016/j.nanoen.2020.105146

[110] Shinde, Y.P., Sonone, P.N., Kendale, R.K., Koinkar, P.M., Ubale, A.U.: Growth of hexagonal shape nanostructured Sb_2O_3 thin films by spray pyrolysis and their structural, morphological, electrical and optical properties. J. Mater. Sci. Mater. Electron. **31**, 17432–17439 (2020). https://doi.org/10.1007/s10854-020-04299-2

[111] Patel, D.B., Chauhan, K.R.: 50% transparent solar cells of CuOx/TiO_2: Device aspects. J. Alloys Compd. **842**, 1-7 (2020).

https://doi.org/10.1016/j.jallcom.2020.155594

[112] Siddiqui, H., Parra, M.R., Pandey, P., Qureshi, M.S., Haque, F.Z.: Utility of copper oxide nanoparticles (CuO-NPs) as efficient electron donor material in bulk-heterojunction solar cells with enhanced power conversion efficiency. J. Sci. Adv. Mater. Devices. **5**, 104–110 (2020). https://doi.org/10.1016/j.jsamd.2020.01.004

[113] Tuama, A.N., Abass, K.H., Bin Agam, M.A.: Efficiency enhancement of nano structured Cu_2O:Ag/ laser etched silicon-thin films fabricated via vacuum thermal evaporation technique for solar cell application. Optik (Stuttg). **247**, 167980 (2021). https://doi.org/10.1016/j.ijleo.2021.167980

[114] Ashika, S.A., Balamurugan, S., Fathima, T.K.S.: Room temperature single-step synthesis of cubic Sb_2O_3 phase and its characterization studies. Emergent Mater. **5**, 227–236 (2022). https://doi.org/10.1007/s42247-022-00372-0

[115] Qassim, Z., Al-Ogaili, A.O.M., Abass, K.H.: Morphology of Copper Oxide Nano-Layer Prepared Via Thermal Evaporation Technique. NeuroQuantology. **20**, 87–94 (2022). https://doi.org/10.14704/nq.2022.20.3.nq22046

[116] Wisz, G., Sawicka-Chudy, P., Wal, A., Sibiński, M., Potera, P., Yavorskyi, R., Nykyruy, L., Płoch, D., Bester, M., Cholewa, M., Chernikova, O.M.: Structure Defects and Photovoltaic Properties of TiO_2:ZnO/CuO Solar Cells Prepared by Reactive DC Magnetron Sputtering. Appl. Sci. **13**, 3613 (2023). https://doi.org/10.3390/app13063613

[117] Jha, K.N., Taneja, N.D.: Vacuum Deposition Plant for Thin Film Circuit. IETE J. Res. **12**, 478–483 (1966).

https://doi.org/10.1080/03772063.1966.11485352

[118] Wasa, K., Kitabatake, M., Adachi, H.: Thin Film Materials Technology. Mater. Technol. 17–69 (2004).

[119] Mattox, D.M.: The Foundations of Vacuum Coating Technology. William Andrew. 1-66 (2003).

[120] Lafferty, J.M.: Vacuum: From art to exact science. Phys. Today. **34**, 211–231 (1981). https://doi.org/10.1063/1.2914357

[121] Wang, S., Li, X., Wu, J., Wen, W., Qi, Y.: Fabrication of efficient metal halide perovskite solar cells by vacuum thermal evaporation: A progress review. Curr. Opin. Electrochem. **11**, 130–140 (2018). https://doi.org/10.1016/j.coelec.2018.10.006

[122] Keqiang, Q., Rongliang, Z., Shinde, Y.P., Sonone, P.N., Ubale, A.U.: Synthesis and characterization of hexagonal and tetrahedral nanocrystalline Sb_2O_3 thin films prepared by chemical spray pyrolysis technique. J. Alloys Compd. **831**, 154777 (2020). https://doi.org/10.1016/j.jallcom.2020.154777

[123] Divya, K. V., Thomas, P., Abraham, K.E.: Exploring the photoluminescence emission behaviour of vacuum deposited Sb_2O_3 thin film having randomly oriented thorn like structures. Mater. Sci. Semicond. Process. **82**, 82–91 (2018). https://doi.org/10.1016/j.mssp.2018.03.031

[124] Search, H., Journals, C., Contact, A., Iopscience, M., Address, I.P.: Surface X-ray diffraction. Iopscience. **55**, 599-651 (1992).

[125] Bunaciu, A.A., Udriştioiu, E. gabriela, Aboul-Enein, H.Y.: X-Ray Diffraction: Instrumentation and Applications. Crit. Rev. Anal. Chem. **45**, 289–299 (2015). https://doi.org/10.1080/10408347.2014.949616

[126] Chen, Q.: Collective model of chiral and wobbling modes in nuclei. Sci. Sin. Phys. Mech. Astron. **46**, 322 (2016). https://doi.org/ 10.1007/978-3-642-16635-8

[127] Fewster, P.F.: The Limits of X-ray Diffraction Theory. Crystals. **13**, 521 (2023). https://doi.org/10.3390/cryst13030521

[128] Stanjek, H.: Basics of X-ray Diffraction. Hyperfine Interactions.**154**, 107–119 (2004).

[129] Moram, M.A., Vickers, M.E.: X-ray diffraction of III-nitrides. Reports Prog. Phys. **72**, 036502 (2009). https://doi.org/10.1088/0034-4885/72/3/036502

[130] Jones, F.W., A, P.R.S.L.: The measurement of particle size by the X-ray method. Proc. R. Soc. London. Ser. A. Math. Phys. Sci. **166**, 16–43 (1938). https://doi.org/10.1098/rspa.1938.0079

[131] Patterson, A.L.: The scherrer formula for X-ray particle size determination. Phys. Rev. **56**, 978–982 (1939). https://doi.org/10.1103/PhysRev.56.978

[132] Kittel, C., Fan, H.Y.: Introduction to Solid State Physics. Am. J. Phys. **25**, 330 (1957). https://doi.org/10.1119/1.1934457

[133] Leggett, G.: Atomic force microscopy. Phy. Today. 50–58 (2005). https://doi.org/10.1002/0470014229.ch1

[134] V. Bellitto: Atomic Force Microscopy - Imaging, Meas., Manip. Surfs. at the Atomic Scale. InTech Janeza Trdine. 9, 267 (2012).

[135] Hiesgen, R., Friedrich, K.A.: Atomic force microscopy. In: John Wiley & Sons, Inc. 395–421 (2011). https://doi.org/10.4011/shikizai.93.321

[136] Marrone, P.: Atomic Force Microscopy. Oxford University Press. 15, 583-605 (2013). https://doi.org/10.1093/acprof:oso/9780199570454.003.0007

[137] Johnson, D., Oatley-Radcliffe, D.L., Hilal, N.: Atomic Force Microscopy (AFM). In: Membrane Characterization. Elsevier B.V. 115–144. (2017). http://dx.doi.org/10.1016/B978-0-444-63776-5.00007-3

[138] Khan, M.K., Wang, Q.Y., Fitzpatrick, M.E.: Atomic Force Microscopy (AFM) for Materials Characterization. Elsevier Ltd. 1–16. (2016). http://dx.doi.org/10.1016/B978-0-08-100040-3.00001-8

[139] Meyer, E.: Atomic force microscopy. Prog. Surf. Sci. **41**, 3–49 (1992).

[140] Marinello, F.: Atomic force microscopy. CIRP Ency. Prod. Eng. 1-5 (2017). http:// doi.org/10.1007/978-3-642-35950-7_6577-3

[141] Hiesgen, R., Friedrich, K.A.: Atomic force microscopy. PEM Fuel Cell Diagnostic Tools. 395–421 (2011). https://doi.org/10.4011/shikizai.93.321

[142] Chen, G.-T., Su, S.-H., Hou, C.-C., Yokoyama, M.: Effects of Thermal Annealing on Performance of Organic Light-Emitting Diodes. J. Electrochem. Soc. **154**, J159 (2007). https://doi.org/10.1149/1.2710226

[143] Soonmin, H.: Atomic force microscopy studies on the surface morphologies of chemical bath deposited CuS thin films. Orient. J. Chem. **32**, 1515–1519 (2016). https://doi.org/10.13005/ojc/320325

[144] Tigau, N., Ciupina, V., Prodan, G., Rusu, G.I., Gheorghies, C., Vasile, E.: The influence of heat treatment on the electrical conductivity of antimony trioxide thin films. J. Optoelectron. Adv. Mater. **5**, 907–912

(2003).

[145] Ristova, M., Kuo, Y., Lee, S.: Influence of the roughness of molybdenum back electrode on the photodiode characteristics under He-Ne illumination. Semicond. Sci. Technol. **18**, 788–793 (2003). https://doi.org/10.1088/0268-1242/18/8/312

[146] Ruiz-Castell, P.: Scanning electron microscopy. In: Between Making And Knowing: Tools In The History Of Materials Research. **pp**. 503–512 (2020).

[147] Microanalysis, X., Microscopy, A.E.: Basic SEM Imaging. Plenum Press. 3–7 (1990).

[148] Vernon, K. D.: Scanning Electron Microscopy: an introduction. Analysis. **13**, 40–44 (2000).

[149] Zhou, W., Apkarian, R., Wang, Z.L., Joy, D.: Fundamentals of scanning electron microscopy (SEM). In: Scanning Microscopy for Nanotechnology: Techniques and Applications. 1–40 (2007).

[150] Cengiz, T.: Scanning Electron Microscopy. Intech. **11**, 13 (2016). http://dx.doi.org/10.5772/intechopen.103956

[151] Dutta, J., Hofmann, H.: Nanomaterials. Mater. Today. **19**, 2–5 (2019)

[152] Yacobi, B.G.: Semiconductor Materials - An Introduction to Basic Principles. Chem. Infor. and Mod. 53, 1689-1699 (2003).

[153] Bari, R.H., Ganesan, V., Potadar, S., Patil, L.A.: Structural, optical and electrical properties of chemically deposited copper selenide films. Bull. Mater. Sci. **32**, 37–42 (2009). https://doi.org/10.1007/s12034-009-0006-z

[154] Mäntele, W., Deniz, E.: UV–VIS absorption spectroscopy: Lambert-Beer reloaded. Spectrochim. Acta - Part A Mol. Biomol. Spectrosc.

173, 965–968 (2017). https://doi.org/10.1016/j.saa.2016.09.037

[155] Pankove, J.I.: Optical processes in semiconductors Prentice-Hall. New Jersey. 92, 36 (1971).

[156] Tauc, J., Menth, A., Wood, D.L.: Optical and magnetic investigations of the localized states in semiconducting glasses. Phys. Rev. Lett. **25**, 749–752 (1970). https://doi.org/10.1103/PhysRevLett.25.749

[157] Hassanien, A.S., Akl, A.A.: Effect of Se addition on optical and electrical properties of chalcogenide CdSSe thin films. Superlattices Microstruct. **89**, 153–169 (2016). https://doi.org/10.1016/j.spmi.2015.10.044

[158] Prasad, R.N.A., Venkata Siva, B., Neeraja, K., Krishna Mohan, N., Rojas, J.I.: Effect of modifier oxides on spectroscopic and optical properties of Pr_3+ doped PbO-Ro_2O_3–WO_3–B_2O_3 glasses (with Ro_2O = Sb_2O_3, Al_2O_3, and Bi_2O_3). J. Lumin. **230**, 117666 (2021). https://doi.org/10.1016/j.jlumin.2020.117666

[159] Urbach, F.: The long-wavelength edge of photographic sensitivity and of the electronic Absorption of Solids. Phys. Rev. **92**, 1324 (1953). https://doi.org/10.1103/PhysRev.92.1324

[160] Melsheimer, J., Ziegler, D.: Band gap energy and Urbach tail studies of amorphous, partially crystalline and polycrystalline tin dioxide. Thin Solid Films. **129**, 35–47 (1985). https://doi.org/10.1016/0040-6090(85)90092-6

[161] Ikhmayies, S.J., Ahmad-Bitar, R.N.: A study of the optical bandgap energy and Urbach tail of spray-deposited CdS:In thin films. J. Mater. Res. Technol. **2**, 221–227 (2013). https://doi.org/10.1016/j.jmrt.2013.02.012

[162] Sharba, K.S., Alkelaby, A.S., Sakhil, M.D., Abass, K.H., Habubi, N.F., Chiad, S.S.: Enhancement of urbach energy and dispersion parameters of polyvinyl alcohol with Kaolin additive. NeuroQuantology. **18**, 66–73 (2020). https://doi.org/10.14704/nq.2020.18.3.NQ20152

[163] Moore, E.A., Smart, L.E.: Optical Properties of Solids. Solid State Chem. An Introd. **1269**, 283–314 (2020). https://doi.org/10.1201/b12047-14

[164] Bhattacharya, J.C.: Refractive index measurement. Opt. Laser Technol. **19**, 29–32 (1987). https://doi.org/10.1016/0030-3992(87)90008-9

[165] Htwe, Z.M., Zhang, Y.D., Yao, C.B., Li, H., Li, H.Y., Yuan, P.: Investigation of third order nonlinear optical properties of undoped and indium doped zinc oxide (InZnO) thin films by nanosecond Z-scan technique. Opt. Mater. (Amst). **52**, 6–13 (2016). https://doi.org/10.1016/j.optmat.2015.12.004

[166] Shrividhya, T., Ravi, G., Hayakawa, Y., Mahalingam, T.: Determination of structural and optical parameters of CuO thin films prepared by double dip technique. J. Mater. Sci. Mater. Electron. **25**, 3885–3894 (2014). https://doi.org/10.1007/s10854-014-2103-z

[167] Benramdane, N., Murad, W.A., Misho, R.H., Ziane, M., Kebbab, Z.: A chemical method for the preparation of thin films of CdO and ZnO. Mater. Chem. Phys. **48**, 119–123 (1997). https://doi.org/10.1016/S0254-0584(97)80104-6

[168] Elmeleegi, H.A., El Mandouh, Z.E.S., Moez, A.A.: Influence of composition on the structure and optoelectronic properties of $Pb_xIn_{25-x}Se_{75}$ thin films. Turkish J. Phys. **38**, 145–154 (2014). https://doi.org/10.3906/fiz-1306-9

[169] El-Denglawey, A., Makhlouf, M.M., Dongol, M.: The effect of thickness on the structural and optical properties of nano Ge-Te-Cu films. Results Phys. **10**, 714–720 (2018). https://doi.org/10.1016/j.rinp.2018.07.023

[170] Mishjil, K.A., Chiad, S.S., Abass, K.H., Habubi, N.F.: Effect of Al Doping on Structural and Optical Parameters of ZnO Thin Films. Mater. Focus. **5**, 471–475 (2016). https://doi.org/10.1166/mat.2016.1344

[171] Aslaksen, E.W.: Optical Dispersion and the Structure of Solids. Phys. Rev. Lett. **24**, 767–768 (1970). https://doi.org/10.1103/PhysRevLett.24.767

[172] Wemple, S.H.: Refractive-index behavior of amorphous semiconductors and glasses. Phys. Rev. B. **7**, 3767–3777 (1973). https://doi.org/10.1103/PhysRevB.7.3767

[173] Hassanien, A.S., Akl, A.A.: Influence of composition on optical and dispersion parameters of thermally evaporated non-crystalline $Cd_{50}S_{50-x}Se_x$ thin films. J. Alloys Compd. **648**, 280–290 (2015). https://doi.org/10.1016/j.jallcom.2015.06.231

[174] Jawad, Z. M., Abass, K. H.: Structural and Dispersion Parameters of PVA-PAAm-CuNW for Optical and antibacterial applications. HIV nursing. 7 (2022). https://doi.org/10.31838/hiv22.02.164

[175] Wemple, S.H., DiDomenico, M.: Behavior of the electronic dielectric constant in covalent and ionic materials. Phys. Rev. B. **3**, 1338–1351 (1971). https://doi.org/10.1103/PhysRevB.3.1338

[176] R S Popovic: Hall Effect Devices–Magnetic Sensors and Characterization of Semiconductors. New Electron. **15**, 82–84 (2004).

[177] Van der Pauw, L.J.: A METHOD OF MEASURING SPECIFIC RESISTIVITY AND HALL EFFECT OF DISCS OF ARBITRARY SHAPE. Philips Res. Repts. **13**,1-9 (1958).

[178] Shaban, S.M., Kamil, F.Q.: Effect of Pb additive on the Grain size and D . C Electrical Properties of Cd 1-x Pb x Se Thin Films. **5**, 1698–1702 (2015).

[179] Epstein, M.: Hall-Effect Devices. Sens. and Actuators. **17**, 39–53 (1989). https://doi.org/10.1109/TMAG.1967.1066071

[180] Woolley, J.C.: Introduction to solid state physics. Mech. and Phy. Solids. **6**, 83 (1957).

[181] Khatibi, A., Razi Astaraei, F., Ahmadi, M.H.: Generation and combination of the solar cells: A current model review. Ener. Scie. and Engineering. **7**, 305-322 (2019). https://doi.org/10.1002/ese3.292

[182] Kietzke, T.: Recent advances in organic solar cells. Adva. in OptoElectronics. 2007, 40285 (2007). https://doi:10.1155/2007/40285

[183] Buryk, O., Druzhinin, A., Yerokhov, V.: Calculation of Efficiency in Solar Cell Based on Porous Silicon. In: Proceedings - 15th International Conference on Advanced Trends in Radioelectronics, Telecommunications and Computer Engineering. 486–490 (2020).

[184] Abass, K.H., Adil, A., Alrubaie, A.J., Rabee, B.H., Kadim, A.M., Talib, S.H., Mohammed, K.A., Jassim, A. saeed.: Fabrication and Characterization of p-SnS/n-Si Solar Cell by Thermal Evaporation Technique and the Effect of Ag-doped on its Efficiency. Int. J. Nanosci. **22**, 0.1 (2022).

[185] Tuama, A.N., Abass, K.H., Agam, M.A.: Fabrication and characterization of Cu_2O:Ag/Si solar cell via thermal evaporation

technique. Int. J. Nanoelectron. Mater. **13**, 601–614 (2020).

[186] Shaji, S., Arato, A., O’Brien, J.J., Liu, J., Alan Castillo, G., Mendivil Palma, M.I., Das Roy, T.K., Krishnan, B.: Chemically deposited Sb_2S_3 thin films for optical recording. J. Phys. D. Appl. Phys. **43**, 12-17 (2010). https://doi.org/10.1088/0022-3727/43/7/075404

[187] Bates, S., Zografi, G., Engers, D., Morris, K., Crowley, K., Newman, A.: Analysis of amorphous and nanocrystalline solids from their X-ray diffraction patterns. Pharm. Res. **23**, 2333–2349 (2006). https://doi.org/10.1007/s11095-006-9086-2

[188] Tarrad, S.N., Hussain, S.A., Al-Asady, F.H.: Study of structural, optical and sensitivity properties of NiPc thin film prepared by thermal evaporation. Int. Conf. Emerg. Appl. Mater. Sci. Technol. Iceamst. **2235**, 020036 (2020). https://doi.org/10.1063/5.0008854

[189] Hassan, E.S., Mubarak, T.H., Abass, K.H., Chiad, S.S., Habubi, N.F., Rahid, M.H., Khadayeir, A.A., Dawod, M.O., Al-Baidhany, I.A.: Structural, Morphological and Optical Characterization of Tin Doped Zinc Oxide Thin Film by (SPT). J. Phys. Conf. Ser. **1234**, 1-10 (2019). https://doi.org/10.1088/1742-6596/1234/1/012013

[190] Li, Y., Jia, R., Zhang, W., Ni, M., Wang, Z.: Stranski-Krastanov model grown ZnO thin films. 5th Int. Conf. Manip. Manuf. Meas. Nanoscale, 3M-NANO 2015 - Conf. Proc. 286–289 (2016). https://doi.org/10.1109/3M-NANO.2015.7425463

[191] Ruiz-Castell, P.: Scanning electron microscopy. PNAS. **11**. 503–512 (2020). https://doi.org/10.1073/pnas.2302624120

[192] Jiang, D., Tang, Q., Weigend, F.: Superatomic Orbitals under Spin − Orbit Coupling. Phy. Chem. Letters. **25**, 3286-3289 (2014).

https://dx.doi.org/10.1021/jz501745z

[193] Divya, K. V., Abraham, K.E.: Multifunctional transition metal doped Sb_2O_3 thin film with high near-IR transmittance, anti-reflectance and UV blocking features. Appl. Surf. Sci. **493**, 1115–1124 (2019). https://doi.org/10.1016/j.apsusc.2019.07.062

[194] Jalili, S., Hajakbari, F., Hojabri, A.: Effect of silver thickness on structural, optical and morphological properties of nanocrystalline Ag/NiO thin films. J. Theor. Appl. Phys. **12**, 15–22 (2018). https://doi.org/10.1007/s40094-018-0275-2

[195] Mohammed, M.K.: Fabrication of ZnO:Al/Si solar cell and enhancement its efficiency via Al-doping. Nano Biomed. and Engin. 11, 170-177 (2010).

[196] Vuković, M., Branković, Z., Poleti, D., Rečnik, A., Branković, G.: Novel simple methods for the synthesis of single-phase valentinite Sb_2O_3. J. Sol-Gel Sci. Technol. **72**, 527–533 (2014). https://doi.org/10.1007/s10971-014-3469-3

[197] N.Esmaeel, S.: STUDY THE EFFECT OF THICKNESS ON THE OPTICAL PROPERTIES OF (Sb_2O_3) THIN FILMS PREPERD BY THERMAL EVAPORATION TECHNIQUE. J. Coll. Educ, 701-713 (2012).

[198] Tigau, N., Ciupina, V., Prodan, G.: The effect of substrate temperature on the optical properties of polycrystalline Sb_2O_3 thin films. J. Cryst. Growth. **277**, 529–535 (2005). https://doi.org/10.1016/j.jcrysgro.2005.01.056

[199] Mohamed, Z.Q., Al-Ogaili, A.O.M., Abass, K.H.: Morphology and optical properties of Cu_2O-Doped CuO nano films prepared via thermal

evaporation technique. In: AIP Conference Proceedings. **2475**, 1-13 (2023).

[200] Ali, A.I., Son, J.Y., Ammar, A.H., Abdel Moez, A., Kim, Y.S.: Optical and dielectric results of $Y_{0.225}Sr_{0.775}CoO_3\pm\delta$ thin films studied by spectroscopic ellipsometry technique. Results Phys. **3**, 167–172 (2013). https://doi.org/10.1016/j.rinp.2013.08.004

[201] Lozovoy, K.A., Korotaev, A.G., Kokhanenko, A.P., Dirko, V. V, Voitsekhovskii, A. V: Surface & Coatings Technology Kinetics of epitaxial formation of nanostructures by Frank–van der Merwe , Volmer – Weber and Stranski – Krastanow growth modes. Surf. Coat. Technol. **384**, 125289 (2020). https://doi.org/10.1016/j.surfcoat.2019.125289

[202] Heo, H., Sung, J.H., Ahn, J., Ghahari, F., Taniguchi, T., Watanabe, K., Kim, P., Jo, M.: Frank – van der Merwe Growth versus Volmer – Weber Growth in Successive Stacking of a Few-Layer Bi_2Te_3/ Sb_2Te_3 by van der Waals Heteroepitaxy : The Critical Roles of Finite Lattice-Mismatch with Seed Substrates. Advan. Elect. Materials. **3**, 1–7 (2017). https://doi.org/10.1002/aelm.201600375

[203] Wang, H., Yao, Z., Jung, G.S., Markus, J., Wang, H., Yao, Z., Jung, G.S., Song, Q., Hempel, M.: Article Frank-van der Merwe growth in bilayer graphene Frank-van der Merwe growth in bilayer graphene. Matter. **4**, 3339–3353 (2021). https://doi.org/10.1016/j.matt.2021.08.017

[204] Caglar, M., Ilican, S., Caglar, Y.: Influence of dopant concentration on the optical properties of ZnO: In films by sol-gel method. Thin Solid Films. **517**, 5023–5028 (2009). https://doi.org/10.1016/j.tsf.2009.03.037

[205] Lovchinov, K., Marinov, G., Petrov, M., Tyutyundzhiev, N., Alexieva, G., Babeva, T.: INFLUENCE of DEPOSITION TEMPERATURE on the STRUCTURAL and OPTICAL PROPERTIES of ELECTROCHEMICALLY NANOSTRUCTURED ZnO FILMS. Comptes Rendus L'Academie Bulg. des Sci. **73**, 190–196 (2020). https://doi.org/10.7546/CRABS.2020.02.06

[206] Abass, K.H., Mohammed, M.K.: Fabrication of ZnO:Al/Si solar cell and enhancement its efficiency via Al-doping. Nano Biomed. Eng. **11**, 170–177 (2019). https://doi.org/10.5101/nbe.v11i2.p170-177

[207] Abass, K.H., Shinen, M.H., Alkaim, A.F.: Preparation of TiO_2 nanolayers via. sol-gel method and study the optoelectronic properties as solar cell applications. J. Eng. Appl. Sci. **13**, 9631–9637 (2018). https://doi.org/10.3923/jeasci.2018.9631.9637

[208] Obaid N. H., Abass, K. H.: Preparation and characterization of thermally evaporated Sb_2O_3 nano structure for a solar cells Applications. A thesis of Master. College of Education for Pure Sciences of University of Babylon (2019).

الخلاصة

تكنولوجيا الخلايا الشمسية السيليكونية التي تهيمن حاليًا على السوق تمتلك تكلفة عالية. من أجل استغلال الطاقة الشمسية بشكل فعال، يجب تكثيف البحث في المواد الجديدة (الأغشية الرقيقة) لإنتاج خلايا شمسية رخيصة وأكثر كفاءة. في هذا العمل، تم تحضير أغشية نانوية Sb_2O_3 نقية ومشوبة بأُكسيد النحاس بنسب وزنية مختلفة .wt(0.06، 0.04، 0.02) وبسُمك مختلف (40، 30، 20) نانومتر مرسبة على الزجاج (المورفولوجية، التركيبية، البصرية، والخصائص الكهربائية) وارضيات p-Si المحفورة بالليزر (خصائص كفاءة الخلايا الشمسية) في بيئة مفرغة (1×10^{-6}) ملي بار من خلال غرفة التبخير الحراري بمعدل ترسيب 0.3 نانومتر.ثانية$^{-1}$. الأغشية المحضرة خضعت للمعالجة الحرارية (التلدين) عند درجة حرارة 473 كلفن لمدة ساعتين.

نتيجة حيود الأشعة السينية أظهرت أن الأغشية النانوية Sb_2O_3 النقية لا تمتلك قمم مميزة، بينما تركيب الطور للاغشية النانوية Sb_2O_3: (0.06، 0.04، 0.02) wt.%CuO عند سُمك 40 نانومتر تظهر وجود قمة صغيرة واحدة عند (31.932°، 31.894°، و31.945°)=2θ على التوالي، وهو ما يتوافق مع معاملات ميلر (040).

تحليل AFM للأغشية النانوية Sb_2O_3 النقية والمشوبة بالنحاس يُظهر شكلًا موحدًا للسطح الحبيبي وتوزيعًا متجانسًا بالإضافة إلى تشتت جسيمات CuO داخل مصفوفة Sb_2O_3. تحليل SEM للأغشية النانوية يُظهر سطحًا أملسًا خاليًا من الجزر والفراغات ويتكون من جسيمات نانوية صغيرة بحجم حبm كروية (NPs). حجم جسيمات الأغشية النانوية يزداد بزيادة السُمك ونسب التشويب.

الخصائص البصرية (الامتصاصية، معامل الامتصاص، والثوابت البصرية) تزداد مع زيادة سُمك ونسب التشويب للأغشية النانوية. هذه السمات للأغشية النانوية يمكن توظيفها في الخلايا الشمسية حيث فجوة الطاقة للانتقال المباشر تقل بسبب اتساع المستويات الفرعية (طاقة أورباخ)، والتي تتفق مع قيمة متوسط فجوة الطاقة من طاقة المذبذب البسيط (Wemple and DiDomenico).

التغيرات في تركيب المادة (التشويب والسمك) تؤدي إلى تغير دوال فقدان الطاقة السطحية والحجمية. نظرا للسمك القليل جدًا للغشاء النانوي، وجد أن الطاقة السطحية أكبر من الطاقة الحجمية. معامل هول ينخفض وتركيز المادة الحاملة في العينات يزداد مع زيادة السُمك ونسبة التشويب للأغشية النانوية.

أداء الخلية الشمسية وكفاءتها تم تقييمها باستخدام منحنيات خصائص I-V تحت الظلام والإضاءة لـ Sb_2O_3/etched p-Si and Sb_2O_3:CuO/etched p-Si. وقد لوحظ أن الكفاءة تزداد مع زيادة سُمك الأغشية النانوية Sb_2O_3 وتزداد مع إضافة نسبة وزنية من CuO إلى Sb_2O_3. أعلى كفاءة كانت 5.965% مع (V_{oc} of 11 V, I_{sc} of 3 mA/cm^2, F.F of 0.180) للأغشية النانوية Sb_2O_3 النقية بسُمك 40 نانومتر، كذلك أعلى كفاءة كانت 7.625% مع (V_{oc} of 12 V, I_{sc} of 3.2 mA/cm^2, F.F of 0.198) لـ Sb_2O_3:0.06wt.%CuO عند نفس السُمك. تحسين كفاءة هذا العمل يمكن أن يعزى إلى الخصائص المعدلة للأغشية النانوية Sb_2O_3 بسبب تحقيق التجانس بواسطة التحكم في عملية الترسيب، السُمك القليل، ومساحة السطح العالية الناتجة عن صغر حجم الجسيمات وعملية الحفر بالليزر.

جمهورية العراق
وزارة التعليم العالي والبحث العلمي
جامعة بابل
كلية التربية للعلوم الصرفة
قسم الفيزياء

كفاءة الخلية الشمسية Sb_2O_3/السليكون المحفور المشوبة بجسيمات CuO النانوية

اطروحة مقدمة
الى مجلس كلية التربية للعلوم الصرفة في جامعة بابل وهي جزء من متطلبات
نيل درجة الدكتوراه فلسفة في التربية/ الفيزياء

من قبل الطالب
علي عبد عون عطيه حمد العزاوي

بكالوريوس علوم فيزياء
جامعة بابل 2010 م

ماجستير تربية فيزياء
جامعة بابل 2019 م

بأشراف
أ. د. فؤاد شاكر هاشم **أ. د. خالد حنين عباس**

2023م **1445هـ**